Title
Crustal extension and magmatism during the mid-Cenozoic ignimbrite flare-up in the Guazapares Mining District and Cerocahui basin regions, northern Sierra Madre Occidental, western Chihuahua, Mexico

Author
Murray, Bryan Patrick

Publication Date
2014

UNIVERSITY OF CALIFORNIA

Santa Barbara

Crustal extension and magmatism during the mid-Cenozoic ignimbrite flare-up in the Guazapares Mining District and Cerocahui basin regions, northern Sierra Madre Occidental, western Chihuahua, Mexico

A dissertation submitted in partial satisfaction of the

requirements for the degree Doctor of Philosophy

in Geological Sciences

by

Bryan Patrick Murray

Committee in charge:

Professor Phillip Gans, Chair

Professor Douglas Burbank

Professor John Cottle

June 2014

The dissertation of Bryan Patrick Murray is approved.

Douglas Burbank

John Cottle

Phillip Gans, Committee Chair

June 2014

Crustal extension and magmatism during the mid-Cenozoic ignimbrite flare-up in the Guazapares Mining District and Cerocahui basin regions, northern Sierra Madre Occidental, western Chihuahua, Mexico

by

Bryan Patrick Murray

ACKNOWLEDGEMENTS

I thank Cathy Busby for her role as primary advisor for this dissertation, and for assisting with reviewing all of the chapters of this dissertation. I thank Luca Ferrari for detailed informal reviews and discussions of this dissertation, and for his assistance while I worked in Juriquilla. I also thank my PhD committee, Phil Gans, Doug Burbank, and John Cottle, for their helpful reviews and critiques of my dissertation.

Each chapter is the result of intellectual collaboration, with myself being the primary author and contributor. Co-authorship of chapter 1 is shared with Cathy Busby, Luca Ferrari, and Luigi Solari; co-authorship of chapter 2 is shared with Cathy Busby; and co-authorship of chapter 3 is shared with Cathy Busby and Angeles Verde-Ramírez.

For financial, logistical, and intellectual contributions, I thank Paramount Gold & Silver Corp., Larry Segerstrom, Danny Sims, Dana Durgin, Armando Valtierra, and Javier Martinez; I also thank Denis Norton for arranging this support. Additional financial support was provided by a UC Mexus grant (2009-2010) to Cathy Busby and Elena Centeno-García, National Science Foundation grant EAR-1019559 to Cathy Busby, a GSA student research grant and UCSB Earth Science and Geography department awards to myself.

Dana Roeber Murray, Jordan Lewis, Adrienne Kentner, and Angeles Verde-Ramírez assisted in the field. Luigi Solari and Carlos Ortega-Obregón (Universidad Nacional Autónoma de México, UNAM) assisted with LA-ICP-MS analyses. Elena Centeno-García and Rufino Lozano Santa Cruz (UNAM) assisted with whole-rock geochemical analyses.

I thank Graham Andrews and Scott Bryan for detailed formal reviews of Chapter 1, and comments by Carol Frost and Keith Putirka helped improve this chapter.

Lastly, and mostly, I thank my wife, Dana Roeber Murray, daughter, Coral, and my family. I couldn't have finished this dissertation without your support!

VITA OF BRYAN PATRICK MURRAY
June 2014

EDUCATION

Bachelor of Science in Geology-Paleobiology, University of California, Los Angeles, 2003

Master of Science in Geology, University of California, Los Angeles, 2007

Doctor of Philosophy in Geological Sciences, University of California, Santa Barbara, 2014

PROFESSIONAL EMPLOYMENT

2013-14: Earth Sciences Instructor, Antelope Valley College
2013: Geology Instructor, El Camino College
2012-13: Geology Lecturer, Pierce College
2011-12: Geology Lecturer, Los Angeles City College
2011: Teaching Associate, Department of Earth Science, University of California, Santa Barbara
2009: Geoscience Intern, Hess Corporation
2008-13: Teaching Assistant, Department of Earth Science, University of California, Santa Barbara
2006: Senior Staff Geologist, Mission Geoscience, Inc.
2005-07: Teaching Assistant, Department of Earth & Space Sciences, University of California, Los Angeles
2004-05: Staff Geologist, SECOR International, Inc.
2003-04: Environmental Education Volunteer, U.S. Peace Corps Jamaica

PUBLICATIONS

Murray, B.P., Busby, C.J., and Verde Ramírez, M.A., [*in review*], Extension and magmatism in the Cerocahui basin, northern Sierra Madre Occidental, western Chihuahua, Mexico: International Geology Review

Murray, B.P., Busby, C.J., Ferrari, L., and Solari, L., 2013, Synvolcanic crustal extension during the mid-Cenozoic ignimbrite flare-up in the northern Sierra Madre Occidental, Mexico: Evidence from the Guazapares Mining District region, western Chihuahua: Geosphere, Vol. 9, No. 5, p. 1201-1235

Murray, B.P., 2013, Evidence of synextensional deposition of the Pickhandle and Jackhammer formations in the northern Calico Mountains, central Mojave Desert, California: Geological Society of America *Abstracts with Programs*, Vol. 45, No. 6, p. 16

Murray, B.P., Busby, C.J., Ferrari, L., and Solari, L., 2010, Tectonic controls on late Oligocene volcanism in the Guazapares Mining District, northwestern Sierra Madre

Occidental, Mexico: Geological Society of America *Abstracts with Programs,* Vol. 42, No. 5, p. 344

Murray, B.P., Horton, B.K., Matos, R., and Heizler, M.T., 2010, Oligocene-Miocene basin evolution in the northern Altiplano, Bolivia: Implications for evolution of the central Andean backthrust belt and high plateau: Geological Society of America Bulletin Vol. 122, No. 9/10, p. 1443-1462

Busby, C.J., Murray, B.P., and Ferrari, L., 2009, Tectonic controls on volcanic styles of a supervolcano field: the Temoris – Cerocahui region of the Copper Canyon, northern Sierra Madre Occidental (Mexico): Geological Society of America *Abstracts with Programs,* Vol. 41, No. 7, p. 56

Murray, B.P., Busby, C.J., and Sims, D.B., 2009, Tectonic setting of the ignimbrite flare-up and epithermal mineralization in the northern Sierra Madre Occidental (Mexico): preliminary evidence from the Guazapares Mining District, western Chihuahua: Geological Society of America *Abstracts with Programs,* Vol. 41, No. 5, p. 31

Murray, B.P., Busby, C.J., and Sims, D.B., 2009, Extensional setting of the Sierra Madre Occidental silicic large igneous province: Precursor to lithospheric rupture, NSF MARGINS Rupturing Continental Lithosphere: Synthesis and New Perspectives, Charleston, SC, April 30 – May 3

Murray, B.P., and Horton, B.K., 2007, Sedimentology and provenance of the synorogenic Peñas and Aranjuez formations, central Andes, Bolivia: Implications for the timing of Eastern Cordillera denudation and initial basin development in the northern Altiplano: Geological Society of America *Abstracts with Programs,* Vol. 39, No. 6, p. 310

Murray, B.P., Horton, B.K., Gillis, R.J., and Matos, R., 2006, Sedimentology and timing of initial basin development in the northern Altiplano recorded by the synorogenic Peñas and Aranjuez Formations, central Andes, Bolivia: Geological Society of America *Abstracts with Programs*, Vol. 38, No. 7, p. 368

AWARDS

Richard V. Fisher Scholarship for Volcanology, UCSB Department of Earth Science, 2009

Leal Mertes Memorial Scholarship, UCSB Department of Geography, 2009

Geological Society of America Research Grant, 2008

Doctoral Scholar Fellowship, UCSB, 2007

Preston Cloud Memorial Award, UCSB Department of Earth Science, 2007

Jackson Award, Geological Society of America Research Grant, 2006

UCLA Office of Instructional Development Mini-grant, 2006

Eugene B. Waggoner Scholarship, UCLA Department of Earth & Space Sciences, 2002

FIELDS OF STUDY

Major Field: Field Geology, Stratigraphy, Physical Volcanology, Sedimentology, Tectonics

Studies in major fields with Professors Cathy J. Busby and Luca Ferrari

ABSTRACT

Crustal extension and magmatism during the mid-Cenozoic ignimbrite flare-up in the Guazapares Mining District and Cerocahui basin regions, northern Sierra Madre Occidental, western Chihuahua, Mexico

by

Bryan Patrick Murray

Silicic large igneous provinces are significant in the geologic record, due to their unusually extensive areal coverage (>100,000 km^2) and large volumes (>250,000 km^3), and may be characteristic of continental regions undergoing broad lithospheric extension. The Sierra Madre Occidental of northwestern Mexico is the biggest and best-preserved silicic large igneous province of the Cenozoic and is considered part of the extensive mid-Cenozoic ignimbrite flare-up that affected much of the southwestern North American Cordillera. Despite its size and preservation, very little is known about the geology of the Sierra Madre Occidental, and the timing and spatial extent of ignimbrite flare-up volcanism in relation to crustal extension is relatively unknown. This study presents new geologic mapping, stratigraphy, zircon U-Pb laser ablation ICP-MS dating, modal analysis, and geochemical data from the Guazapares Mining District and Cerocahui basin regions, two adjacent areas of the northern Sierra Madre Occidental in western Chihuahua. The rock exposure and topographic relief in this previously unmapped ~450 km^2 area make it ideal for studying the relationships between silicic large igneous province volcanism and crustal extension.

Three informal formations are identified in the study area: (1) the ca. 27.5 Ma Parajes formation, a ~1-km-thick succession of primarily welded silicic outflow ignimbrite sheets erupted from sources within ~50–100 km of the study area that were active during the Early Oligocene pulse of the mid-Cenozoic ignimbrite flare-up; (2) the ca. 27–24.5 Ma Témoris formation, composed primarily of locally erupted mafic-intermediate lavas and associated intrusions with interbedded alluvial deposits, likely related to rocks of the Southern Cordillera basaltic andesite province that were intermittently erupted across all of the northern Sierra Madre Occidental following the Early Oligocene ignimbrite pulse; and (3) the ca. 24.5–23 Ma Sierra Guazapares formation, composed of silicic vent to proximal facies ignimbrites, lavas, plugs, and reworked equivalents that record the initiation of explosive and effusive silicic fissure magmatism in the study area during the Early Miocene pulse of the mid-Cenozoic ignimbrite flare-up. The Guazapares Mining District and Cerocahui basin regions share this stratigraphy, but the rocks in the Cerocahui basin consist of a much higher proportion of alluvial deposits.

The main geologic structures in the Guazapares Mining District and Cerocahui basin regions are NNW–trending normal faults, with an estimated minimum of 20% total horizontal extension. Many normal faults bound half-graben basins that show evidence of syndepositional extension. Normal faulting began by ca. 27.5 Ma during deposition of the youngest ignimbrites of the Parajes formation, concurrent with the end of the Early Oligocene silicic ignimbrite pulse of the ignimbrite flare-up to the east and before magmatism began in the study area. Preexisting normal faults localized mafic-intermediate volcanic vents of the Témoris formation and silicic vents of the Sierra Guazapares formation, and were active during deposition of these formations. In addition, the localization and timing of epithermal mineralization in the Guazapares Mining District appears to be favored where pre-to-synvolcanic extensional structures are in close association with Sierra Guazapares formation rhyolite plugs.

The timing of extensional faulting and magmatism in the Guazapares Mining District and Cerocahui regions is consistent with regional-scale Middle Eocene to Early Miocene southwestward migration of active volcanism and extension in the northern Sierra Madre Occidental. Extension accompanied mafic-intermediate and silicic volcanism in the study area, and overlapped with the peak of mid-Cenozoic ignimbrite flare-up in the Sierra Madre Occidental; this supports the interpretation that there is likely a relationship between lithospheric extension and silicic large igneous province magmatism.

TABLE OF CONTENTS

CHAPTER 1: SYNVOLCANIC CRUSTAL EXTENSION DURING THE MID-CENOZOIC IGNIMBRITE FLARE-UP IN THE NORTHERN SIERRA MADRE OCCIDENTAL, MEXICO: EVIDENCE FROM THE GUAZAPARES MINING DISTRICT REGION, WESTERN CHIHUAHUA..1

ABSTRACT..1
INTRODUCTION..3
GEOLOGIC SETTING..7
LITHOLOGY & STRATIGRAPHY 11
Parajes formation..29
Description*..*29
Interpretation*..*33
Témoris Formation 34
Description*..*35
Interpretation*..*40
Sierra Guazapares Formation 41
Description*..*45
Interpretation*..*46
Lithostratigraphic Summary 47
GEOLOGIC STRUCTURES & BASIN DEVELOPMENT.......................................49
Synvolcanic Half-Graben Basins...49
Relative Timing and Amount of Extensional Deformation...................................51
AGE CONSTRAINTS...53
Methodology 53
Results...60
Parajes formation*..*60
Témoris Formation*...*61
Sierra Guazapares Formation*..*61
Age Interpretations...63
DISCUSSION...64
Volcanic & Tectonic Evolution..64
Regional Correlations..69
Regional Timing of Volcanism and Extension 72
Extensional Effects on Volcanism 75
CONCLUSIONS 75
REFERENCES CITED..77

CHAPTER 2: EPITHERMAL MINERALIZATION CONTROLLED BY SYNEXTENSIONAL MAGMATISM IN THE GUAZAPARES MINING DISTRICT OF THE SIERRA MADRE OCCIDENTAL SILICIC LARGE IGNEOUS PROVINCE, MEXICO...85

ABSTRACT..85
INTRODUCTION..87

GEOLOGIC BACKGROUND **89**
Regional Volcanic Stratigraphy **90**
Timing of Crustal Extension **92**
Timing of Epithermal Mineralization **93**
Volcanic Terminology **94**
GEOLOGY OF THE GUAZAPARES MINING DISTRICT **95**
Lithology and Depositional Setting **95**
Mineralization in the Guazapares Mining District **102**
Guazapares Fault Zone **103**
RESOURCE AREAS OF THE GUAZAPARES FAULT ZONE **104**
San Antonio Resource Area **104**
Monte Cristo Resource Area **111**
Sangre de Cristo Fault Half-Graben Basin Development ***116***
La Union Resource Area **121**
DISCUSSION **123**
REFERENCES CITED **125**

CHAPTER 3: EXTENSION AND MAGMATISM IN THE CEROCAHUI BASIN, NORTHERN SIERRA MADRE OCCIDENTAL, WESTERN CHIHUAHUA, MEXICO **130**

ABSTRACT **130**
INTRODUCTION **131**
GEOLOGIC SETTING **135**
Regional Geology **135**
Guazapares Mining District **137**
THE CEROCAHUI BASIN **139**
Basin Stratigraphy and Relation to Extensional Structures **144**
Silicic outflow ignimbrites of pre-basinal origin (Toi & Tp) ***146***
Bahuichivo Volcanics (Tbl & Tbv): lowermost Cerocahui basin fill ***147***
Cerocahui clastic unit (Tcc & Tcs): Cerocahui basin fill ***151***
Basalt lavas: uppermost Cerocahui basin fill ***162***
Silicic hypabyssal intrusions: post-basinal magmatism ***162***
DEPOSITIONAL AGE CONSTRAINTS **164**
Methodology & Age Interpretations **164**
Results **167**
DISCUSSION **169**
Cerocahui Basin Evolution **169**
Regional Correlations **174**
CONCLUSIONS **175**
REFERENCES CITED **177**

APPENDIX 1: **182**
APPENDIX 2: **184**
APPENDIX 3: **212**
APPENDIX 4: **214**

CHAPTER 1

SYNVOLCANIC CRUSTAL EXTENSION DURING THE MID-CENOZOIC IGNIMBRITE FLARE-UP IN THE NORTHERN SIERRA MADRE OCCIDENTAL, MEXICO: EVIDENCE FROM THE GUAZAPARES MINING DISTRICT REGION, WESTERN CHIHUAHUA

(previously published as: Murray, B.P., Busby, C.J., Ferrari, L., and Solari, L., 2013, *Geosphere*, Vol. 9, No. 5, p. 1201-1235)

ABSTRACT

The timing and spatial extent of mid-Cenozoic ignimbrite flare-up volcanism of the Sierra Madre Occidental silicic large igneous province of Mexico in relation to crustal extension is relatively unknown. Extension in the Sierra Madre Occidental has been variably interpreted to have preceded, postdated, or begun during Early Oligocene flare-up volcanism of the silicic large igneous province. New geologic mapping, zircon U-Pb laser ablation ICP-MS dating, modal analysis, and geochemical data from the Guazapares Mining District region along the western edge of the northern Sierra Madre Occidental silicic large igneous province have identified three informal synextensional formations. The ca. 27.5 Ma Parajes formation is a ~1-km-thick succession composed primarily of welded to nonwelded silicic outflow ignimbrite sheets erupted from distant sources. The 27–24.5 Ma Témoris formation is interpreted as an andesitic volcanic center composed of locally erupted mafic to intermediate composition lavas and associated intrusions, with interbedded andesite-clast fluvial and debris flow deposits, and an upper section of thin distal silicic outflow ignimbrites. The 24.5–23 Ma Sierra Guazapares formation is composed of silicic vent facies ignimbrites to proximal ignimbrites, lavas, plugs, dome-collapse deposits, and fluvially- or

debris flow-reworked equivalents. These three formations record (1) the accumulation of outflow ignimbrite sheets, presumably erupted from calderas mapped ~50–100 km east of the study area that were active during the Early Oligocene pulse of the mid-Cenozoic ignimbrite flare-up; (2) development of an andesitic volcanic field in the study area, likely related to rocks of the Southern Cordillera basaltic andesite province that were intermittently erupted across all of the northern Sierra Madre Occidental toward the end of and following the Early Oligocene ignimbrite pulse; and (3) the initiation of explosive and effusive silicic fissure magmatism in the study area during the Early Miocene pulse of the mid-Cenozoic ignimbrite flare-up.

The main geologic structures identified in the Guazapares Mining District region are NNW–trending normal faults, with an estimated minimum of 20% total horizontal extension. Normal faults were active during deposition of all three formations (Parajes, Témoris, and Sierra Guazapares), and bound half-graben basins that show evidence of synvolcanic extension (e.g., growth strata) during deposition. Normal faulting began by ca. 27.5 Ma during deposition of the youngest ignimbrites of the Parajes formation, concurrent with the end of the Early Oligocene silicic ignimbrite pulse to the east and before magmatism began in the study area. In addition, preexisting normal faults localized andesitic volcanic vents of the Témoris formation and silicic vents of the Sierra Guazapares formation, and some faults were reactivated during, as well as after, deposition of these formations.

We interpret extensional faulting and magmatism in the Guazapares Mining District region to be part of a regional-scale Middle Eocene to Early Miocene southwestward migration of active volcanism and crustal extension in the northern Sierra Madre Occidental. We show that extension accompanied silicic volcanism in the Guazapares region, and overlapped with the peak of mid-Cenozoic ignimbrite flare-up in the Sierra Madre

Occidental; this supports the interpretation that there is a relationship between lithospheric extension and silicic large igneous province magmatism.

INTRODUCTION

Silicic large igneous provinces are significant in the geologic record, due to their unusually extensive areal coverage (>100,000 km^2), large volumes (>250,000 km^3), and potential to induce environmental change (e.g., Bryan, 2007; Cather et al., 2009; Jicha et al., 2009; Bryan and Ferrari, 2013). Compositions within silicic large igneous provinces range from basalt to high-silica rhyolite, but are volumetrically dominated (>80%) by dacite-rhyolite compositions, with >75% of the total magmatic volume emplaced during short duration (~1-5 Myr) pulses over a maximum province lifespan of ~50 Myr (Bryan, 2007; Bryan and Ernst, 2008). Previous studies suggest that silicic large igneous provinces may be characteristic of continental regions undergoing broad lithospheric extension and typically initiate as prerifting magmatic events (Bryan et al., 2002; Bryan, 2007; Best et al., 2013; Bryan and Ferrari, 2013). Therefore, determining the timing of extensional deformation in relation to magmatism is an important consideration toward understanding silicic large igneous province processes, as crustal extension is suggested as one mechanism that favors the generation of large silicic magma volumes (Hildreth, 1981; Wark, 1991; Hanson and Glazner, 1995) as well as very large magnitude explosive silicic eruptions (Aguirre-Díaz and Labarthe-Hernández, 2003; Costa et al., 2011).

The Sierra Madre Occidental of western Mexico is the third largest silicic large igneous province of the Phanerozoic and is the largest and best-preserved of the Cenozoic (Fig. 1; Bryan, 2007; Ferrari et al., 2007). It extends for ~1200 km south from the U.S.-Mexico border to the Trans-Mexican Volcanic Belt, forming a high plateau with an average

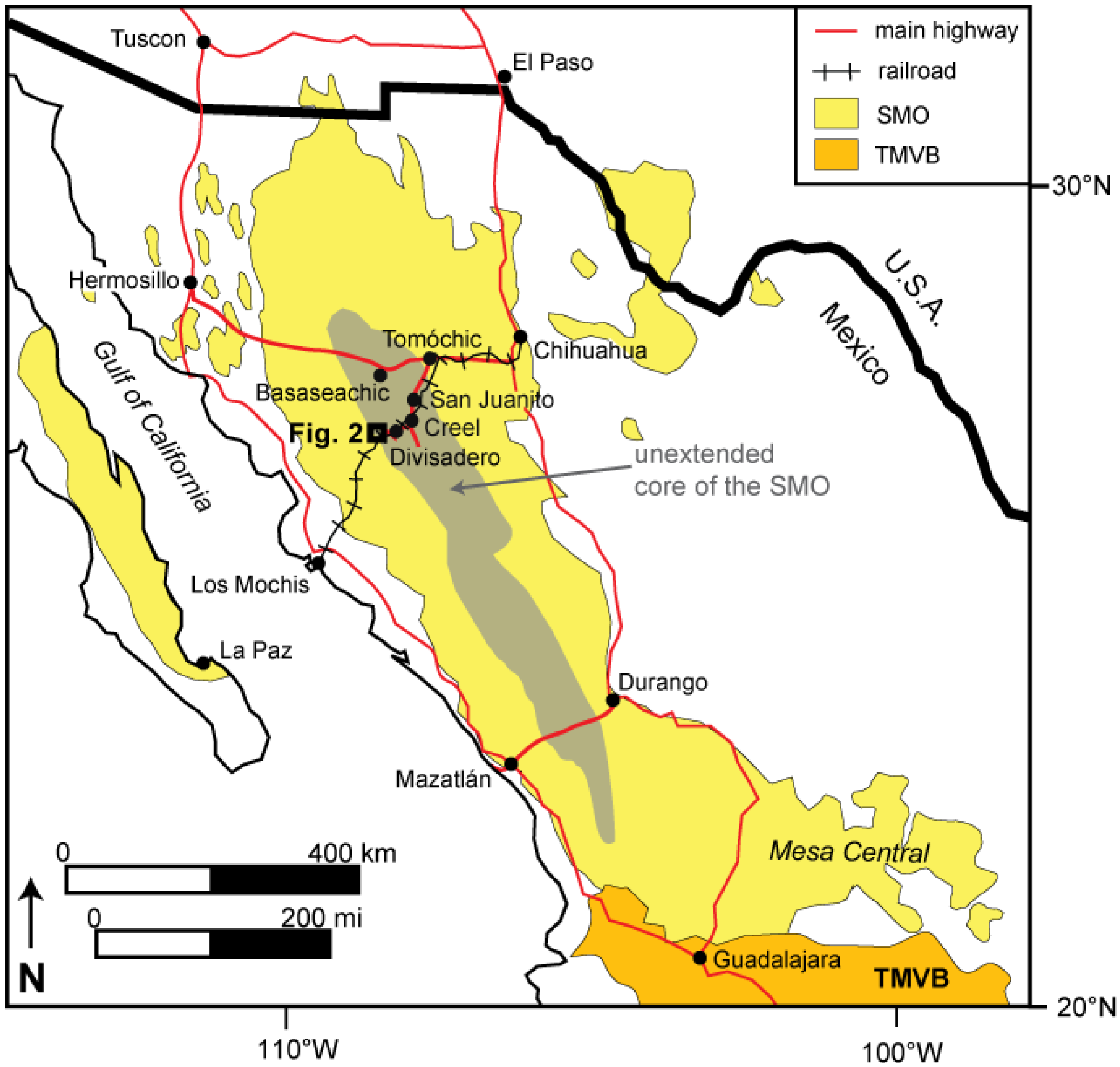

Figure 1. Generalized map of western Mexico showing the extent of the Sierra Madre Occidental (SMO) silicic large igneous province (light yellow) and the relatively unextended core (dark gray) of the SMO (after Henry and Aranda-Gómez, 2000; Ferrari et al., 2002; Bryan et al., 2013). The location of the Guazapares Mining District region (Fig. 2) is indicated. TMVB—Trans-Mexican Volcanic Belt.

elevation >2000 m, consisting primarily of Oligocene to Early Miocene ignimbrites that cover an estimated area of 300,000–400,000 km^2 with an average thickness of 1 km (McDowell and Keizer, 1977; McDowell and Clabaugh, 1979; Aguirre-Díaz and Labarthe-Hernández, 2003). The volcanism of the Sierra Madre Occidental silicic large igneous province is contemporaneous with, and is considered part of, the extensive mid-Cenozoic ignimbrite flare-up that affected much of the southwestern North American Cordillera from the Middle Eocene to Late Miocene (e.g., Coney, 1978; Armstrong and Ward, 1991; Ward, 1991; Ferrari et al., 2002; Lipman, 2007; Cather et al., 2009; Henry et al., 2010; Best et al., 2013). The core of the Sierra Madre Occidental is relatively unextended in comparison to the surrounding Late Oligocene to Miocene extensional belts of the southern Basin and Range to the east and the Gulf Extensional Province to the west (Fig. 1; Nieto-Samaniego et al., 1999; Henry and Aranda-Gómez, 2000). Rocks related to the silicic large igneous province extend beyond the Sierra Madre Occidental proper (Fig. 1), to the Mesa Central and parts of the southern Basin and Range in eastern Chihuahua and Durango (Gunderson et al., 1986; Aguirre-Díaz and McDowell, 1991, 1993), as well as southwesternmost mainland Mexico and Baja California Sur (Umhoefer et al., 2001; Ferrari et al., 2002).

A large part of the Sierra Madre Occidental remains unmapped and undated (>90%; Swanson et al., 2006). Previous work in the Sierra Madre Occidental has been primarily restricted to the southern region of the igneous province (e.g., Nieto-Samaniego et al., 1999; Ferrari et al., 2002), the vicinity of the Mazatlán–Durango highway in the central region (e.g., McDowell and Keizer, 1977; McDowell and Clabaugh, 1979; Henry and Fredrikson, 1987), and the areas around the Hermosillo–Chihuahua City highway and the Tomóchic–Creel road in the northern region (e.g., Swanson, 1977; Swanson and McDowell, 1984, 1985; Wark et al., 1990; Cochemé and Demant, 1991; Wark, 1991; McDowell and Mauger, 1994; Albrecht and Goldstein, 2000; Swanson et al., 2006; McDowell, 2007; McDowell and McIntosh, 2012) (Fig. 1). As a result, the age relationships between ignimbrite flare-up volcanism and crustal extension remain unclear. Previous workers have suggested that significant crustal extension in the region did not occur until after the peak of large volume ignimbrite flare-up volcanism, which was inferred to have occurred between ca. 32 and 28 Ma (Early Oligocene; e.g., McDowell and Clabaugh, 1979; Wark et al., 1990; McDowell and Mauger, 1994; Gans, 1997; Grijalva-Noriega and Roldán-Quintana, 1998). However, other studies have inferred that initial regional extension is recorded by the onset of large volume Early Oligocene ignimbrite flare-up volcanism (e.g., Aguirre-Díaz and McDowell, 1993), or that extensional deformation began before the flare-up (e.g., Dreier, 1984; Ferrari et al., 2007). Uncertainty regarding the timing of extension relative to ignimbrite flare-up volcanism is also a problem in the Basin and Range of the western U.S., where previous studies have inferred that extension either preceded, postdated, or began during ignimbrite flare-up volcanism (e.g., Gans et al., 1989; Best and Christiansen, 1991; Axen et al., 1993; Best et al., 2013).

The Guazapares Mining District region of western Chihuahua, Mexico is located ~250 km southwest of Chihuahua City in the northern Sierra Madre Occidental (Fig. 1). The excellent rock exposure and topographic relief in this previously unmapped area make it ideal for studying the relationships between silicic large igneous province volcanism and crustal extension. In this paper, we show that extension preceded the onset of magmatism in the study area. We demonstrate that extension was active in the study area during deposition of ca. 27.5 Ma outflow ignimbrites, presumably derived from calderas of similar ages identified to the north and east by other workers. Extension continued during growth of a ca. 27–24.5 Ma andesitic volcanic center in the study area, followed by continued extension during ca. 24.5–23 Ma silicic flare-up magmatism in the study area. This study shows how extensional structures controlled the siting of the andesitic and silicic volcanic vents and shallow-level intrusions. This study also shows that the onset of extension in the study area overlaps with the end of peak Oligocene silicic magmatism to the east, and that extension in the study area preceded and coincided with a second peak of magmatism in the Miocene, which is represented in the study area. Last, we show that our data supports the interpretation that silicic flare-up magmatism swept southwestward with time, due to rollback and/or removal of the slab that was subducting beneath western Mexico.

GEOLOGIC SETTING

Previous regional-scale studies in the Sierra Madre Occidental subdivided volcanic rocks into: (1) the Late Cretaceous to Eocene Lower Volcanic Complex of dominantly andesitic composition; (2) the Eocene to Early Miocene Upper Volcanic Supergroup of dominantly silicic composition; and (3) the Early Oligocene to Early Miocene basaltic andesite volcanic rocks of the Southern Cordillera basaltic andesite province (McDowell and Keizer, 1977; Cameron et al., 1989; Ferrari et al., 2007). The Lower Volcanic Complex is believed to underlie most of the Upper Volcanic Supergroup (Aguirre-Díaz and McDowell, 1991; Ferrari et al., 2007), although the thick ignimbrite cover of the Upper Volcanic Supergroup obscures much of the geologic relationships between these two subdivisions in most areas. The volcanic rocks of the Lower Volcanic Complex generally consist of intermediate composition lavas and lesser silicic tuffs and are interpreted as the products of normal steady-state (i.e., non-flare-up-style) continental subduction-related magmatism broadly contemporaneous with the Laramide orogeny in western North America (McDowell and Keizer, 1977; McDowell et al., 2001).

The ~1-km-thick Upper Volcanic Supergroup broadly refers to the products of large-volume flare-up-style (i.e., high output rate and large eruptive volumes) silicic magmatism, also known as the mid-Cenozoic ignimbrite flare-up, and defines the extent of the Sierra Madre Occidental silicic large igneous province (McDowell and Keizer, 1977; Bryan, 2007; Ferrari et al., 2007). The Upper Volcanic Supergroup is composed of Eocene to Early Miocene silicic ignimbrites, lavas, and intrusions, and lesser intermediate to mafic lavas (McDowell and Keizer, 1977; McDowell and Clabaugh, 1979; Aguirre-Díaz and McDowell, 1991, 1993; Ferrari et al., 2002; Ferrari et al., 2007; McDowell, 2007). The large volume of silicic ignimbrites and high output rate suggest multiple caldera and fissure sources for these volcanic deposits (e.g., Swanson and McDowell, 1984; Aguirre-Díaz and Labarthe-Hernández, 2003; Swanson et al., 2006; McDowell, 2007). Ferrari et al. (2002; 2007) proposed that there were at least two main pulses of large volume silicic ignimbrite flare-up volcanism in the Sierra Madre Occidental during the mid-Cenozoic, one during the Early Oligocene (ca. 32–28 Ma) and another during the Early Miocene (ca. 24–20 Ma). The Early Oligocene ignimbrite pulse is inferred to have occurred throughout the Sierra Madre Occidental, while the Early Miocene ignimbrite pulse was inferred to be volumetrically more significant in the southern Sierra Madre Occidental and less abundant, with more mafic compositions, in the north (Ferrari et al., 2002; Ferrari et al., 2007; Bryan et al., 2013). The Early Oligocene pulse is estimated to have contributed at least half to three-quarters (>200,000 km^3) of the erupted volume of the Upper Volcanic Supergroup, but at least 50,000-100,000 km^3 was erupted during the Early Miocene pulse (Cather et al., 2009; Bryan et al., 2013). McDowell and McIntosh (2012) suggested that most ignimbrites in the northern and central Sierra Madre Occidental were erupted during discrete time intervals (36–33.5 Ma and 31.5–28 Ma). In addition, an older Eocene pulse of ignimbrite eruptions between 46 and

42 Ma is only recognized along the eastern margin of the Sierra Madre Occidental, and an interval of ca. 24 Ma ignimbrite eruptions that coincides with the Early Miocene pulse of Ferrari et al. (2002; 2007) is observed in the western regions of the igneous province (McDowell and McIntosh, 2012), west of our study area.

During the final stages of, and after each silicic ignimbrite pulse of the Upper Volcanic Supergroup, basaltic andesite lavas were intermittently erupted across all of the northern Sierra Madre Occidental (Ferrari et al., 2007). In the northern part of the Sierra Madre Occidental these rocks were generally considered part of the Southern Cordillera basaltic andesite province (Cameron et al., 1989) with ages ranging from 33 to 17.6 Ma, although they mostly are Oligocene (Cameron et al., 1989, and references therein; Ferrari et al., 2007). The rocks of the Southern Cordillera basaltic andesite province have been interpreted as magmatism recording the initiation of crustal extension across the region (e.g., Cameron et al., 1989; Cochemé and Demant, 1991; Gans, 1997; McDowell et al., 1997; González León et al., 2000; Ferrari et al., 2007).

Several prior studies have recognized significant crustal extension in the Sierra Madre Occidental immediately following the Early Oligocene ignimbrite pulse of the Upper Volcanic Supergroup (e.g., McDowell and Clabaugh, 1979; Wark et al., 1990; McDowell and Mauger, 1994; Gans, 1997; Grijalva-Noriega and Roldán-Quintana, 1998). The earliest evidence of extensional faulting in the northern Sierra Madre Occidental is found in central Chihuahua (younger than 29 Ma), immediately following the Early Oligocene ignimbrite pulse (McDowell and Mauger, 1994). In east-central Sonora, the earliest age of crustal extension is possibly as old as 27 Ma and synvolcanic deposition in many normal-fault basins was active by 24 Ma, following the peak of Early Oligocene ignimbrite flare-up volcanism (Gans, 1997; McDowell et al., 1997; Gans et al., 2003). However, extension in the Sierra

Madre Occidental may have begun as early as the Eocene, prior to the eruption of the Early Oligocene ignimbrite pulse, based on the orientation and age of epithermal vein deposits (Dreier, 1984) and a moderate angular unconformity between the Lower Volcanic Complex and Upper Volcanic Supergroup (e.g., Ferrari et al., 2007). Direct evidence of Early Eocene (pre–Upper Volcanic Supergroup) extensional faulting is observed in the Mesa Central region to the east of the core of the southern Sierra Madre Occidental and includes a moderate angular unconformity within continental clastic and andesitic volcanic sequences and subvolcanic intrusions along normal faults (Aranda-Gómez and McDowell, 1998; Aguillón-Robles et al., 2009; Tristán-González et al., 2009), as well as ca. 32 Ma synvolcanic normal faults that were active until ca. 24 Ma (Aguirre-Díaz and McDowell, 1993; Luhr et al., 2001). However, Eocene-age extensional faulting has not been documented in the Sierra Madre Occidental proper.

The Guazapares Mining District of western Chihuahua is located at the western edge of the relatively unextended core of the northern Sierra Madre Occidental, at the boundary with the highly extended Gulf Extensional Province (Fig. 1). Previous geologic studies in this ~300 km^2 region were restricted to regional 1:50,000 and 1:250,000 geologic mapping by the Mexican Geological Survey (Minjárez Sosa et al., 2002; Ramírez Tello and Garcia Peralta, 2004) and mining company reports (e.g., Roy et al., 2008; Wood and Durgin, 2009; Gustin, 2011, 2012). On these older maps and reports, Paleocene–Eocene Lower Volcanic Complex andesitic rocks were inferred to underlie the Oligocene Upper Volcanic Supergroup silicic ignimbrites, but we show here that these rocks (which we informally refer to as the Témoris formation) are both underlain and overlain by silicic ignimbrites, and therefore cannot be assigned to the Lower Volcanic Complex. Prior to this study there were no geochronological data from the Guazapares Mining District region and the closest reported dates were from Upper Volcanic Supergroup ignimbrites approximately 50 km to the northeast near Divisadero (~30 Ma; Swanson et al., 2006).

LITHOLOGY & STRATIGRAPHY

New geologic mapping in the Guazapares Mining District region (Figs. 2, 3, and 4; Supplemental File 1)[1] provides the basis for the subdivision of three informally named formations described in the following (from oldest to youngest): (1) the Parajes formation, consisting mainly of silicic outflow ignimbrites; (2) the Témoris formation, composed mainly of mafic to intermediate composition lavas and intrusions; and (3) the Sierra Guazapares formation, consisting of silicic vent-proximal ignimbrites, lavas, and subvolcanic intrusions (Fig. 5).

The volcanic and volcaniclastic terminologies used in this paper are those of Fisher and Schmincke (1984), Fisher & Smith (1991), and Sigurdsson et al. (2000). Following Fisher and Schmincke (1984), volcaniclastic refers to all fragmental rocks made dominantly of volcanic detritus: these include (1) pyroclastic fragmental deposits, inferred to have been directly fed from an eruption, e.g., pyroclastic fall, ignimbrites, autoclastic flow breccias, etc.; (2) reworked fragmental deposits, inferred to result from downslope reworking of unconsolidated eruption-fed fragmental deposits, e.g., block-and-ash-flow deposits commonly pass downslope into debris flow and fluvial deposits; and (3) epiclastic deposits, made of volcanic fragments inferred to have been derived from erosion of pre-existing rock. When the distinctions cannot be made, the general term volcaniclastic is applied. Delicate pyroclastic detritus such as pumice, shards, or euhedral crystals cannot be derived from

[1] Supplemental File 1: Geologic map of the Guazapares Mining District region (1:25,000 scale), submitted as an additional file with dissertation

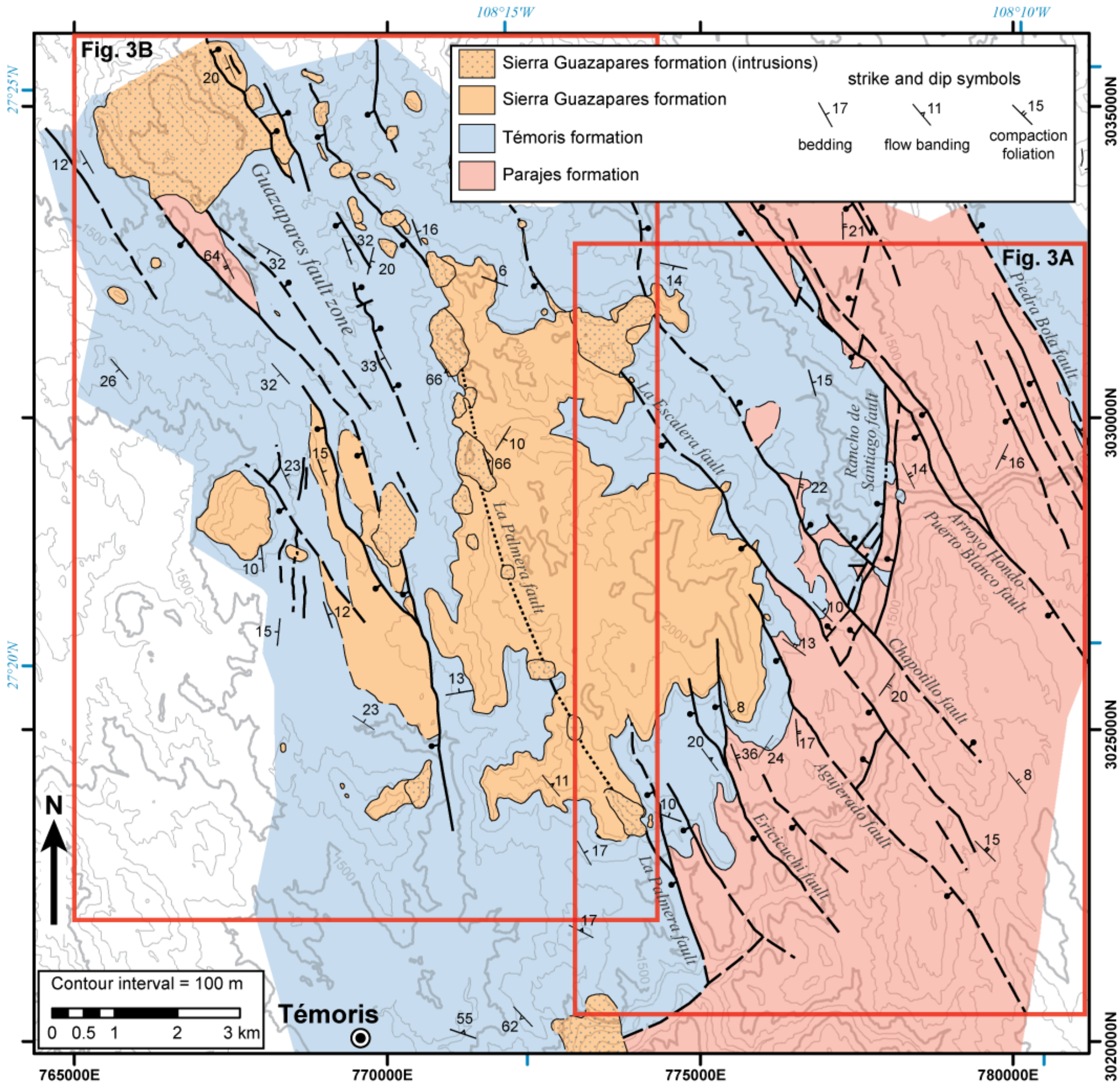

Figure 2. Simplified geologic map of the Guazapares Mining District region, showing the extent of the three formations discussed herein (see Fig. 5) and the locations of major faults. Boxes indicate the locations of the detailed geologic maps of Figure 3. See Supplemental File 1 (see footnote 1) for more detailed geologic mapping of the study area. Coordinates in black are Universal Transverse Mercator (UTM) zone 12, North American Datum 1927 (NAD27).

Figure 3 (*next 5 pages*). Geologic maps of portions of the Guazapares Mining District region; key to the map units and symbols is given in Figure 3C. Topographic base map from Instituto Nacional de Estadística, Geografía e Informática (INEGI); original 1:50,000 scale ITRF92 datum projected to NAD27 UTM zone 12. The entire geologic map for the study area is presented in Supplemental File 1 (see footnote 1). (A) (*2 pages*) Geologic map of the southeastern portion of the Guazapares Mining District region between Puerto La Cruz and Rancho de Santiago, east of Témoris. The locations of cross-sections A–A', B–B', and C–C' (Fig. 4) are indicated. (B) (*2 pages*) Geologic map of the Guazapares fault zone between Témoris and Monte Cristo. (C) Geologic map key, with lithostratigraphic correlation chart for the map units of the Guazapares Mining District region, based on depositional relationships and geochronology presented in this study. The lithology of the map units is described in Table 1.

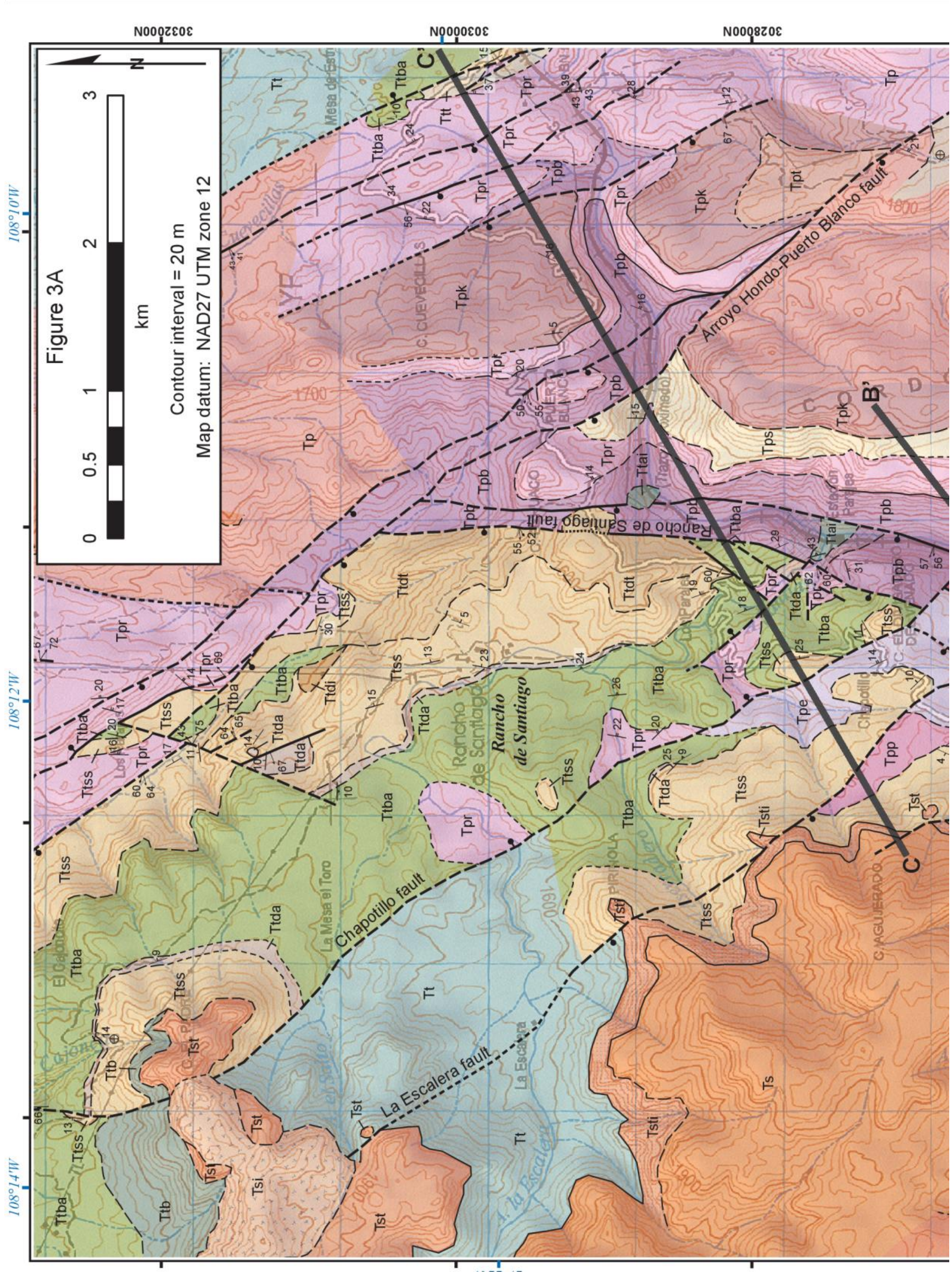
Figure 3A
0 0.5 1 2 3
km
Contour interval = 20 m
Map datum: NAD27 UTM zone 12
N
3032000N
3030000N
3028000N
108°10'W
108°12'W
108°14'W
27°22'N
Rancho de Santiago fault
Arroyo Hondo-Puerto Blanco fault
Chapotillo fault
La Escalera fault
Rancho de Santiago
C
C'
B'
Tp
Tpr
Tpb
Tpk
Tpt
Tps
Tpe
Tpp
Tt
Ttba
Ttb
Ttss
Ttda
Ttdf
Ttdi
Ttai
Tst
Tsti
Tsi
Ts
C. CUEVECILLAS
La Mesa el Toro
La Escalera
C. AGUJERADO

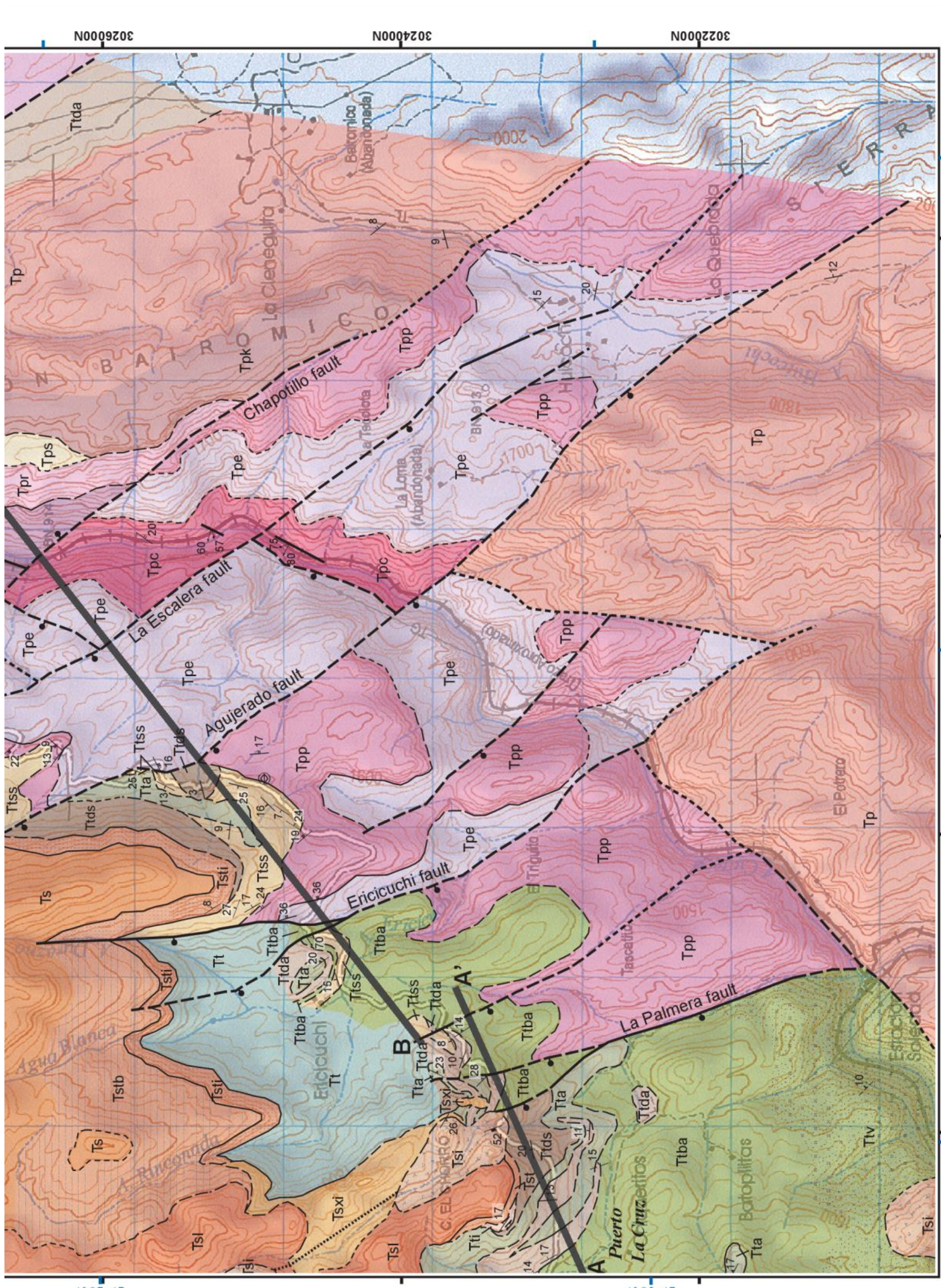

3026000N
3024000N
3022000N
774000E
776000E
778000E
27°20'N
27°18'N
Chapotillo fault
La Escalera fault
Agujerado fault
Ericicuchi fault
La Palmera fault
La Cieneguita
La Quebrada
Huisochi
La Loma (Abandonada)
El Potrero
Agua Blanca
A. Rinconada
Ericicuchi
El Triguito
Tascate
Batopilitas
Puerto La Cruz
A
A'
B
Tp
Tpp
Tpe
Tpc
Tpk
Tpr
Tps
Ttda
Ttba
Tt
Ts
Tsl
Tstb
Tsti
Ttss
Ttds
Tta
Tsxi
Ttv
Tsi

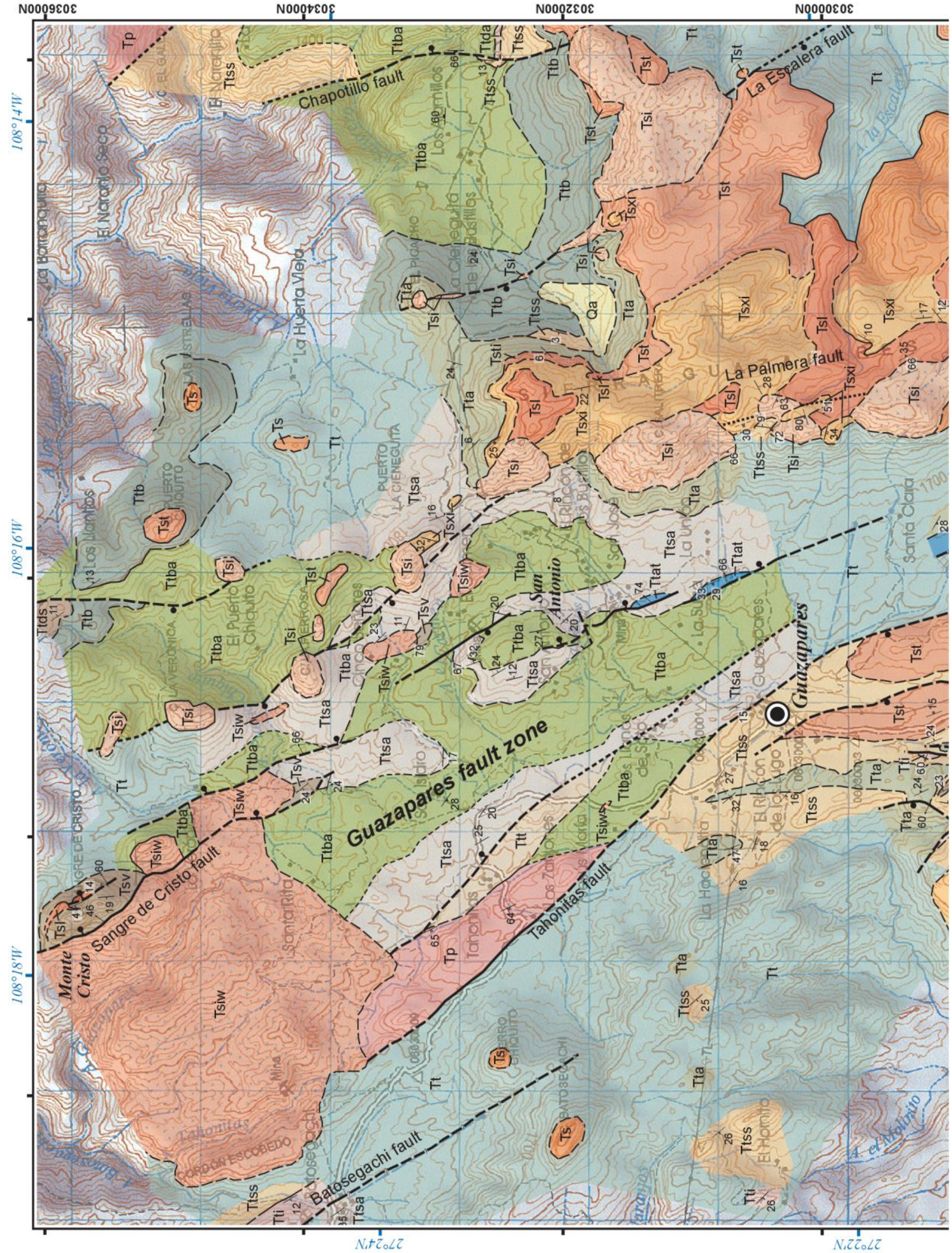
3036000N
3034000N
3032000N
3030000N
108°14'W
108°16'W
108°18'W
27°24'N
27°22'N
Guazapares fault zone
Sangre de Cristo fault
Tahonitas fault
Batosegachi fault
Chapotillo fault
La Escalera fault
La Palmera fault
Guazapares
San Antonio
Monte Cristo

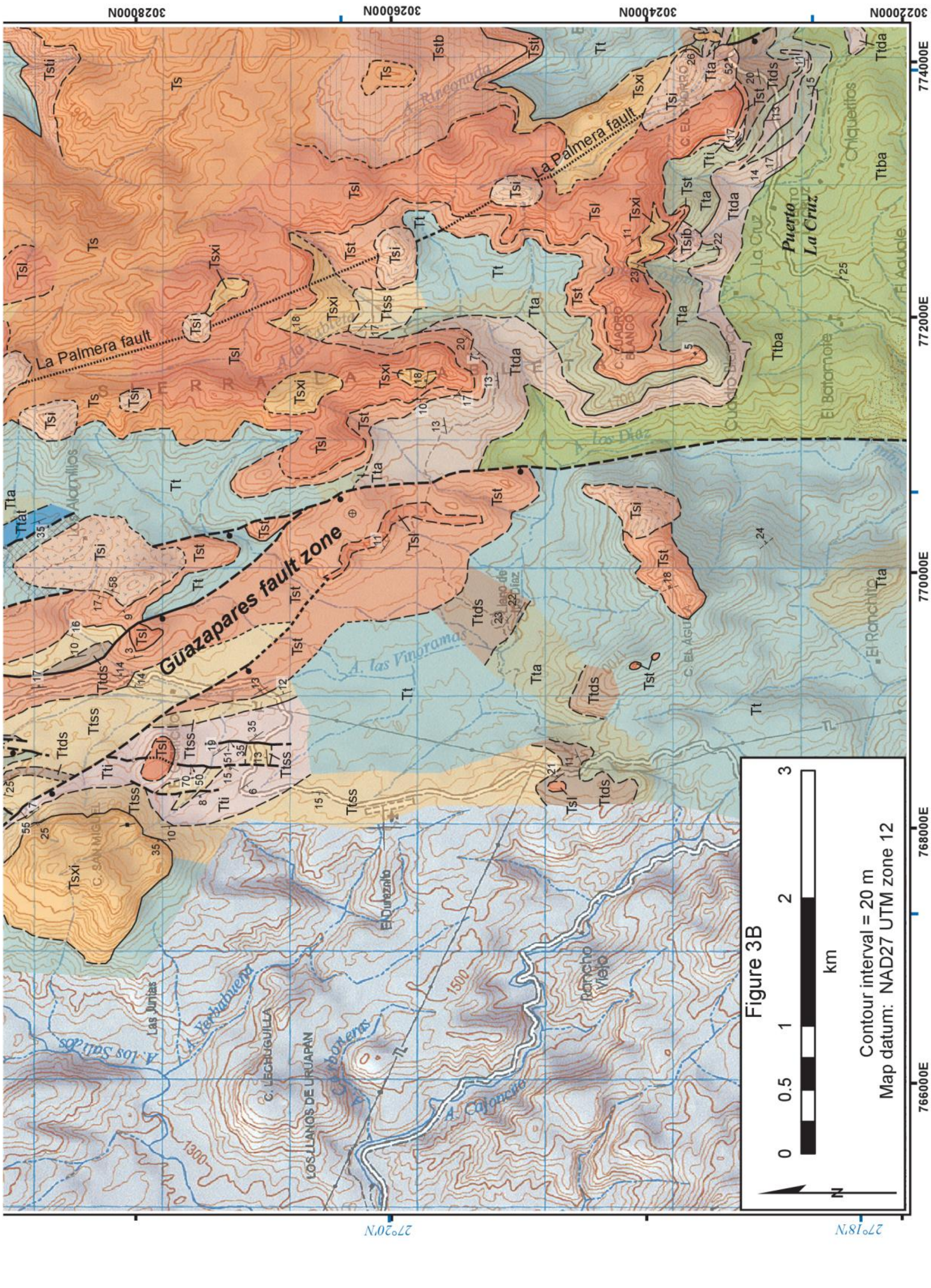
Figure 3B
Contour interval = 20 m
Map datum: NAD27 UTM zone 12
km
0
0.5
1
2
3
N
Guazapares fault zone
La Palmera fault
3028000N
3026000N
3024000N
3022000N
766000E
768000E
770000E
772000E
774000E
27°20'N
27°18'N
Puerto La Cruz
El Batamote
El Ranchito
Rancho Viejo
El Durazno
Las Juntas
LOS LLANOS DE LIRUAPAN
C. LECHUGUILLA
C. SAN MIGUEL
C. CUADRO BLANCO
A. Rinconada
A. los Diaz
A. las Vinoramas
A. Cajoncito
A. Yerbabuena
A. los Saltos
Chiquetitos
El Aguaje
Tsl
Ts
Tsi
Tsxi
Tst
Tsti
Tstb
Tsib
Tt
Tta
Ttda
Ttds
Ttss
Tti
Ttba
Ttat
Ttst

Figure 3C: lithostratigraphic correlation chart and key to map symbols

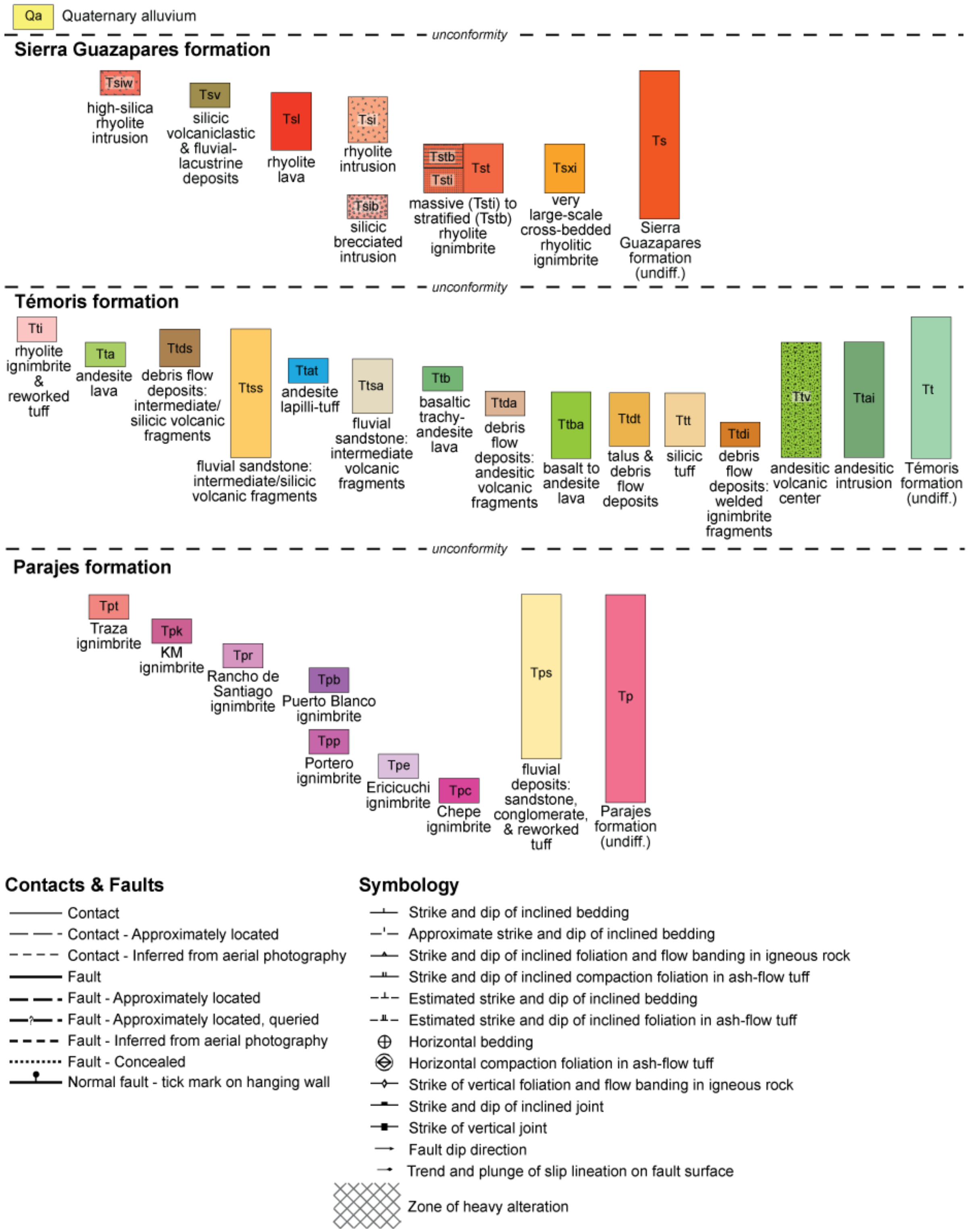

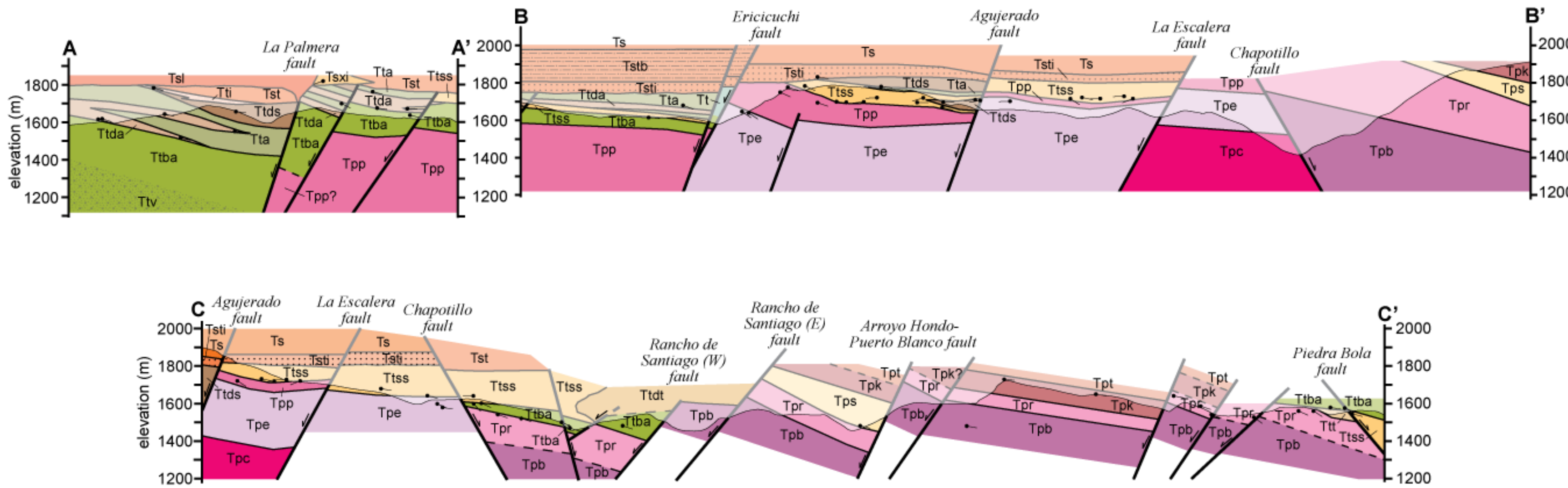

Figure 4. Geologic cross-sections for the area between Puerto La Cruz and east of Rancho de Santiago (Fig. 3A), showing major normal faults and the synvolcanic half-graben basins bounded by the La Palmera, Agujerado, Rancho de Santiago, and Arroyo Hondo–Puerto Blanco faults. Sections are same scale as Figure 3A, with no horizontal or vertical exaggeration. Rock units inferred above topography are indicated by subdued color shades and bedding orientation is shown by tick marks. See Figure 3C for rock unit abbreviations.

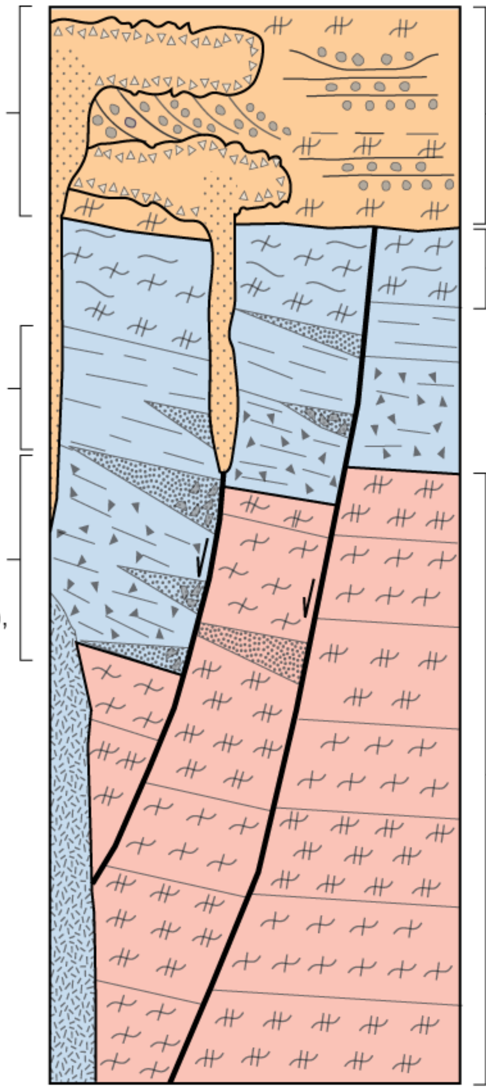

Figure 5. Generalized stratigraphic column of the Guazapares Mining District region, depicting the characteristics and depositional relationships between the Parajes formation, Témoris formation, and the Sierra Guazapares formation.

erosion of preexisting rock, so their presence in fluvial or debris flow deposits indicates that at least some of the deposit consists of reworked pyroclastic material, indicating broadly coeval explosive volcanism. Similarly, if a debris flow deposit is dominated by one volcanic clast type, it can be inferred to record reworking of a block-and-ash-flow deposit or flow breccia. However, the presence of a broad range of volcanic clast types is not proof of an epiclastic origin, because a wide variety of volcanic clast types can become incorporated into an eruption-triggered debris flow; in that case, a distinction between reworked and epiclastic cannot be made, and the deposit is simply a volcaniclastic debris flow deposit. Debris-flow deposits with blocks of welded ignimbrite, however, cannot be derived by any downslope reworking process known in outflow ignimbrite fields, and instead likely record erosion of preexisting rocks, so those can be classified as epiclastic (note that intracaldera ignimbrites commonly have blocks of welded ignimbrite cannibalized from the caldera wall during ongoing collapse; see discussion in Schermer and Busby, 1994).

The three formations in the Guazapares Mining District region are subdivided into 30 distinct lithologic units by outcrop and thin section characteristics, mineralogy, chemical composition, and inferred volcanic or sedimentary processes (Fig. 3C; Table 1). These lithologic units include volcanic rocks (e.g., lavas, ignimbrites), volcaniclastic rocks (e.g., sandstone, conglomerate, breccia), and hypabyssal intrusions (e.g., plugs, dikes). Modal point-count analyses were carried out for 39 samples, chosen to represent most of the volcanic and hypabyssal map units (Fig. 6). Reconnaissance whole-rock geochemical analyses were performed on 15 relatively unaltered samples of volcanic rock and hypabyssal intrusions from the Témoris and Sierra Guazapares formations (Fig. 7; Table 2).

TABLE 1 (next 5 pages) LITHOLOGIC DESCRIPTIONS OF THE MAP UNITS OF THE GUAZAPARES MINING DISTRICT		
Map unit*	**Lithology**	**Description**
Qa	alluvium	Unconsolidated very poorly sorted debris flow deposits. Gray to light gray; boulders to 5 m. Derived primarily from the Sierra Guazapares formation.
Tsiw	high-silica rhyolite intrusion	Hypabyssal intrusions (dikes and plugs). White to light pink; aphyric to 10% phenocrysts (to 1 mm): plagioclase, biotite, trace quartz. Subvertical flow banding. In Monte Cristo region (Fig. 3B), intruded into gray andesitic feldspar porphyry (likely part of Témoris formation). Similar in appearance to rhyolitic fault talus breccia (Tsv).
Tsv	silicic volcaniclastic & fluvial-lacustrine deposits†	Volcaniclastic lithofacies (too small to show at map scale of Fig. 3 and Supplemental File 1). Consists of: Rhyolitic fault talus breccia: clast-supported rhyolitic block to lapilli breccia; white to light orange; primarily monomictic; angular lapilli to blocks (>2 m) with some flow banding. Aphyric to trace quartz and plagioclase phenocrysts. Contains zones of to 20% andesitic blocks that are to 1.5 m. Block breccia transitions laterally into lapilli breccia, with the block fragment size decreasing northeastward away from the Sangre de Cristo fault (Fig. 3B) from >2 m blocks to lapilli-sized fragments supported in an ash matrix of same composition. Massive to bedded silicic lapilli-tuff: nonwelded lapilli-tuff, light red to gray; <5% phenocrysts: plagioclase, biotite; trace to 20% lithic fragments (intermediate volcanic). Slight fluvial reworking (planar lamination, sorting, cut-and-fill structures), bedding to 5 m-thick. Local white reworked ash layers and red very fine-grained thinly bedded sandstone. Lacustrine deposits: fine- to medium-grained sandstone with graded bedding (Bouma Sequences A, B) and small scale basal scouring; mudstone with planar lamination to very thinly bedded; water-lain ash layers. Tan to white. Soft sediment slumping and folding. Fluvial sandstone: medium- to coarse-grained sandstone; white to light gray; moderate to poor sorting; subangular silicic volcanic lithic fragments; massive with faint laminations, cut-and-fill, and trough cross-bedding structures. Minor clast-supported breccia with subangular cobble to boulder silicic lapilli-tuff fragments interpreted as hyperconcentrated debris flows of reworked silicic volcanic material.
Tsi	rhyolite intrusion	Hypabyssal intrusions (plugs and dikes). Light red to pink, typically with light pink subvertical flow banding; aphanitic groundmass with 5-20% phenocrysts: plagioclase (to 3 mm), biotite (1 mm), trace quartz. Likely source for rhyolite lavas (Tsl).
Tsib	silicic brecciated intrusion	Hypabyssal intrusion. White to light gray; silicic blocks (to 20 cm) supported in crystal-rich aphanitic groundmass with 40% phenocrysts: plagioclase, hornblende, quartz; locally massive and nonbrecciated.

Tsl	rhyolite lava	Lava flows. Light gray to reddish gray, with light pink banding; 5-20% phenocrysts: plagioclase (to 4 mm), biotite (to 2 mm), quartz. Lavas consist of a 3-15 m-thick autoclastic breccia base of flow-banded blocks, a coherent middle portion (at least 30 m thick) with well developed to minor flow banding, and a flow top autoclastic breccia with flow-banded blocks and sediment infilling the spaces between blocks. Spherulites and quartz-filled vugs are common, and thundereggs are typically found within the top portion of a lava. A ~4 m thick, basal block and ash flow is locally observed. Rhyolite hypabyssal intrusions (Tsi) are likely the source for these lavas.
Tst	massive to stratified rhyolite ignimbrite	Nonwelded to partially welded tuff to lapilli-tuff. Light pink, tan, or white groundmass; 5-25% phenocrysts (to 2 mm): plagioclase, biotite; trace to 25 % (locally 40-50%) yellow-white long-tube pumice fragments (to 15 mm); <5-40% lithic fragments (red, orange, gray intermediate volcanic, trace white silicic volcanic; to 20 mm). Crudely to well stratified; thickly to very thickly bedded (<1 m to ~10 m-thick); mild to intense fluvial reworking locally observed (clast rounding, sorting, cross-bedding, and cut-and-fill structures). Tstb: more fluvially reworked and more thinly bedded than Tsti. Tsti: primary silicic nonwelded ignimbrite with thicker massive bedding and less intense reworked sections.
Tsxi	very large-scale cross-bedded rhyolitic ignimbrite	Nonwelded lapilli-tuff to tuff-breccia. Light pink, tan, or white groundmass; 5-10% phenocrysts (<1 mm): plagioclase, biotite, quartz; 5-10% (locally to 50%) tan to white long-tube pumice fragments (to 20 mm); alternating lithic-rich (>50%) and lithic-poor (<30%) stratification with ~0.5-50 cm lithic fragments (gray and red intermediate volcanic and white silicic volcanic). Cross-bedding with ~5 m-thick sets (to ~20 m-thick).
Tti	rhyolite ignimbrite and reworked tuff	Nonwelded to partially welded lapilli-tuff and fluvially reworked tuff/lapilli-tuff. Light pink to white groundmass; 5-10% phenocrysts: plagioclase, biotite (to 2 mm), trace quartz, trace K-feldspar; <5-50% white and tan long-tube pumice fragments (5 mm, to 10 mm); 5-30% lithic fragments (gray and red intermediate volcanic; <5 mm, to 30 mm). Individual ignimbrites are generally 5-10 m-thick with compaction foliation. Reworked tuffs and lapilli-tuffs are well to crudely stratified, very thinly to medium bedded; contain well to very poorly sorted, subangular to subrounded intermediate and silicic volcanic clasts.
Tta	andesite lava	Nonvesicular lava flows. Gray; 5-10% phenocrysts (typically weathered out): plagioclase, clinopyroxene. Average lava flow thickness ~15 m, lavas generally have flow-top and bottom autoclastic breccias and resistant flow-banded coherent interior.
Ttat	andesite lapilli-tuff	Lapilli-tuff. Gray groundmass; trace phenocrysts: plagioclase; 15-30% intermediate volcanic and silicic tuff lithic fragments (to 4 mm).
Ttb	basaltic trachyandesite lava	Amygdaloidal lava flows. Dark gray to brick red; 5-20% phenocrysts: plagioclase (some flow-alignment of laths), olivine (altered to iddingsite), clinopyroxene; zeolite amygdules. Average lava flow thickness ~2 m, lavas have vesicular top and bottom, locally with coherent flow interior. Local multi-lobed flows with blocky autoclastic flow breccia (Fig. 10D).

Ttba	basalt to andesite lava	Predominantly amygdaloidal lava flows. Gray to dark gray with local red hematitic and green propylitic alteration; 5-25% phenocrysts: plagioclase (some flow-alignment of laths), clinopyroxene; zeolite amygdules. Average lava flow thickness ~5 m, lavas are typically brecciated and vesicular with secondary zeolite infilling vesicles and autoclastic flow breccia interstices fragments, with lesser flow-banded and nonvesicular lavas with flow-top and bottom autoclastic breccias.
Ttv	andesitic volcanic center (lavas, dikes, hypabyssal intrusions)	Complexly intruded hematite-stained basalt to andesite lavas (Ttba, Tta), andesitic block and ash flows, aphyric basaltic andesite hypabyssal intrusions with quartz veinlets, and andesitic dikes or intrusions with subvertical flow banding and to 10% phenocrysts (plagioclase, clinopyroxene). Dark gray to reddish gray.
Ttai	andesitic intrusions	Hypabyssal intrusions (dikes and sills). Dark gray with local red hematitic and green propylitic alteration; aphanitic groundmass with 5-10% phenocrysts: plagioclase, clinopyroxene.
Ttt	silicic tuff	Nonwelded to partially welded tuff. White to light tan groundmass; trace-10% phenocrysts (<1 mm): plagioclase, biotite, ± hornblende, ± quartz; trace to 25% lapilli-sized lithic fragments (red intermediate volcanic).
Ttss	fluvial sandstone: intermediate and silicic volcanic fragments	Feldspathic litharenite. Tan to red; moderately to poorly sorted, subrounded to subangular, predominantly fine- to medium-grained, to very coarse-grained. Clasts consist of feldspar and intermediate and silicic volcanic lithic fragments with trace biotite. Contains very thin layers of matrix-supported granule to pebble pumice and silicic tuff fragments. Thinly to thickly bedded, with horizontal bedding and trough cross-bedding. Local red siltstone and clast-supported granule to pebble conglomerates with silicic tuff and intermediate volcanic fragments.
Ttds	debris flow deposits: intermediate and silicic volcanic fragments	Matrix-supported polymictic breccia and conglomerate. Tan to red; massive to medium to very thickly bedded, average bed thickness ~5 m; subangular to angular pebble to large cobble intermediate volcanic and lesser silicic tuff clasts, fine- to medium-grained sand matrix (locally silicic ash-rich with quartz and biotite crystals). Channel-cut and scour surfaces between individual beds; interbedded with sandstone (Ttss) lenses.
Ttsa	fluvial sandstone: intermediate volcanic fragments	Feldspathic litharenite. Dark tan to reddish purple; moderately to poorly sorted, subrounded to subangular, medium- to coarse-grained with trace granules. Clasts consist of feldspar and intermediate volcanic lithic fragments. Contains lenses of clast-supported pebble conglomerates and matrix-supported pebble to cobble breccia with intermediate volcanic fragments. Thinly to thickly bedded.
Ttda	debris flow deposits: intermediate volcanic fragments	Matrix-supported breccia and conglomerate. Tan; massive to very thickly bedded, nongraded, average bed thickness ~10 m; angular to subrounded pebble to boulder (to 1.5 m) intermediate volcanic clasts, medium-grained sand matrix. Channel-cut and scour surfaces between individual beds.
Ttdt	talus and debris flow deposits	Debris flows: matrix-supported breccia; tan to gray; massive to very crudely stratified; angular pebble to boulder intermediate volcanic clasts (mostly small boulder [<0.5 m], to 2 m), with welded silicic ignimbrite clasts found upsection (to 5 m), fine-to-medium-grained sand matrix. Talus: clast-supported monolithic breccia; tan to gray; massive; angular cobble to boulder intermediate volcanic clasts (most >0.5 m, to 4 m), limited fine- to medium-grained sand matrix. Localized slide blocks of bedded sandstone to 15 m-thick (Fig. 10B).

Ttdi	debris flow deposits with welded silicic ignimbrite fragments	Matrix-supported polymictic breccia. Tan to red; massive; primarily subangular to angular cobble to boulder silicic welded ignimbrite clasts, lesser pebble intermediate volcanic clasts, fine-to-medium-grained sand to silt matrix. Larger (1-2 m) ignimbrite boulders weather to form small hoodoos (Fig. 10A).
Tpt	Traza ignimbrite	Welded to nonwelded lapilli-tuff. Dark tan (welded) to white (nonwelded) groundmass; 20% phenocrysts: plagioclase, pyroxene, trace quartz; gray fiamme; 30% lithic fragments (red intermediate volcanic, gray silicic volcanic and welded tuff; to 50 mm). Thickness: >40 m. Basal 1 m-thick vitrophyre, transitions upsection from welded to nonwelded, top not exposed.
Tpk	KM ignimbrite	Densely welded to nonwelded lapilli-tuff. Brownish red (welded) and white to light gray (nonwelded) groundmass; <5% phenocrysts: plagioclase, trace quartz; 30% gray fiamme (to 30 mm); 5-10% lithic fragments (red and gray intermediate volcanic). Thickness: ~40 to 100 m. Basal 0.5 m thick black vitrophyre below a ~ 10 m thick red densely welded lower portion that transitions upsection into a white partially welded to nonwelded top. Weathered-out pumice lenses (to 10 cm) near top.
Tpr	Rancho de Santiago ignimbrite	Welded to nonwelded lapilli-tuff. Welded portion: red to pinkish gray groundmass; weak eutaxitic texture; 5-20% phenocrysts: plagioclase (to 3 mm), pyroxene, ± hornblende, ± quartz; 10-20% gray fiamme with dark gray rims (altered to pink with orange rims near faults), typically to 30 mm, maximum 1 m-length); trace to 5% lithic fragments (red intermediate volcanic and gray silicic volcanic). Nonwelded portion: white to tan groundmass; <5% phenocrysts: plagioclase, clinopyroxene, hornblende; noncompacted pumice fragments (to 35 mm); 10-25% lithic fragments (red and brown intermediate volcanic and gray silicic volcanic). Thickness: ~80 to 200 m. Basal 2 m-thick vitrophyre unit with 2 black vitrophyres separated by ~0.5 m-thick welded tuff. Transitions upsection from welded to nonwelded top. Weathered-out pumice lenses (to 25 mm) in upper middle portion of unit. Fewer phenocrysts upsection. Larger size of lithic fragments and fiamme found in easternmost exposures.
Tpb	Puerto Blanco ignimbrite	Welded to nonwelded lapilli-tuff. Nonwelded lower portion: tan to white groundmass; <5% phenocrysts: plagioclase, with trace biotite, hornblende, pyroxene, quartz; 15% white pumice fragments (to 30 mm); 30-40% lithic fragments (red and gray intermediate volcanic, to 50 mm). Welded portion: tan groundmass; 10-15% phenocrysts: plagioclase, biotite, with trace hornblende, quartz; 5% yellow fiamme (to 10 cm), mostly occur as weathered-out lenses in outcrop; 15-20% lithic fragments (red & gray intermediate volcanic, to 30 mm). Nonwelded top: white to light pink groundmass; 15-20% phenocrysts: plagioclase, biotite; 10-15% yellowish-white long-tube pumice fragments; 10% lithic fragments (red and gray intermediate volcanic; to 15 mm). More than 190 m-thick, base not exposed.
Tpp	Portero ignimbrite	Densely welded to welded lapilli-tuff. Pink groundmass; eutaxitic texture; trace to 25% phenocrysts: plagioclase, pyroxene, ± hornblende, trace quartz; 20% dark reddish-gray fiamme (to 30 cm); trace to 10% lithic fragments (red and gray volcanic; to 15 mm). Thickness: ~20 to 180 m. Basal 1 m-thick vitrophyre, top eroded. Increased amount of phenocrysts, lithic fragments, and vapor-phase alteration upsection.

Tpe	Ericicuchi ignimbrite	Welded to nonwelded lapilli-tuff. Reddish-gray (welded) to light gray or white (nonwelded) groundmass; compaction foliation; 5-15% phenocrysts: plagioclase, pyroxene, ± biotite, ± hornblende, trace quartz; 5-10% dark gray fiamme with orange rims (to 10 mm), noncompacted white to brown pumice in nonwelded portion; trace to 10% (locally to 30%) lithic fragments (red, purple, and orange intermediate and gray silicic volcanic; to 2 mm, locally to 30 mm). Thickness: ~210 m. Base located in inaccessible cliff exposures, transitions upsection from welded interior to nonwelded top.
Tpc	Chepe ignimbrite	Densely welded lapilli-tuff. Light red groundmass; eutaxitic texture; 30% phenocrysts: quartz (embayed), plagioclase, biotite (to 2 mm), hornblende; 15% pink-orange colored fiamme. More than 140 m-thick, base not exposed. Likely correlative to the Divisadero tuff of Swanson et al. (2006) (see text).
Tps	fluvial reworked tuff, sandstone, and conglomerate	Reworked tuff: white; white pumice fragments; 5-10% crystal fragments: plagioclase, biotite, hornblende; <5% lithic fragments (~1 cm), thinly-to-thickly-bedded. Sandstone: orange to tan; moderately well to poorly sorted, fine- to medium-grained, white pumice and tuff fragments; cross-bedding and graded bedding; local well-sorted pumice-rich granule lenses. Conglomerate: reddish orange; matrix-supported; massive; monomictic; subrounded pebble to cobble silicic ignimbrite (welded to nonwelded) clasts, fine-to-medium-grained sand matrix.
*Figure 3; Supplemental File 1 (see footnote 1)		
[†]further descriptions of the silicic volcaniclastic and fluvial-lacustrine deposits (Tsv) are given in Chapter 2		

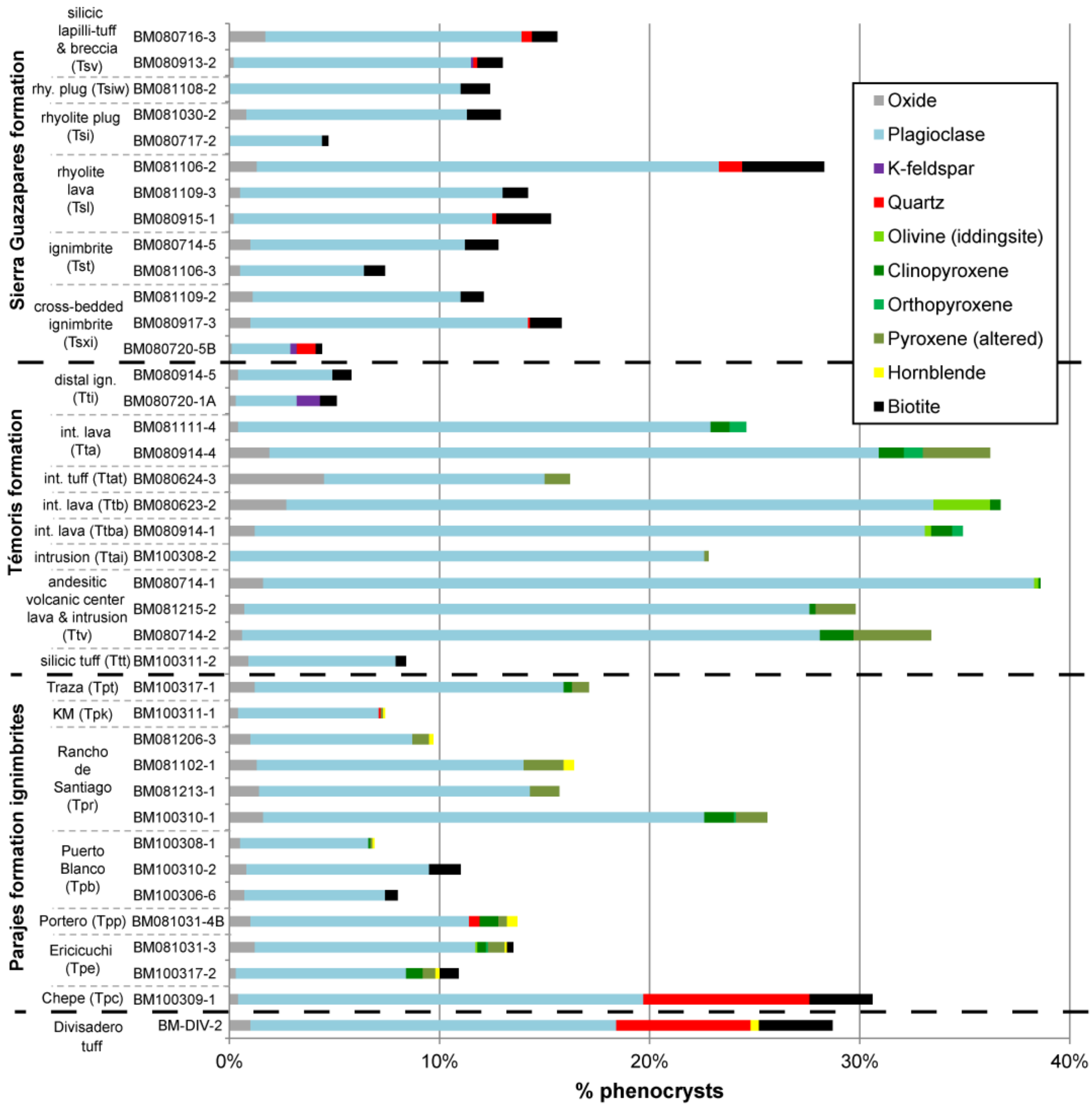

Figure 6. Modal point-count analyses of representative volcanic and intrusive rocks from the three formations of the Guazapares Mining District region showing the percentage of phenocrysts in each sample. Map unit symbols correspond to Figure 3 and Table 1. DIV-2 is a sample of the upper Divisadero tuff (e.g., Swanson et al., 2006) collected from Divisadero, ~50 km east-northeast of the Guazapares Mining District region, and analyzed during this study for compositional comparison with welded ignimbrites of the Parajes formation. One thin section was analyzed per sample, with 1000 point counts per thin section. GPS coordinates of the samples and details of individual modal point-count analyses, including the proportions of lithic, pumice, and volcanic glass fragments in each sample, are shown in Appendix 1.

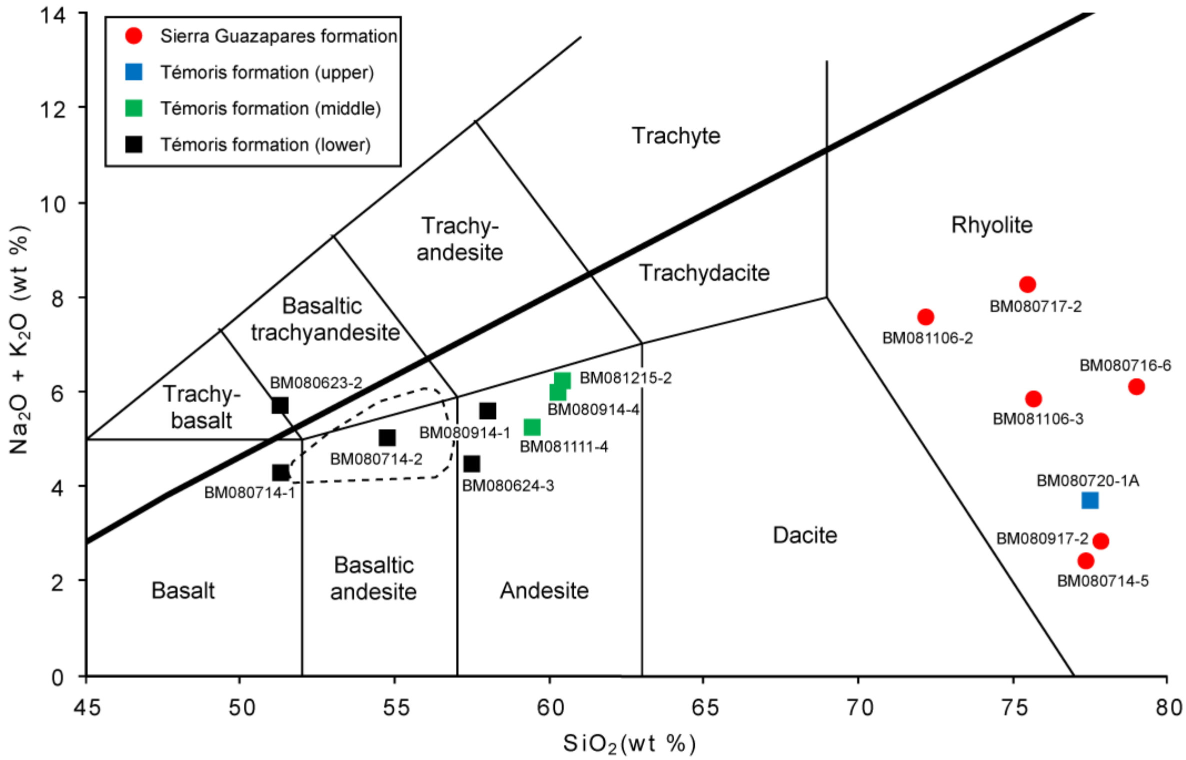

Figure 7. Total alkali-silica (TAS) classification diagram (after Le Bas et al., 1986) for selected volcanic rocks of the Guazapares Mining District region. The boundary between the alkaline and subalkaline fields (thicker line) is after Irvine and Baragar (1971). Samples were analyzed from the Témoris formation (squares) and the Sierra Guazapares formation (circles). Details of each analysis and GPS coordinates of samples are given in Table 2 and sample locations are plotted in Supplemental File 1 [see footnote 1]. The field of the Southern Cordillera basaltic andesites, based on Figure 5 of McDowell et al. (1997) is included here for comparison (dashed line).

TABLE 2. WHOLE-ROCK GEOCHEMICAL ANALYSES FROM VOLCANIC ROCKS AND INTRUSIONS

Sample	Map unit	Formation	SiO_2	TiO_2	Al_2O_3	FeO	MnO	MgO	CaO	Na_2O	K_2O	P_2O_5	Rock name	UTM (E)	UTM (N)
BM080716-6	Tsiw	Sierra Guazapares	79.00	0.15	13.32	0.82	0.03	0.45	0.11	2.37	3.73	0.02	high-silica rhyolite	767384	3035292
BM080717-2	Tsi	Sierra Guazapares	75.47	0.18	14.27	0.75	0.05	0.33	0.65	4.18	4.08	0.03	rhyolite	770929	3030949
BM081106-2	Tsl	Sierra Guazapares	72.18	0.39	15.35	2.00	0.07	0.63	1.69	3.64	3.93	0.12	rhyolite	769571	3028001
BM080917-2	Tsl	Sierra Guazapares	77.84	0.21	13.20	0.96	0.06	1.22	3.64	0.42	2.41	0.02	rhyolite (altered)*	772612	3023830
BM081106-3	Tst	Sierra Guazapares	75.67	0.25	13.58	1.34	0.03	0.61	2.63	1.29	4.56	0.04	rhyolite	769700	3028097
BM080714-5	Tst	Sierra Guazapares	77.36	0.25	13.51	1.14	0.06	1.06	4.19	0.67	1.75	0.00	rhyolite (altered)*	773778	3023239
BM080720-1A	Tti	Témoris (upper)	77.50	0.24	13.28	1.25	0.09	1.16	2.77	0.54	3.16	0.01	rhyolite (altered)*	768484	3027285
BM081111-4	Tta	Témoris (middle)	59.44	0.98	18.82	5.96	0.12	2.27	6.84	3.69	1.55	0.33	andesite	775962	3025047
BM080914-4	Tta	Témoris (middle)	60.28	0.98	17.82	6.68	0.09	2.14	5.71	3.84	2.15	0.31	andesite	773279	3023255
BM081215-2	Ttv	Témoris (middle)	60.42	1.29	16.68	6.92	0.20	2.27	5.44	4.33	1.89	0.56	andesite	772106	3020880
BM080624-3	Ttat	Témoris (lower)	57.49	1.02	16.93	7.55	0.15	4.92	7.19	3.26	1.22	0.27	andesite	770411	3028744
BM080623-2	Ttb	Témoris (lower)	51.29	1.88	17.85	10.40	0.15	4.68	6.98	3.50	2.21	1.08	basaltic trachyandesite	769959	3035621
BM080914-1	Ttba	Témoris (lower)	58.00	1.00	19.27	6.40	0.15	2.31	6.95	3.79	1.80	0.33	andesite	773051	3023001
BM080714-1	Ttv	Témoris (lower)	51.30	1.38	20.09	9.40	0.20	3.65	9.30	3.36	0.93	0.38	basalt	771758	3021619
BM080714-2	Ttv	Témoris (lower)	54.76	1.13	19.50	7.85	0.12	3.56	7.72	3.65	1.37	0.33	basaltic andesite	771841	3021629

Notes: Calculated on anhydrous basis, normalized to 100%. Universal Transverse Mercator (UTM) coordinates are based on the North American Datum 1927 (NAD27) zone 12. Locations of the samples are shown on Supplemental File 1 (see footnote 1). Map unit labels correspond to Table 1.

* Na_2O and K_2O leaching - likely due to hydrothermal alteration of albite and orthoclase

Parajes formation

The Parajes formation is primarily exposed in the eastern part of the study area; continuous stratigraphic sequences are found in the vicinity of Rancho de Santiago (Fig. 3A). The base of this formation is not exposed in the study area. The formation is composed of seven lithologically distinct silicic ignimbrites, with lesser locally interbedded sandstone, conglomerate, and reworked tuff (Figs. 6, 8 and 9; Table 1). Individual ignimbrites are informally named in this study, and are distinguished based on phenocryst assemblages and outcrop characteristics such as degree of welding, weathering style, color, and percentage and type of pumice and/or fiamme and lithic fragments (Figs. 6 and 8; Table 1).

Description

Each ignimbrite of the Parajes formation has a densely welded to partially welded lower part that passes upward into a less welded to nonwelded top (Figs. 8 and 9A), forming a single cooling unit, as well as a single flow unit with normal coarse-tail grading of lithic fragments and inverse coarse-tail grading of pumice. Where the bases of ignimbrites are exposed, 0.5–2-m-thick basal vitrophyres are present. The ignimbrites are generally crystal-poor to crystal-moderate (<20%) with a dacitic phenocryst assemblage (no chemical analyses were done) consisting primarily of plagioclase and pyroxene phenocrysts, with minor amounts of hornblende, biotite, and quartz in some ignimbrites; sanidine is lacking in all of the ignimbrites of the Parajes formation (Fig. 6). The thickness of individual ignimbrites range from ~20 to ~210 m; the total thickness of the Parajes formation is ~1 km (Fig. 8; Table 1). Some ignimbrites appear to thicken due to ponding in paleotopographic lows (e.g., Rancho de Santiago [Tpr] and KM [Tpk] ignimbrites); ponded thicknesses are 2.5 times greater than nonponded parts of the same ignimbrite (Figs. 3A and 4; Table 1).

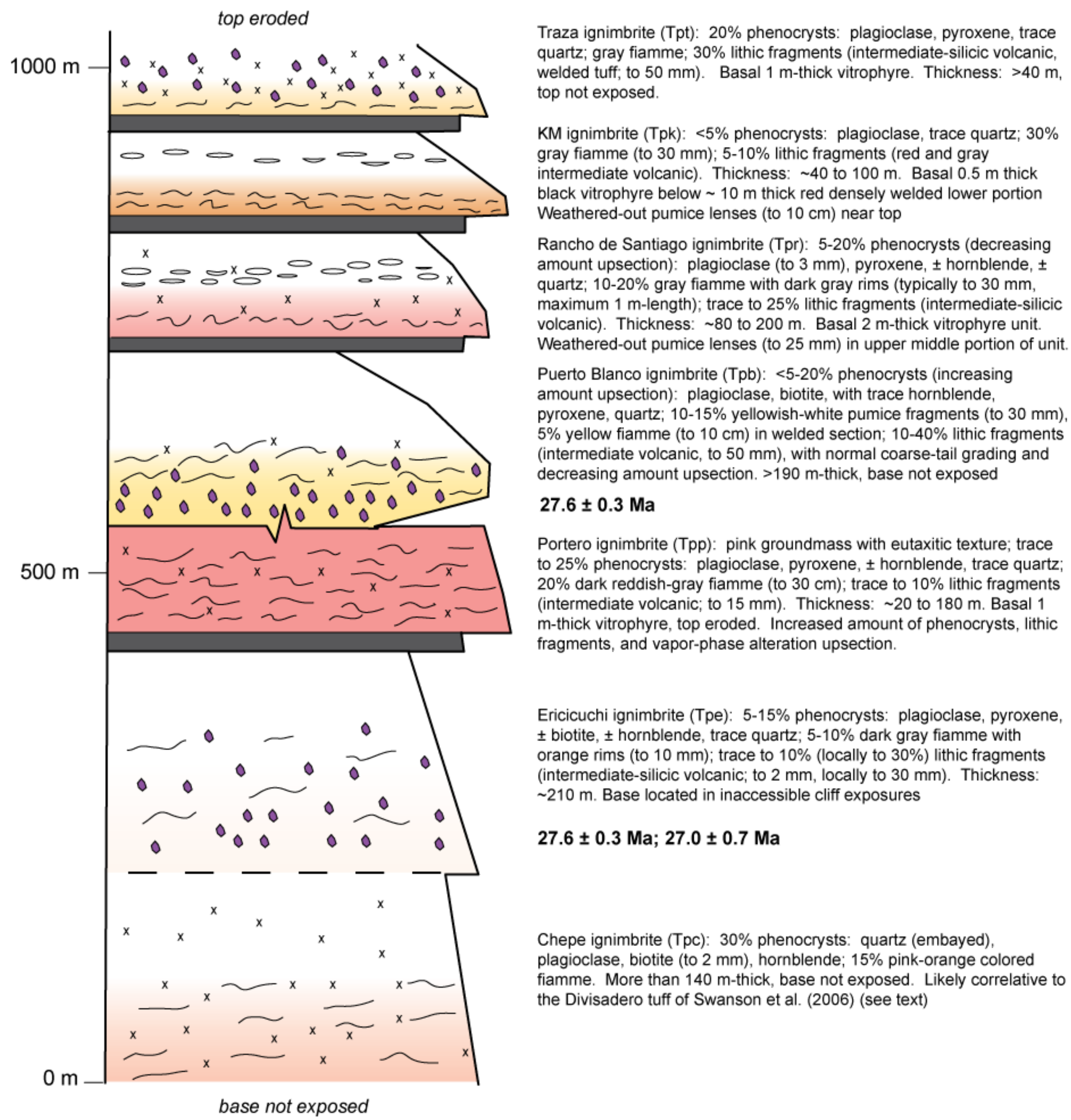

Figure 8. Generalized stratigraphic column describing the key characteristics of the seven distinct ignimbrites of the Parajes formation (see Table 1 for detailed descriptions). Zircon U-Pb LA–ICP–MS ages of the two ignimbrites dated from the Parajes formation are indicated by bold text (Fig. 14; Table 3).

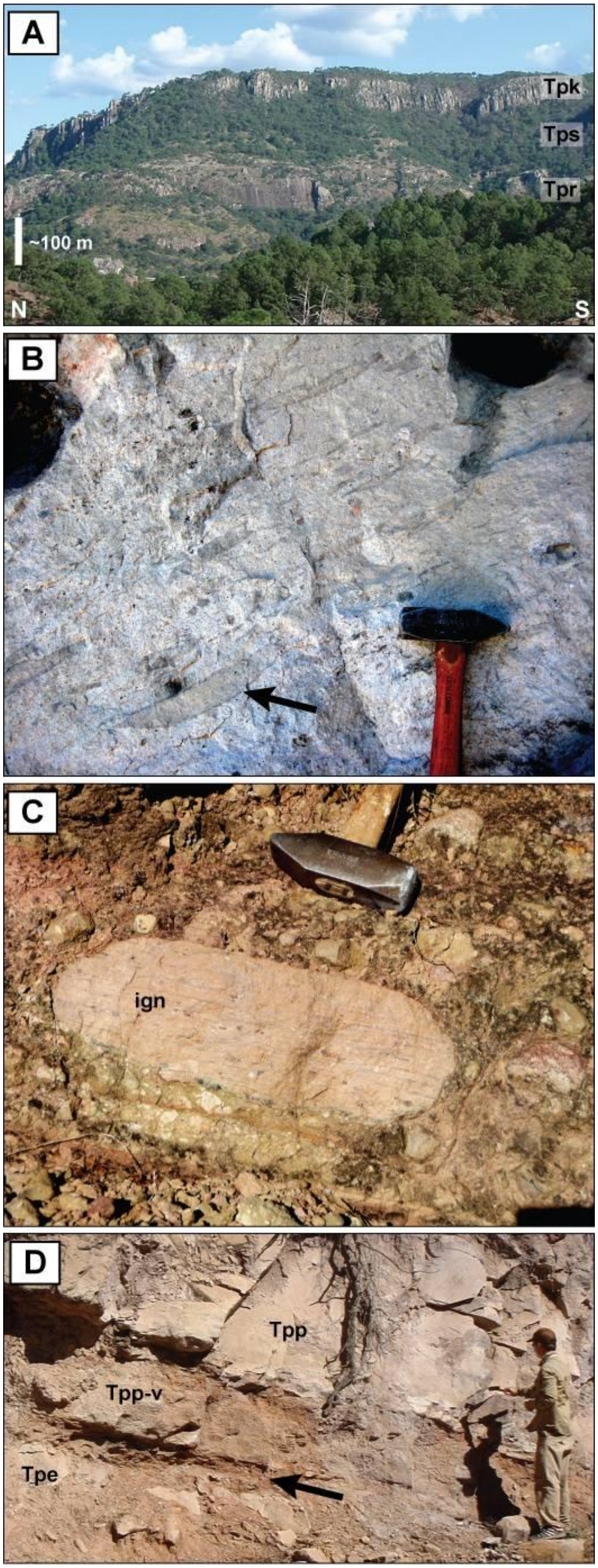

Figure 9. Representative photographs of the Parajes formation; locations of photos are given (NAD27 UTM zone 12). Unit abbreviations as in Table 1. (A) View east towards Cordón Bairomico from Chapotillo (777340E 3027305N; Fig. 3A), with the cliff-forming welded portions of the KM ignimbrite (Tpk) and Rancho de Santiago ignimbrite (Tpr) separated by a ~150-m-thick sequence of reworked tuff and sandstone (Tps). (B) Welded ignimbrite near the base of the Rancho de Santiago ignimbrite (Tpr), with large dark-rimmed gray fiamme (e.g., arrow) at 780913E 3028802N. Head of hammer is ~12.5 cm. (C) Subrounded welded ignimbrite clast with eutaxitic texture (ign) below hammer (head is ~12.5 cm), likely derived from the Parajes formation, in a monomictic matrix-supported pebble-to-cobble conglomerate (Tps) deposited above the Rancho de Santiago ignimbrite (Tpr) near Mesa de Cristal (777551E 3033189N; Supplemental File 1 [see footnote 1]). (D) Depositional contact between the nonwelded upper portion of the Ericicuchi ignimbrite (Tpe) and the densely welded lower portion the Portero ignimbrite (Tpp) with basal ~1-m-thick vitrophyre (Tpp-v) at 775567E 3024552N. A thin (<1 m) layer of fine-to-medium-grained sandstone is observed along the contact between the two units (arrow).

Each ignimbrite of the Parajes formation has distinguishing outcrop and/or compositional characteristics, described in ascending stratigraphic order (Figs. 6 and 8; Table 1). The Chepe, Ericicuchi, and Portero ignimbrites form the oldest continuous stratigraphic sequence, which is only found on the southwest (footwall) side of the Chapotillo fault in the Guazapares Mining District region (Fig. 3A). The Chepe ignimbrite (Tpc) is the only crystal-rich (~30%) ignimbrite in the study area, with embayed quartz and biotite phenocrysts to 2 mm in diameter. The Ericicuchi ignimbrite (Tpe) has dark gray fiamme to 1 cm in length, typically with orange rims, and it has a mafic phenocryst assemblage that includes pyroxene, hornblende, and biotite. The Portero ignimbrite (Tpp) is characterized by a pink groundmass with eutaxitic texture in the densely welded lower portion, dark reddish-gray fiamme to 30 cm-length, and trace quartz phenocrysts.

The Puerto Blanco, Rancho de Santiago, KM, and Traza ignimbrites form a second, younger continuous stratigraphic sequence that is only found on the northeast (hanging wall) side of the Chapotillo fault (Fig. 3A); the depositional relationship between the two stratigraphic sequences on either side of the fault is not known, but is considered younger than the previously described sequence on the footwall based on the sense of fault offset (Fig. 4) and inferred regional correlations (described in the Discussion following). The base of the Puerto Blanco ignimbrite (Tpb) is not exposed; however the exposed portion of its lower part, as well as its upper part, are nonwelded, with a welded middle. The Puerto Blanco ignimbrite (Tpb) has the greatest amount and size of lithic fragments (10%–40%, to 5 cm) compared to the other ignimbrites of the Parajes formation, with normal coarse-tail grading and upsection decrease in lithic fragments (from ~40% to 10%); it also shows an upsection increase in phenocrysts (from <5% to 20%) and an upsection increase in fiamme, which are distinctively yellow. The Rancho de Santiago ignimbrite (Tpr) is similar in appearance and composition to the Portero ignimbrite (Tpp) described above, but has gray fiamme with dark gray rims (Fig. 9B); these are generally 3 cm (to 1 m) in length. It has a 2-m-thick basal vitrophyre at the contact with the underlying Puerto Blanco ignimbrite. The KM ignimbrite (Tpk) is similar to the underlying Rancho de Santiago ignimbrite (Tpr), but is distinguished by the presence of a brownish-red, ~10-m-thick, crystal-poor (<5%) lower welded section and an overall lower lithic fragment content (5%–10%). The youngest unit of the Parajes formation is the Traza ignimbrite (Tpt), which is similar in appearance to both the Chepe and Puerto Blanco ignimbrites, but is distinguished by having gray fiamme and a moderate crystal content (20%) with trace quartz and no biotite.

Sedimentary rocks occur locally between ignimbrite units. A ~150-m-thick sequence of reworked tuff and cross-bedded sandstone with fragments of tuff and pumice (Tps) is between the Rancho de Santiago ignimbrite (Tpr) and KM ignimbrite (Tpk) southwest of the Arroyo Hondo–Puerto Blanco fault (Figs. 3A and 4). Also present at this stratigraphic interval in the Mesa de Cristal area east of Rancho de Santiago (Supplemental File 1 [see footnote 1]) is a monomictic matrix-supported pebble to cobble conglomerate with welded ignimbrite clasts similar in appearance to ignimbrites of the Parajes formation (Fig. 9C). In addition, a thin (<1 m) layer of fine- to medium-grained sandstone is present along the contact between the Ericicuchi ignimbrite (Tpe) and Portero ignimbrites (Tpp) (Fig. 9D).

Interpretation

The Parajes formation represents medial facies of silicic outflow ignimbrite sheets, based on the sheet-like geometry of the flow units, the moderate thicknesses of flow units (each <~200-m-thick, locally thicker where ponded by paleotopography), the presence of welding textures and vitrophyres, and the lack of associated lithic lag breccias. No caldera or vent-proximal lithofacies have been identified for these outflow ignimbrites, so the locations of their sources are not known. However, lithic fragments and fiamme within the Rancho de Santiago ignimbrite (Tpr) increase in size eastward, suggesting that the source for this ignimbrite is located toward this direction. Based on flow thicknesses and degree of welding relative to distance from the source recorded in large-volume silicic ignimbrites in the western U.S. (e.g., Smith, 1960; Lipman, 2007), the ignimbrites of the Parajes formation were likely erupted from calderas located within 50–100 km. The large size and concentration of lithic fragments within the Puerto Blanco ignimbrite (Tpb) are suggestive of a somewhat closer source.

Sedimentary rocks (Tps) interbedded with the ignimbrites of the Parajes formation record both erosion of welded units and reworking of unconsolidated pyroclastic debris, with deposition by fluvial and debris flow processes (Figs. 9C, 9D). The debris flow deposits are massive, poorly sorted matrix-supported conglomerates, while fluvial sandstones and fluvially reworked tuffs have trough cross-bedding, normal grading, and well-sorted granule conglomerate lenses. The clasts in these sedimentary rocks are predominantly silicic volcanic fragments, including welded and nonwelded tuff and pumice (e.g., Fig. 9C); there are no andesitic volcanic fragments in these rocks. This suggests that the Parajes formation ignimbrites were uplifted and partly eroded prior to deposition of overlying andesitic rocks of the Témoris formation.

Témoris Formation

The Témoris formation overlies the Parajes formation in angular unconformity, and is best exposed in the central and western portions of the study area in the vicinity of Puerto La Cruz and Guazapares (Fig. 3). This formation is primarily composed of mafic to intermediate composition lavas (flow-banded and/or vesicular) and hypabyssal intrusions, intercalated conglomerates, breccias, and sandstones dominated by mafic to intermediate volcanic lithic fragments, and lesser thin silicic nonwelded ignimbrites and reworked silicic tuff (Figs. 6, 7 , and 10; Tables 1 and 2). This formation has undergone mild hematitic and propylitic alteration, with infilling of vesicles and autoclastic flow breccia interstices with zeolite minerals; the most intense alteration is in the rocks within the Guazapares fault zone (Fig. 3B).

Description

The basal deposits of the Témoris formation consist of sandstones with silicic tuff fragments (Ttss), matrix- to clast-supported breccias with welded silicic ignimbrite boulders (Ttdi, Ttdt; Figs. 10A, 10B), and lesser interbedded silicic tuffs (Ttt). The welded ignimbrite clasts were derived from the underlying Parajes formation, indicating continued erosion of this formation. One ignimbrite of the Parajes formation (Portero ignimbrite, Tpp), located east of Ericicuchi near 12R 775504E 3024974N (Universal Transverse Mercator coordinates, North American Datum 1927; Fig. 3A), contains clastic dikes directly below the Parajes–Témoris formation contact. These dikes are composed of overlying Témoris formation sandstone that infills fissures formed in the top of the Portero ignimbrite.

The Témoris formation is subdivided into three sections based on volcanic rock compositions and types (Figs. 6, 7, and 11; Tables 1 and 2; Appendix 1). These subdivisions have gradational contacts and consist of: (1) a lower section of pyroxene-plagioclase ± olivine-bearing amygdaloidal basalt, basaltic andesite, and andesite lavas and autoclastic flow breccias (Ttba, Ttb; Figs. 10C, 10D); (2) a middle section of pyroxene-plagioclase-bearing flow-banded andesite lavas (Tta; Fig. 10E); and (3) an upper section of several thin (<5-m-thick) primary and reworked rhyolite ignimbrites (Tti; Figs. 10F, 10G); this upper section is only locally preserved beneath the angular unconformity with the overlying Sierra Guazapares formation. Conglomerates, breccias, and sandstones with well-sorted gravel

Figure 10 (*next 2 pages*). Representative photographs of the Témoris formation; locations of photos are given (NAD27 UTM zone 12). Unit abbreviations as in Table 1. (A) Matrix-supported polymictic breccia with cobble-to-boulder-sized welded silicic ignimbrite clasts (ign) and lesser pebble-sized mafic to intermediate volcanic clasts (below ign boulder) from the basal section of the Témoris formation (Ttdi), weathering to form a small hoodoo in the Rancho de Santiago area (776990E 3031055N). The large (1–2 m) welded ignimbrite boulders (ign) were likely derived from the Parajes formation. (B) Clast-supported monolithic breccia of angular intermediate volcanic cobble-to-boulder-sized clasts (Ttdt), which includes a 15-m-thick slide block of bedded sandstone (ss), in the Rancho de Santiago half-graben basin adjacent to Rancho de Santiago fault (777781E 3028522N; Fig. 3A). (C) Autoclastic flow breccia on top of andesitic lava (Ttba) at 769403E 3032339N. (D) Blocky autoclastic flow breccia in basaltic trachyandesite lavas (Ttb) at 771976E 3032195N. (E) Andesite lava (Tta) with basal autoclastic flow breccia infilling a channel (arrow) incised into underlying reddish orange sandstone (Ttsa) and debris flow deposits (Ttda) in the middle section of the Témoris formation in the Puerto La Cruz area (773685E 3022996N). (F) Lithic-rich 2–3-m-thick ignimbrite deposit (Tti), with ~30% mafic-intermediate and silicic volcanic lithic fragments to 3 cm, deposited over medium-bedded sandstone (Ttss) at 768484E 3027278N. (G) Medium-bedded matrix-supported tuffaceous conglomerate (reworked tuff) from the upper section of the Témoris formation (Ttds), with subangular to subrounded mafic-intermediate and silicic volcanic clasts. Located in the Puerto La Cruz measured section (~25 m; Fig. 11D) at 773391E 3023300N. Head of hammer is ~12.5 cm. (H) Sandstone (Ttsa) filling in depression on top of amygdaloidal basalt lava (Ttba) at 771675E 3021604N. (I) Matrix-supported polymictic conglomerate with subangular to subrounded mafic-intermediate and silicic volcanic clasts (Ttds), interbedded fine- to medium-grained sandstone (Ttss), located in the half-graben basin adjacent to the Agujerado fault (776328E 3025345N; Fig. 3A). A white pumice-rich lens (wht) is located near base of the 33-cm-long hammer, and a thin (~1 cm) siltstone layer is located directly above the head of hammer (arrow). (J) Matrix-supported polymictic breccia from the upper section of the Témoris formation (775590E 3025137N), with subangular to subrounded mafic-intermediate volcanic and silicic ignimbrite clasts (Ttds). Breccia grades upsection into sandstone with a thin white pumice-rich lens located below the head of the 38-cm-long hammer (arrow). (K) Down-dip view of sandstone from the upper section of the Témoris formation (Ttss), with trough cross-bedding (e.g., arrow) and lenses of white pumice and tuff fragments at 767952E 3027759N. Hammer in photo is 38-cm-long. (L) Wet sediment-lava (peperitic) intermixing along the depositional contact between orange-tan sandstone (Ttss) and reddish-gray basaltic andesite (Ttba) at 776571E 3032292N. Hammer in photo is 38 cm.

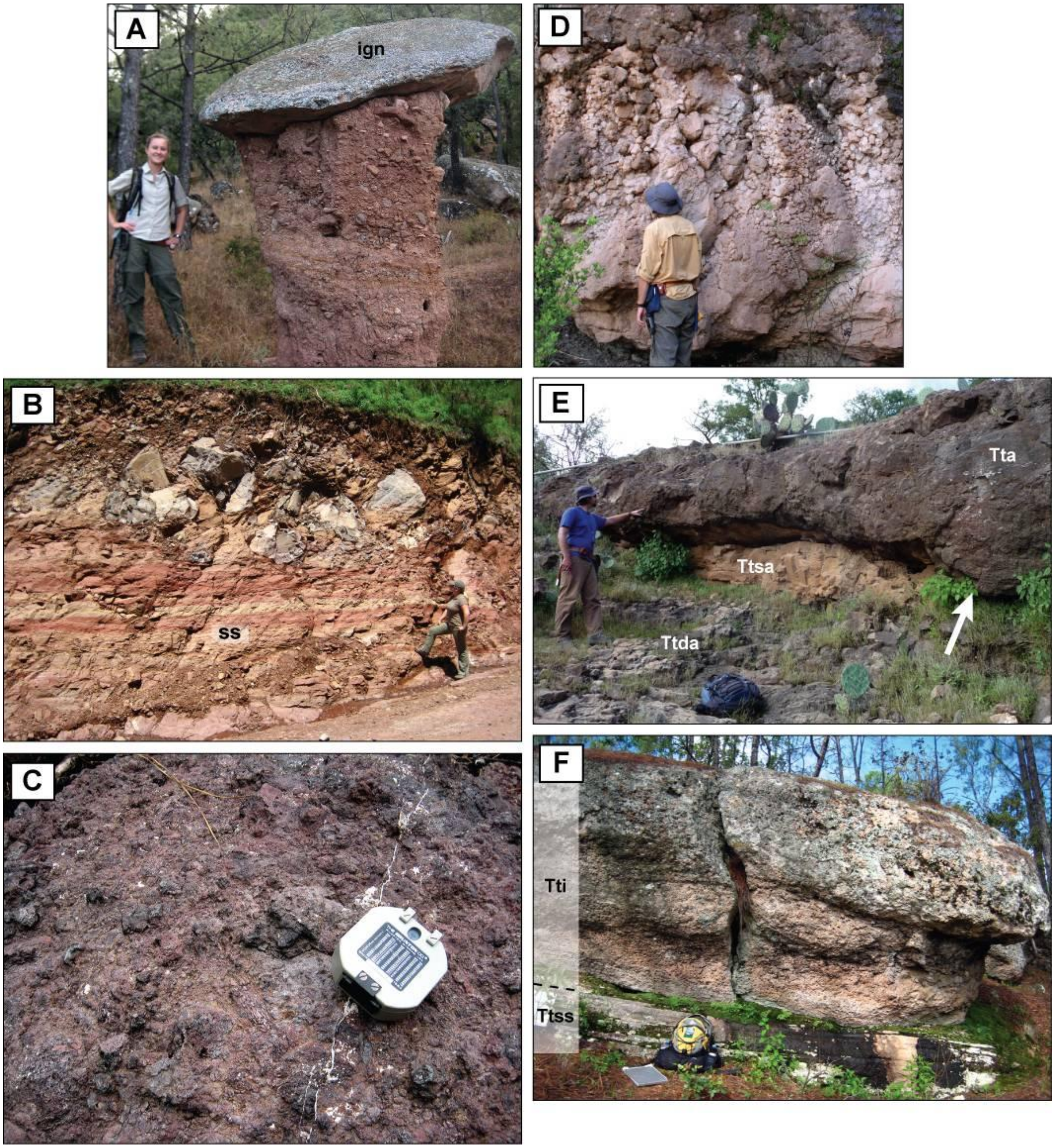
A
ign
D
B
ss
E
Tta
Ttsa
Ttda
C
F
Tti
Ttss

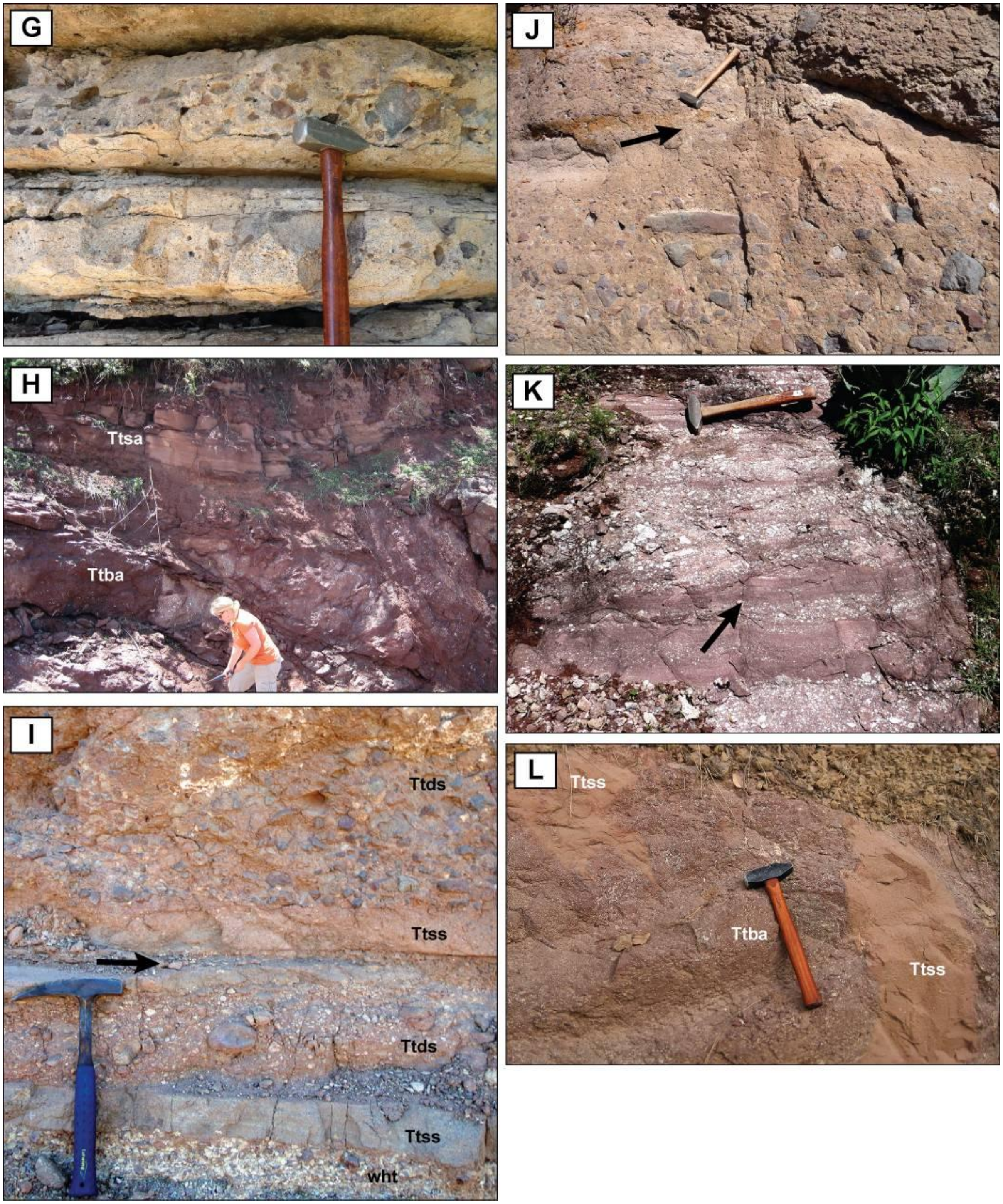
G
J
H
Ttsa
Ttba
K
I
Ttds
Ttss
Ttds
Ttss
wht
L
Ttss
Ttba
Ttss

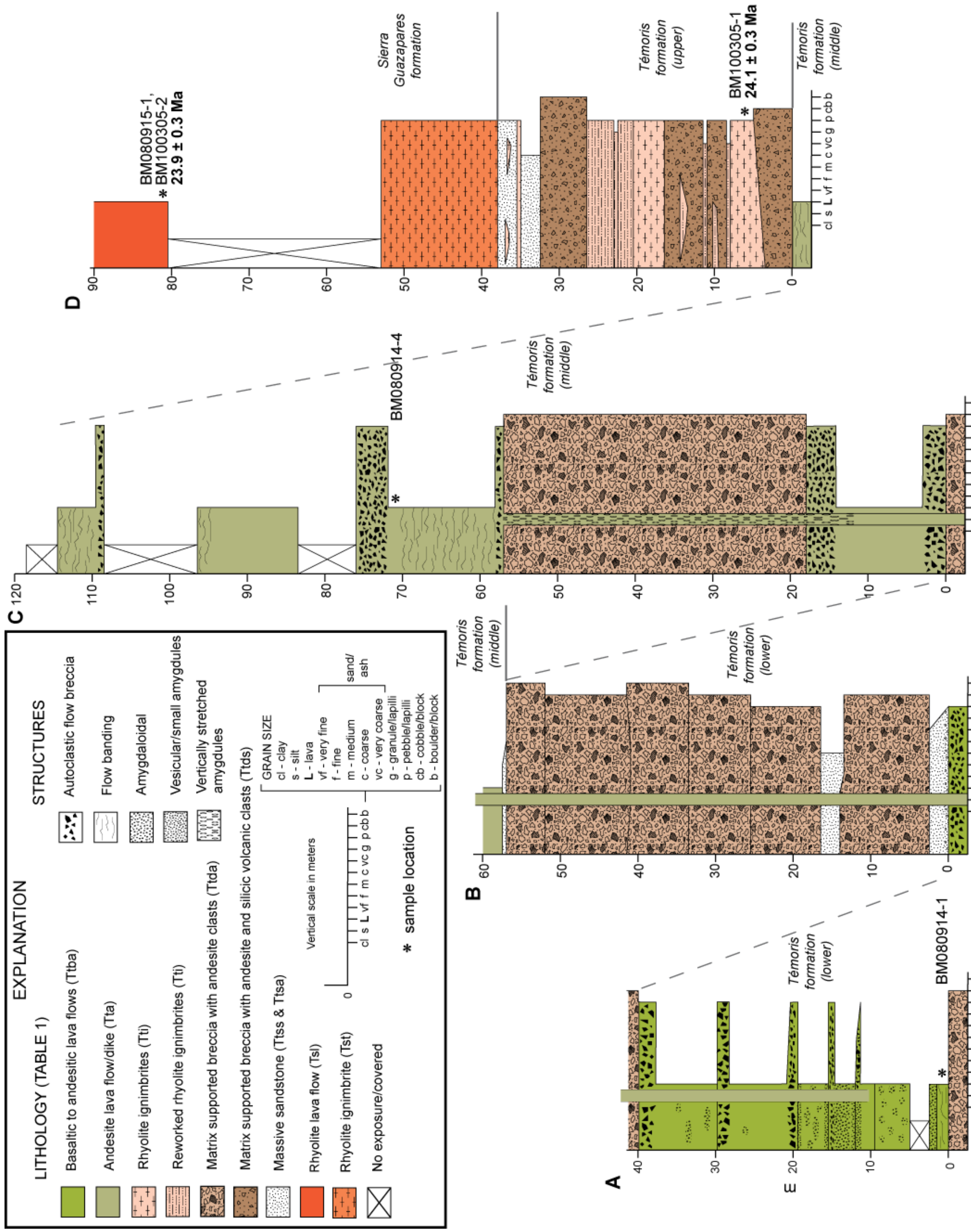

Figure 11. Four continuous measured stratigraphic sections (A–D) of the Témoris formation to Sierra Guazapares formation in the Puerto La Cruz area, east of Témoris (see Fig. 3A), with lithologies, depositional structures, and stratigraphic positions of analyzed samples (Figs. 6, 7, and 14; Tables 2 and 3; Appendices 1 and 2). The three subdivisions of the Témoris formation and the boundary between the Témoris and Sierra Guazapares formations are indicated.

lenses and trough cross-bedding are interbedded with and laterally interfinger with all of the volcanic rocks listed above (Figs. 10B, 10F–10K, and 11; Table 1). These volcaniclastic deposits contain detritus similar in composition to the interstratified lavas and ignimbrites: amygdaloidal and flow-banded basaltic andesite to andesite clasts dominate the lower and middle sections of the Témoris formation (Ttda, Ttsa, Ttdt), while the upper section of the Témoris formation has mixed mafic-intermediate and silicic volcanic clasts, including pumice fragments in tuffaceous sandstones and tuffaceous conglomerates (Ttss, Ttds, Tti). Lavas and autoclastic flow breccias locally infill channels incised into the underlying sedimentary rock (Fig. 10E), and wet sediment-magma (peperitic) interactions are locally observed where lavas were apparently emplaced over wet sand (Fig. 10L).

In the area around Témoris, the Témoris formation thickens from ~100–400 m to >700 m (Fig. 3; Supplemental File 1 [see footnote 1]). There, basalt to andesite lavas of the lower and middle sections of the Témoris formation are heavily hematite stained and are complexly intruded by numerous andesitic dikes and aphyric hypabyssal rocks (Ttv; Table 1).

Interpretation

The rocks of the Témoris formation are interpreted as the products of vent to proximal mafic to intermediate composition magmatism and distal silicic ignimbrite volcanism. Deposition in a terrestrial environment, likely part of alluvial fan systems (e.g., Kelly and Olsen, 1993; Blair and McPherson, 1994; Hampton and Horton, 2007; Murray et al., 2010), is indicated by interstratified matrix-supported debris flow breccias and conglomerates (Ttda, Ttds, Ttdi), clast-supported avalanche and/or talus breccias (Ttdt), well-sorted stratified and cross-bedded fluvial sandstones and conglomerates (Ttas, Ttss), and some lavas infilling fluvial channels and forming peperites within them (Fig. 10). The composition of fragments in the fluvial and debris flow deposits is similar to that of the interstratified volcanic rocks, indicating intrabasinal reworking of eruptive products. The upper section of rhyolite ignimbrites in the Témoris formation likely erupted from distal sources, because they are thin and nonwelded, with a high proportion of interstratified fluvially reworked tuff (Tti; Figs. 10F-G; Table 1).

We interpret the Témoris area to be the site of an andesitic volcanic center in the Témoris formation, based on dramatic thickening of the lava section, abundant plugs and dikes, and increased alteration (Fig. 3; Supplemental File 1 [see footnote 1]). This andesitic volcanic center, roughly defined by map unit Ttv, greatly thickens towards its subvolcanic intrusion-dominated core located along the ridge east of Témoris, with a minimum volume of 9 km^3 based on the mapped area and exposed thickness (Fig. 3; Supplemental File 1 [see footnote 1]). A feeder dike emanating from the volcanic center can be traced upward into an andesitic lava flow in the Puerto La Cruz area (Fig. 11). In addition, andesitic dikes crosscut rocks of the Témoris formation away from the volcanic center, locally along faults.

Sierra Guazapares Formation

The Sierra Guazapares formation comprises much of the central and northwestern part of the study area, with best exposures located along the N-S-trending ridge east of Guazapares (Fig. 3; Supplemental File 1 [see footnote 1]). This formation is composed of plagioclase-biotite ± quartz ± sanidine-bearing rhyolitic ignimbrites, rhyolite lavas, flow-banded rhyolite hypabyssal intrusions, and lesser silicic volcaniclastic deposits (Figs. 3, 6, 7, and 12; Table 1). The Sierra Guazapares formation is flat-lying to gently-dipping (<10°) and overlies the Témoris formation in low to moderate angular unconformity (Fig. 13A). The Sierra Guazapares formation is >200-m-thick; it is not known how much of the formation is preserved, because the top is eroded. The formation locally infills lows cut into older stratigraphic units, recording paleotopography produced by erosion or faulting.

Figure 12 (*next page*). Representative photographs of the Sierra Guazapares formation; locations of photos given (NAD27 UTM zone 12). Unit abbreviations as in Table 1. (A) Massive to stratified rhyolite ignimbrites (Tsti) forming prominent cliff north of Ericicuchi. Photo taken from 775509E 3024976N. (B) Tuffaceous sandstone (reworked tuff) with cross bedding (arrow) in stratified rhyolite ignimbrite unit (Tst); very fine-to-medium-grained, well to moderately sorted, subrounded. Head of hammer is 12.5 cm (771650E 3031928N). (C) View west from 769131E 3028438N at very large-scale cross-bedded rhyolitic ignimbrite unit (Tsxi) forming a ~30 m-tall cliff face (arrow) at Cerro San Miguel on west side of Guazapares fault zone (Fig. 3B). (D) Very large-scale cross-bedded rhyolitic ignimbrite (Tsxi), with person (outlined) standing on set boundary. The orientation of cross-stratification is emphasized by black dashed lines. Dark colored band to left of person (arrow) is a lithic-rich layer with ~50% lithic fragments (Fig. 12E), lighter colored bands contain ~10-20% lithic fragments (771904E 3026715N). (E) Close-up of lithic-rich layer in silicic surge-like ignimbrite (Tsxi) in Figure 12D, with reddish mafic-intermediate volcanic fragments (e.g., arrow) likely derived in part from the Témoris formation, having diameters ranging from 0.5 cm to 50 cm. White pumice and crystal fragments are present in an ash matrix (771904E 3026715N). (F) Subvertically flow-banded crystal-poor to aphyric rhyolitic hypabyssal intrusion (Tsi), Cerro Salitrera plug (770909E 3030955N; Fig. 3B). Red dashed lines emphasize orientation of flow banding. (G) Depositional contact between a rhyolite lava (Tsl; lower right) and overlying very large-scale cross-bedded rhyolitic ignimbrite (Tsxi; upper left). Map board (~30 cm-length) is located along the contact. The top of the rhyolite lava consists of an autoclastic flow breccia that has a red sandy matrix surrounding the flow-banded blocks, interpreted as sand infilling in the top of the lava prior to eruption of the rhyolitic ignimbrite (772569E 3023871N).

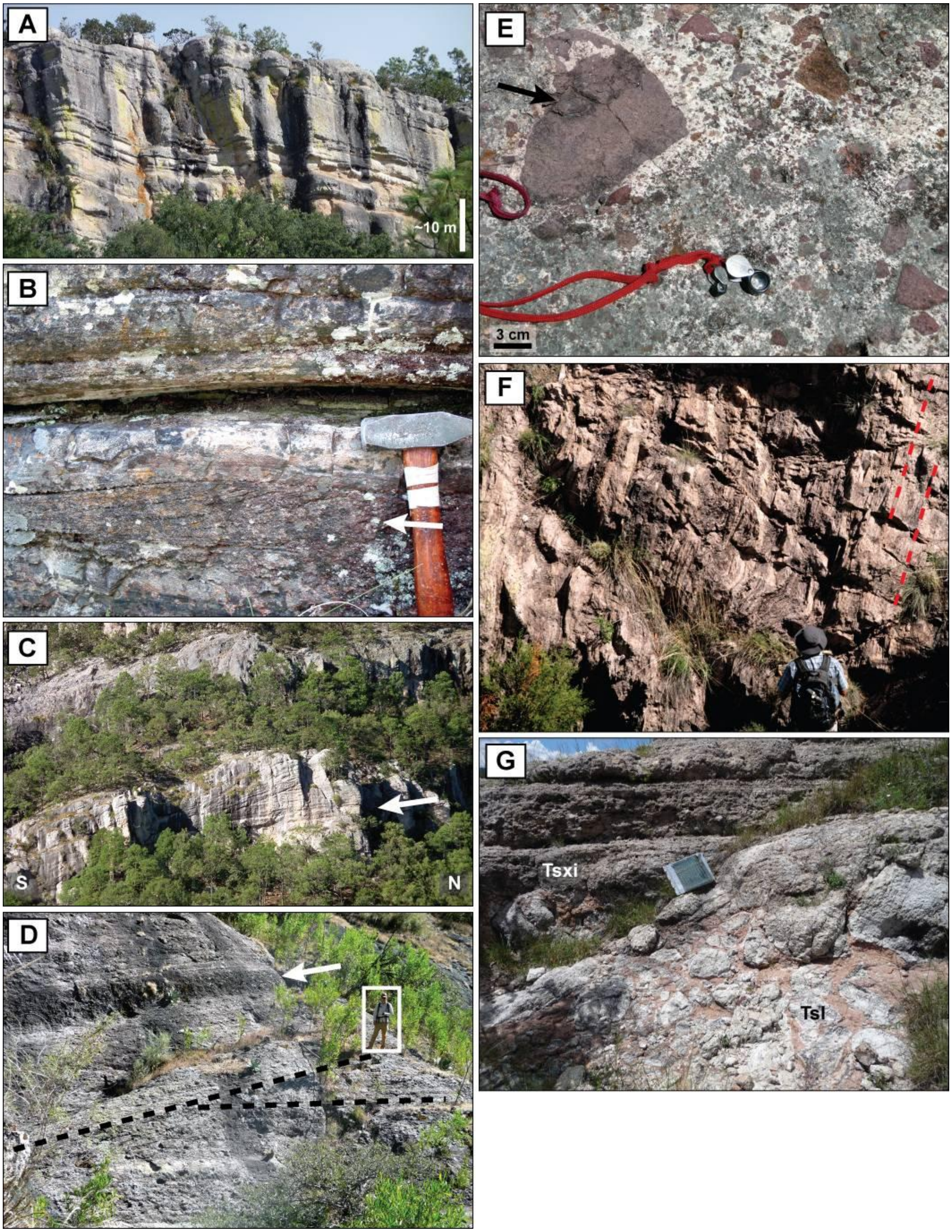
A
~10 m
B
C
S
N
D
E
3 cm
F
G
Tsxi
Tsl

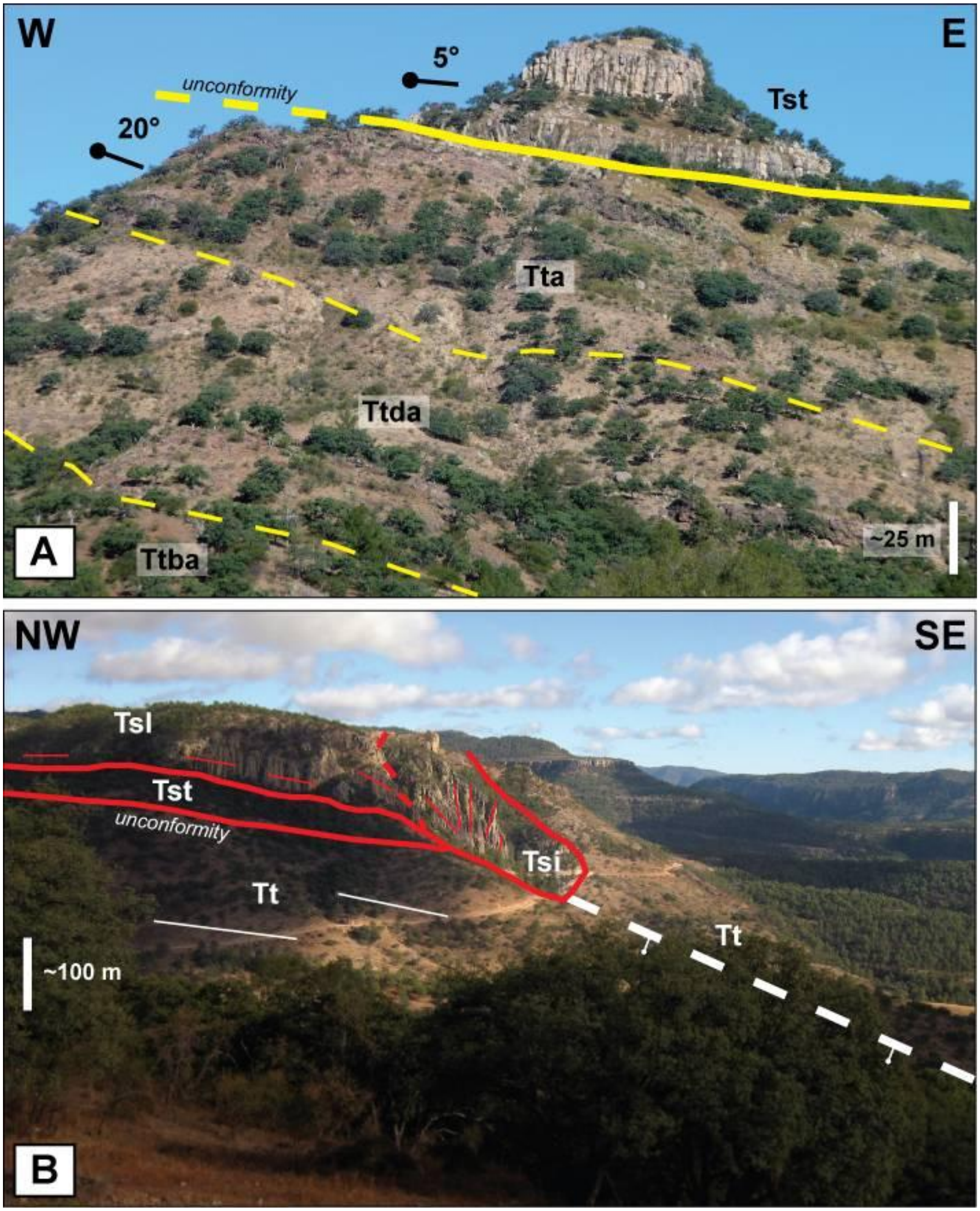

Figure 13. Interpreted photographs of depositional relationships between the Témoris formation and the Sierra Guazapares formation; locations of photos given (NAD27 UTM zone 12). Unit abbreviations as in Table 1. (A) Angular unconformity between gently-dipping (~5° NE) massive and stratified rhyolite ignimbrites of the Sierra Guazapares formation (Tst) and the underlying moderately-dipping (~20° E) lavas (Ttba, Tta) and debris flow deposits (Ttda) of the Témoris formation. View north towards Cerro Cuadro Blanco (Fig. 3B) from 772093E 3022247N. (B) View northeast from 772915E 3021769N towards silicic plug (Tsi) that intrudes the La Palmera fault and is the source for the silicic lava (Tsl) that flowed to the northwest over silicic ignimbrites of the Sierra Guazapares formation (Tst) and tilted rocks of the Témoris formation (Tt). The dip of flow banding (thin red lines) in the lava increases in proximity to the plug, where the flow banding is subvertical.

Description

The dominant lithofacies of the Sierra Guazapares formation is massive to stratified nonwelded to partially welded rhyolite ignimbrites (Tst; Fig. 12A; Table 1). Locally, these ignimbrites show evidence of reworking, including sorting and rounding of lithic, pumice, and crystal fragments, stratification and cut-and-fill structures, and small- to medium-scale cross-lamination (Fig. 12B).

Very large-scale cross-bedded rhyolitic ignimbrites (Tsxi) form a distinctive lithofacies of the Sierra Guazapares formation (Fig. 12C, 12D; Table 1). These deposits are mainly restricted to a linear belt ~11-km-long and 3-km-wide within and immediately adjacent to the Guazapares fault zone–La Palmera fault (Fig. 3B) and laterally grade away from this linear belt into massive to stratified ignimbrites (Tst; Figs. 3 and 5; Supplemental File 1). The very large-scale cross-bedded ignimbrites have average set heights of ~5 m; some are as great as ~20 m (Figs. 12C, 12D). The cross-bedding in these ignimbrites is defined by alternating lithic-rich (>50%) and lithic-poor (<30%) layers (Fig. 12D). The lithic fragments are very coarse-grained, with blocks to 50-cm-diameter; these are dominantly mafic to intermediate volcanic rocks likely derived from the underlying Témoris formation (Fig. 12E). The matrix of the very large-scale cross-bedded ignimbrites is an unsorted mixture of angular pumice, euhedral crystals, and glass shards, and the very large-scale cross-beds lack internal laminations, sorting, or other fine-scale sedimentary structures indicative of reworking by water.

Rhyolite lavas (Tsl) and hypabyssal intrusions (Tsi, Tsiw, Tsib) occur in the same linear belt along the Guazapares fault zone–La Palmera fault as the very large-scale cross-bedded ignimbrites, and also occur along additional NNW-striking faults in the region (Figs. 2 and 3; Supplemental File 1 [see footnote 1]). The silicic hypabyssal intrusions (Fig. 12F) are typically plugs with related dikes that intrude the ignimbrites (Tst, Tsxi) of the Sierra Guazapares formation, and some of the plugs pass continuously upward into rhyolite lavas (Tsl) (Fig. 13B). The rhyolite lavas typically overlie the ignimbrites, but are locally interstratified (Fig. 12G).

In addition to silicic ignimbrites, lavas, and plugs, the Sierra Guazapares formation also includes a volcaniclastic unit (Tsv) in the Monte Cristo area (Fig. 3B). This unit includes a rhyolitic breccia associated with the growth of a rhyolite dome complex (Tsiw) that overlies and interfingers with normal graded sandstones, mudstones with soft-sediment deformation features, and moderately to poorly sorted sandstone with trough cross-bedding and cut-and-fill structures (Table 1; Chapter 2).

Interpretation

We interpret the very large-scale cross-bedded ignimbrites to be vent-proximal lag breccias deposited from energetic, turbulent pyroclastic density currents erupted during several events from a major fissure vent along the Guazapares fault zone–La Palmera fault (Figs. 2 and 3). Their linear map distribution indicates they were erupted from fissure vents, rather than a central vent, and likely formed coarse-grained ramparts. Interstratified silicic lavas and plugs are concentrated along either side of the same fault zone, in the same linear map distribution, supporting the interpretation that the Guazapares fault zone–La Palmera fault controlled the siting of an 11-km-long silicic fissure vent.

The very large-scale cross-bedded ignimbrites (Tsxi) represent a gradation between the pyroclastic surge and pyroclastic flow end members of pyroclastic density current classification (e.g., Fisher and Schmincke, 1984; Branney and Kokelaar, 2002). The abundant very coarse-grained lithic layers in these cross-bedded ignimbrites are similar to lithic lag breccias described from other vent to proximal ignimbrites (e.g., Fisher and

Schmincke, 1984; Carey, 1991; Freundt et al., 2000; Branney and Kokelaar, 2002). The angularity of the lithic components and their derivation from the underlying Témoris formation suggests they were fragmented and incorporated into the pumice-rich pyroclastic material as it ascended through the vent. However, the very large-scale cross-stratification is unusual for ignimbrite lithic lag breccias. Very large-scale cross-bedding has been described in vent to proximal ignimbrites in other localities, including Mount St. Helens (e.g., Rowley et al., 1985), Tenerife (e.g., Brown and Branney, 2004), Santorini (e.g., Gertisser et al., 2009), and Volcán Villarrica, Chile (e.g., Silva Parejas et al., 2010), however, these cross-bedded ignimbrites are generally dominated by ash- to lapilli-sized material and do not contain the large lithic blocks such as in the very large-scale cross-bedded ignimbrite (Tsxi) described here.

Given their coarse-grained nature and large-scale cross-stratification, the very large-scale cross-bedded ignimbrites (Tsxi) suggest deposition from highly-energetic low-concentration pyroclastic flows in a vent to proximal setting, due to the high amount of turbulent energy required to produce these very large bedforms while transporting the large lithic fragments (e.g., Wright et al., 1981; Carey, 1991; Branney and Kokelaar, 2002). The gradational lateral transition from very large-scale cross-bedded ignimbrites (Tsxi) into massive to stratified ignimbrites (Tst) within 1–2 km of the Guazapares fault zone–La Palmera fault (Fig. 3; Supplemental File 1 [see footnote 1]) suggests decreased turbulence and an increased pyroclastic sedimentation rate farther from the vent.

Lithostratigraphic Summary

The three informal formations defined in the Guazapares Mining District region represent three distinct volcanic episodes:

(1) The Parajes formation consists of welded to nonwelded silicic outflow ignimbrite sheets that were erupted from caldera sources within 50–100 km of the study area, with intercalated volcaniclastic rocks derived from erosion of these ignimbrites.

(2) The lower and middle Témoris formation consists dominantly of locally erupted mafic to intermediate composition lavas and associated subvolcanic intrusions, including an andesitic center in the area around Témoris, as well as fault-controlled dikes that likely fed flows outside the main center. The lower and middle Témoris formation also contains interstratified volcaniclastic fluvial and debris flow deposits. Detritus at the base of the formation that was derived from the underlying Parajes formation silicic ignimbrites records erosion of that formation, perhaps along fault scarps. In contrast, the andesitic detritus that dominates higher in the section could record resedimentation of primary eruptive products, such as the collapsing fronts of lavas, or block-and-ash flows or tephras, although erosion of constructional volcanic features or fault scarps is also probable, particularly for polymictic deposits. The distal thin nonwelded silicic ignimbrites and sedimentary rocks of the upper section of the Témoris formation record waning of local mafic to intermediate volcanism prior to the onset of local silicic volcanism, and indicate continuing or recurring silicic ignimbrite-forming eruptions from distant sources.

(3) The Sierra Guazapares formation records the local eruption of silicic volcanic rocks within the Guazapares Mining District region. These include ignimbrites with vent facies lithic lag breccias that formed very large-scale cross-beds along either side of an 11-km-long fault-controlled fissure, which also controlled the emplacement of silicic plugs and eruption of silicic lavas. The Sierra Guazapares formation also includes silicic fault talus breccias and interstratified silicic lavas and volcaniclastic rocks that interfinger with lacustrine deposits preserved in a half-graben basin.

GEOLOGIC STRUCTURES & BASIN DEVELOPMENT

The main geologic structures in the Guazapares Mining District region are primarily NNW-trending normal faults, including the Guazapares fault zone and faults to the northeast of Témoris (Figs. 2, 3, and 4; Supplemental File 1 [see footnote 1]). The Guazapares fault zone extends from Témoris northward to the Monte Cristo resource area, and is a complex system of NNW-striking normal faults with numerous splays that dip both east and west, with several changes of fault dip polarity along strike (Fig. 3B; and Supplemental File 1 [see footnote 1]; Chapter 2). This fault zone hosts the majority of mineralization within the mining district (e.g., Gustin, 2012). The normal faults located northeast of Témoris have significant vertical offset and bound half-graben basins (Figs. 3A & 4). Although many of the half graben faults die out upsection, making them relatively easy to recognize, faults of the Guazapares fault zone were reactivated many times, and cut all formations (Figs. 2 and 5), making their earlier history more difficult to document.

Synvolcanic Half-Graben Basins

Several normal faults bound half-graben basins in the Guazapares Mining District region, including: the NNW-striking, W-dipping Arroyo Hondo–Puerto Blanco, La Palmera, and Agujerado faults; the NNE-striking, W-dipping Rancho de Santiago fault; and the NNW-striking, E-dipping Sangre de Cristo fault (Figs. 3 and 4). In general, these half-graben basins contain sedimentary and volcanic deposits that thicken and/or coarsen towards basin-bounding normal faults, faults, which either terminate at the fault or thin onto the footwall, indicating synextensional deposition (Fig. 4). Angular unconformities occur between each of the formations and fanning dips (e.g., Fig. 13A) indicate synextensional deposition, with the

Parajes and Témoris formations dipping more steeply than the gently dipping to flat-lying Sierra Guazapares formation.

The upper part of the Parajes formation (younger than the Puerto Blanco ignimbrite [Tpb]) was likely deposited into synvolcanic extensional basins, based on the variable thicknesses of individual outflow ignimbrite sheets and distribution of interbedded sedimentary rocks across faults. Evidence for synextensional deposition includes (1) the presence of reworked tuff, sandstone, and conglomerate (Tps) above the Rancho de Santiago ignimbrite (Tpr) within the half-graben basin adjacent to Arroyo Hondo–Puerto Blanco fault and in the Mesa de Cristal area, which thicken toward and terminate at faults and are not present on the footwall blocks, and (2) thickening of the Rancho de Santiago ignimbrite (Tpr) within the half-graben basin bounded by the Arroyo Hondo–Puerto Blanco fault (~200 m-thick), relative to the ~80 m thickness on the footwall block (Figs. 3A, 4, and 9C; Supplemental File 1 [see footnote 1]).

Synextensional deposition of the Témoris formation is evident in the three half-graben basins bounded by the La Palmera, Agujerado, and Rancho de Santiago–Arroyo Hondo–Puerto Blanco faults (Figs. 3A and 4). In these basins, the Témoris formation is deposited in angular unconformity on the more steeply dipping Parajes formation, and the thickness and average grain size of sedimentary deposits increases dramatically eastward towards each of the basin-bounding normal faults (Fig. 4). In the half-graben bounded by the Agujerado fault, a coarse-grained debris flow (Ttds) deposited proximal to the basin-bounding fault interfingers basinward with finer grained sandstone and siltstone (Ttss; Figs. 3A and 4B).

The largest of the three synvolcanic half-grabens of the Témoris formation is the Rancho de Santiago basin, which is unique in that it developed as a half-graben bounded by two W-dipping normal faults on the eastern side of the basin; the southernmost fault is the NNE-striking Rancho de Santiago fault, which is crosscut on the north end by the NNW-striking Arroyo Hondo–Puerto Blanco fault (Fig. 3A). In this basin, a clast-supported breccia (Ttdt) containing large (to 4 m) intermediate volcanic and lesser silicic ignimbrite rock fragments, as well as slide blocks of fractured but intact sedimentary strata up to 15 m-thick and 20 m-long, is adjacent to the Rancho de Santiago fault (Figs. 3A, 4C, and 10B; Table 1). This breccia is interpreted as talus and avalanche deposits that were shed from the uplifted footwall fault scarps directly into the half-graben basin to the west.

Synvolcanic extension during emplacement of the Sierra Guazapares formation is recorded by silicic fault talus deposits, reworked tuffs, and fluvial-lacustrine deposits (Tsv) preserved within the half-graben basin bounded by the Sangre de Cristo fault in the Monte Cristo resource area at the northern mapped end of the Guazapares fault zone (Fig. 3B; Table 1; Chapter 2). In this basin, a rhyolitic fault talus breccia thickens and coarsens towards the Sangre de Cristo fault and interfingers basinward with basal lacustrine sedimentary rocks. Additional evidence of synvolcanic extension in this basin includes the development of a normal fault within the hanging wall block of the Sangre de Cristo fault that provided a conduit for a small silicic plug and coulee (Tsl) to intrude and flow over the actively depositing volcaniclastic unit (Tsv; Fig. 3B; Chapter 2).

Relative Timing and Amount of Extensional Deformation

Extensional deformation in the Guazapares Mining District region was concurrent with deposition of at least the upper part of the Parajes formation, the Témoris formation, and the Sierra Guazapares formation, with continued extension following deposition of the Sierra Guazapares formation. Pre–Sierra Guazapares formation extension is suggested by the low to moderate angular unconformities between the Témoris formation and the underlying

Parajes formation and the overlying Sierra Guazapares formation (Fig. 13A). Older normal faults that offset the Parajes and Témoris formations localized the vents and silicic plugs of the Sierra Guazapares formation, which utilized these preexisting structures as pathways for magma accent (e.g., La Palmera and La Escalera faults, Guazapares fault zone; Figs. 2, 3, and 13B, Supplemental File 1 [see footnote 1]). In addition, unfaulted Sierra Guazapares formation lavas bury some faults that offset the Parajes and Témoris formations (Figs. 2, 3, and 4; Supplemental File 1 [see footnote 1]).

Further evidence of pre–Sierra Guazapares formation extension includes greater fault offsets of the older formations compared to offset of the Sierra Guazapares formation (Figs. 3A and 4). The minimum vertical displacement of the base of the Témoris formation across the Ericicuchi fault is >300 m, ~110 m across the Agujerado fault, and >450 m across the La Palmera fault (Fig. 4). In comparison, these faults offset the Sierra Guazapares formation to a lesser degree: the base of the Sierra Guazapares formation is only offset ~60 m across the Ericicuchi fault, ~30 m across the Agujerado fault, and ~100 m across the La Palmera fault (Fig. 4). This shows that a significant amount of extensional deformation (at least 350 m vertical displacement) occurred prior to the eruption of the Sierra Guazapares formation.

A minimum of 20% total horizontal extension is estimated in the Guazapares Mining District region (for the area shown in Fig. 4), based on the vertical displacement of stratigraphic units across normal faults. This amount of extension is significantly lower than that of the Gulf Extensional Province to the west in Sonora, where ~90% extension is estimated to have occurred (Gans, 1997). The structural style also differs between these two areas; high-angle normal faults are found in the Guazapares Mining District region, while highly extended core complexes are located in Sonora (e.g., Gans, 1997; Wong et al., 2010).

Although not directly quantifiable, several faults within the Guazapares Mining District region appear to accommodate considerable amounts of deformation based solely on the juxtaposition of stratigraphic units. The La Palmera fault has significant vertical offset (over 450 m) based on the offset of the Parajes–Témoris formation contact; the Parajes formation is exposed on the footwall, but is not exposed in the hanging wall, which suggests that it is deeply buried beneath Témoris formation deposits there (Figs. 2 and 4). A distinct lithologic boundary in the Parajes formation occurs across the Chapotillo fault, as the younger outflow ignimbrite sheets in the hanging wall of this fault are not exposed on the footwall to the southwest (Fig. 3A). Postdepositional drag folding related to normal fault deformation is observed in the Témoris formation adjacent to many of the NNW-striking faults with significant offset (e.g., La Palmera, Agujerado, and La Escalera faults, Figs. 3A and 4); the underlying Parajes formation has small-scale normal faulting to accommodate this deformation.

AGE CONSTRAINTS

Methodology

We report new U-Pb zircon ages from each of the three informally defined formations, providing constraints on the age of the previously undated volcanic rocks of the Guazapares Mining District region. Laser ablation–inductively coupled plasma–mass spectrometry (LA–ICP-MS) U-Pb analyses were performed at the Laboratorio de Estudios Isotópicos, Centro de Geociencias, Universidad Nacional Autónoma de México on zircons separated from 13 silicic rock samples (Fig. 14; Table 3; Appendix 2). The zircons were hand-picked under binocular microscope, mounted in an epoxy cast, polished, and imaged by cathodoluminescence (CL). The zircons selected for U-Pb geochronology were analyzed

Figure 14 (*next 2 pages*). Summary of zircon U-Pb LA–ICP–MS analyses for samples listed in Table 3, with mean $^{206}Pb/^{238}U$ ages of the youngest zircon population (interpreted emplacement age) for each sample is listed. Tera-Wasserburg concordia plots with inset probability density distribution plots are arranged by major stratigraphic division and lithologic unit. MSWD—mean square of weighted deviates. Parajes formation: (A-B) Ericicuchi ignimbrite (Tpe); (C) Puerto Blanco ignimbrite (Tpb). Témoris formation: (D) silicic tuff interbedded in sandstone from the basal deposits of the formation; (E-F) silicic ignimbrites (Tti) from near the top of the formation. Sierra Guazapares formation: (G) very large-scale cross-bedded rhyolitic ignimbrite (Tsxi); (H-J) rhyolitic lavas (Tsl); (K-L) rhyolitic plugs (Tsi); (M) rhyolitic fault talus breccia clast from the Monte Cristo resource area. Details on the experiments and mean age plots are given in Appendix 2.

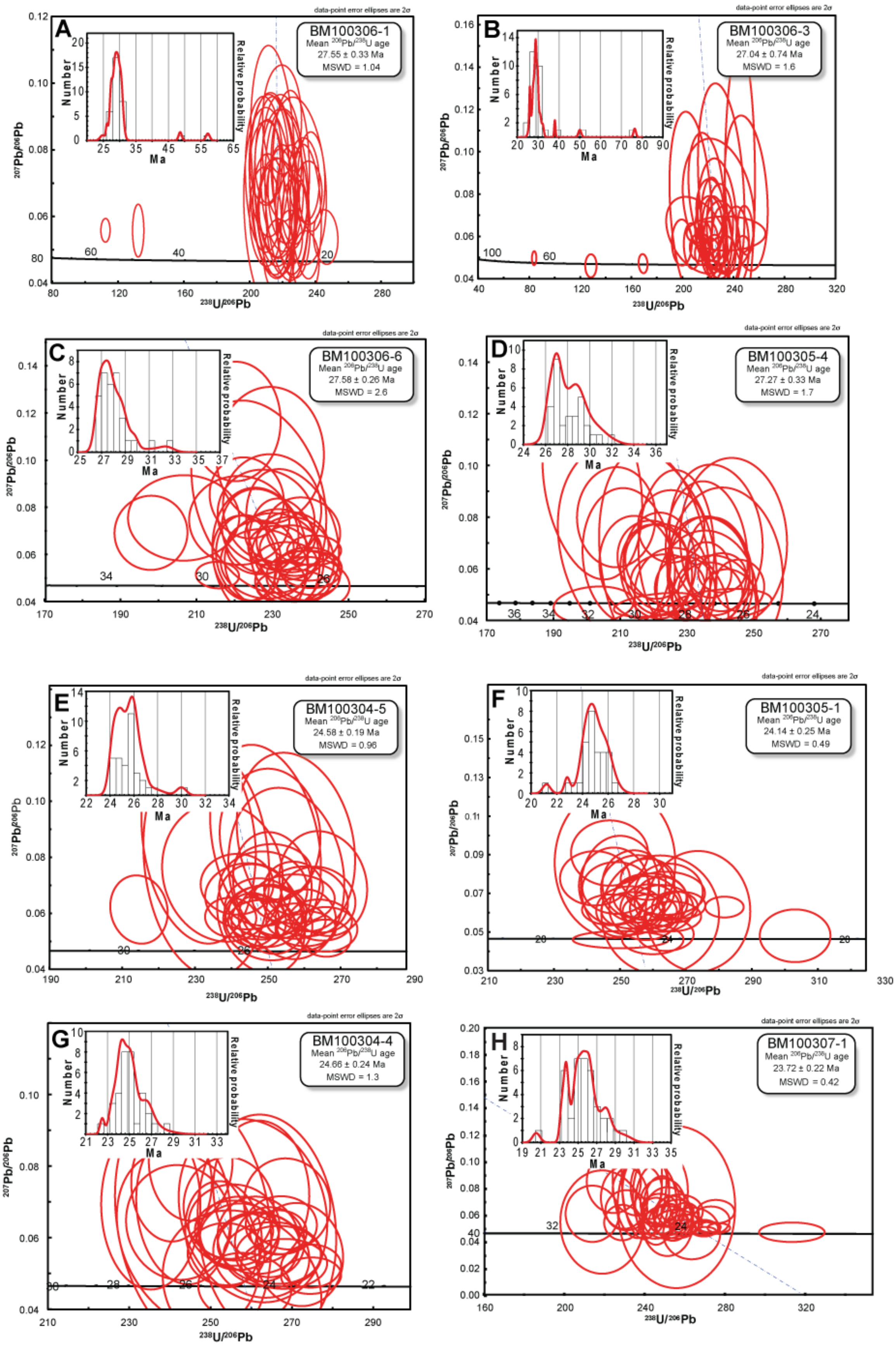

A
BM100306-1
Mean 206Pb/238U age
27.55 ± 0.33 Ma
MSWD = 1.04
B
BM100306-3
Mean 206Pb/238U age
27.04 ± 0.74 Ma
MSWD = 1.6
C
BM100306-6
Mean 206Pb/238U age
27.58 ± 0.26 Ma
MSWD = 2.6
D
BM100305-4
Mean 206Pb/238U age
27.27 ± 0.33 Ma
MSWD = 1.7
E
BM100304-5
Mean 206Pb/238U age
24.58 ± 0.19 Ma
MSWD = 0.96
F
BM100305-1
Mean 206Pb/238U age
24.14 ± 0.25 Ma
MSWD = 0.49
G
BM100304-4
Mean 206Pb/238U age
24.66 ± 0.24 Ma
MSWD = 1.3
H
BM100307-1
Mean 206Pb/238U age
23.72 ± 0.22 Ma
MSWD = 0.42
data-point error ellipses are 2σ
207Pb/206Pb
238U/206Pb
Number
Relative probability
Ma

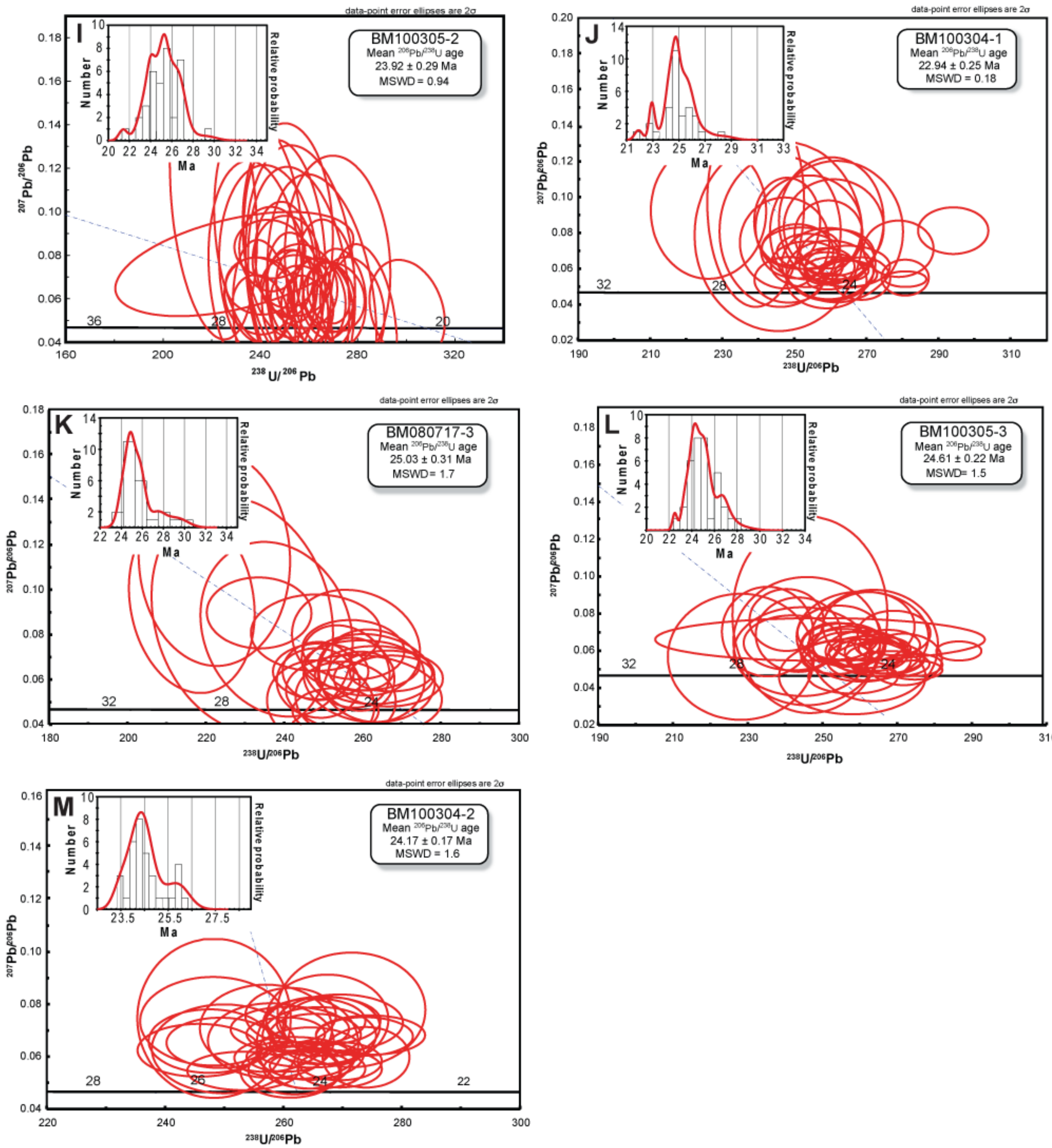
data-point error ellipses are 2σ
I
BM100305-2
Mean 206Pb/238U age
23.92 ± 0.29 Ma
MSWD = 0.94
Number
Relative probability
Ma
207Pb/206Pb
238U/206Pb
J
BM100304-1
Mean 206Pb/238U age
22.94 ± 0.25 Ma
MSWD = 0.18
K
BM080717-3
Mean 206Pb/238U age
25.03 ± 0.31 Ma
MSWD = 1.7
L
BM100305-3
Mean 206Pb/238U age
24.61 ± 0.22 Ma
MSWD= 1.5
M
BM100304-2
Mean 206Pb/238U age
24.17 ± 0.17 Ma
MSWD = 1.6

TABLE 3. SUMMARY OF ZIRCON U-Pb LA-ICP-MS RESULTS

Sample	Map unit	Lithology	Age (Ma)*	±2σ (Ma)	n	MSWD	UTM (E)	UTM (N)
BM100304-2	Tsv	rhyolite breccia (clast)	24.2	0.2	24	1.6	767557	3035421
			25.8	*0.5*	9	1.9		
BM100305-3	Tsi	rhyolite plug	24.6	0.2	23	1.5	774042	3023376
BM080717-3	Tsi	rhyolite plug	25.0	0.3	18	1.7	770970	3030952
BM100304-1	Tsl	rhyolitic lava flow	22.9	0.3	3	0.18	767453	3035862
			25.1	*0.2*	22	1.5		
BM100305-2	Tsl	rhyolite lava flow	23.9	0.3	8	0.94	773462	3023389
			25.7	*0.3*	23	1.5		
BM100307-1	Tsl	rhyolite lava flow	23.7	0.2	5	0.97	771277	3030018
			25.8	*0.3*	17	1.7		
BM100304-4	Tsxi	cross-bedded ignimbrite	24.7	0.2	19	1.3	767878	3027817
BM100305-1	Tti	rhyolite lapilli tuff	24.1	0.3	10	0.49	773365	3023281
			25.6	*0.3*	17	1.6		
BM100304-5	Tti	rhyolite lapilli tuff	24.6	0.2	12	0.96	768511	3027340
			26.1	*0.3*	20	1.5		
BM100305-4	Ttss	silicic tuff	27.3	0.3	18	1.7	776588	3031515
			29.7	*0.7*	11	2.1		
BM100306-6	Tpb	nonwelded silicic ignimbrite	27.6	0.3	31	2.6	778205	3029101
BM100306-3	Tpe	nonwelded silicic ignimbrite	27.0	0.7	6	2.5	776541	3026289
			29.0	*0.3*	16	1.6		
BM100306-1	Tpe	nonwelded silicic ignimbrite	27.6	0.3	6	1.04	775513	3024576
			29.6	*0.3*	22	1.6		

Notes: LA-ICP-MS—laser ablation–inductively coupled plasma–mass spectrometry. Ages in italics represent the zircon antecryst (proposed by Charlier et al., 2004; crystals that predate crystallization and eruption of a host magma, but formed during an earlier phase of related magmatism) age population in a given sample. The youngest age population of each sample is interpreted as the preferred eruption or emplacement age. n—number, MSWD—mean square of weighted deviates. Universal Transverse Mercator (UTM; E—east, N—north) coordinates are based on the North American Datum 1927 (NAD27) zone 12. Map unit labels correspond to Table 1. Locations of the samples are shown on Supplemental File 1 (see footnote 1). Details of each analysis are given in Appendix 2.

* Mean $^{206}Pb/^{238}U$ age

following the procedure reported by Solari et al. (2010), employing a Resonetics M050 excimer laser ablation workstation coupled to a Thermo XSeries II ICP-MS. Based on CL imaging, one ablation site was selected on each zircon analyzed, located either in the middle, near rim, or core of the crystal (Appendix 3). The Plešovice standard zircon (ca. 337 Ma; Sláma et al., 2008) was used as a bracketing standard, interdispersed and measured after every 5 unknown zircons. The observed uncertainties of the $^{206}Pb/^{238}U$, $^{207}Pb/^{206}Pb$, and $^{208}Pb/^{232}Th$ ratios, during the different sessions in which the current samples were analyzed, as measured on the Plešovice standard zircon, were 0.65%, 1.0%, and 1.1%, respectively. These values are quadratically propagated to the quoted uncertainties of the unknown zircons, to take into account the heterogeneities of the natural standard zircon. A second standard (NIST 610) is used to recalculate the elemental concentrations for each zircon, measured together with the isotopes of interest for U-Pb geochronology. The common Pb correction cannot be performed measuring the ^{204}Pb isotope with the current setup; common Pb is evaluated using the $^{207}Pb/^{206}Pb$ ratio, graphing the results using Tera-Wasserburg diagrams (Tera and Wasserburg, 1972). If a correction is needed, the algebraic method of Andersen (2002) is used. Filters are then applied to reduce outliers: largely discordant analyses (e.g., > 50% discordant) and those with > 4% 1σ error on the corrected $^{206}Pb/^{238}U$ ratio are eliminated. A further screening is applied to check for possible microscopic inclusions of minerals other than zircons that could have been inadvertently hit during the analysis. This screening is performed during data reduction, employing a script written in R (UPb.age; Solari and Tanner, 2011). Additional screenings are performed, checking for analyses with high P and light rare earth elements, which could be indicative of apatite inclusions, and those few analyses which present high concentrations of U and Th (generally >1000 ppm), which could yield to a Pb loss and a consequent discordant or, in any case, younger and geologically meaningless ages.

Concordia plots, probability density distribution and histogram plots, mean age, and age-error calculations were performed using Isoplot v. 3.70 (Ludwig, 2008). The mean $^{206}Pb/^{238}U$ age is especially useful for the Tertiary ages presented here, because the ^{207}Pb measurement is problematic in these young zircons and the consequent uncertainty on the $^{207}Pb/^{206}Pb$ ratio is not a good indicator of geologically meaningful discordance. In Tertiary zircons, it is also common to observe scattering of the mean $^{206}Pb/^{238}U$ ages that yields MSWD (mean square of weighted deviates) values that are largely >1, an indication that a mixed age population possibly exists. An example of this scenario was presented by Bryan et al. (2008). In order to recognize possible different age components in samples that showed an initial MSWD of >3, the deconvolution method, based on the mixture modeling method of Sambridge and Compston (1994), was implemented in Isoplot.

When two mixture components are recognized, their respective mean $^{206}Pb/^{238}U$ ages are plotted together with errors and recalculated MSWD. The mean $^{206}Pb/^{238}U$ age of the older mixture component in a sample represents the crystallization age of inherited zircons within the host magma, while the younger mean $^{206}Pb/^{238}U$ age population represents the phenocryst crystallization age of the sample. This youngest age population of each sample is interpreted as the preferred eruption or emplacement age of the rock, as it is consistent (within error) with stratigraphic relationships in the study area. Age results are presented in the following and summarized in Figure 14 and Table 3; detailed analytical data are given in Appendix 2.

Results

Parajes formation

Three samples were dated from the Parajes formation (Figs. 14A–14C; Table 1), including two samples from the Ericicuchi ignimbrite (Tpe) and one sample from the Puerto Blanco ignimbrite (Tpb). Sample BM100306-1 is Ericicuchi ignimbrite (Tpe), which has separated zircons that are bipyramidal to short and stubby, and to 220 µm long. Under CL, the zircons show uniform areas with limited luminescence; in a few cases, oscillatory zoning is present around possible inherited cores. The U-Pb geochronological analysis, as well as the screening and filtering, shows the presence of inherited cores that are slightly discordant but older than 40 Ma. Most of the analyzed, nearly concordant crystals range from ca. 26 Ma to 31 Ma (Fig. 14A). Two zircon age populations can be distinguished: the oldest population has a mean age of 29.6 ± 0.3 Ma (n = 22, MSWD = 1.6), whereas the youngest has a mean age of 27.6 ± 0.3 Ma (n = 6, MSWD = 1.04). A second sample from the Ericicuchi ignimbrite (sample BM100306-3; Fig. 14B) yielded fewer and smaller zircon crystals (to 180 µm in length) that are euhedral to subhedral with a prevalence of stubby morphologies with short pyramidal terminations. These zircons show bright CL zoning around darker cores. The U-Pb geochronology for this sample also revealed the presence of inherited cores of ca. 76, 50 and 38 Ma and two main zircon age populations consisting of an older grouping having a mean age of 29.0 ± 0.3 Ma (n = 16, MSWD = 1.6) and a younger grouping with a mean age of 27.0 ± 0.7 Ma (n = 6, MSWD = 2.5). The third sample of the Parajes formation is from the Puerto Blanco ignimbrite (Tpb; sample BM100306-6; Fig. 14C). The zircons in this sample are larger (to 260 µm in length) with elongated shapes that are mostly prismatic with well-developed pyramids. Under CL they show evident bright rims developed outside darker zones. The dated zircons define a homogeneous group with few outliers and have a mean age of 27.6 ± 0.3 Ma (n = 31, MSWD = 2.6).

Témoris Formation

Three samples of silicic tuffs from basal and upper sections of the Témoris formation were dated (Figs. 14D–14F; Table 3). Sample BM100305-4 was collected from the basal section of the Témoris formation (Fig. 14D) and has zircons to 300 μm in length that are prismatic and elongated. Under CL, the zircons are characterized by darker cores surrounded by bright zones. Despite similar crystal morphologies, two zircon age populations are identified; the oldest group has a mean age of 29.7 ± 0.7 Ma (n = 11, MSWD = 2.1), whereas the youngest mean age is 27.3 ± 0.3 Ma (n = 18, MSWD = 1.7). Sample BM100304-5 was collected from the upper section of the Témoris formation (Tti; Fig. 14E) and has zircons that are indistinguishable in size, morphology, and CL imaging from those of the previous sample. Two well-constrained zircon age populations are also defined; the oldest has a mean age of 26.1 ± 0.3 Ma (n = 20, MSWD = 1.5), whereas the youngest mean age is 24.6 ± 0.2 Ma (n = 12, MSWD= 0.96). Sample BM100305-1 is from the uppermost section of the Témoris formation (Tti), ~35 m below the Sierra Guazapares formation contact (Figs. 11 and 14F). Its zircons are also prismatic and very elongated, although they are somewhat smaller (to 200 μm in length) in this sample. Under CL, the zircons are also characterized by darker cores surrounded by bright zones. U-Pb analyses identified two zircon age populations in this sample; the oldest group yields a mean age of 25.6 ± 0.3 Ma (n = 17, MSWD = 1.6), whereas the youngest group yields a mean age of 24.1 ± 0.3 Ma (n = 10, MSWD = 0.49).

Sierra Guazapares Formation

Seven samples from the various lithologies of the Sierra Guazapares formation were chosen for U-Pb geochronology (Figs. 14G–14M; Table 3). Sample BM100304-4 was collected from the very large-scale cross-bedded ignimbrite unit (Tsxi; Fig. 14G). It has somewhat small (to 150 µm) euhedral zircons that range in shape from prismatic to stubby and bipyramidal morphologies. CL imaging is not different from the previously described samples, although cores are not as evident as in other samples. The dated zircons define only one coherent group, in which the mean age is 24.7 ± 0.2 Ma (n = 19, MSWD = 1.3).

Three rhyolite lava (Tsl) samples were analyzed. Sample BM100307-1 (Fig. 14H) is characterized by prismatic euhedral zircons (to 300 µm in length) with the same CL characteristics as those previously described. Two zircon age groups are also defined; the oldest group yields a mean age of 25.8 ± 0.3 Ma (n = 17, MSWD = 1.7), whereas the mean age of the youngest group is 23.7 ± 0.2 Ma (n = 5, MSWD = 0.42). Sample BM100305-2 (Fig. 14I) also has prismatic zircons (to 200 µm in length) with most showing oscillatory zoning. U-Pb zircon dating of this sample defines two age populations; the oldest group with a mean age of 25.7 ± 0.3 Ma (n = 23, MSWD = 1.5) and the youngest group with a mean age of 23.9 ± 0.3 Ma (n = 8, MSWD = 0.94). Sample BM100304-1 (Fig. 14J) was collected from a small lava in the Monte Cristo area (Fig. 3B). It also has prismatic zircons (to 180 µm in length), although in this sample they are somewhat more needle shaped. Two age populations are identified in this sample; the oldest has a mean age of 25.1 ± 0.2 Ma (n = 22, MSWD = 1.5), whereas a few grains define the youngest group with a mean age of 22.9 ± 0.3 Ma (n = 3, MSWD = 0.18).

Two samples collected from rhyolite plugs (Tsi) were analyzed. Sample BM080717-3 (Fig. 14K) is characterized by stubby to bipyramidal zircons (to 150 µm in length) that are sector zoned under CL. Its U-Pb dating yields only one age group, with a mean age of 25.0 ± 0.3 Ma (n = 18, MSWD = 1.7). The zircons belonging to the sample BM100305-3 (Fig. 14L) are prismatic and large (to 340 μm in length). The U-Pb dating yields a homogeneous age group, with a mean age of 24.6 ± 0.2 Ma (n = 23, MSWD = 1.5).

Sample BM100304-2 was collected from a clast in a rhyolitic breccia locally exposed in the Monte Cristo area (Tsv; Figs. 3B and 14M). Its zircons are prismatic and large (to 250 μm in length). Two age populations are recognized; the oldest group has a mean age of 25.8 ± 0.5 Ma (n = 9, MSWD = 1.9), whereas the youngest group has a mean age of 24.2 ± 0.2 Ma (n = 24, MSWD = 1.6).

Age Interpretations

Previous dating of silicic volcanic rocks in the Sierra Madre Occidental using zircon U-Pb LA-ICP-MS showed that zircon ages are occasionally older (to 1-4 Myr) than the ages obtained from the same rocks using K/Ar and $^{40}Ar/^{39}Ar$ dating methods (Bryan et al., 2008). The older zircon ages in their study are attributed to the presence of 'antecrysts', a term proposed by Charlier et al. (2004) to describe crystals that predate the crystallization and eruption of a host magma, but formed during an earlier phase of related magmatism. In a region of long-lived magmatism like the Sierra Madre Occidental, the antecryst ages could predate the phenocryst age by more than 10 Myr, making it difficult to distinguish antecrysts from xenocrysts (Bryan et al., 2008). In addition, the occurrence of antecrysts tends to be greater in the younger silicic volcanic rocks of a sequence, when the probability of remelting partially molten or solidified upper crustal rocks formed during a preceding magmatic phase is higher (Bryan et al., 2008).

The presence of antecrysts in a zircon population for a sample will tend to produce initial MSWD values much greater than unity and probability density function curves of zircon ages that are positively skewed and asymmetric, and/or have broad, bimodal, or polymodal peaks. In comparison, a well-defined unimodal peak likely indicates the crystallization age of phenocrysts with limited antecrysts, which is a close approximation to the eruption age of the host magma (Charlier et al., 2004; Bryan et al., 2008).

The ages obtained for most of the samples dated for this study in the Guazapares Mining District region suggest the presence of antecrysts in the zircon population. The probability density function curves tend to be positively skewed and asymmetric, and several have broad or bimodal peaks (Fig. 14; Appendix 2). The oldest zircon population in a sample represents the crystallization age of antecrysts, which generally correspond to zircons with crystal core to middle ablation sites. In comparison, the youngest zircon population indicates the age of phenocryst crystallization and typically represents the zircons with middle to near-rim ablation sites. The antecryst age populations in these samples tend to be ~1.5–2 Myr older than the phenocryst age populations (Table 3); antecryst ages tend to cluster around 29.5 Ma for samples from the Parajes formation and 25.5 Ma for samples from the overlying Témoris and Sierra Guazapares formations.

DISCUSSION

Volcanic & Tectonic Evolution

The new geologic mapping and geochronology presented in this study show that the three informal formations in the Guazapares Mining District region (Fig. 5) record Late Oligocene to Early Miocene synextensional volcanic activity during the mid-Cenozoic ignimbrite flare-up in the northern Sierra Madre Occidental: (1) the synextensional deposition of outflow ignimbrite sheets (Parajes formation) at ca. 27.5 Ma, which were likely erupted from calderas ~50–100 km from the study area; these overlap in time with the end of peak ignimbrite flare-up volcanism to the east; (2) synextensional growth of an andesitic volcanic center (Témoris formation) between ca. 27 Ma and ca. 24.5 Ma; and (3) synextensional silicic fissure magmatism (Sierra Guazapares formation), including vent-facies ignimbrites, lavas, and intrusions, between ca. 24.5 and ca. 23 Ma (Fig. 15).

Stratigraphic and structural evidence show that the outflow ignimbrite sheets of the Parajes formation younger than the 27.6 ± 0.3 Ma Puerto Blanco ignimbrite (Tpb) were deposited in a developing half-graben basin (Fig. 15A). It is uncertain whether the older outflow ignimbrite sheets in the formation (older than 27.5 Ma) were deposited in half-graben basins. The Parajes formation was tilted by extension and partly eroded from normal fault footwalls prior to and during deposition of the overlying Témoris formation (Figs. 4, 9C, and 10A).

The ca. 27–24.5 Ma Témoris formation records the onset of magmatism in the area, which was primarily andesitic, with compositions ranging from basalt to andesite (Fig. 7). Like the Parajes formation, the Témoris formation was deposited in synvolcanic half-graben basins (Fig. 15B). Fluvial and debris flow processes developed alluvial fan systems that prograded into the half-grabens to become interbedded with andesitic lavas. At least some of these alluvial deposits were likely eroded from andesitic lavas exposed in uplifted normal fault footwall blocks, although some of the detritus could also have been reworked from unconsolidated primary volcanic fragmental eruptive products (Fig. 15B). Normal faults in the study area control the siting of some vents of the Témoris formation, including andesitic feeder dikes along normal faults and the andesitic volcanic center (Ttv) in the area around Témoris, which is located at the southern projection of the Guazapares fault zone (Figs. 2 and 3; Supplemental File 1 [see footnote 1]). The presence of distal silicic ignimbrites (Tti) in the uppermost part of the mafic to andesitic Témoris formation, below the silicic ignimbrite-dominated Sierra Guazapares formation (Figs. 5, 11, and 13A) records a hiatus between local

Figure 15 (*next page*). Schematic block diagrams illustrating the tectonic and volcanic evolution of the three formations in Guazapares Mining District region during the Late Oligocene to Early Miocene. The colors correspond to the geologic map units in Figure 3C. (A) By ca. 27.5 Ma, outflow ignimbrite sheets of the Parajes formation were erupted from medial sources during the end of the Early Oligocene pulse of the mid-Cenozoic ignimbrite flare-up in northern Mexico. The base of this stratigraphic division is not exposed in the field area; it is inferred that the Parajes formation is deposited over the pre-Oligocene Lower Volcanic Complex (LVC) based on regional studies (e.g., Ferrari et al., 2007). At least the upper part of the Parajes formation was deposited during crustal extension, indicated by reworked tuffs, cross-bedded sandstones, and pebble-to-cobble conglomerates with Parajes formation ignimbrite clasts interbedded between outflow ignimbrite sheets and thinning of ignimbrites on normal fault footwall blocks. Continued uplift and partial erosion of the formation occurred prior to eruption of the Témoris formation. (B) Between ca. 27 and 24.5 Ma, the Témoris formation was erupted from an andesitic volcanic center sited along the Guazapares fault zone and from smaller vents located along normal faults in the region. Primary volcanic rocks and volcaniclastic rocks derived from intrabasinal reworking of eruptive products were deposited into alluvial fan systems in synvolcanic half-graben basins. (C) Following a period of waning locally erupted mafic to intermediate volcanism in the region marked by an increase in distal ignimbrite deposition in the upper section of the Témoris formation, the Sierra Guazapares formation was erupted during the Early Miocene ignimbrite pulse of the mid-Cenozoic ignimbrite flare-up, ca. 24.5–23 Ma. Fissure vents are located along preexisting normal faults in the Guazapares Mining District region; there is a lateral volcanic facies transition away from the faults from vent (very large-scale cross-bedded ignimbrites, lavas, plugs) to proximal with slight fluvial reworking (massive to stratified ignimbrites). Rhyolitic plugs intrude normal faults and are the source for many of the rhyolitic lavas.

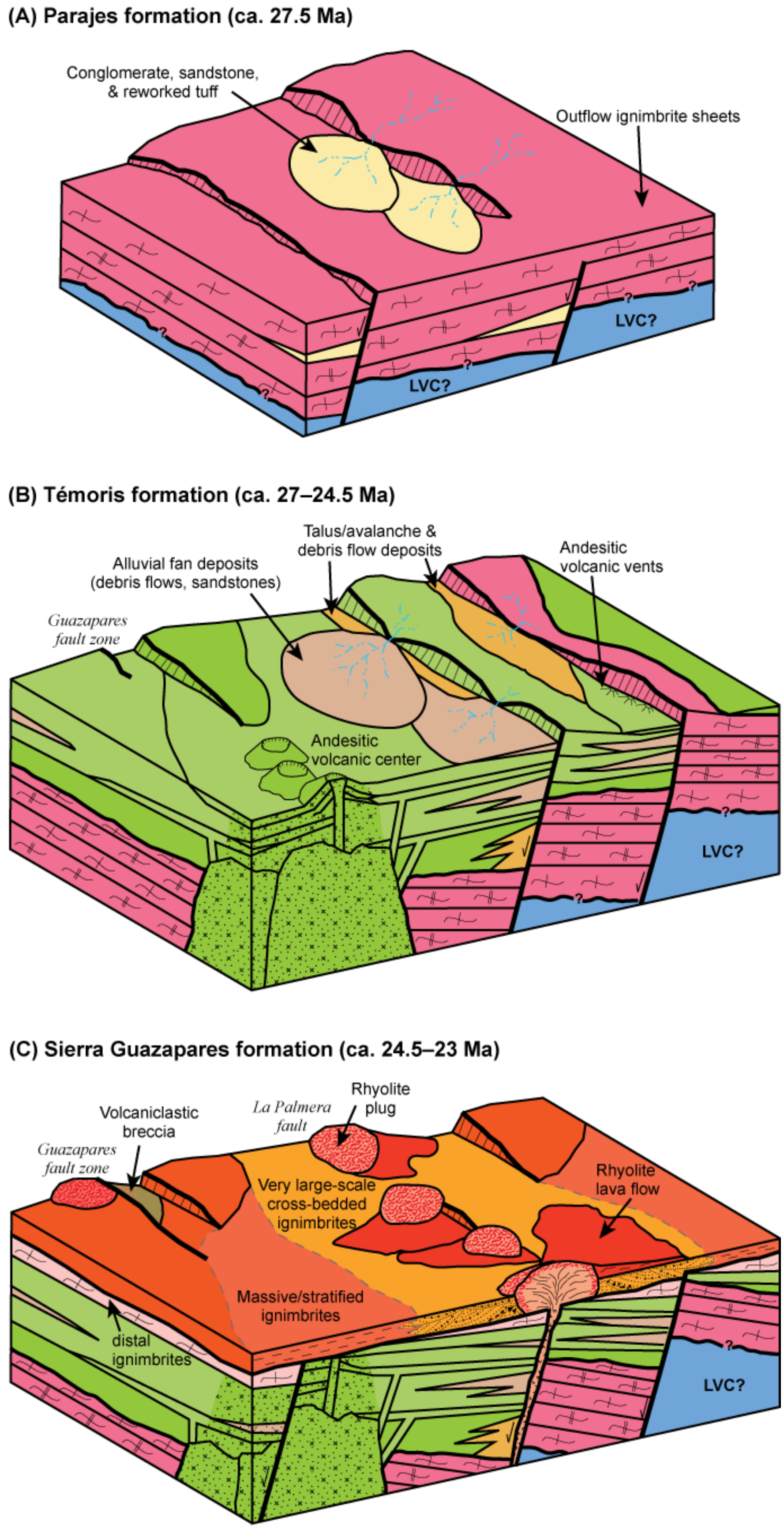
(A) Parajes formation (ca. 27.5 Ma)
Conglomerate, sandstone, & reworked tuff
Outflow ignimbrite sheets
LVC?
LVC?
(B) Támoris formation (ca. 27–24.5 Ma)
Talus/avalanche & debris flow deposits
Andesitic volcanic vents
Alluvial fan deposits (debris flows, sandstones)
Guazapares fault zone
Andesitic volcanic center
LVC?
(C) Sierra Guazapares formation (ca. 24.5–23 Ma)
Rhyolite plug
La Palmera fault
Volcaniclastic breccia
Guazapares fault zone
Very large-scale cross-bedded ignimbrites
Rhyolite lava flow
Massive/stratified ignimbrites
distal ignimbrites
LVC?

andesitic and silicic magmatism in the region, modified by extension, tilting, and erosion, to produce an angular unconformity.

The ca. 24.5–23 Ma Sierra Guazapares formation records the onset of silicic magmatism within the Guazapares Mining District region. Based on composition and geochronology (Figs. 6, 7, and 14; Table 3), the vent to proximal facies along the Guazapares fault zone–La Palmera fault records several eruption events of high-energy explosive volcanism that resulted in deposition of very large-scale cross-bedded ignimbrites with lag breccias (Tsxi) in a wedge that defines a linear, fault-controlled fissure-type vent system (Figs. 3 and 15C). The eruptive style of each event of the Sierra Guazapares formation likely transitioned into effusive volcanism, with the emplacement of rhyolite plugs along the fissures and the deposition of related rhyolite lavas over the ignimbrites (e.g., Fig. 13B). This sequence of fissure-fed ignimbrites and effusive lava and plugs is similar to the fissure ignimbrite eruption model proposed by Aguirre-Díaz and Labarthe-Hernández (2003) to explain the origin of large volume silicic ignimbrites and related effusive volcanic deposits in other extended regions of the Sierra Madre Occidental. Their model suggests that during crustal extension, a volatile-rich silicic magma chamber reaches high crustal levels and encounters preexisting normal faults that provide a conduit for magma ascent. Magma decompression follows, resulting in an explosive eruption event with deposition of proximal pyroclastic volcanic facies adjacent to the fault-controlled vents; silicic lava domes and dikes follow the pyroclastic rocks and close the vents as the magma becomes depleted of volatiles (e.g, Aguirre-Díaz and Labarthe-Hernández, 2003). Each explosive and effusive volcanic event of the Sierra Guazapares formation may have progressed in a fashion similar to this fissure ignimbrite eruption model proposed by Aguirre-Díaz and Labarthe-Hernández (2003), with several silicic magma chambers interacting at high crustal levels with the Guazapares fault zone–La Palmera fault to develop a fissure-vent system. Further mapping is needed in the region to determine whether the fissure continues to the south of Témoris, where resistant silicic intrusions are obvious from a distance (Fig. 2; Supplemental File 1 [see footnote 1]).

Regional Correlations

New stratigraphic and geochronologic data presented in this study indicate that mafic to intermediate volcanic rocks in the study area are not related to the Lower Volcanic Complex as proposed by previous workers (e.g., Ramírez Tello and Garcia Peralta, 2004; Roy et al., 2008; Wood and Durgin, 2009; Gustin, 2011, 2012). The Témoris formation instead represents a period of mafic to intermediate volcanism that occurred between two ignimbrite pulses of the mid-Cenozoic ignimbrite flare-up in the northern Sierra Madre Occidental and preceded local silicic ignimbrite flare-up magmatism in the study area.

The ca. 27.5 Ma Parajes formation is interpreted as medial welded to nonwelded silicic outflow ignimbrite sheets erupted at the end of the Early Oligocene pulse of the mid-Cenozoic ignimbrite flare-up in the Sierra Madre Occidental (ca. 36-27 Ma; Ferrari et al., 2007; Cather et al., 2009; McDowell and McIntosh, 2012), based on the similar eruption ages and physical characteristics to ignimbrite sequences described elsewhere in the region (e.g., Swanson et al., 2006; McDowell, 2007 and references therein). Possible sources for the outflow ignimbrites of the Parajes formation include: (1) vent to proximal volcanic facies of similar ages previously identified ~100 km towards the north and northeast near Basaseachic and Tomóchic (e.g., McDowell, 2007 and references therein; McDowell and McIntosh, 2012), and (2) several calderas identified <50 km to the north, south, and east of the Guazapares Mining District region (e.g., Ferrari et al., 2007 and references therein) (Fig. 16).

Based on phenocryst assemblages and an eruption age older than 27.5 Ma, the oldest flow unit of the Parajes formation, the Chepe ignimbrite (Tpc; Table 1), is tentatively

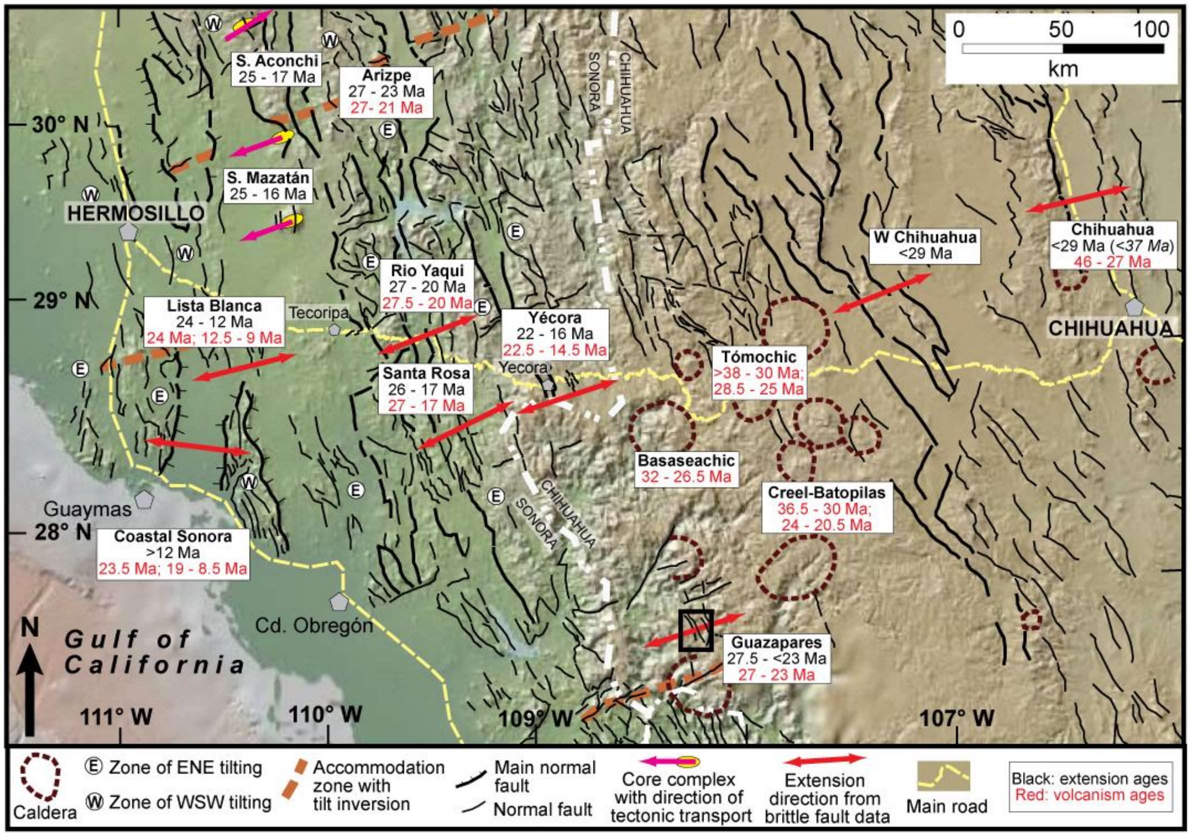

Figure 16. Map of the northern Sierra Madre Occidental showing the timing of extensional deformation and post–Lower Volcanic Complex locally derived volcanism (e.g., intracaldera facies, lavas) in the region relative to Guazapares (this study, black box in figure). Known and inferred calderas in the region are indicated, as well as main Tertiary faults and the direction of crustal extension (modified from Ferrari et al., 2007). Generally, the age of the volcanism is increasingly younger towards the southwest, and although the timing of extension is less constrained, there also appears to be an increasingly younger trend towards the southwest of the study area in the Gulf Extensional Province of Sonora. Ages of extension and volcanism are from Bagby (1979), Cameron et al. (1989), Wark et al. (1990), Swanson et al. (2006), González León et al. (2000), McDowell (2007), Ferrari et al. (2007, and references therein), Wong et al. (2010), McDowell and McIntosh (2012), Bryan et al. (2013), and this study.

correlated with the regionally extensive Divisadero tuff of Swanson et al. (2006). The Divisadero tuff is distinctive for its crystal-rich nature (to ~40% phenocrysts) of mostly large (to 4 mm) grains of plagioclase and deeply embayed quartz. It is highly variable in thickness (~10–300 m) and has multiple cooling units with densely welded red-brown interiors that grade upward to poorly welded white tops (Swanson et al., 2006). We sampled the upper Divisadero tuff near Divisadero, southwest of Creel (sample DIV-2; Fig. 6; Table 1), to compare it with the Chepe ignimbrite (Tpc) of this study. Both have a very similar crystal-rich nature with large plagioclase, biotite, and embayed quartz phenocrysts, and the Chepe ignimbrite, like the Divisadero tuff, is densely welded. However, further investigation is needed to confirm this regional correlation, such as pumice and zircon geochemistry, and U-Pb zircon geochronology on the Divisadero tuff, which was previously dated by Swanson et al. (2006) using the K-Ar method as 29.9 ± 0.7 and 29.8 ± 0.5 Ma (±1σ errors). The Divisadero tuff extends from San Juanito to Divisadero for a length of ~60 km (Swanson et al., 2006); our tentative correlation would expand the extent of the Divisadero tuff an additional ~45 km southwest to a total length of ~105 km (Fig. 1).

In several localities in the northern Sierra Madre Occidental, mafic to intermediate composition volcanism followed the large-volume eruptions of the Early Oligocene ignimbrite pulse (the Southern Cordillera basaltic andesite province); the Témoris formation in the Guazapares Mining District region may be related to this period of mafic to intermediate composition volcanism. The mafic to intermediate composition volcanic rocks in other parts of the Sierra Madre Occidental are roughly coeval with or slightly younger than the ca. 27–24.5 Ma Témoris formation. In addition, the composition of Témoris formation rocks is similar to those of the Southern Cordillera basaltic andesite province (Fig. 7).

The age of the 24.5–23 Ma Sierra Guazapares formation generally coincides with the onset of the regional Early Miocene (ca. 24–20 Ma) ignimbrite pulse of the mid-Cenozoic ignimbrite flare-up (e.g., Ferrari et al., 2002; Ferrari et al., 2007; McDowell and McIntosh, 2012; Bryan et al., 2013). Although the Early Miocene ignimbrite pulse is volumetrically significant in the southern Sierra Madre Occidental (Ferrari et al., 2002; Ferrari et al., 2007), in the northern and central Sierra Madre Occidental this ignimbrite pulse was previously thought to be less abundant and restricted to the westernmost part of the silicic large igneous province (Ferrari et al., 2007; McDowell and McIntosh, 2012; Bryan et al., 2013). The Sierra Guazapares formation thus represents a previously unrecognized part of the Early Miocene ignimbrite pulse that may have been more widespread, east of the area where rocks erupted during this pulse have been previously recognized in the northern Sierra Madre Occidental.

Regional Timing of Volcanism and Extension

Previous studies have interpreted that a transition from andesitic arc magmatism in a compressional (Laramide) stress regime accompanying rapid plate convergence (Lower Volcanic Complex), to silicic ignimbrite flare-up magmatism in an extensional stress regime (Upper Volcanic Supergroup), was the result of decreased convergence between the Farallon and North American plates beginning in the Late Eocene ca. 40 Ma (Wark et al., 1990; Aguirre-Díaz and McDowell, 1991; Ward, 1991; Wark, 1991; Grijalva-Noriega and Roldán-Quintana, 1998; Ferrari et al., 2007). After the end of the Laramide orogeny in Mexico (Late Eocene), the Farallon plate was removed from the base of the North American plate by either steepening (slab rollback) and possible detachment of the deeper part of the subducted slab (e.g., Ferrari et al., 2007; Henry et al., 2010; Best et al., 2013; Busby, 2013), or through the development of a slab window (e.g., Wong et al., 2010). Based on the available age distribution of volcanic rocks in the southwestern U.S. and the Sierra Madre Occidental, the locus of magmatism is inferred to have migrated eastward (inboard) from the trench in Cretaceous to Eocene time, followed by a general southwestward migration of the arc-front magmatism towards the trench commencing by ca. 40 Ma in response to these Farallon–North American plate interactions (e.g., Coney and Reynolds, 1977; Damon et al., 1981; Ferrari et al., 1999; Gans et al., 2003; Ferrari et al., 2007; Henry et al., 2010; Wong et al., 2010; McDowell and McIntosh, 2012; Bryan et al., 2013; Busby, 2013). This plate tectonic interpretation is similar to space-time models of mid-Cenozoic volcanism proposed in the western U.S. (e.g., Coney and Reynolds, 1977; Damon et al., 1981; Gans et al., 1989; Best and Christiansen, 1991; Christiansen and Yates, 1992; Axen et al., 1993; Humphreys, 1995; Dickinson, 2002, 2006; Henry et al., 2010; Best et al., 2013; Busby, 2013). However, at a more detailed level this age trend shows greater complexity, as the Early Oligocene pulse of the ignimbrite flare-up occurred in a wide belt throughout the entire Sierra Madre Occidental at essentially the same age without internal migration patterns, and volcanism reappears in the rear-arc east of the arc front in the Middle to Late Miocene (Ferrari et al., 2007; Bryan et al., 2013).

The timing of the onset of extension relative to southwestward-migrating volcanism in the Sierra Madre Occidental has been poorly constrained, due at least in part to sparse map data. At the regional scale, the onset of extension possibly migrated episodically from east to west along the entire Sierra Madre Occidental, roughly corresponding to the southwestward migration of the arc front toward the trench; however, in detail volcanism in a given area may be pre extensional, synextensional, or postextensional (Ferrari et al., 2007). Although no direct evidence has been found for Eocene extension in the eastern Sierra Madre Occidental proper, there is evidence of an initial episode of extensional faulting during the Early Eocene in the Mesa Central region to the east of the southern Sierra Madre Occidental (Aranda-

Gómez and McDowell, 1998; Aguillón-Robles et al., 2009; Tristán-González et al., 2009) and at its easternmost boundary east of Durango during the Early Oligocene (32.3-30.6 Ma; Luhr et al., 2001), east of the unextended core. The earliest initiation of upper-crustal extension that developed regionally is inferred to have occurred ca. 30 Ma, marked by the widespread eruption of the Southern Cordillera basaltic andesite province (Cameron et al., 1989). The timing of this event immediately followed the peak of ignimbrite flare-up volcanism of the Early Oligocene pulse and coincided with a decline in silicic explosive volcanism (Bryan and Ferrari, 2013). Following this regional event, extensional deformation generally became focused in the Gulf Extensional Province to the west of the unextended core of the Sierra Madre Occidental and the timing of initial extensional deformation appears to have migrated westward with time in this region (Fig. 16; Gans, 1997; Gans et al., 2003).

Our new geologic mapping and geochronological data from the Guazapares Mining District region is broadly consistent with the interpretations that the inception of volcanism and extension generally migrated southwestward with time across the Sierra Madre Occidental. The Late Oligocene age (ca. 27 Ma) of initial local volcanism in the study area is younger than Late Eocene to Early Eocene volcanism to the northeast, and older than to coeval with Late Oligocene to Early Miocene volcanism to the west (Fig. 16). Our data clearly show that extension in the study area not only preceded local mafic to intermediate volcanism ca. 27 Ma and local silicic ignimbrite flare-up magmatism during the Early Miocene pulse ca. 24.5 Ma, but also overlapped in time with the end of the Early Oligocene pulse of the ignimbrite flare-up in the northern Sierra Madre Occidental, which occurred about 50–150 km to the north and east at ca. 32–28 Ma (Fig. 16). The Late Oligocene age (ca. 27.5 to after 23 Ma) of extension in the Guazapares Mining District region is slightly older than to roughly coeval with the onset of extension further west in Sonora (Fig. 16), where sedimentation in fault-bound grabens and rapid footwall cooling of core complexes also began at the end of the Oligocene to Early Miocene (Gans, 1997; McDowell et al., 1997; Wong et al., 2010).

Extensional Effects on Volcanism

Although much more mapping and dating are needed, we suggest that widespread crustal extension in northwestern Mexico may have played an important role in the later stages of magmatic development of the Sierra Madre Occidental silicic large igneous province. As magmatism migrated southwestward during the Late Oligocene to Miocene toward the Gulf of California, previously extended or currently extending crust likely influenced the composition of melts and promoted the localization of volcanic vents along favorable structures. Extension has been inferred to favor the generation and storage of melt (e.g., Hildreth, 1981; McKenzie and Bickle, 1988; White and McKenzie, 1989; Wark, 1991; Hanson and Glazner, 1995), and crustal thinning and active normal faulting is inferred to promote the ascent of basaltic magma, which results in crustal melting and the formation of silicic magma compositions (e.g., Johnson and Grunder, 2000; Ferrari et al., 2010). Although much of the pre–30 Ma volcanic and structural relationships are unclear, the inferred relationship between lithospheric extension and magmatism is supported by the synextensional nature of the of the Late Oligocene to Early Miocene mid-Cenozoic ignimbrite flare-up in the Sierra Madre Occidental silicic large igneous province, as observed in the Guazapares Mining District region.

CONCLUSIONS

New geologic mapping and zircon U-Pb LA-ICP-MS ages indicate that the Late Oligocene to Early Miocene rocks of the Guazapares Mining District region record synextensional volcanism in the northern Sierra Madre Occidental. Three informal formations are recognized: (1) the Parajes formation, consisting of silicic outflow ignimbrite sheets erupted from distant sources by ca 27.5 Ma, during the end of the Early Oligocene pulse of the mid-Cenozoic ignimbrite flare-up; (2) the ca. 27–24.5 Ma Témoris formation, comprising locally erupted mafic to intermediate composition volcanic rocks, including an andesitic volcanic center; and (3) the ca. 24.5–23 Ma Sierra Guazapares formation, consisting of vent to proximal silicic ignimbrites, lavas, and plugs erupted by fissure magmatism during the onset of the Early Miocene pulse of the mid-Cenozoic ignimbrite flare-up.

The main geologic structures in the Guazapares Mining District region are NNW-trending normal faults, several of which bound synvolcanic half-graben basins that began to form by the time of deposition of the upper part of the Parajes formation, and continued to develop during deposition of the Témoris and Sierra Guazapares formations. Much of the crustal extension occurred prior to the eruption of the Sierra Guazapares formation, with the earliest evidence of crustal extension by ca. 27.5 Ma. A minimum of 20% total horizontal extension is estimated in the Guazapares Mining District region. Preexisting extensional structures controlled the localization of andesitic and silicic volcanic vents and shallow level intrusions of the Témoris and Sierra Guazapares formations. The age of volcanism and extensional faulting in the Guazapares Mining District region generally corresponds to regional models inferring a post-Eocene southwestward migration of volcanism and crustal extension in the northern Sierra Madre Occidental.

In summary, this study presents direct evidence that crustal extension occurred in the western part of the northern Sierra Madre Occidental during the end of the Early Oligocene pulse of the ignimbrite flare-up. Extension in the Guazapares Mining District region preceded and continued during the onset of local magmatism, consisting first of mafic to andesitic magmatism, followed by silicic magmatism related to the Early Miocene pulse of the ignimbrite flare-up. Regional crustal extension in northwestern Mexico may have played an important role in the magmatic development of the Sierra Madre Occidental silicic large igneous province during the mid-Cenozoic ignimbrite flare-up, promoting the generation of silicic and intermediate magmas and the localization of volcanic eruptions along favorable preexisting geologic structures.

REFERENCES CITED

Aguillón-Robles, A., Tristán-González, M., Aguirre-Díaz, G. J., and Bellon, H., 2009, Syn-extensional intra-plate trachydacite-rhyolitic dome volcanism of the Mesa Central, southern Sierra Madre Occidental volcanic province, Mexico: Journal of Volcanology and Geothermal Research, v. 187, no. 1-2, p. 33-52.

Aguirre-Díaz, G. J., and Labarthe-Hernández, G., 2003, Fissure ignimbrites: Fissure-source origin for voluminous ignimbrites of the Sierra Madre Occidental and its relationship with Basin and Range faulting: Geology, v. 31, no. 9, p. 773–776.

Aguirre-Díaz, G. J., and McDowell, F. W., 1991, The volcanic section at Nazas, Durango, Mexico, and the possibility of widespread Eocene volcanism within the Sierra Madre Occidental: Journal of Geophysical Research, v. 96, no. B8, p. 13373-13388.

Aguirre-Díaz, G. J., and McDowell, F. W., 1993, Nature and timing of faulting and synextensional magmatism in the southern Basin and Range, central-eastern Durango, Mexico: Geological Society of America Bulletin, v. 105, p. 1435-1444.

Albrecht, A., and Goldstein, S. L., 2000, Effects of basement composition and age on silicic magmas across an accreted terrane-Precambrian crust boundary, Sierra Madre Occidental, Mexico: Journal of South Americam Earth Sciences, v. 13, p. 255-273.

Anderson, T., 2002, Correction of common lead in U–Pb analyses that do not report ^{204}Pb: Chemical Geology, v. 192, p. 59-79.

Aranda-Gómez, J. J., and McDowell, F. W., 1998, Paleogene extension in the southern basin and range province of Mexico: Syndepositional tilting of Eocene red beds and Oligocene volcanic rocks in the Guanajuato Mining District: International Geology Review, v. 40, p. 116-134.

Armstrong, R. L., and Ward, P. L., 1991, Evolving geographic patterns of Cenozoic magmatism in the North American Cordillera: the temporal and spatial association of magmatism and metamorphic core complexes: Journal of Geophysical Research, v. 96, no. B8, p. 13,201-13,224.

Axen, G. J., Taylor, W. J., and Bartley, J. M., 1993, Space-time patterns and tectonic controls of Tertiary extension and magmatism in the Great Basin of the western United States: Geological Society of America Bulletin, v. 105, p. 56-76.

Bagby, W. C., 1979, Geology, geochemistry, and geochronology of the Batopilas quadrangle, Sierra Madre Occidental, Chihuahua, Mexico [PhD thesis]: University of California, Santa Cruz, 271 p.
Best, M. G., and Christiansen, E. H., 1991, Limited extension during peak Tertiary volcanism, Great Basin of Nevada and Utah: Journal of Geophysical Research, v. 96, p. 13509-13528.
Best, M. G., Christiansen, E. H., and Gromme, S., 2013, Introduction: The 36-18 Ma southern Great Basin, USA, ignimbrite province and flareup: Swarms of subduction-related supervolcanoes: Geosphere, v. 9, p. 260-274.
Blair, T. C., and McPherson, J. G., 1994, Alluvial fans and their natural distinction from rivers based on morphology, hydraulic processes, sedimentary processes, and facies assemblages: Journal of Sedimentary Research, v. A64, no. 3, p. 450-489.
Branney, M. J., and Kokelaar, P., 2002, Pyroclastic Density Currents and the Sedimentation of Ignimbrites, Geological Society [London] Memoir No. 27, 150 p.
Brown, R. J., and Branney, M. J., 2004, Bypassing and diachronous deposition from density currents: Evidence from a giant regressive bed form in the Poris ignimbrite, Tenerife, Canary Islands: Geology, v. 32, no. 5, p. 445-448.
Bryan, S., 2007, Silicic large igneous provinces: Episodes, v. 30, no. 1, p. 1-12.
Bryan, S. E., and Ernst, R. E., 2008, Revised definition of Large Igneous Provinces (LIPs): Earth-Science Reviews, v. 86, p. 175-202.
Bryan, S. E., and Ferrari, L., 2013, Large igneous provinces and silicic large igneous provinces: Progress in our understanding over the last 25 yr: Geological Society of America Bulletin, v. 125, no. 7/8, p. 1053-1078.
Bryan, S. E., Ferrari, L., Reiners, P. W., Allen, C. M., Petrone, C. M., Ramos-Rosique, A., and Campbell, I. H., 2008, New insights into crustal contributions to large-volume rhyolite generation in the mid-Tertiary Sierra Madre Occidental Province, Mexico, revealed by U-Pb geochronology: Journal of Petrology, v. 49, no. 1, p. 47-77.
Bryan, S. E., Orozco-Esquivel, T., Ferrari, L., and López-Martínez, M., 2013, Pulling apart the mid to late Cenozoic magmatic record of the Gulf of California: Is there a Comondú arc?, *in* Gomez-Tuena, A., Straub, S. M., and Zellmer, G. F., eds., Orogenic Andesites and Crustal Growth, Geological Society of London Special Publication 385 (*in press*).
Bryan, S. E., Riley, T. R., Jerram, D. A., Leat, P. T., and Stephens, C. J., 2002, Silicic volcanism: An undervalued component of large igneous provinces and volcanic rifted margins, *in* Menzies, M. A., Klemperer, S. L., Ebinger, C. J., and J., B., eds., Volcanic Rifted Margins: Geological Society of America Special Paper 362, p. 97-118.
Busby, C. J., 2013, Birth of a plate boundary ca. 12 ma in the Ancestral Cascades arc, Walker Lane belt of California and Nevada: Geosphere, v. 9, no. 5, p. 1147-1160.
Cameron, K. L., Nimz, G. J., Niemeyer, S., and Gunn, S., 1989, Southern Cordilleran basaltic andesite suite, southern Chihuahua, Mexico: a link between Tertiary continental arc and flood basalt magmatism in North America: Journal of Geophysical Research, v. 94, no. B6, p. 7817-7840.
Carey, S. N., 1991, Transport and deposition of tephra by pyroclastic flows and surges, *in* Fisher, R. V., and Smith, G. A., eds., Sedimentation in Volcanic Settings, SEPM Special Publication No. 45: Tulsa, OK, SEPM (Society for Sedimentary Geology), p. 39-57.

Cather, S. M., Dunbar, N. W., McDowell, F. W., McIntosh, W. C., and Scholle, P. A., 2009, Climate forcing by iron fertilization from repeated ignimbrite eruptions: The icehouse -silicic large igneous province (SLIP) hypothesis: Geosphere, v. 5, no. 3, p. 315-324.

Charlier, B. L. A., Wilson, C. J. N., Lowenstern, J. B., Blake, S., Van Calsteren, P. W., and Davidson, J. P., 2004, Magma generation at a large, hyperactive silicic volcano (Taupo, New Zealand) revealed by U-Th and U-Pb systematics in zircons: Journal of Petrology, v. 46, p. 3-32.

Christiansen, R. L., and Yates, R. S., 1992, Post-Laramide geology of the western U.S. Cordillera, *in* Burchfiel, B. C., Lipman, P. W., and Zoback, M. L., eds., The Cordilleran Orogen: conterminous U. S.: The Geology of North America, Decade of North American Geology, Volume G-3: Boulder, CO, Geological Society of America, p. 261-406.

Cochemé, J. J., and Demant, A., 1991, Geology of the Yécora area, northern Sierra Madre Occidental, Mexico, *in* Pérez-Segura, E., and Jacques-Ayala, C., eds., Studies in Sonoran Geology: Geological Society of America Special Paper 254, p. 81-94.

Coney, P. J., 1978, Mesozoic-Cenozoic Cordilleran plate tectonics, *in* Smith, R. B., and Eaton, G. P., eds., Cenozoic tectonics and regional geophysics of the Western Cordillera: Geological Society of America Memoir 152: Boulder, CO, Geological Society of America, p. 33-50.

Coney, P. J., and Reynolds, S. J., 1977, Cordilleran Benioff zones: Nature, v. 270, p. 403-406.

Costa, A., Gottsmann, J., Melnik, O., and Sparks, R. S. J., 2011, A stress-controlled mechanism for the intensity of very large magnitude explosive eruptions: Earth and Planetary Science Letters, v. 310, no. 1-2, p. 161-166.

Damon, P. E., Shafiqullah, M., and Clark, K. F., 1981, Age trends of igneous activity in relation to metallogenesis in the southern Cordillera: Arizona Geological Society Digest, v. 14, p. 137-154.

Dickinson, W. R., 2002, The Basin and Range Province as a composite extensional domain: International Geology Review, v. 44, p. 1-38.

Dickinson, W. R., 2006, Geotectonic evolution of the Great Basin: Geosphere, v. 2, no. 7, p. 353-368.

Dreier, J., 1984, Regional tectonic control of epithermal veins in the Western United States and Mexico, *in* Wilkins, J., ed., Gold and silver deposits of the Basin and Range Province, Western U.S.A., Arizona Geological Society Digest, v. 15, p. 28-50.

Ferrari, L., Bryan, S., Rosique, A. R., Allen, C., Lopez, M., and Rankin, A., 2010, Relationships between rates of silicic magma generation, eruption and extensional tectonics: Insights from the Bolanos Graben, Southern Sierra Madre Occidental, Mexico: Geophysical Research Abstracts, v. 12, p. EGU2010-3825-1.

Ferrari, L., López-Martinez, M., Aguirre-Díaz, G., and Carrasco-Núñez, G., 1999, Space-time patterns of Cenozoic arc volcanism in central Mexico: From the Sierra Madre Occidental to the Mexican Volcanic Belt: Geology, v. 27, p. 303-306.

Ferrari, L., López-Martínez, M., and Rosas-Elguera, J., 2002, Ignimbrite flare-up and deformation in the southern Sierra Madre Occidental, western Mexico: Implications for the late subduction history of the Farallon plate: Tectonics, v. 21, no. 4, p. 1-24.

Ferrari, L., Valencia-Moreno, M., and Bryan, S., 2007, Magmatism and tectonics of the Sierra Madre Occidental and its relation with the evolution of the western margin of North America, *in* Alaniz-Álvarez, S. A., and Nieto-Samaniego, Á. F., eds., Geology

of México: Celebrating the Centenary of the Geological Society of México: Geological Society of America Special Paper 422, p. 1-39.
Fisher, R. V., and Schmincke, H. U., 1984, Pyroclastic Rocks: Berlin, Springer Verlag, 472 p.
Fisher, R. V., and Smith, G. A., 1991, Sedimentation in volcanic settings: SEPM (Society for Sedimentary Geology) Special Publication No. 45: Tulsa, OK, SEPM (Society for Sedimentary Geology), 257 p.
Freundt, A., Wilson, C. J. N., and Carey, S. N., 2000, Ignimbrites and block-and-ash flow deposits, *in* Sigurdsson, H., Houghton, B. F., McNutt, S. R., Rymer, H., and Stix, J., eds., Encyclopedia of Volcanoes: San Diego, CA, Academic Press, p. 581-600.
Gans, P. B., 1997, Large-magnitude Oligo-Miocene extension in southern Sonora: Implications for the tectonic evolution of northwest Mexico: Tectonics, v. 16, p. 388-408.
Gans, P. B., Blair, K. D., MacMillan, I., Wong, M. S., and Roldán-Quintana, J., 2003, Structural and magmatic evolution of the Sonoran rifted margin: A preliminary report: Geological Society of America Abstracts with Programs, v. 35, no. 4, p. 21.
Gans, P. B., Mahood, G. A., and Schermer, E. R., 1989, Synextensional magmatism in the Basin and Range Province: a case study from the eastern Great Basin: Geological Society of America Special Paper 233, p. 1-53.
Gertisser, R., Preece, K., and Keller, J., 2009, The Plinian Lower Pumice 2 eruption, Santorini, Greece: Magma evolution and volatile behaviour: Journal of Volcanology and Geothermal Research, v. 186, no. 3-4, p. 387-406.
González León, C. M., McIntosh, W. C., Lozano-Santacruz, R., Valencia-Moreno, M., Amaya-Martínez, R., and Rodríguez-Castañeda, J. L., 2000, Cretaceous and Tertiary sedimentary, magmatic, and tectonic evolution of north-central Sonora (Arizpe and Bacanuchi Quadrangles), northwest Mexico: Geological Society of America Bulletin, v. 112, no. 4, p. 600-610.
Grijalva-Noriega, F. J., and Roldán-Quintana, J., 1998, An overview of the Cenozoic tectonic and magmatic evolution of Sonora, northwestern Mexico: Revista Mexicana de Ciencias, v. 15, no. 2, p. 145-156.
Gunderson, R., Cameron, K. L., and Cameron, M., 1986, Mid-Cenozoic high-K calc-alkalic volcanism in eastern Chihuahua, Mexico: Geology and geochemistry of the Benevides-Pozos area: Geological Society of America Bulletin, v. 97, p. 737-753.
Gustin, M. M., 2011, Technical report on the San Miguel project, Guazapares Mining District, Chihuahua, Mexico, prepared for Paramount Gold and Silver Corp.: Reno, NV, Mine Development Associates, 149 p.
Gustin, M. M., 2012, Updated technical report on the San Miguel project gold and silver resources, Guazapares Mining District, Chihuahua, Mexico, prepared for Paramount Gold and Silver Corp.: Reno, NV, Mine Development Associates, 176 p.
Hampton, B. A., and Horton, B. K., 2007, Sheetflow fluvial processes in a rapidly subsiding basin, Altiplano plateau, Bolivia: Sedimentology, v. 54, p. 1121–1147.
Hanson, R. B., and Glazner, A. F., 1995, Thermal requirements for extensional emplacement of granitoids: Geology, v. 23, no. 3, p. 213-216.
Henry, C., and Aranda-Gómez, J. J., 2000, Plate interactions control middle-late Miocene, proto-Gulf and Basin and Range extension in the southern Basin and Range: Tectonophysics, v. 218, p. 1-26.

Henry, C. D., and Fredrikson, G., 1987, Geology of part of southern Sinaloa, Mexico, adjacent to the Gulf of California: Geological Society of America Map and Chart Series, MCH067, 1 sheet, scale 1:250,000, 14 p.

Henry, C. D., McIntosh, W., McDowell, F. W., Lipman, P. W., Chapin, C. E., and Richardson, M. T., 2010, Distribution, timing, and controls of the mid-Cenozoic ignimbrite flareup in western North America: Geological Society of America Abstracts with Programs, v. 42, no. 5, p. 144.

Hildreth, W., 1981, Gradients in silicic magma chambers: Implications for lithospheric magmatism: Journal of Geophysical Research, v. 86, no. B11, p. 10153-10192.

Humphreys, E. D., 1995, Post-Laramide removal of the Farallon Slab, western United States: Geology, v. 10, p. 987-990.

Irvine, T. N., and Baragar, W. R. A., 1971, A guide of the chemical classification of common volcanic rocks: Canadian Journal of Earth Science, v. 8, p. 523-548.

Jicha, B. R., Scholl, D. W., and Rea, D. K., 2009, Circum-Pacific arc flare-ups and global cooling near the Eocene-Oligocene boundary: Geology, v. 37, no. 4, p. 303-306.

Johnson, J. A., and Grunder, A. L., 2000, The making of intermediate composition magma in a bimodal suite: Duck Butte Eruptive Center, Oregon, USA: Journal of Volcanology and Geothermal Research, v. 95, p. 175-195.

Kelly, S. B., and Olsen, H., 1993, Terminal fans - a review with reference to Devonian examples: Sedimentary Geology, v. 85, p. 339-374.

Le Bas, M. J., Le Maitre, R. W., Streckeisen, A., and Zanettin, B., 1986, A chemical classification of volcanic rocks based on the total alkali–silica diagram: Journal of Petrology, v. 27, p. 745-750.

Lipman, P. W., 2007, Incremental assembly and prolonged consolidation of Cordilleran magma chambers: Evidence from the Southern Rocky Mountain volcanic field: Geosphere, v. 3, no. 1, p. 42-70.

Ludwig, K. L., 2008, Isoplot 3.70. A geochronological toolkit for Microsoft Excel: Berkeley Geochronology Center Special Publication No.4, p. 1-77.

Luhr, J. F., Henry, C. D., Housh, T. B., Aranda-Gómez, J. J., and McIntosh, W. C., 2001, Early extension and associated mafic alkalic volcanism from the southern Basin and Range Province: Geology and petrology of the Rodeo and Nazas volcanic fields, Durango (Mexico): Geological Society of America Bulletin, v. 113, p. 760–773.

McDowell, F. W., 2007, Geologic transect across the northern Sierra Madre Occidental volcanic field, Chihuahua and Sonora, Mexico: Geological Society of America Digital Map and Chart Series 6, 70 p.

McDowell, F. W., and Clabaugh, S. E., 1979, Ignimbrites of the Sierra Madre Occidental and their relation to the tectonic history of western Mexico, *in* Chapin, C. E., and Elston, W. E., eds., Ash-Flow Tuffs: Geological Society of America Special Paper 180, p. 113-124.

McDowell, F. W., and Keizer, R. P., 1977, Timing of mid-Tertiary volcanism in the Sierra Madre Occidental between Durango City and Mazatlan, Mexico: Geological Society of America Bulletin, v. 88, p. 1479-1487.

McDowell, F. W., and Mauger, R. L., 1994, K-Ar and U-Pb zircon chronology of Late Cretaceous and Tertiary magmatism in central Chihuahua State, Mexico: Geological Society of America Bulletin, v. 106, p. 118-132.

McDowell, F. W., and McIntosh, W. C., 2012, Timing of intense magmatic episodes in the northern and central Sierra Madre Occidental, western Mexico: Geosphere, v. 8, no. 6, p. 1502-1526.
McDowell, F. W., Roldán-Quintana, J., and Amaya-Martínez, R., 1997, Interrelationship of sedimentary and volcanic deposits associated with Tertiary extension in Sonora, Mexico: Geological Society of America Bulletin, v. 109, no. 10, p. 1349-1360.
McDowell, F. W., Roldán-Quintana, J., and Connelly, J. N., 2001, Duration of Late Cretaceous-early Tertiary magmatism in east-central Sonora, Mexico: Geological Society of America Bulletin, v. 113, p. 521-531.
McKenzie, D., and Bickle, M. J., 1988, The volume and composition of melt generated by extension of the lithosphere: Journal of Petrology, v. 29, p. 625-679.
Minjárez Sosa, I., Montaño Jiménez, T. R., Ochoa Granillo, J. A., Grijalva Noriega, F. J., Ochoa Landín, L. H., Herrera Urbina, S., Guzmán Espinosa, J. B., and Mancilla Gutiérrez, A. A., 2002, Carta Geológico-Minera Ciudad Obregón G12-3 Sonora, Chihuahua y Sinaloa: Servicio Geológico Mexicano, scale 1:250,000.
Murray, B. P., Horton, B. K., Matos, R., and Heizler, M. T., 2010, Oligocene–Miocene basin evolution in the northern Altiplano, Bolivia: Implications for evolution of the central Andean backthrust belt and high plateau: Geological Society of America Bulletin, v. 122, no. 9/10, p. 1443-1462.
Nieto-Samaniego, Á. F., Ferrari, L., Alaniz-Álvarez, S. A., Labarthe-Hernández, G., and Rosas-Elguera, J., 1999, Variation of Cenozoic extension and volcanism across the southern Sierra Madre Occidental volcanic province, Mexico: Geological Society of America Bulletin, v. 111, no. 3, p. 347-363.
Ramírez Tello, E., and Garcia Peralta, Á. A., 2004, Carta Geológico-Minera Témoris G12-B39 Chihuahua: Servicio Geológico Mexicano, scale 1:50,000.
Rowley, P. D., MacLeod, N. S., Kuntz, M. A., and Kaplan, A. M., 1985, Proximal bedded deposits related to pyroclastic flows of May 18, 1980, Mount St. Helens, Washington: Geological Society of America Bulletin, v. 96, no. 11, p. 1373-1383.
Roy, D., Trinder, I. D., and Lustig, G., 2008, Report on the San Miguel project, Guazapares Mining District, Chihuahua, Mexico for Paramount Gold and Silver Corp.: Toronto, Ontario, A.C.A. Howe International Limited, 205 p.
Sambridge, M. S., and Compston, W., 1994, Mixture modeling of multi-component data sets with application to ion-probe zircon ages: Earth and Planetary Science Letters, v. 128, p. 373-390.
Schermer, E. R., and Busby, C. J., 1994, Jurassic magmatism in the central Mojave Desert: Implications for preservation of continental arc volcanic sequences: Geological Society of America Bulletin, v. 106, p. 767-790.
Sigurdsson, H., Houghton, B. F., McNutt, S. R., Rymer, H., and Stix, J., 2000, Encyclopedia of Volcanoes: San Diego, California, Academic Press, 1471 p.
Silva Parejas, C., Druitt, T. H., Robin, C., Moreno, H., and Naranjo, J.-A., 2010, The Holocene Pucón eruption of Volcán Villarrica, Chile: deposit architecture and eruption chronology: Bulletin of Volcanology, v. 72, p. 677-692.
Sláma, J., Košler, J., Condon, D. J., Crowley, J. L., Gerdes, A., Hanchar, J. M., Horstwood, M. S. A., Morris, G. A., Nasdala, L., Norberg, N., Schaltegger, U., Schoene, B., Tubrett, M. N., and Whitehouse, M. J., 2008, Plešovice zircon - A new natural reference material for U-Pb and Hf isotopic microanalysis: Chemical Geology, v. 249, p. 1-35.

Smith, R. L., 1960, Zones and zonal variations in welded ash flows: U.S. Geological Survey Professional Paper 354-F, p. 149-159.
Solari, L. A., Gómez-Tuena, A., Bernal, J. P., Pérez-Arvizu, O., and Tanner, M., 2010, U-Pb zircon geochronology by an integrated LA-ICPMS microanalytical workstation: Achievements in precision and accuracy: Geostandards and Geoanalytical Research, v. 34, no. 1, p. 5-18.
Solari, L. A., and Tanner, M., 2011, UPb.age, a fast data reduction script for LA-ICP-MS U-Pb geochronology: Revista Mexicana de Ciencias Geológicas, v. 28, no. 1, p. 83-91.
Swanson, E. R., 1977, Reconnaissance geology of the Tomochic-Ocampo area, Sierra Madre Occidental, Chihuahua, Mexico [Ph.D. thesis]: University of Texas, Austin, 123 p.
Swanson, E. R., Kempter, K. A., McDowell, F. W., and McIntosh, W. C., 2006, Major ignimbrites and volcanic centers of the Copper Canyon area: A view into the core of Mexico's Sierra Madre Occidental: Geosphere, v. 2, no. 3, p. 125-141.
Swanson, E. R., and McDowell, F. W., 1984, Calderas of the Sierra Madre Occidental volcanic field, western Mexico: Journal of Geophysical Research, v. 89, p. 8787-8799.
Swanson, E. R., and McDowell, F. W., 1985, Geology and geochronology of the Tomochic caldera, Chihuahua, Mexico: Geological Society of America Bulletin, v. 96, p. 1477-1482.
Tera, F., and Wasserburg, G., 1972, U-Th-Pb systematics in three Apollo 14 basalts and the problem of initial Pb in lunar rocks: Earth and Planetary Science Letters, v. 14, p. 281-304.
Tristán-González, M., Aguirre-Díaz, G. J., Labarthe-Hernández, G., Torres-Hernández, J., and Bellon, H., 2009, Post-Laramide and pre-Basin and Range deformation and implications for Paleogene (55–25 Ma) volcanism in central Mexico: A geological basis for a volcano-tectonic stress model: Tectonophysics, v. 471, p. 136-152.
Umhoefer, P. J., Dorsey, R., Willsey, S., Mayer, L., and Renne, P., 2001, Stratigraphy and geochronology of the Comondú Group near Loreto, Baja California Sur, Mexico: Sedimentary Geology, v. 144, p. 125-147.
Ward, P. L., 1991, On plate tectonics and the geologic evolution of southwestern North America: Journal of Geophysical Research, v. 96, no. B7, p. 12,479-12,496.
Wark, D. A., 1991, Oligocene ash flow volcanism, northem Sierra Madre Occidental: role of mafic and intermediate-composition magmas in rhyolite genesis: Journal of Geophysical Research, v. 96, no. B8, p. 13,389-13,411.
Wark, D. A., Kempter, K. A., and McDowell, F. W., 1990, Evolution of waning subduction-related magmatism, northern Sierra Madre Occidental, Mexico: Geological Society of America Bulletin, v. 102, p. 1555-1564.
White, R. S., and McKenzie, D. P., 1989, Magmatism at rift zones: the generation of volcanic continental margins and flood basalts: Journal of Geophysical Research, v. 94, p. 7685-7729.
Wong, M. S., Gans, P. B., and Scheier, J., 2010, The $^{40}Ar/^{39}Ar$ thermochronology of core complexes and other basement rocks in Sonora, Mexico: Implications for Cenozoic tectonic evolution of northwestern Mexico: Journal of Geophysical Research, v. 115, no. B07414, doi: 10.1029/2009JB007032.
Wood, D. R., and Durgin, D. C., 2009, Technical report project update: San Miguel project, Chihuahua, Mexico, prepared for Paramount Gold and Silver Corp.: Sparks, Nevada, Delve Consultants, L.L.C., 86 p.

Wright, J. V., Self, S., and Fisher, R. V., 1981, Towards a facies model for ignimbrite-forming eruptions, *in* Self, S., and Sparks, R. S., eds., Tephra Studies: Dordrecht, Netherlands, D. Reidel, p. 433-439.

CHAPTER 2

EPITHERMAL MINERALIZATION CONTROLLED BY SYNEXTENSIONAL MAGMATISM IN THE GUAZAPARES MINING DISTRICT OF THE SIERRA MADRE OCCIDENTAL SILICIC LARGE IGNEOUS PROVINCE, MEXICO

ABSTRACT

Epithermal mineralization in the Guazapares Mining District is closely related to extensional deformation and magmatism during the mid-Cenozoic ignimbrite flare-up of the Sierra Madre Occidental silicic large igneous province, Mexico. Three Late Oligocene–Early Miocene synextensional formations are identified by detailed volcanic lithofacies mapping in the study area: (1) ca. 27.5 Ma Parajes formation, composed of silicic outflow ignimbrite sheets; (2) ca. 27–24.5 Ma Témoris formation, consisting primarily of locally erupted mafic-intermediate composition lavas and interbedded fluvial and debris flow deposits; (3) ca. 24.5–23 Ma Sierra Guazapares formation, composed of silicic vent to proximal ignimbrites, lavas, subvolcanic intrusions, and volcaniclastic deposits. Epithermal low- to intermediate-sulfidation, gold-silver-lead-zinc vein and breccia mineralization appears to be associated with emplacement of Sierra Guazapares formation rhyolite plugs and is favored where pre-to-synvolcanic extensional structures are in close association with these hypabyssal intrusions.

Several resource areas in the Guazapares Mining District are located along the easternmost strands of the Guazapares Fault Zone, a NW-trending normal fault system that hosts most of the epithermal mineralization in the mining district. This study describes the geology that underlies three of these areas, which are, from north to south: (1) The Monte Cristo resource area, which is underlain primarily by Sierra Guazapares formation rhyolite dome collapse breccia, lapilli-tuffs, and fluvially reworked tuffs that interfinger with

lacustrine sedimentary rocks in a synvolcanic half-graben bounded by the Sangre de Cristo Fault. Deposition in the hanging wall of this half-graben was concurrent with the development of a rhyolite lava dome-hypabyssal intrusion complex in the footwall; mineralization is concentrated in the high-silica rhyolite intrusions in the footwall and along the syndepositional fault and adjacent hanging wall graben fill. (2) The San Antonio resource area, underlain by interstratified mafic-intermediate lavas and fluvial sandstone of the Témoris formation, faulted and tilted by two en echelon NW-trending normal faults with opposing dip-directions. Mineralization occurs along subvertical structures in the accommodation zone between these faults. There are no silicic intrusions at the surface within the San Antonio resource area, but they outcrop ~0.5 km to the east, where they are intruded along the La Palmera Fault, and are located ~120 m-depth in the subsurface. (3) The La Unión resource area, which is underlain by mineralized andesite lavas and lapilli-tuffs of the Témoris Formation. Adjacent to the La Union resource area is Cerro Salitrera, one of the largest silicic intrusions in the area. The plug that forms Cerro Salitrera was intruded along the La Palmera Fault, and was not recognized as an intrusion prior to our work.

We show here that epithermal mineralization is Late Oligocene to Miocene-age and hosted in extensional structures, younger than the ages of mineralization inferred from unpublished mining reports for the region. We further infer that mineralization was directly related to the emplacement of silicic intrusions of the Sierra Guazapares formation, when the mid-Cenozoic ignimbrite flare-up of the Sierra Madre Occidental swept westward into the study area at ca. 24.5–23 Ma.

INTRODUCTION

The Sierra Madre Occidental of northwestern Mexico is the largest Cenozoic silicic igneous province on Earth (300,000–400,000 km3; Aguirre-Díaz and Labarthe-Hernández, 2003; Bryan, 2007; Ferrari et al., 2007; Bryan and Ferrari, 2013). The Sierra Madre Occidental also hosts one of the largest (800,000 km^2) and most productive (at least 80 million ounces gold, 4.5 billion ounces silver produced) epithermal precious mineral deposits on Earth (Dreier, 1984; Staude and Barton, 2001). As important as these mineral deposits are, there is a limited understanding of the relationships between the timing of epithermal mineralization and the magmatic and tectonic history of the Sierra Madre Occidental, particularly at the mining district level. Regional tectonic controls on the development of epithermal veins in western North America have been proposed (e.g., Dreier, 1984; Price et al., 1988), and Staude and Barton (2001) suggested that Jurassic to Late Cenozoic mineralization is commonly associated with coeval magmatic and tectonic events. Camprubí et al. (2003) supported this interpretation, suggesting that the age of the volcanic host rock is close to the age of the epithermal mineral deposit. However, the details of the structural setting of the precious mineral deposits, and their relationship to specific magmatic and tectonic events, remain poorly known for most of the Sierra Madre Occidental.

The Guazapares Mining District of western Chihuahua, Mexico, is located ~250 km southwest of Chihuahua City in the northern Sierra Madre Occidental (Fig. 1), within the Sierra Madre Occidental Gold-Silver Belt of northwestern Mexico. Previous work in the Guazapares Mining District has consisted entirely of unpublished mining company reports, with the except for our recently published work (Murray et al., 2013). These unpublished reports (e.g., Roy et al., 2008; Wood and Durgin, 2009; Gustin, 2011, 2012) indicate that mineralization in the Guazapares Mining District is spatial associated with the north-

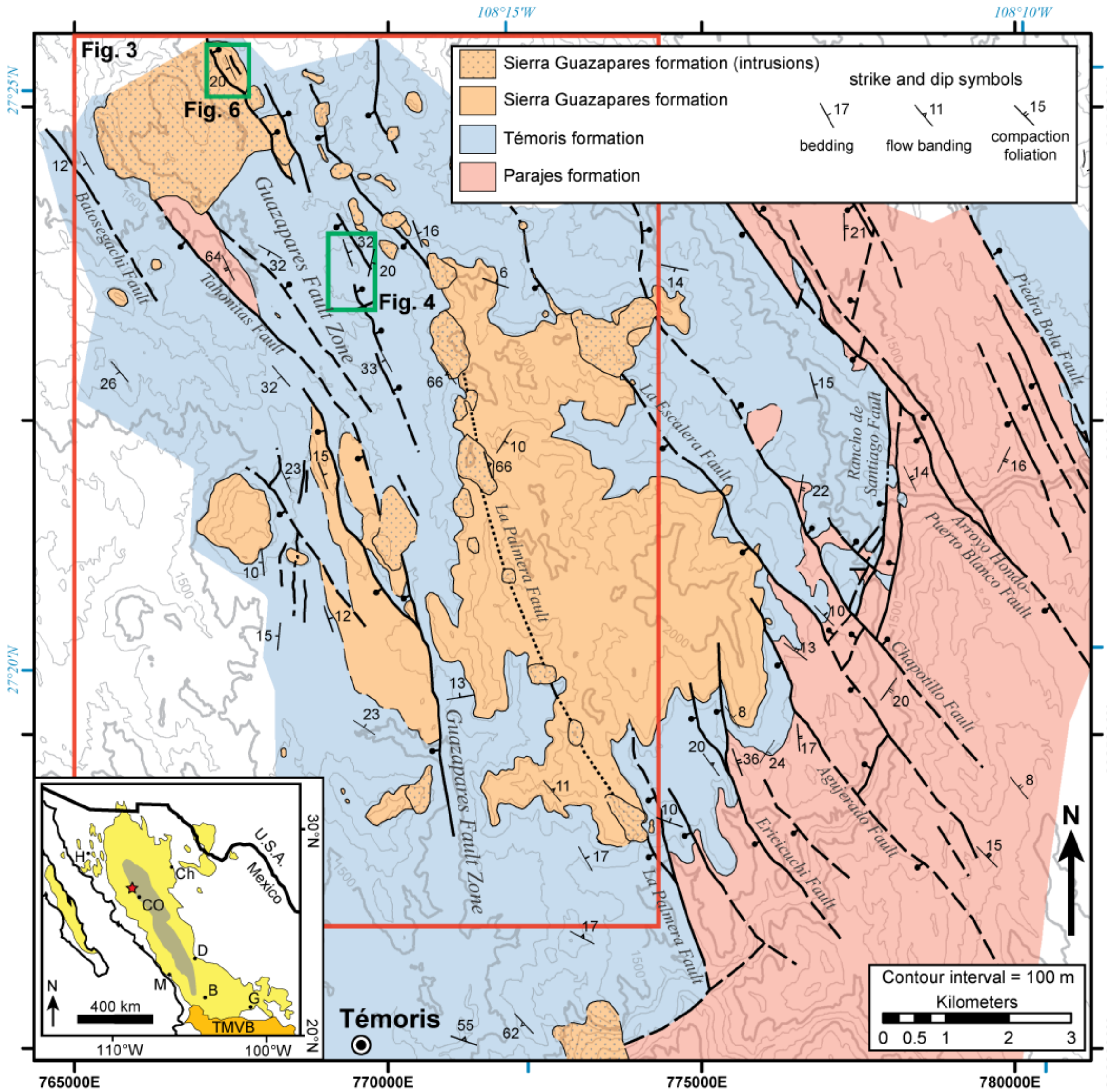

Figure 1. Simplified geologic map of the Guazapares Mining District region, showing the extent of the three formations (Fig. 2) and the location of major faults (after Murray et al., 2013). The Guazapares Mining District lies north of the town of Témoris, which is a stop on the famous Copper Canyon train. The red box indicates the location of Figure 3, which focuses on the Guazapares Fault Zone; for detailed discussion of the entire map area, see Murray et al. (2013). The green boxes indicate the locations of the San Antonio (Fig. 4) and Monte Cristo (Fig. 6) resource areas. Inset map of western Mexico shows the extent of the Sierra Madre Occidental (SMO) silicic large igneous province (light yellow) and the relatively unextended core (dark gray) of the SMO (after Henry and Aranda-Gómez, 2000; Ferrari et al., 2002; Bryan et al., 2013). The star indicates the location of the Guazapares Mining District (this study). B—San Martín de Bolaños Mining District, CO— Cuenca de Oro basin, Ch—Ciudad Chihuahua, D—Durango, G—Guanajuato Mining District, H—Hermosillo, M—Mazatlán, TMVB—Trans-Mexican Volcanic Belt.

northwest trending, steeply dipping structures of the Guazapares Fault Zone and consists of multi-phase, epithermal, low-to-intermediate-sulfidation, gold-silver-lead-zinc vein and breccia deposits. These studies focus mainly on the alteration and mineralization zones within the mining district, and less on the physical volcanology of the host rocks. Here, we assess the mining district in the context of the broader geologic setting and regional volcanotectonic evolution, by mapping volcanic and intrusive lithofacies and their relationships with faults, with additional petrographic, geochemical, and geochronological data on the igneous rocks. The approach described above has been previously employed to reconstruct the volcanic and tectonic history of the Guazapares Mining District region (Murray et al., 2013). In this study, we describe the broader magmatic and tectonic controls on epithermal mineralization in the Guazapares Mining District and present new interpretations based on detailed volcanic lithofacies mapping in the locations of active mining prospects within the Guazapares Mining District, to interpret the magmatic and structural setting of these mineral deposits. We propose that epithermal mineralization is favored where pre-to-synvolcanic extensional structures are reactivated or become active during emplacement of rhyolite hypabyssal intrusions of the silicic large igneous province, and that the timing of mineralization is either synchronous or follows emplacement of these intrusions.

GEOLOGIC BACKGROUND

The Sierra Madre Occidental silicic large igneous province is considered part of the extensive mid-Cenozoic ignimbrite flare-up that affected much of the southwestern North American Cordillera from the Middle Eocene to Late Miocene (e.g., Coney, 1978; Armstrong and Ward, 1991; Ward, 1991; Ferrari et al., 2002; Lipman, 2007; Cather et al., 2009; Henry et al., 2010; Best et al., 2013). The Sierra Madre Occidental trends for ~1200 km southwest from the U.S.-Mexico border to the Trans-Mexican Volcanic Belt (Fig. 1), consisting primarily of Oligocene to Early Miocene ignimbrites that cover an area of ~400,000 km^2 with an average thickness of 1 km (McDowell and Keizer, 1977; McDowell and Clabaugh, 1979; Aguirre-Díaz and Labarthe-Hernández, 2003; Bryan and Ferrari, 2013). The core of the Sierra Madre Occidental is relatively unextended in comparison to the surrounding Late Oligocene- to Miocene-age extensional belts of the southern Basin and Range to the east and the Gulf Extensional Province to the west (Fig. 1; Nieto-Samaniego et al., 1999; Henry and Aranda-Gómez, 2000; Ferrari et al., 2013).

Regional Volcanic Stratigraphy

Previous regional studies have subdivided the Late Cretaceous to mid-Cenozoic rocks of the Sierra Madre Occidental into: (1) the Late Cretaceous to Eocene Lower Volcanic Complex, dominantly intermediate in composition; (2) the Eocene to Early Miocene Upper Volcanic Supergroup, dominantly silicic in composition; and (3) the Early Oligocene to Early Miocene Southern Cordillera basaltic andesite (SCORBA) (McDowell and Keizer, 1977; Cameron et al., 1989; Ferrari et al., 2007). This transition from intermediate arc magmatism (Lower Volcanic Complex) to silicic and mafic-intermediate magmatism (Upper Volcanic Supergroup and SCORBA) is interpreted as the result of decreased convergence between the Farallon and North American plates beginning in the Late Eocene ca. 40 Ma (Wark et al., 1990; Aguirre-Díaz and McDowell, 1991; Ward, 1991; Wark, 1991; Grijalva-Noriega and Roldán-Quintana, 1998; Ferrari et al., 2007). After the end of the Laramide orogeny in Mexico (Late Eocene), the Farallon plate is interpreted to have been removed from the base of the North American plate, likely by slab rollback (e.g., Ferrari et al., 2007; Henry et al., 2010) or through the development of a slab window (e.g., Dickinson and Snyder, 1979;

Wong et al., 2010). Removal of the slab resulted in a general southwestward migration of the arc-front magmatism towards the trench, commencing by ca. 40 Ma, in response to these Farallon–North American plate interactions (e.g., Coney and Reynolds, 1977; Damon et al., 1981; Ferrari et al., 1999; Gans et al., 2003; Ferrari et al., 2007; Henry et al., 2010; McDowell and McIntosh, 2012; Bryan et al., 2013).

The Lower Volcanic Complex of the Sierra Madre Occidental is interpreted as continental subduction-related magmatism broadly contemporaneous with the Laramide orogeny in western North America (McDowell and Keizer, 1977; McDowell et al., 2001; Staude and Barton, 2001). This complex consists of mainly intermediate composition lavas and lesser silicic tuffs, as well as granodioritic to granitic intrusions that represent magma chambers beneath volcanoes. The Lower Volcanic Complex is inferred to underlie most of the Upper Volcanic Supergroup (Aguirre-Díaz and McDowell, 1991; Ferrari et al., 2007) and this simple scheme has been widely used to interpret the geology of many areas in the Sierra Madre Occidental in the absence of geochronology or observed stratigraphic relations.

The Upper Volcanic Supergroup of the Sierra Madre Occidental is composed mainly of Eocene to Early Miocene silicic ignimbrites, lavas, and intrusions (McDowell and Keizer, 1977; McDowell and Clabaugh, 1979; Aguirre-Díaz and McDowell, 1991, 1993; Ferrari et al., 2002; Ferrari et al., 2007; McDowell, 2007). These rocks represent the products of large-volume silicic large igneous province magmatism during the mid-Cenozoic ignimbrite flare-up that affected much of the southwestern North American Cordillera from the Middle Eocene to Late Miocene (e.g., McDowell and Keizer, 1977; Ferrari et al., 2007; Lipman, 2007; Cather et al., 2009; Henry et al., 2010; Best et al., 2013). The emplacement of the Upper Volcanic Supergroup appears to have an episodic nature, with major pulses of large volume ignimbrite volcanism during the Eocene (ca. 46–42 Ma), Early Oligocene (ca. 32–28

Ma), and Early Miocene (ca. 24–20 Ma) (Ferrari et al., 2002; Ferrari et al., 2007; Cather et al., 2009; McDowell and McIntosh, 2012).

During the final stages of, and after each silicic ignimbrite pulse of the Upper Volcanic Supergroup, mafic to intermediate composition lavas were intermittently erupted in the northern Sierra Madre Occidental (Ferrari et al., 2007); these rocks are referred to as Southern Cordillera basaltic andesite (SCORBA) by Cameron et al. (1989). These rocks have been interpreted as magmas recording the initiation of regional crustal extension following the Early Oligocene pulse of the Upper Volcanic Supergroup (e.g., Cameron et al., 1989; Cochemé and Demant, 1991; Gans, 1997; McDowell et al., 1997; González León et al., 2000; Ferrari et al., 2007), although, as discussed below, we find evidence for extension before and during silicic volcanism of the Upper Volcanic Supergroup.

Timing of Crustal Extension

The timing of crustal extension in the northern Sierra Madre Occidental in relation to silicic ignimbrite flare-up volcanism is poorly constrained. Previous workers have suggested that significant crustal extension in the Sierra Madre Occidental did not occur until after the Early Oligocene peak of Upper Volcanic Supergroup volcanism (e.g., McDowell and Clabaugh, 1979; Cameron et al., 1989; Wark et al., 1990; McDowell and Mauger, 1994; Gans, 1997; McDowell et al., 1997; Grijalva-Noriega and Roldán-Quintana, 1998). Alternatively, other studies have inferred that either the onset of large volume Early Oligocene ignimbrite flare-up volcanism records initial regional extension (e.g., Aguirre-Díaz and McDowell, 1993), or that extension may have began as early as the Eocene, based on the orientation and age of epithermal vein deposits (Dreier, 1984) and a moderate angular unconformity between the Lower Volcanic Complex and Upper Volcanic Supergroup (e.g., Ferrari et al., 2007). In this paper, we summarize evidence, described in detail by Murray et al. (2013), that extension in the Guazapares Mining District began during the Early Oligocene ignimbrite pulse (ca. 32–28 Ma), which occurred to the east of the study area, and continued through the Early Miocene ignimbrite pulse (ca. 24–20 Ma), which occurred within the Guazapares Mining District.

Timing of Epithermal Mineralization

As noted above, metallic mineralization is widespread in northwestern Mexico, and has been inferred to be broadly coeval with regional Late Jurassic to Late Cenozoic magmatic events (e.g., Staude and Barton, 2001; Camprubí et al., 2003). The majority of low-sulfidation epithermal deposits in Mexico range from Eocene to Miocene age (Albinson et al., 2001; Camprubí et al., 2003). Based on the assumption that the age of the volcanic host rock is an approximation of the age of epithermal mineral deposits, and supported by limited direct dating of adularia from mineral deposits, Camprubí et al. (2003) proposed that there are three main phases of epithermal mineralization in the Sierra Madre Occidental: (1) a first phase between ca. 48 and 40 Ma, related to Laramide magmatism; (2) a second phase between ca. 40 and 27 Ma, related to the Early Oligocene pulse of the ignimbrite flare-up; and (3) a third phase between ca. 23 and 18 Ma, related to the Early Miocene pulse of the ignimbrite flare-up (Camprubí et al., 2003). Laramide-age mineralization is hosted by the Lower Volcanic Complex, generally in E-W trending veins oriented perpendicular to the least compressional stress direction (Dreier, 1984; Price et al., 1988; Camprubí et al., 2003). Many of these epithermal deposits are likely buried beneath the ignimbrite sheets of the Upper Volcanic Supergroup (Staude and Barton, 2001). It has been inferred that the majority of epithermal deposits in Mexico formed during Upper Volcanic Supergroup magmatism, which created a NW-trending mineralized belt from Guerrero to Chihuahua, at a distance of up to ~250 km from the Pacific coast (Camprubí et al., 2003). Epithermal veins of this age are generally orientated NW-SE, interpreted to be normal to the direction of maximum regional extension (e.g., Dreier, 1984; Price et al., 1988). Mineral deposits hosted in the Upper Volcanic Supergroup have been widely assumed to be related to the Early Oligocene ignimbrite pulse, because the Early Miocene pulse was not widely recognized (Camprubí et al., 2003), except for recent studies in the southern Sierra Madre Occidental (Ferrari et al., 2002; Ferrari et al., 2013). However, for the most part, the mineralization lacks precise age control because the host rocks in most of the Sierra Madre Occidental are very poorly mapped and dated.

Volcanic Terminology

The use of volcanic-volcaniclastic terminology in the literature is often ambiguous. The terminology we use in this paper are those of Fisher and Schmincke (1984), Fisher & Smith (1991), Sigurdsson et al. (2000), and Jerram and Petford (2011). Three main types of volcanic rocks are found in the Guazapares Mining District: extrusive (e.g., lavas, domes), hypabyssal (e.g., plugs), and volcaniclastic. Following Fisher and Schmincke (1984), volcaniclastic refers to all fragmental rocks made dominantly of volcanic detritus: these include (1) pyroclastic fragmental deposits, inferred to have been directly fed from an eruption, e.g., pyroclastic fall, ignimbrites, pyroclastic surges, dome-collapse breccias, block-and-ash flows, autoclastic flow breccias; (2) reworked fragmental deposits, inferred to result from downslope reworking of unconsolidated eruption-fed fragmental deposits, e.g., block-and-ash flow deposits commonly pass downslope into debris flow and fluvial deposits, and delicate pyroclastic detritus (pumice, shards, or euhedral crystals) indicate limited transportation of unconsolidated primary volcanic material; and (3) epiclastic deposits, made of volcanic fragments inferred to have been derived from erosion of preexisting rock. When the distinctions cannot be made, the general term volcaniclastic is applied.

GEOLOGY OF THE GUAZAPARES MINING DISTRICT

Lithology and Depositional Setting

The rock types and depositional setting of the Guazapares Mining District region are briefly summarized below to provide a stratigraphic and tectonic framework; further detailed descriptions of these deposits and the history of volcanic and tectonic development are provided by Murray et al. (2013).

Three informal formations are recognized in the Guazapares Mining District region (Figs. 1 and 2), consisting of: (1) silicic outflow ignimbrites of the Parajes formation, (2) mafic to andesitic volcanic rocks and intrusions of the Témoris formation; and (3) vent-related silicic ignimbrites, lavas, and plugs of the Sierra Guazapares formation. These rocks record Late Oligocene to Early Miocene (Upper Volcanic Supergroup) synextensional deposition and magmatism during the mid-Cenozoic ignimbrite flare-up (Murray et al., 2013). Older regional geologic maps (e.g., Minjárez Sosa et al., 2002; Ramírez Tello and Garcia Peralta, 2004) and recent mining company reports (e.g., Roy et al., 2008; Wood and Durgin, 2009; Gustin, 2011, 2012) in the Guazapares Mining District have widely referred to the andesitic rocks that underlie ridge-capping silicic volcanic rocks as "Lower Volcanic Complex", but our new mapping and geochronology over a broader region (Figs. 2 and 3) shows that those andesitic rocks (Témoris formation) are sandwiched between silicic volcanic rocks below and above (Parajes and Sierra Guazapares formations, respectively). Thus, the andesitic rocks in the Guazapares Mining District are not Eocene rocks; instead, they record local development of a ca. 27–24.5 Ma andesitic center in the Upper Volcanic Supergroup, under an extensional strain regime (Murray et al., 2013), as summarized in the following.

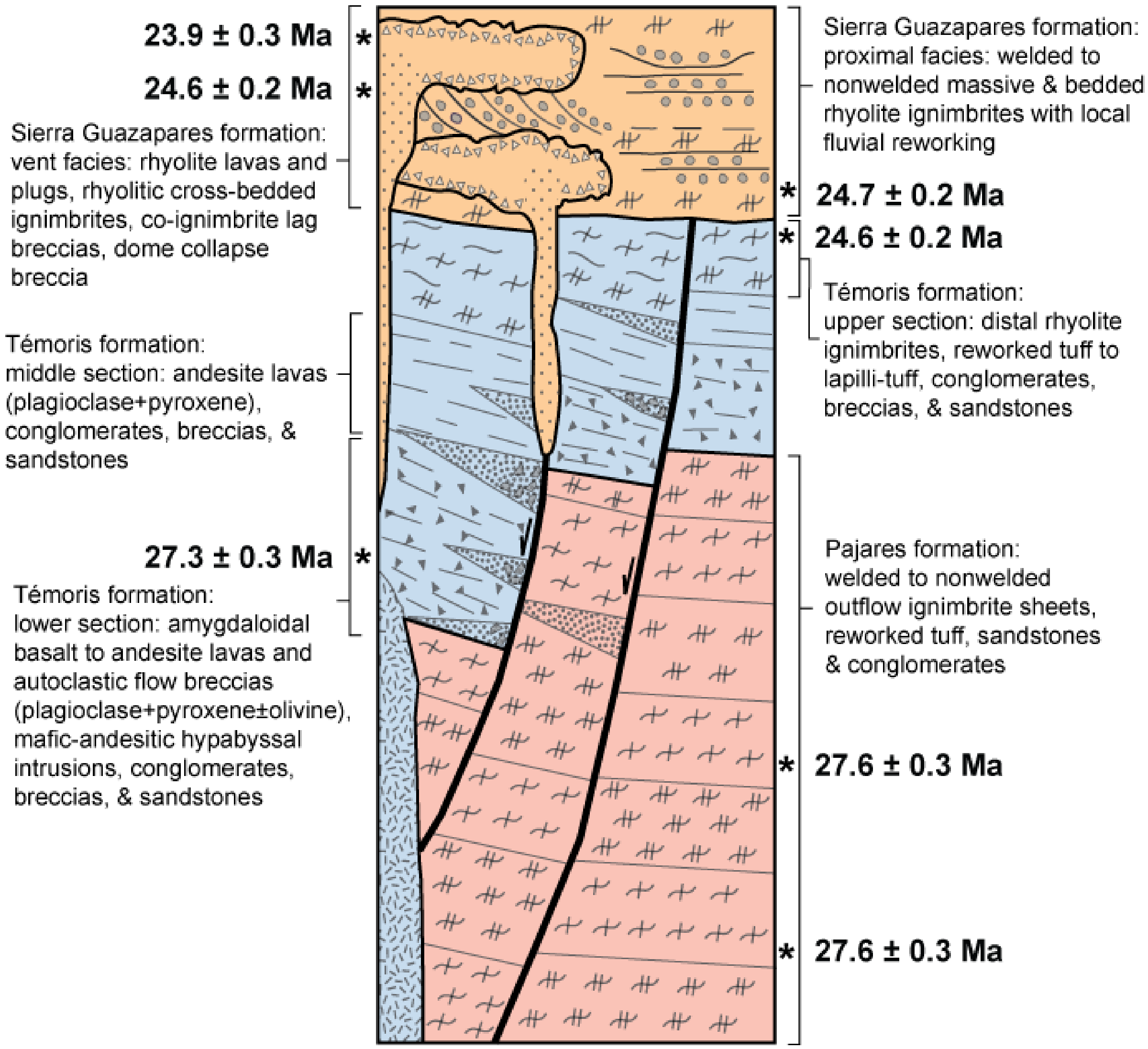

Figure 2. Generalized stratigraphic column of the Guazapares Mining District region, depicting the characteristics and depositional relationships between the Parajes formation, Témoris formation, and the Sierra Guazapares formation (after Murray et al., 2013). Age data are from zircon U-Pb laser ablation ICP-MS geochronology by Murray et al. (2013).

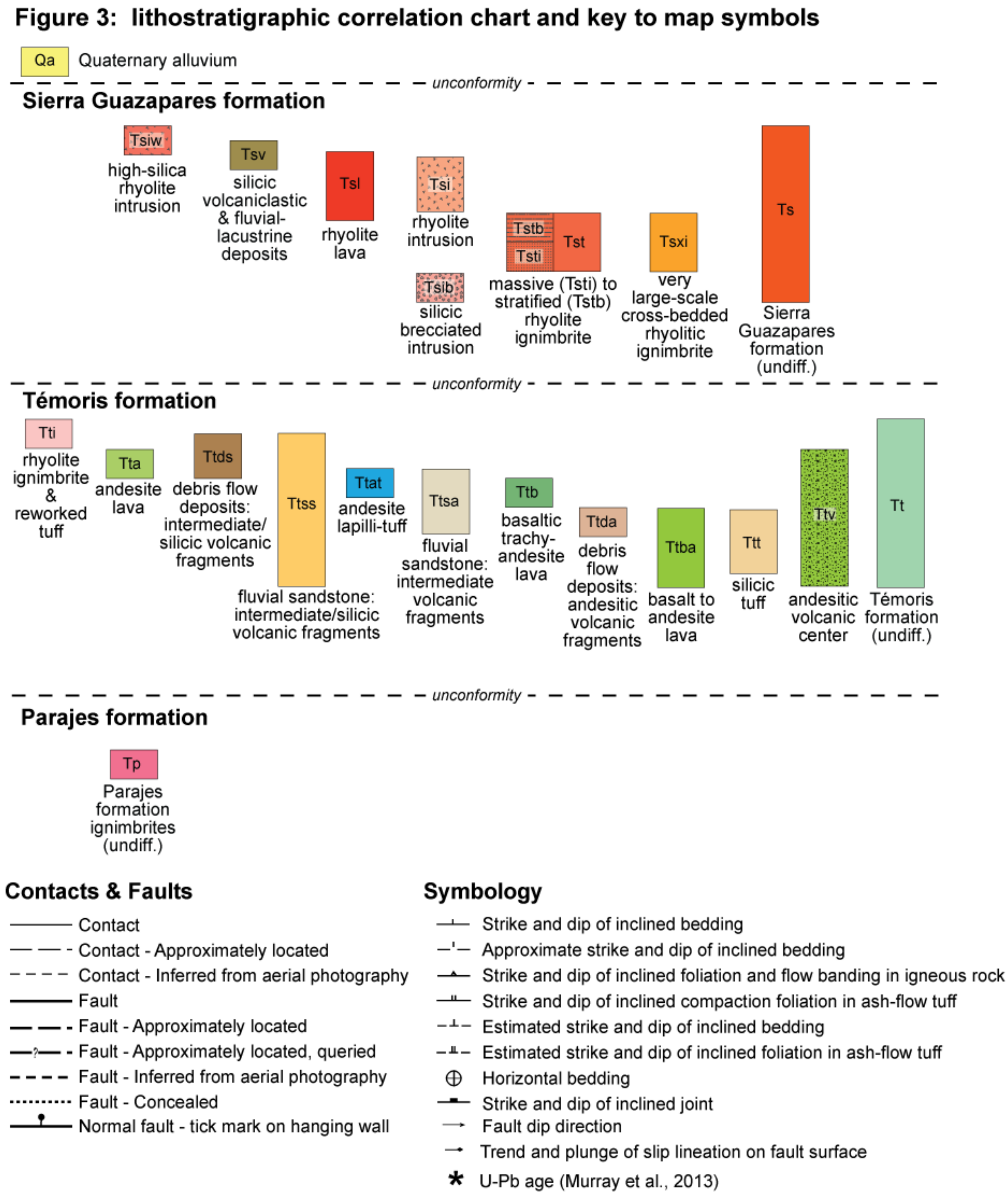

Figure 3 (*this and next 2 pages*). Geologic map of the Guazapares Fault Zone between Monte Cristo and ~2 km north of Témoris, with lithostratigraphic correlation chart for the map units of the Guazapares Mining District and key to map symbols (after Murray et al., 2013). See Table 1 of Chapter 1 for lithologic descriptions of the map units. Red boxes indicate the locations of Figures 4 and 6. Resource areas discussed herein are (from north to south): Monte Cristo, San Antonio, and La Union. Age data are from zircon U-Pb laser ablation ICP-MS geochronology by Murray et al. (2013).

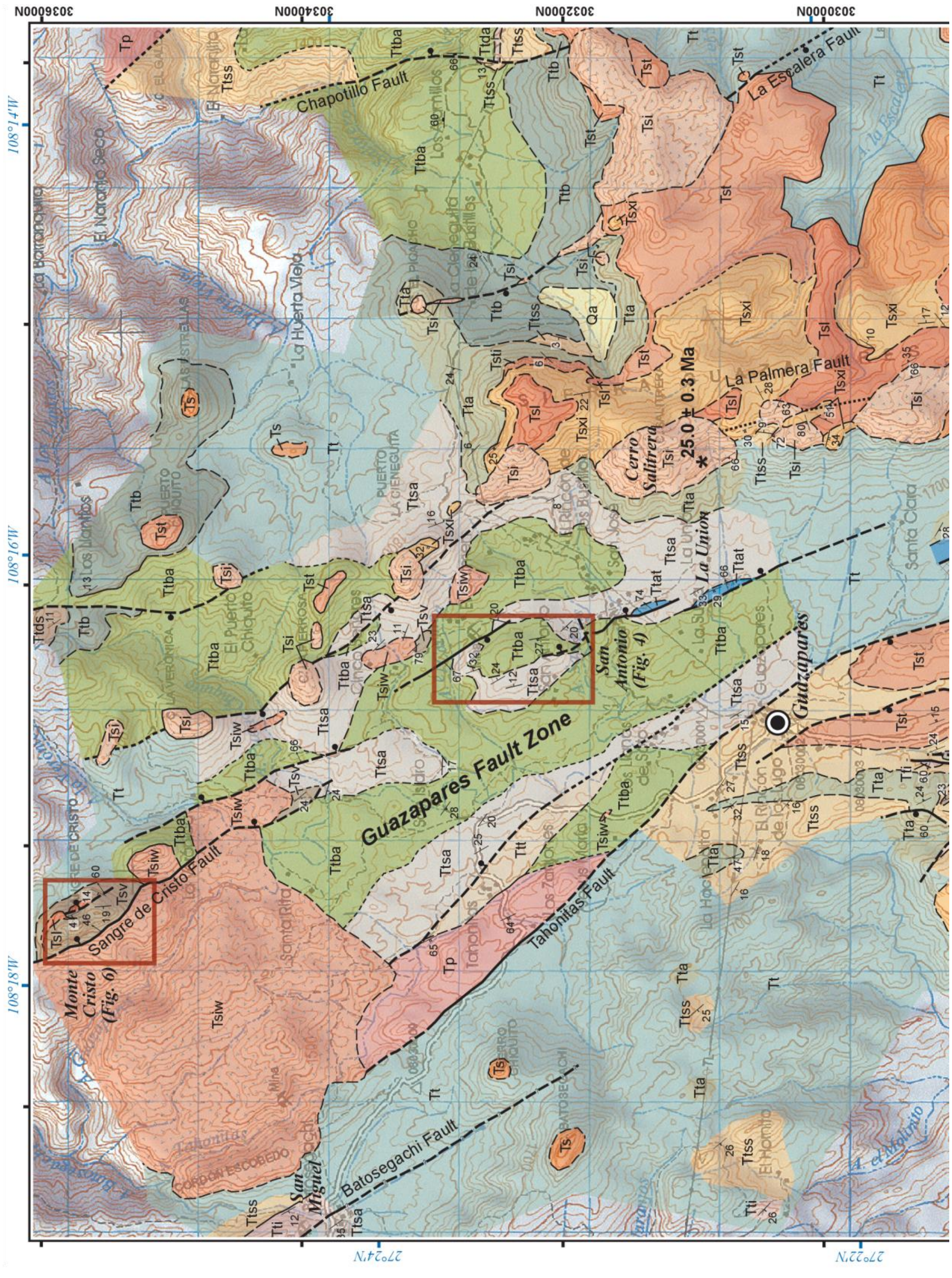

3036000N
3034000N
3032000N
3030000N
108°14'W
108°16'W
108°18'W
27°24'N
27°22'N
Chapotillo Fault
La Escalera Fault
La Palmera Fault
25.0 ± 0.3 Ma
Cerro Salitrera
La Union
San Antonio (Fig. 4)
Guazapares Fault Zone
Guazapares
Sangre de Cristo Fault
Monte Cristo (Fig. 6)
Tahonitas Fault
Batosegachi Fault
San Miguel

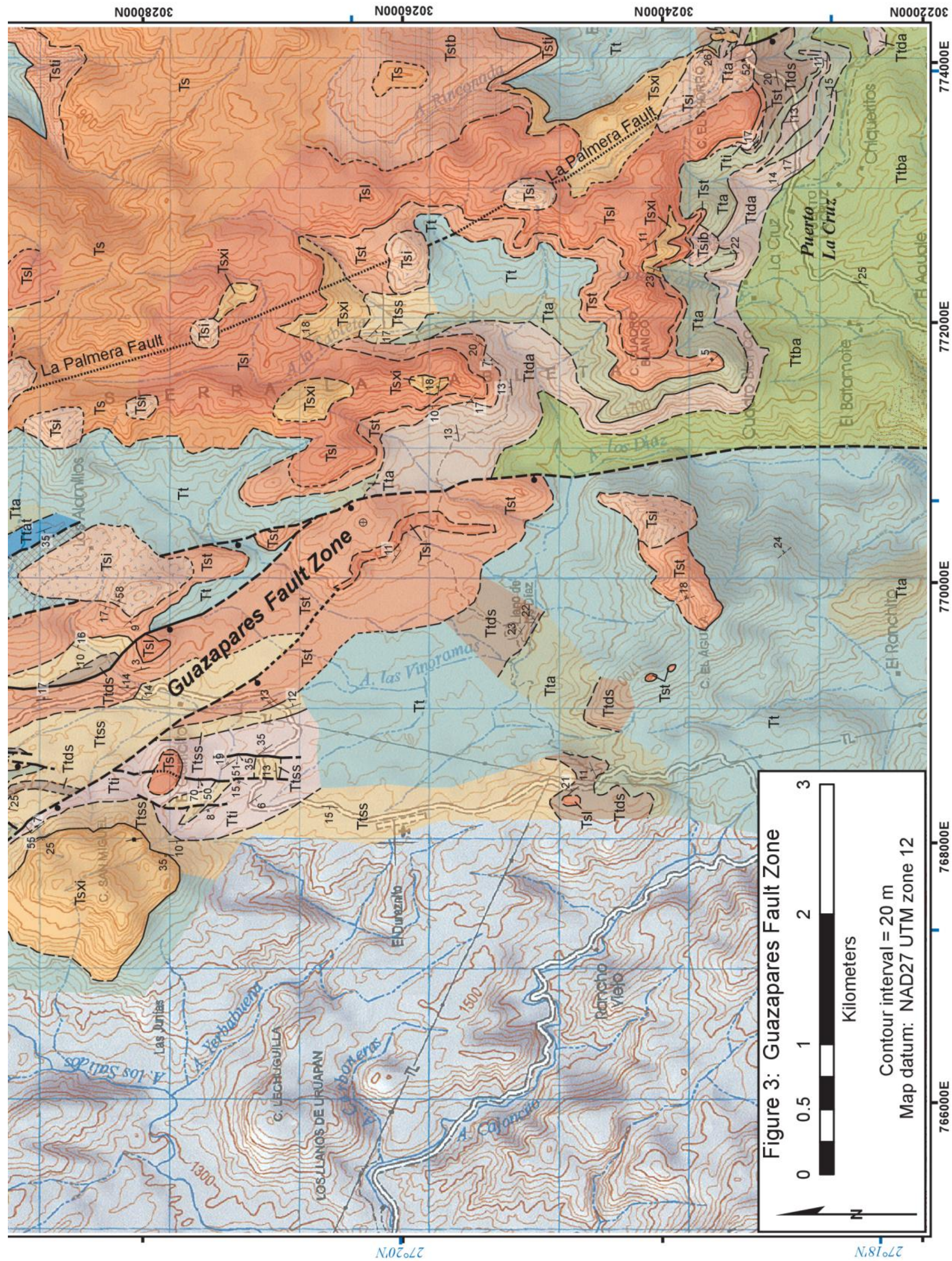

Figure 3: Guazapares Fault Zone

The Parajes formation is composed of seven lithologically distinct welded to nonwelded silicic outflow ignimbrite sheets, with lesser locally interbedded sandstone, conglomerate, and reworked tuff derived from erosion of these ignimbrites. These rocks mainly outcrop to the northeast of Témoris (Fig. 1), where they clearly underlie the Témoris formation and lie within extensional basins (Murray et al., 2013). The silicic outflow ignimbrite sheets were erupted ca. 27.5 Ma (Fig. 2), during the end of the Early Oligocene pulse of the mid-Cenozoic ignimbrite flare-up. The source of these ignimbrites is likely calderas of similar age that lie mainly 50-100 km to the east of the study area (Murray et al., 2013).

The Témoris formation records local mafic to intermediate composition magmatism and distal silicic ignimbrite volcanism, as well as sedimentation in graben-filling alluvial fan systems, between ca. 27 and 24.5 Ma (Fig. 2). The Témoris formation is subdivided into three sections with gradational contacts (Fig. 2), composed of: (1) a lower section of amygdaloidal basalt, basaltic andesite, and andesite lavas and autoclastic flow breccias, with locally interbedded silicic tuff in the lowermost deposits; (2) a middle section of flow-banded andesite lavas; and (3) an upper section of distal thin nonwelded rhyolite ignimbrites and tuffaceous volcaniclastic deposits (reworked and epiclastic) (Murray et al., 2013). Volcaniclastic debris flow breccias and fluvial conglomerates and sandstones are interbedded with all of the volcanic rocks listed above; these deposits contain detritus similar in composition to the interstratified volcanic rocks, suggesting resedimentation of primary eruptive products. The lavas and associated subvolcanic intrusions of the lower and middle sections of the Témoris formation were derived primarily from an andesitic center sited in the area around Témoris (Fig. 3), as well as from fault-controlled dikes that likely fed flows outside this main center. The distal ignimbrites and sedimentary rocks of the upper section of the Témoris formation record a local eruptive hiatus between mafic-andesitic magmatism of the Témoris Formation and silicic magmatism of the Sierra Guazapares formation.

The Sierra Guazapares formation records the local emplacement of silicic volcanic and hypabyssal rocks from fault-controlled fissure vents across a region that includes the Guazapares Mining District, between ca. 24.5 and 23 Ma (Fig. 2), at the onset of the Early Miocene pulse of the mid-Cenozoic ignimbrite flare-up. Vent to proximal volcanic rocks of this formation crop out in an 11-km long and 3 km-wide linear belt along the La Palmera Fault–Guazapares Fault Zone (Fig. 3). These include rhyolitic ignimbrites with lithic lag breccias and very large-scale cross bedding that laterally transition away from this linear belt into massive to stratified ignimbrites. Rhyolite plugs, some of which pass continuously upward into rhyolite lavas that overlie the ignimbrites, also outcrop in this linear belt, as well as along other faults within the study area (Figs. 1 and 3).

The main geologic structures in the Guazapares Mining District region are NNW-trending normal faults, including the Guazapares Fault Zone and faults to the northeast of Témoris (Figs. 1 and 3). Several normal faults located northeast of Témoris (Fig. 1) bound half-graben basins and have significant displacement, with ~100 to >450 m vertical offset and at least 20% total horizontal extension (Murray et al., 2013). Evidence of syndepositional extension, including growth strata and angular unconformities between each formation, indicates that these half-graben basins began to form by the time the upper part of the Parajes formation was erupted (ca. 27.5 Ma) and continued to develop during deposition of the Témoris and Sierra Guazapares formations. Several of these preexisting extensional structures controlled the localization of andesitic and silicic volcanic vents and shallow level intrusions of the Témoris and Sierra Guazapares formations (Murray et al., 2013).

Mineralization in the Guazapares Mining District

Rocks of the Témoris formation host the majority of mineralization in the Guazapares Mining District and have experienced minor to intense alteration, including propylitic, argillic, hematitic, and silicic. The highest degrees of alteration in the Guazapares Mining District are concentrated in Témoris formation rocks along NW-trending structures associated with the Guazapares Fault Zone (described below). In general, these rocks have experienced multi-phase, low- to intermediate-sulfidation, epithermal mineralization characterized by silver-gold with variably low amounts of lead and zinc (<0.4%, Roy et al., 2008) occurring within quartz veins, quartz-vein breccias, silicified hydrothermal breccias, and quartz-carbonate-pyrite veinlet stockworks, similar to alteration found in other districts within the Sierra Madre Occidental gold-silver belt (Gustin, 2012). The Parajes formation that underlies the Témoris formation is also mineralized, although alteration is restricted to fine fractures as opposed to fissure veins (Gustin, 2012). The Sierra Guazapares formation is generally unaltered in comparison to the underlying formations (Gustin, 2012; Murray et al., 2013); however, altered rocks in the Monte Cristo resource area, described in detail below, belong to the linear belt of Sierra Guazapares formation silicic vent facies rocks and intrusions along the La Palmera Fault–Guazapares Fault Zone.

The epithermal mineral deposits in the Guazapares Mining District have been extracted since the 17th century, with major mining operations active from 1860–1900 and 1959–1968 (Roy et al., 2008). These early operations produced silver (up to 300 g/ton) and minor gold from the highest grade, near-surface oxidized portions of the mineralized structures of the Guazapares Fault Zone, while later operations used shafts to access subsurface deposits (up to 156 g/ton silver, 144 g/ton gold) (Roy et al., 2008). Within the last 15 years, the rising price of gold and silver has renewed interest in exploiting the resources of the Guazapares Mining District, and new exploration of the area has been conducted via drilling, trenching, and geologic mapping (Roy et al., 2008; Wood and Durgin, 2009; Gustin, 2011, 2012).

Guazapares Fault Zone

The Guazapares Fault Zone extends from Témoris northward to the Monte Cristo resource area immediately west of a prominent ridge composed of Sierra Guazapares formation rocks (Figs. 1 and 3); the northern and southern termini of the fault zone are not known but it appears to continue beyond the map area, as do the silicic intrusions associated with the mineralized zones along it, which is important for future prospecting. The Guazapares Fault Zone is a ~3 to 5 km-wide system of NNW-striking normal faults with numerous splays that dip both east and west, with several changes of fault dip polarity along strike. The strikes of the faults in the Guazapares Fault Zone appear to bend slightly west near their northern mapped extent close to the Monte Cristo resource area, where the width of the fault zone increases (Fig. 3). The faults in the Guazapares Fault Zone host the majority of mineralization within the mining district, and several resource areas, including the San Antonio, Monte Cristo, and La Union areas (all three discussed below), are located along a series of faults on the eastern side of the fault zone (Fig. 3) referred to as the "main Guazapares structure" by Roy et al. (2008).

Several zones of mineralization are located west of the main Guazapares structure of the Guazapares Fault Zone (Fig. 3). The San Miguel resource area is located along the NW-striking, SW-dipping Batosegachi Fault, which has been interpreted as a right-lateral strike-slip fault with a normal-slip component (D. Sims, pers. commun.). We identified the NW-striking Tahonitas Fault, located between the Batosegachi Fault and main Guazapares structure (Fig. 3). A few resource areas are located along the Tahonitas Fault (although none yet developed enough to be labeled on Fig. 3); however, it appears to be a major structure within the mining district, with a ~50 m-wide zone of argillic and propylitic alteration and quartz veining that is located on the western edge of a fault-bounded outcrop of Parajes formation ignimbrite (Tp; Fig. 3). The Tahonitas Fault forms a lithologic boundary within the mining district, with the rhyolite ignimbrite-dominated upper section of the Témoris formation located to the southwest of the southern section of the fault and the mafic-to-andesitic-dominated lower and middle sections of the Témoris formation located to the northeast of the structure (Fig. 3).

RESOURCE AREAS OF THE GUAZAPARES FAULT ZONE

This study presents and interprets new detailed geologic maps and cross-sections of the San Antonio and Monte Cristo resource areas (Figs. 4, 5, 6, 7, and 8) located along main mineralized structure of the Guazapares Fault Zone (Fig. 3); it also briefly describes the discusses the La Union resource area, located along the same structure. These interpretations are based on detailed geologic mapping, used to describe the stratigraphy and structural geology of each resource area.

San Antonio Resource Area

The San Antonio resource area (Fig. 4) lies along the Guazapares Fault Zone approximately 2 km NNE of the pueblo of Guazapares (Fig. 3). Previous mining company reports have identified an approximately 350 m-wide by 1 km-long mineralized zone within the center of the San Antonio resource area, with subvertical NW-trending mineralized structures that are steeply west-dipping in the north and steeply east-dipping in the south (Roy et al., 2008; Gustin, 2012). Based on our study, we interpret this resource area to be the

Figure 4 (*next page*). Geologic map and cross-sections of the San Antonio resource area of the Guazapares Fault Zone (Fig. 3). The red striped area indicates the region of intense epithermal mineralization with subvertical NW-trending vuggy and banded quartz/chalcedony-amethyst veinlet stockworks and rare discrete quartz veins in the accommodation zone between two normal faults with opposing dip directions. Cross-sections A–A' and B–B' of the San Antonio resource area based on surficial geologic mapping, showing the change in normal fault and bedding dip orientations between the northern and southern portions of the resource area. Base map from (Roy et al., 2008). Descriptions of the lithologic units are given in Table 1.

Figure 4: San Antonio resource area

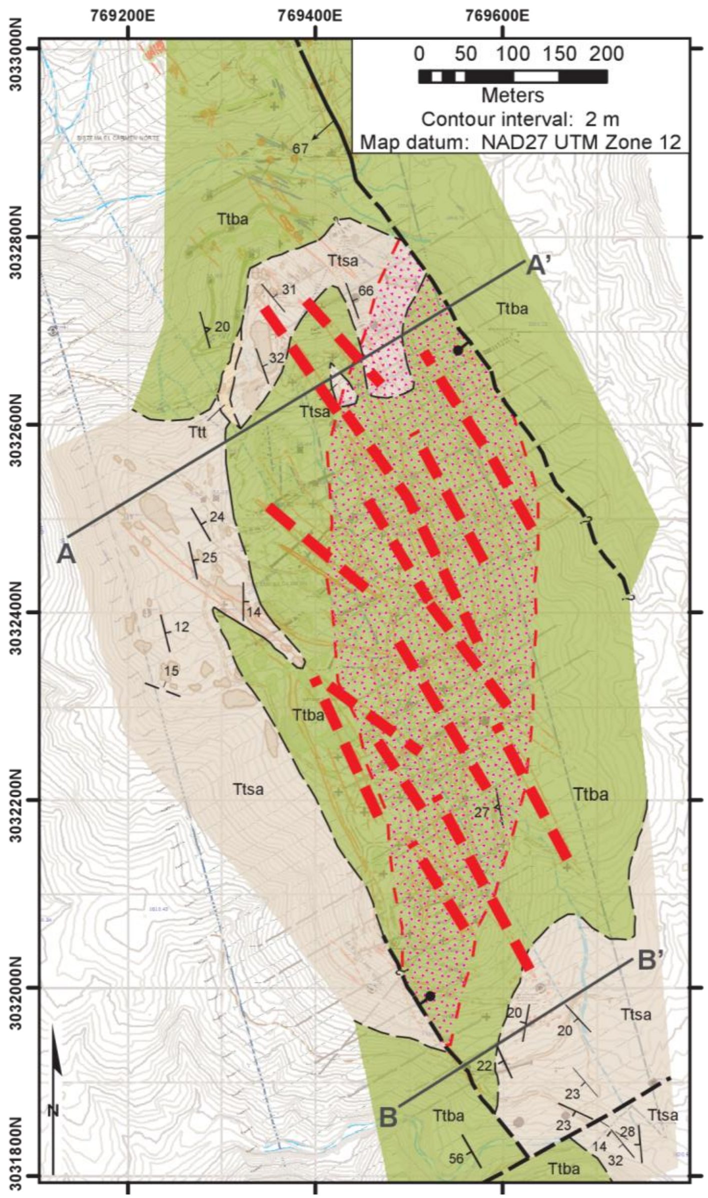

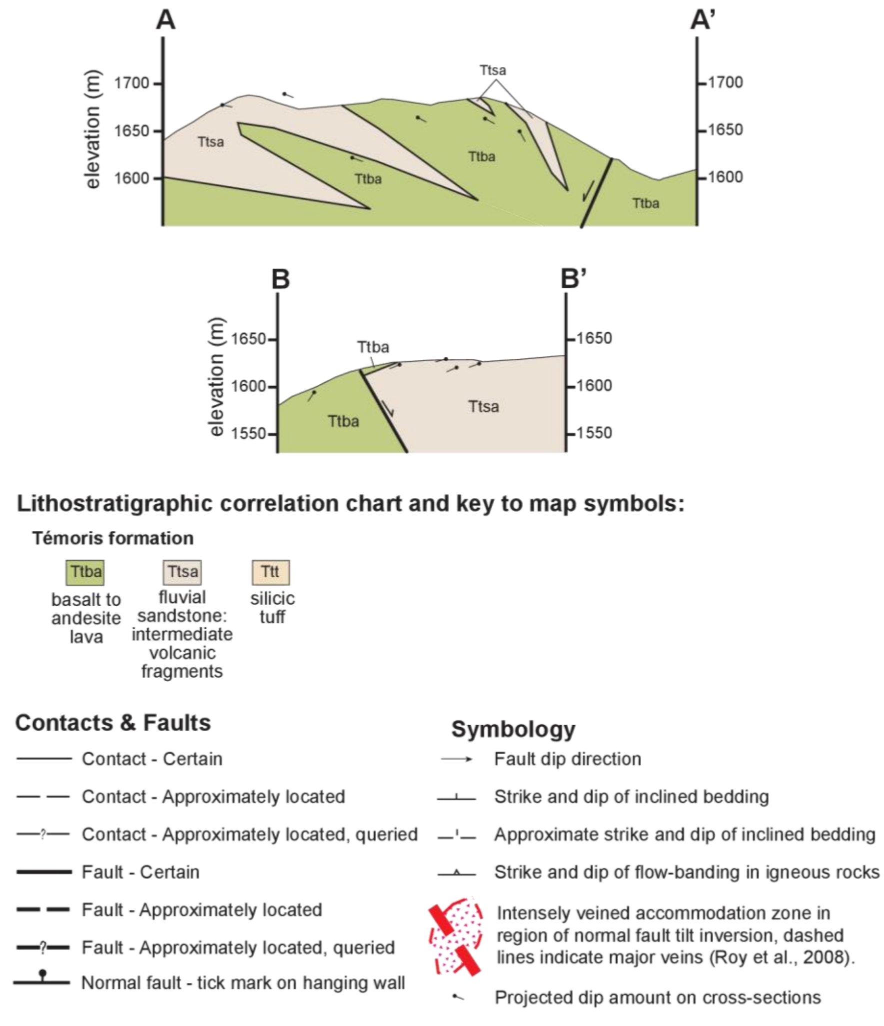

location of an accommodation zone between two opposite dipping normal faults that hosts mineralization (Fig. 5).

The rocks exposed at the San Antonio resource area are part of the lower section of the Témoris formation, consisting of mafic to intermediate composition lavas and autoclastic flow breccias (Ttba) interstratified with lithic-rich sandstone with mafic to intermediate volcanic rock fragments (Ttsa) and lesser silicic lapilli-tuff (Ttt) (Table 1). The lavas laterally interfinger with the sandstones and infill channels, and sandstones occur as lenses within the lava and locally have trough cross-bedding and gravel lenses. The presence of these sedimentary structures and the channelization of deposits suggest deposition in a fluvial environment (Fig. 5A).

The main geologic structures in the San Antonio resource area are two NW-trending normal faults with opposing dip directions: a W-dipping fault in the northern section of the area and an E-dipping fault in the southern section, separated laterally by ~400 m (Fig. 4). The volcanic and sandstone deposits of the Témoris formation are tilted toward each of these normal faults, resulting in opposite bedding dip directions in the northern and southern sections of the resource area (Fig. 4). We interpret the area between these two normal faults, where the dip orientation of the faults and bedding changes, as an antithetic accommodation zone dominated by extensional deformation with negligible right-lateral strike-slip motion (e.g., Faulds and Varga, 1998).

The majority of mineralization in the San Antonio resource area is concentrated in the antithetic accommodation zone in the center of the area, between the two main normal faults (Figs. 4 and 5). The volcanic rocks are weakly altered to unaltered in the northern and southern sections of the area and are strongly silicified towards the center of the area (Fig. 4), with mineralization dominated by silver (~10% gold) and occurring as subvertical NW-

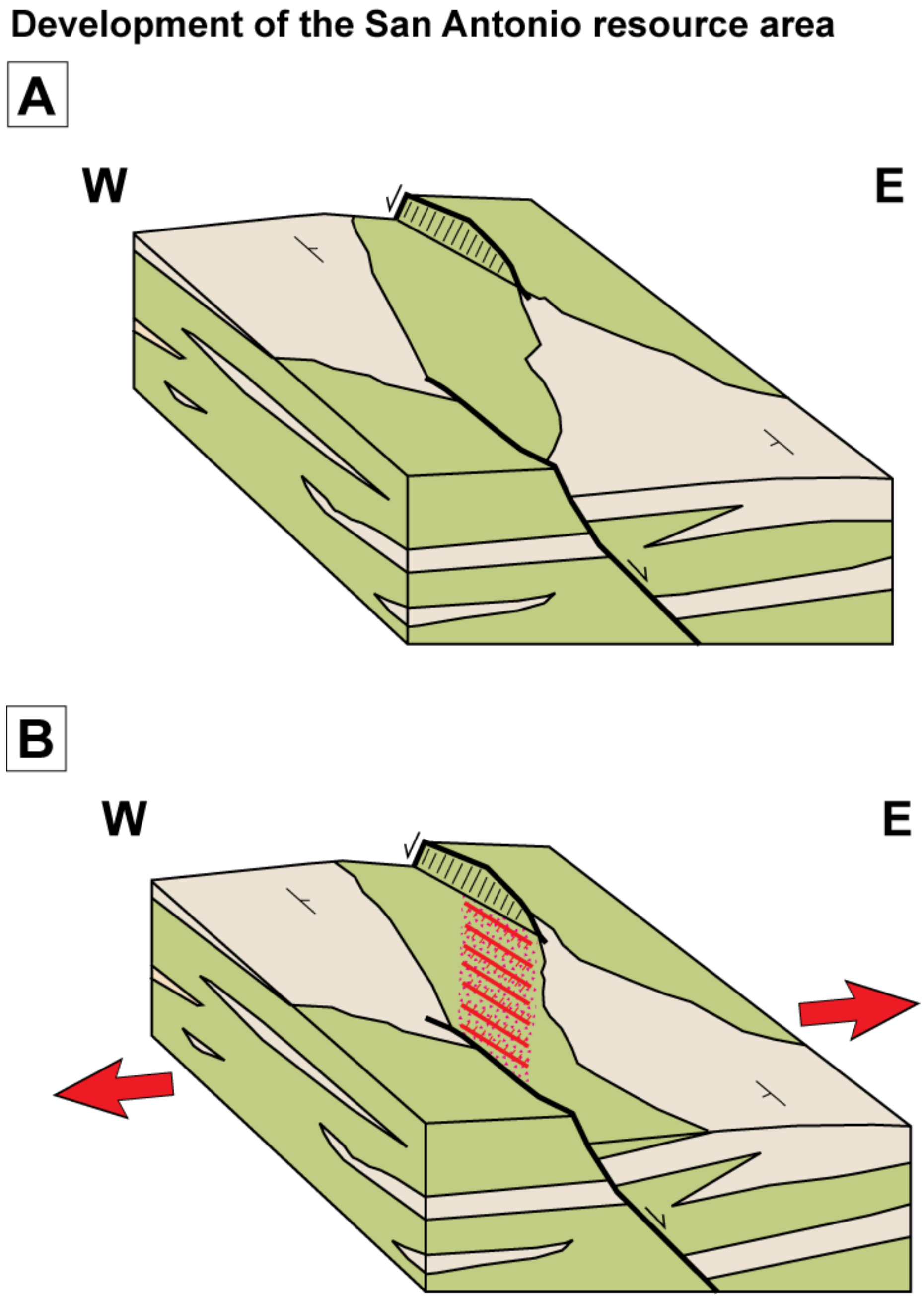

Figure 5. Schematic block diagrams illustrating the evolution of the San Antonio resource area. Colors correspond to the geologic map units in Figure 4. (A) Lava, sandstone, and lesser silicic tuff of the Témoris formation were deposited in a fluvial environment and offset across two normal faults (a W-dipping fault in the north and E-dipping fault in the south). (B) Continued NE-SW-directed extension resulted in the formation of subvertical NW-trending dilational structures (red lines, hash marks indicated dip direction) in the antithetic accommodation zone between the two normal faults. This accommodation zone corresponds with a zone of intense silicic alteration (red triangles) within the resource area.

Table 1: Lithologic units of the San Antonio & Monte Cristo resource areas (next 2 pages)		
Map Unit*	**Lithology**	**Description**
Tai	andesitic intrusions	Hypabyssal intrusion. Dark gray with local red hematitic & green propylitic alteration; aphanitic groundmass with 5-10% phenocrysts: plagioclase, clinopyroxene.
Tsvb	bedded silicic lapilli-tuff	Silicic lapilli-tuff. Light red to gray; nonwelded; <5% phenocrysts: plagioclase, biotite; up to 20% lithic fragments (intermediate volcanic). Fluvial reworking with bedding structures (planar lamination, cut-and-fill structures), bedding up to 2 m thick. Local white reworked tuff layers.
Tsl	rhyolite lava/intrusion	Lava flow & hypabyssal intrusion. White to light gray, with light pink flow banding; 5% phenocrysts: plagioclase, biotite, trace hornblende. Irregular top surface of flow.
Tsvf	fluvial sandstone: silicic volcanic fragments	Feldspathic litharenite. White to light gray; moderately to poorly sorted, subangular, medium-to-coarse-grained. Clast consist of silicic lithic fragments and feldspar. Massive with faint laminations, also contains cut-and-fill and trough cross-bedding structures. Minor clast-supported breccia with subangular cobble-boulder silicic lapilli-tuff fragments. Interpreted as hyperconcentrated debris flows of reworked silicic volcanic material.
Tsvm	massive silicic lapilli-tuff	Silicic lapilli-tuff. Light red to gray; nonwelded; <5% phenocrysts: plagioclase, biotite; trace lithic fragments (intermediate volcanic). Slight fluvial reworking with crude bedding up to 5 m thick. Local red very fine-grained, thinly bedded sandstone.
Tsvfb; Tsvfl	rhyolitic fault talus breccia	Fault talus breccia. White to light orange; primarily monolithic rhyolite breccia, block-supported, angular blocks (>2 m), lesser flow-banded blocks. Blocks are aphyric, with trace quartz and plagioclase phenocrysts, in an ash-lapilli groundmass of same composition. Contains local zones of up to 20% intermediate blocks. Block breccia (Tsvfb) transitions laterally into lapilli breccia (Tsvfl) of same composition. The block fragment size decreases northeastward away from the Sangre de Cristo Fault, from >2 m blocks to lapilli-sized fragments supported in an ash matrix. Fragments are similar in appearance to high-silica rhyolite intrusion (Tsiw).
Tsiw	high-silica rhyolite intrusion	Hypabyssal intrusion (dome/plug). White to light pink; aphyric to 10% phenocrysts (up to 1 mm): plagioclase, biotite, trace quartz. Subvertical flow banding. Intruded into gray andesitic feldspar porphyry (likely part of Témoris formation). Similar in appearance to rhyolitic fault talus breccia (Tsvd).
Tsvl	lacustrine sandstone & mudstone	Mudstone and sandstone. Tan to white. Sandstone: Feldspathic litharenite; fine-to-medium-grained sandstone with graded bedding (Bouma Sequence A, B) and small scale basal scouring. Mudstone: planar laminated to very thinly bedded, contains thin tuff layers. Soft sediment slumping and folding.

Ttba	basalt to andesite lava	Predominantly amygdaloidal lava flows. Gray to dark gray with local red hematitic & green propylitic alteration; 5-25% phenocrysts: plagioclase (some flow-alignment of laths), clinopyroxene; zeolite amygdules. Average lava flow thickness ~5 m, lavas are typically brecciated and vesicular with secondary zeolite infilling vesicles and autoclastic flow breccia interstices fragments, with lesser flow-banded and nonvesicular lavas with flow-top and bottom autoclastic breccias.
Ttsa	fluvial sandstone: intermediate volcanic fragments	Feldspathic litharenite. Dark tan to reddish purple; moderately to poorly sorted, subrounded to subangular, medium-to-coarse-grained with trace granules. Clasts consist of feldspar and intermediate volcanic lithic fragments. Contains lenses of clast-supported pebble conglomerates and matrix-supported pebble to cobble breccia with intermediate volcanic fragments. Thinly to thickly bedded.
Ttt	silicic tuff	Nonwelded to partially welded tuff. White to light tan groundmass; trace-10% phenocrysts (<1 mm): plagioclase, biotite, ± hornblende, ± quartz; trace to 25% lapilli-sized lithic fragments (red intermediate volcanic).
* Figures 4 and 6		

trending vuggy and banded quartz/chalcedony-amethyst veinlet stockworks and rare discrete quartz veins (Gustin, 2012). The location of the antithetic accommodation zone corresponds with this zone of silicification, suggesting that subvertical dilational structures formed in the area between the two normal faults during continued extension (Fig. 5B); these influenced the localization of mineralization by opening up NW-trending cracks that provided conduits for mineralizing fluids. As discussed below, mineralization probably occurred during or following the emplacement of silicic intrusions of the Sierra Guazapares formation.

Monte Cristo Resource Area

The Monte Cristo resource area (Fig. 6) lies along the northern mapped portion of the Guazapares Fault Zone, approximately 5.5 km NNW of Guazapares (Fig. 3). The main geologic structure in the resource area is the Sangre de Cristo Fault, a NNW-striking, E-dipping normal fault that juxtaposes highly-altered hypabyssal intrusions in the footwall with much less altered volcaniclastic fill on the hanging wall (Figs. 6 and 7A). Zircon U-Pb laser ablation ICP-MS geochronology by Murray et al. (2013) and our new geologic mapping here shows that the rocks in the Monte Cristo resource area record deposition of the Sierra Guazapares formation (ca. 23 Ma) in a synvolcanic half-graben that formed within an actively growing rhyolite dome-hypabyssal intrusive complex (Figs. 7 and 8).

The footwall of the Sangre de Cristo Fault consists of subvolcanic intrusions of white high-silica rhyolite (Murray et al., 2013), which are aphyric and subvertically flow-banded (Tsiw; Fig. 7B; Table 1). These hypabyssal rocks intrude gray andesitic feldspar porphyry of the Témoris formation and are offset by the Sangre de Cristo Fault, indicating emplacement prior to the most recent motion along this fault. The white high-silica rhyolite intrusions in the footwall of the Sangre de Cristo Fault hosts most of the multi-phase gold-silver-bearing mineralization in the Monte Cristo resource area (Gustin, 2012), with subvertical quartz veins

Figure 6 (*next page*). Geologic map and cross-section of the Monte Cristo resource area, with volcanic and volcaniclastic sedimentary rocks located on the hanging wall of the east-dipping Sangre de Cristo Fault and a rhyolite intrusion in the footwall. Cross-section A–A' of the Monte Cristo resource area based on surficial geologic mapping, showing the distribution and depositional relationships of the synvolcanic half-graben deposits. Reddish-pink triangles denote the region of heavy quartz mineralization of the footwall and within ~10 m of the Sangre de Cristo Fault. Descriptions of the lithologic units are given in Table 1.

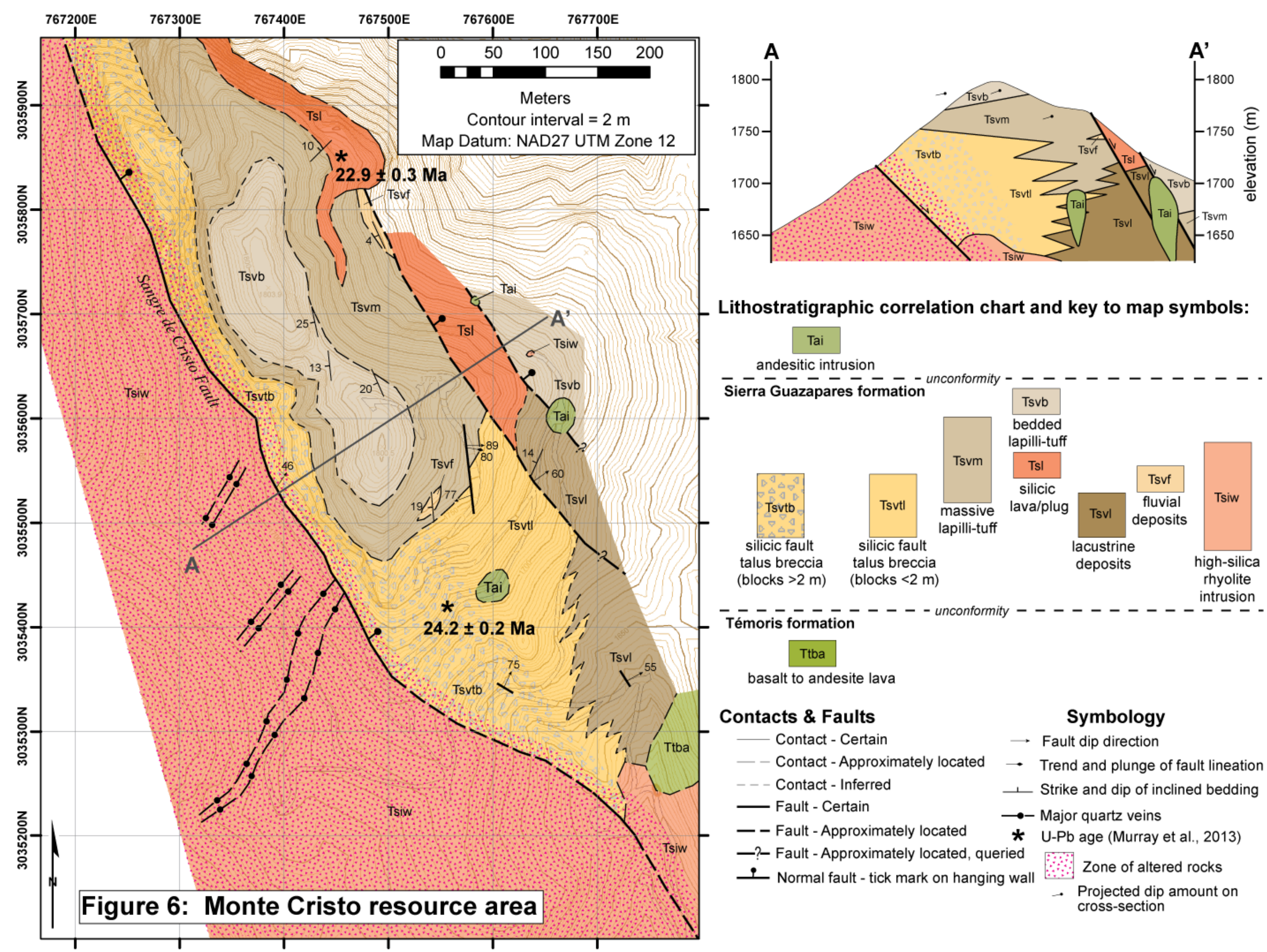

Figure 6: Monte Cristo resource area

Figure 7 (*next page*). Photographs from the Monte Cristo resource area; locations of photos given (NAD27 UTM zone 12). All map units referred to here are shown on Figure 6. (A) The Sangre de Cristo Fault in the northwestern section of the resource area, with white aphyric high-silica rhyolite intrusion (Tsiw) in the footwall (right) and tan hematized fault talus breccia composed of rhyolitic blocks (Tsvtb) in the hanging wall (left). Photograph taken at 767366E 3035552N. (B) White aphyric high-silica rhyolite intrusion (Tsiw) from the roots of the rhyolite dome-hypabyssal intrusion complex in the footwall of the Sangre de Cristo Fault. Subvertical flow-banding visible on left side of photograph. Hammer (33 cm-tall) for scale. Photograph taken at 767764E 3035213N. (C) White rhyolitic fault talus breccia (Tsvtl) on the hanging wall of the Sangre de Cristo Fault, showing primarily monomictic composition similar in appearance to the footwall rhyolite intrusions, with a small percentage of dark-colored andesitic blocks. Groundmass is composed of the same material as the rhyolitic blocks. Head of hammer is ~12.5 cm. Photograph taken at 767632E 3035526N. (D) Turbiditic fine-to-medium-grained sandstone exhibiting graded bedding with Bouma sequence A and B (arrow) in lacustrine sedimentary unit (Tsvl) in the basal half-graben fill on the hanging wall of the Sangre de Cristo Fault. Laminated mudstone and water-laid tuff layers underlie the turbiditic sandstone. Hammer head (~17.5 cm-length) for scale. Photo taken at 767640E 3035559N. (E) Soft sediment folding (arrow, above ~30 cm-length notebook) in mudstone in the basal lacustrine half-graben fill (Tsvl), on the hanging wall of the Sangre de Cristo Fault. Photo taken at 767641E 3035551N. (F) Bedded lapilli-tuff unit (Tsvb) in the half-graben fill on the hanging wall of the Sangre de Cristo Fault. A cut-and-fill structure (yellow dashed line) truncates white tuffaceous sandstone (wss) below, and is filled with coarse sandstone (tss). Photograph taken at 767486E 3035634N.

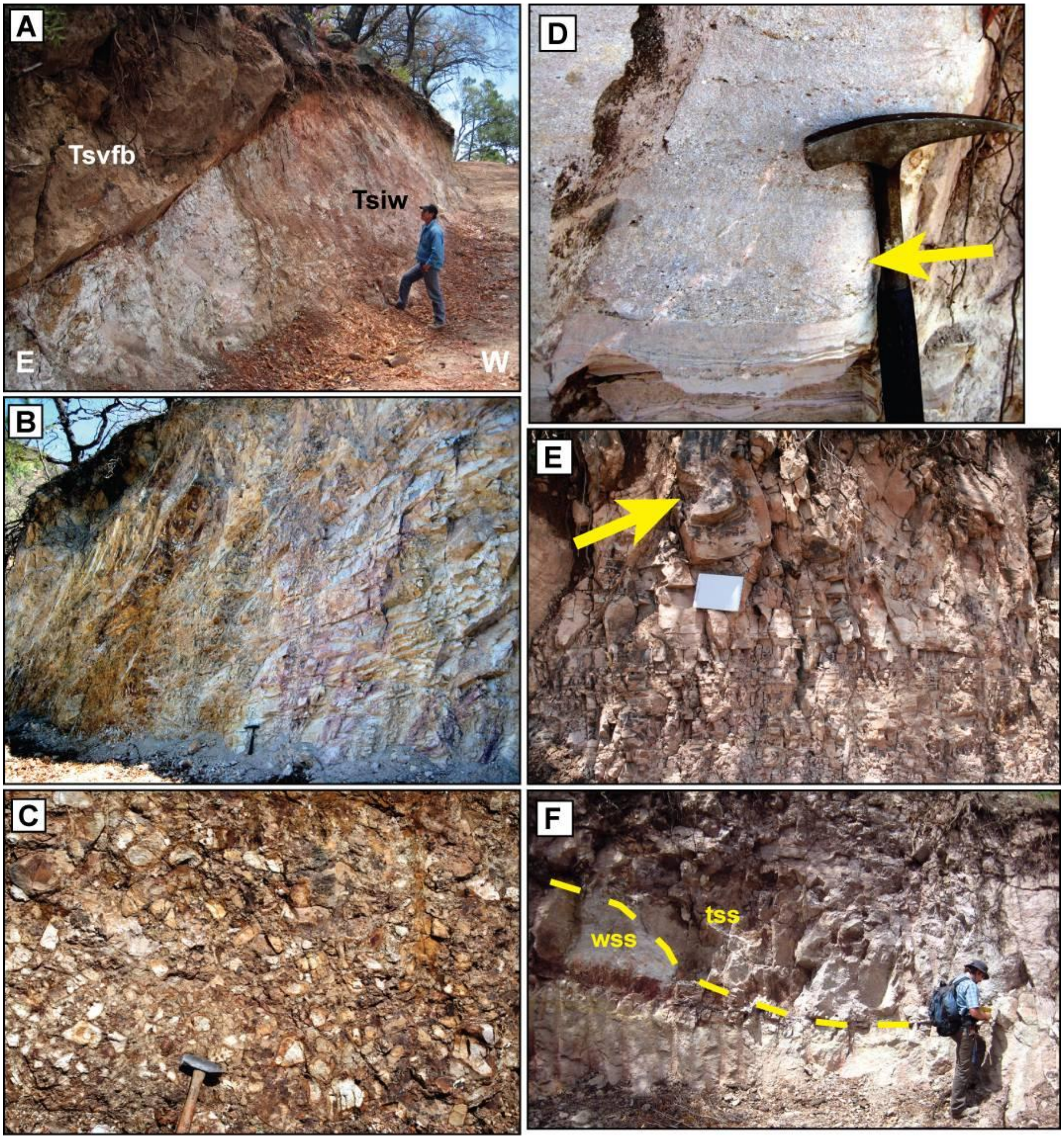
A
Tsvfb
Tsiw
E
W
B
C
D
E
F
tss
wss

striking both northwest and northeast. The northeast vein orientation appears to be unique to the Monte Cristo resource area, since mostly NW-striking veins are found in the other resource areas within the Guazapares Mining District. Three major quartz veins that cut the white rhyolite intrusions in the footwall block are sited along small-offset NE-striking faults that terminate at the Sangre de Cristo Fault (Fig. 6), suggesting that the age of quartz mineralization of these veins predates the most recent motion on the Sangre de Cristo Fault. Siliceous sinter mineralization in the hanging wall is limited to rocks within ~10 m of the Sangre de Cristo Fault, which may have served as a conduit for to silica-rich mineralizing fluids migrating up the basin margin (Gustin, 2012).

We infer that the white high-silica rhyolite hypabyssal intrusions represent high-level subvolcanic magma chambers that had several feeder plugs above them that were the source of an overlying small lava dome field (Fig. 8). Continued extensional deformation on the Sangre de Cristo Fault led to uplift and erosion of the dome field and feeder plugs, resulting in unroofing the high-level subvolcanic magma chambers and deposition of the erosional material into the adjacent half-graben basin.

Sangre de Cristo Fault Half-Graben Basin Development

The dominant unit in the hanging wall of the Sangre de Cristo Fault is a massive rhyolitic breccia (Tsvtb, Tsvtl; Table 1) located adjacent to the fault (Fig. 6). Although mining company reports have described this as a hydrothermal breccia, we interpret the massive rhyolitic breccia as a fault talus breccia of rocks derived directly from a concurrently growing rhyolite dome-hypabyssal intrusion complex that was located on the footwall of the Sangre de Cristo Fault (Fig. 8B) because it lacks quartz veining and secondary silicification in the groundmass (except within 10 m of the Sangre de Cristo Fault) that is typical of hydrothermal breccias. The massive rhyolitic breccia is very similar in appearance to the

Figure 8 (*next page*). Interpretive cross-section diagrams (not to scale) showing the phases of basin development and inferred timing of magmatism and mineralization within the Monte Cristo resource area. Active faulting is denoted with arrows. (A) Initial motion along the Sangre de Cristo Fault created a small half-graben basin, in which lacustrine sediments (Tsvl) were deposited. (B) Continued basin subsidence led to growth of fault talus deposits adjacent to Sangre de Cristo Fault (Tsvtb, Tsvtl) that interfingering with and prograded over the lacustrine deposits. Emplacement of the white rhyolite intrusion (Tsiw) located on the footwall of the Sangre de Cristo Fault is likely related to the eruption of a rhyolite dome complex, which was the source of the fault talus breccia shed into the adjacent half-graben basin. (C) Growth of the rhyolite dome-hypabyssal intrusion complex on the footwall led to continued deposition of fault talus breccias in the Sangre de Cristo half-graben (Tsvtb, Tsvtl), which transition northeastward into block-and-ash flow deposits and lesser reworked tuff of the massive silicic lapilli-tuff unit (Tsvm). Younger rhyolite intrusions mineralized the older intrusions in the footwall and the half-graben fill adjacent to the bounding fault. (D) Syndepositional normal faulting within the hanging wall block developed concurrently with deposition of the massive lapilli-tuff unit. (E) Emplacement of a silicic plug and coulée (Tsl) along the normal fault within the hanging wall block during deposition of the massive lapilli-tuff unit. (F) Deposition of the bedded lapilli-tuff unit (Tsvb) records fluvial deposition of detritus shed from the lava dome complex during waning volcanism, or during migration of lava dome volcanism away from the basin. (G) Postdepositional normal faulting on the Sangre de Cristo Fault, and smaller faults within the hanging wall, tilted the strata, offset the white rhyolite intrusion and silicic plug/coulée, and down-dropped the bedded lapilli-tuff unit to the east.

Development of the Sangre de Cristo half-graben basin

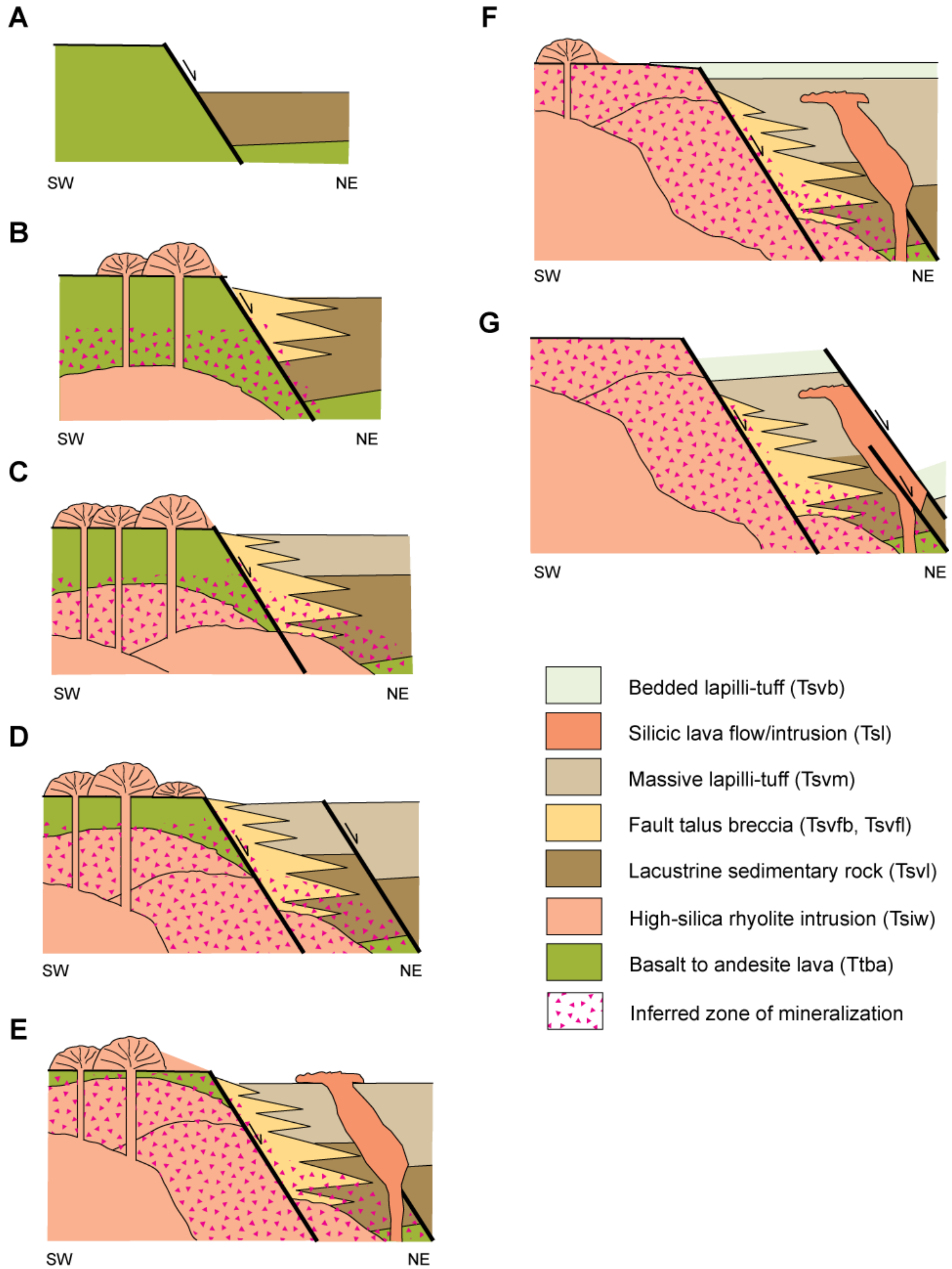

white high-silica rhyolite intrusions in the footwall of the Sangre de Cristo Fault; it is white, angular, predominantly block-supported, and monomictic, composed of aphyric to weakly porphyritic rhyolite, with minor flow-banded blocks, and an ash matrix of the same composition (Fig. 7C). Locally, the breccia contains up to 20% andesitic blocks. The block fragment size decreases rapidly away from the Sangre de Cristo Fault, from >2 m blocks adjacent to the fault to lapilli-sized fragments ~200 m from the fault towards the northeast. These observations are consistent with the interpretation that this unit represents fault talus deposits, with rhyolitic and lesser andesitic material avalanched off of a rhyolite dome complex located on the footwall of the Sangre de Cristo Fault into the adjacent half-graben basin to the east (Fig. 8B). The age of a rhyolite block within this fault talus breccia has been dated at 24.2 ± 0.2 Ma by U-Pb zircon LA-ICP-MS (Murray et al., 2013), showing it was derived from part of the Sierra Guazapares Formation, which is dominated by vent facies silicic volcanic rocks.

The rhyolitic fault talus breccias overlie, and the basal deposits interfinger with, sedimentary rocks that we infer are lacustrine (Figs. 8A-B). The lacustrine sedimentary rocks outcrop on the eastern side of the Monte Cristo resource area (Fig. 6), and consist of mudstone, normal-graded sandstones, and well-laminated subaqueous fallout tuff (Tsvl; Table 1; Fig. 7D). The light gray turbiditic fine-to-medium-grained sandstones exhibit Bouma sequence A and B (Fig. 7D), and grade upward into planar finely laminated to very thinly bedded mudstone and tuffs. The presence of lacustrine sedimentary rocks at the base of the section suggests that extension and half-graben formation likely preceded or was coeval with the onset of silicic magmatism at this locality. Soft-sediment deformation structures are present (Fig. 7E), suggesting that these lacustrine deposits were deformed by subsequent fault motion and/or volcanic activity.

The rhyolitic fault talus breccias pass gradationally upward and outward (Figs. 6 and 8C) into a predominantly massive monomict silicic lapilli-tuff unit (Tsvm; Table 1). This lithologic unit is primarily gray to very light red lapilli-tuff with angular rhyolite clasts similar to those in the breccia. We interpret the massive lapilli-tuff unit to represent block-and-ash-flow deposits, perhaps shed from a lava dome that was slightly more distal from the basin. Locally interbedded with the massive silicic lapilli-tuff unit are light gray, massive, moderately to poorly sorted, medium-to-coarse-grained sandstones and conglomerates (Tsvf; Table 1), which are also dominated by crystal-poor rhyolite, but have a higher degree of sorting and more rounding of grains. These sandstones and conglomerates also have cut-and-fill structures and trough cross-bedding indicating fluvial deposition. The sandstones could represent material reworked from unconsolidated primary volcanic deposits, or they could record erosion of the lava domes, but their monomict character indicates a very restricted source area (i.e., the rhyolite dome field).

Interstratified with the massive silicic lapilli-tuff unit (Tsvm) in the northern part of the Monte Cristo resource area is a white to gray silicic lava (Tsl; Table 1) that maps continuously into a feeder dike (Figs. 6 and 8E). This silicic lava differs in appearance from the aphyric rhyolitic hypabyssal intrusions in footwall block and the blocks of the fault talus breccia and lapilli tuffs; in comparison, this unit is crystal-poor, with ~5% plagioclase and biotite and trace hornblende. The extrusive lava part of this unit is thick and stubby, which is interpreted as a coulée (e.g., Fink and Anderson, 2000). The top surface of the coulée is slightly irregular with planar thinly bedded very fine-to-fine-grained sandstone and tuff layers filling in the depressions between it and the overlying massive lapilli-tuff unit. This age of this lava flow is 22.9 ± 0.3 Ma by U-Pb zircon LA-ICP-MS (Murray et al., 2013). The feeder dike of this coulée follows a normal fault that offsets the massive silicic lapilli-tuff unit

(Figs. 6 and 8D-E); this supports our interpretation that extension and rhyolite intrusive activity were coeval since this dike follows a pre-existing normal fault (Fig. 8E) and is cut by an additional fault (Fig. 8G).

The massive silicic lapilli-tuff unit (Tsvm) passes gradationally upward into a bedded silicic lapilli-tuff unit (Fig. 8F), composed of well-stratified silicic lapilli-tuff, tuff and sandstone (Tsvb: Table 1). The clasts are dominantly composed of the same crystal-poor rhyolite present in the massive silicic lapilli-tuff (Tsvm) and the fault talus breccia (Tsvtb, Tsvtl) units, but is finer grained, better sorted, subangular to subrounded, and has abundant sedimentary structures typical of fluvial deposition, such as cut-and-fill structures and planar-lamination (Fig. 7F). We interpret this unit to record fluvial deposition of detritus eroded from the lava dome complex during waning volcanism, or during migration of lava dome volcanism away from this part of the basin (Fig. 8F). The bedded lapilli tuff is offset by a second intrabasinal normal fault (Fig. 8G). Some footwall uplift must have occurred after emplacement of the bedded lapilli tuff unit, as the youngest exposed units are tilted; however, we infer that most of the displacement on the Sangre de Cristo Fault occurred during formation of the half-graben, emplacement of the dome-hypabyssal intrusion complex, and mineralization (Fig. 8).

La Union Resource Area

Like the San Antonio and Sangre de Cristo resource areas, the La Union resource area is located on the eastern edge of the Guazapares Fault Zone, close (<1 km) to the Sierra Guazapares formation plugs exposed along the La Palmera Fault to the east (Fig. 3). We did not map this area in detail, as there were no detailed topographic maps constructed for it like there were at the other two resource areas, nor does it contain numerous road cuts to expose its rocks to view (rocks within the Guazapares Fault Zone generally have less exposure and are more vegetated than the surrounding ridges).

The rocks exposed at the La Union resource area are similar to those of the San Antonio resource area to the north, consisting of Témoris formation mafic to intermediate composition lava and flow breccia (Ttba), andesitic volcanic lithic-rich sandstone (Ttsa), andesitic lapilli-tuff (Ttat), and lesser silicic tuffs (Fig. 3). Mineralization in the La Union resource area consists of locally intense multi-phase brecciation and silicification grading laterally into quartz-veinlet stockwork zones (Gustin, 2012). The main structures that host the mineralization are two NNW-trending, E-dipping normal faults, offset laterally by ~100 m (Fig. 3); smaller mineralized structures are located at this offset, which is likely a synthetic accommodation zone (e.g., Faulds and Varga, 1998) between these two faults.

Located less than 1 km to the east of the La Union resource area is Cerro Salitrera, one of the largest silicic intrusions (~0.6 km^2) of the Sierra Guazapares formation intruded along the La Palmera Fault (Fig. 3). We suggest that mineralization in the La Union resource area is likely related to the close proximity of the Cerro Salitrera plug. As reported in an unpublished mining company report (Gustin, 2012), the inferred gold concentration in the La Union resource area is one of the highest in the Guazapares Mining District (~35 g Au/ton), with much lower gold concentrations reported at the resource areas that are further away from this intrusion (i.e., ~10 g Au/ton at the San Antonio resource area); however, this report does not recognize the Cerro Salitrera plug, nor does it relate the mineralization to proximity to the intrusion.

DISCUSSION

This study hypothesizes that mineralization in the Guazapares Mining District was possibly related to Late Oligocene to Miocene silicic magmatism in the Sierra Madre Occidental at ca. 24.5–23 Ma (Sierra Guazapares formation). The epithermal deposits in the study area are likely related to the emplacement of Sierra Guazapares formation rhyolite hypabyssal intrusions less than 2 Myr after deposition of the Témoris formation, with normal faults and accommodation zones providing conduits for intrusion-related hydrothermal fluids and a location for precious metal mineralization. The geology of three resource areas along the Guazapares Fault Zone presented in this study supports the interpretation that rhyolite hypabyssal intrusions are related to mineralization along preexisting extensional structures. In the Monte Cristo resource area, deposition in the hanging wall of a synvolcanic half-graben was concurrent with the development of a rhyolite lava dome-hypabyssal intrusion complex in the footwall. Postvolcanic extensional deformation unroofed the top of a subvolcanic rhyolite magma chamber that is now exposed at the surface in the footwall of the Sangre de Cristo Fault. Mineralization emanates upward from the high-silica rhyolite intrusions and is concentrated in the footwall and along the Sangre de Cristo Fault and adjacent hanging wall graben fill. There are no silicic intrusions at the surface within the San Antonio and La Union resource areas, however, they crop out ~0.5–1 km to the east, where they intruded along the La Palmera Fault. In comparison to the Monte Cristo resource area, these hypabyssal intrusions are exposed at the shallower feeder plug level, suggesting that at least some of the plugs probably unite downward into a larger magma body and that the San Antonio and La Union resource areas are likely closer to silicic intrusions than surface mapping indicates. Drill core data from Paramount Gold & Silver supports this interpretation, indicating that subsurface silicic intrusions are located at ~120 m-depth beneath the San Antonio resource area and at ~40–90 m-depth beneath the La Union resource area (Roy et al., 2008).

Similar associations between silicic magmatism, mineralization, and extensional structures has been recognized in other mining districts within the Sierra Madre Occidental, notably in the districts of the Cuenca de Oro basin located ~60 km southeast of the Guazapares Mining District, and the San Martín de Bolaños and Guanajuato districts in the southern region of the Sierra Madre Occidental (Fig. 1). The Cuenca de Oro basin is includes the El Sauzal, Batopilas, and Piedras Verdes mining districts (Sellepack, 1997; Feinstein, 2007). Epithermal mineralization within these mining districts is generally hosted along north-to-northeast-trending fractures and faults in intermediate igneous rocks that are related to extension in the region (Wilkerson et al., 1988; Goodell, 1995; Sellepack, 1997; Galvan-Gutierrez, 2005; Feinstein, 2007). The highest degree of epithermal mineralization in the Batopilas Mining District is concentrated around the Laramide-age Tahonas granodiorite, which is interpreted as the hydrothermal heat source in the district during and slightly following emplacement of the intrusion (Wilkerson et al., 1988). Further south in the Sierra Madre Occidental in the San Martín de Bolaños Mining District, epithermal mineralization that is hosted primarily in Early Miocene andesitic volcanic rocks occurred between 23.7 to 21.3 Ma; the source of mineralizing fluids is interpreted to be related to a rhyolitic intrusion emplaced in the western escarpment of the Bolaños graben (Scheubel et al., 1988). The timing of mineralization and emplacement of the rhyolitic intrusion in the San Martín de Bolaños Mining District generally corresponds to the Early Miocene pulse of ignimbrite flare-up volcanism that occurred throughout the Sierra Madre Occidental (e.g., Ferrari et al., 2007). However, unlike in the Guazapares Mining District, the mineralized structures this district appear to be unrelated to major extension of the Bolaños graben, which occurred later between 22–18 Ma (Scheubel et al., 1988; Ferrari et al., 2007). The Guanajuato Mining District in the southeastern region of the Sierra Madre Occidental has a mineralization history more similar to the Guazapares Mining District. Epithermal mineralization in this district is hosted in NW to NE-trending regional extensional fault systems; the timing of this mineralization is closely associated to magmatic and hydrothermal activity related to the mid-Oligocene emplacement of rhyolite domes near the intersection of these pre-existing regional fault systems (Randall R. et al., 1994).

Our study suggests a direct relationship between silicic intrusion emplacement, epithermal mineralization, and crustal extension in the Guazapares Mining District of the Sierra Madre Occidental. Although further research is needed, based on this study and previous studies within the Sierra Madre Occidental, there appears to be at least limited validity to the inferred relationship between epithermal mineralization and major magmatic events in the Sierra Madre Occidental (e.g., Camprubí et al., 2003). Although pre-existing extensional structures are not necessary for the formation of epithermal veins, their presence appears to favor the emplacement of silicic intrusions and provides additional conduits for the circulation and precipitation of mineralized hydrothermal fluids related to these intrusions.

REFERENCES CITED

Aguirre-Díaz, G. J., and Labarthe-Hernández, G., 2003, Fissure ignimbrites: Fissure-source origin for voluminous ignimbrites of the Sierra Madre Occidental and its relationship with Basin and Range faulting: Geology, v. 31, no. 9, p. 773–776.

Aguirre-Díaz, G. J., and McDowell, F. W., 1991, The volcanic section at Nazas, Durango, Mexico, and the possibility of widespread Eocene volcanism within the Sierra Madre Occidental: Journal of Geophysical Research, v. 96, no. B8, p. 13373-13388.

Aguirre-Díaz, G. J., and McDowell, F. W., 1993, Nature and timing of faulting and synextensional magmatism in the southern Basin and Range, central-eastern Durango, Mexico: Geological Society of America Bulletin, v. 105, p. 1435-1444.

Albinson, T., Norman, D. I., Cole, D., and Chomiak, B. A., 2001, Controls on formation of low-sulfidation epithermal deposits in Mexico: Constraints from fluid inclusion and stable isotope data: Society of Economic Geologists Special Publications, v. 8, p. 1-32.

Armstrong, R. L., and Ward, P. L., 1991, Evolving geographic patterns of Cenozoic magmatism in the North American Cordillera: the temporal and spatial association of magmatism and metamorphic core complexes: Journal of Geophysical Research, v. 96, no. B8, p. 13,201-13,224.

Best, M. G., Christiansen, E. H., and Gromme, S., 2013, Introduction: The 36-18 Ma southern Great Basin, USA, ignimbrite province and flareup: Swarms of subduction-related supervolcanoes: Geosphere, v. 9, p. 260-274.

Bryan, S., 2007, Silicic large igneous provinces: Episodes, v. 30, no. 1, p. 1-12.

Bryan, S. E., and Ferrari, L., 2013, Large igneous provinces and silicic large igneous provinces: Progress in our understanding over the last 25 yr: Geological Society of America Bulletin, v. 125, no. 7/8, p. 1053-1078.

Bryan, S. E., Orozco-Esquivel, T., Ferrari, L., and López-Martínez, M., 2013, Pulling apart the mid to late Cenozoic magmatic record of the Gulf of California: Is there a Comondú arc?, *in* Gomez-Tuena, A., Straub, S. M., and Zellmer, G. F., eds., Orogenic Andesites and Crustal Growth, Geological Society of London Special Publication 385 (*in press*).

Cameron, K. L., Nimz, G. J., Niemeyer, S., and Gunn, S., 1989, Southern Cordilleran basaltic andesite suite, southern Chihuahua, Mexico: a link between Tertiary continental arc and flood basalt magmatism in North America: Journal of Geophysical Research, v. 94, no. B6, p. 7817-7840.

Camprubí, A., Ferrari, L., Cosca, M. A., Cardellach, E., and Canals, À., 2003, Ages of epithermal deposits in Mexico: Regional significance and links with the evolution of Tertiary volcanism: Economic Geology, v. 98, p. 1029-1037.

Cather, S. M., Dunbar, N. W., McDowell, F. W., McIntosh, W. C., and Scholle, P. A., 2009, Climate forcing by iron fertilization from repeated ignimbrite eruptions: The icehouse-silicic large igneous province (SLIP) hypothesis: Geosphere, v. 5, no. 3, p. 315-324.

Cochemé, J. J., and Demant, A., 1991, Geology of the Yécora area, northern Sierra Madre Occidental, Mexico, *in* Pérez-Segura, E., and Jacques-Ayala, C., eds., Studies in Sonoran Geology: Geological Society of America Special Paper 254, p. 81-94.

Coney, P. J., 1978, Mesozoic-Cenozoic Cordilleran plate tectonics, *in* Smith, R. B., and Eaton, G. P., eds., Cenozoic tectonics and regional geophysics of the Western Cordillera: Geological Society of America Memoir 152: Boulder, CO, Geological Society of America, p. 33-50.

Coney, P. J., and Reynolds, S. J., 1977, Cordilleran Benioff zones: Nature, v. 270, p. 403-406.

Damon, P. E., Shafiqullah, M., and Clark, K. F., 1981, Age trends of igneous activity in relation to metallogenesis in the southern Cordillera: Arizona Geological Society Digest, v. 14, p. 137-154.

Dickinson, W. R., and Snyder, W. S., 1979, Geometry of subducted slabs related to the San Andreas transform: Journal of Geology, v. 87, p. 609-627.

Dreier, J., 1984, Regional tectonic control of epithermal veins in the Western United States and Mexico, *in* Wilkins, J., ed., Gold and silver deposits of the Basin and Range Province, Western U.S.A., Arizona Geological Society Digest, v. 15, p. 28-50.

Faulds, J. E., and Varga, R. J., 1998, The role of accommodation zones and transfer zones in the regional segmentation of extended terranes, *in* Faulds, J. E., and Stewart, J. H., eds., Accommodation Zones and Transfer Zones: The regional segmentation of the Basin and Range Province: Boulder, CO, Geological Society of America Special Paper 323, p. 1-45.

Feinstein, M. N., 2007, Contributions to the geology of the Cuenca de Oro: Chihuahua, Mexico [M.S. thesis]: University of Texas, El Paso, 168 p.

Ferrari, L., López-Martinez, M., Aguirre-Díaz, G., and Carrasco-Núñez, G., 1999, Space-time patterns of Cenozoic arc volcanism in central Mexico: From the Sierra Madre Occidental to the Mexican Volcanic Belt: Geology, v. 27, p. 303-306.

Ferrari, L., López-Martínez, M., Orozco-Esquivel, T., Bryan, S. E., Duque-Trujillo, J., Lonsdale, P., and Solari, L., 2013, Late Oligocene to Middle Miocene rifting and synextensional magmatism in the southwestern Sierra Madre Occidental, Mexico: The beginning of the Gulf of California rift: Geosphere, v. 9, no. 5, p. 1161-1200.

Ferrari, L., López-Martínez, M., and Rosas-Elguera, J., 2002, Ignimbrite flare-up and deformation in the southern Sierra Madre Occidental, western Mexico: Implications for the late subduction history of the Farallon plate: Tectonics, v. 21, no. 4, p. 1-24.

Ferrari, L., Valencia-Moreno, M., and Bryan, S., 2007, Magmatism and tectonics of the Sierra Madre Occidental and its relation with the evolution of the western margin of North America, *in* Alaniz-Álvarez, S. A., and Nieto-Samaniego, Á. F., eds., Geology of México: Celebrating the Centenary of the Geological Society of México: Geological Society of America Special Paper 422, p. 1-39.

Fink, J. H., and Anderson, S. W., 2000, Lava domes and coulees, *in* Sigurdsson, H., Houghton, B. F., McNutt, S. R., Rymer, H., and Stix, J., eds., Encyclopedia of Volcanoes: San Diego, CA, Academic Press, p. 307-319.

Fisher, R. V., and Schmincke, H. U., 1984, Pyroclastic Rocks: Berlin, Springer Verlag, 472 p.

Fisher, R. V., and Smith, G. A., 1991, Sedimentation in volcanic settings: SEPM (Society for Sedimentary Geology) Special Publication No. 45: Tulsa, OK, SEPM (Society for Sedimentary Geology), 257 p.

Galvan-Gutierrez, V. H., 2005, Regional and local patterns of mineralization in the Lower Batopilas and Urique rivers in Sierra Madre of Chihuahua, Mexico [M.S. thesis]: University of Texas, El Paso, 115 p.

Gans, P. B., 1997, Large-magnitude Oligo-Miocene extension in southern Sonora: Implications for the tectonic evolution of northwest Mexico: Tectonics, v. 16, p. 388-408.

Gans, P. B., Blair, K. D., MacMillan, I., Wong, M. S., and Roldán-Quintana, J., 2003, Structural and magmatic evolution of the Sonoran rifted margin: A preliminary report: Geological Society of America Abstracts with Programs, v. 35, no. 4, p. 21.

González León, C. M., McIntosh, W. C., Lozano-Santacruz, R., Valencia-Moreno, M., Amaya-Martínez, R., and Rodríguez-Castañeda, J. L., 2000, Cretaceous and Tertiary sedimentary, magmatic, and tectonic evolution of north-central Sonora (Arizpe and Bacanuchi Quadrangles), northwest Mexico: Geological Society of America Bulletin, v. 112, no. 4, p. 600-610.

Goodell, P. C., 1995, Porphyry copper deposits along the Batopilas lineament,Chihuahua, Mexico, *in* Pierce, F. W., and Bolm, J. G., eds., Porphyry copper deposits of the American Cordillera: Arizona Geological Society Digest, v. 20, p. 544.

Grijalva-Noriega, F. J., and Roldán-Quintana, J., 1998, An overview of the Cenozoic tectonic and magmatic evolution of Sonora, northwestern Mexico: Revista Mexicana de Ciencias, v. 15, no. 2, p. 145-156.

Gustin, M. M., 2011, Technical report on the San Miguel project, Guazapares Mining District, Chihuahua, Mexico, prepared for Paramount Gold and Silver Corp.: Reno, NV, Mine Development Associates, 149 p.

Gustin, M. M., 2012, Updated technical report on the San Miguel project gold and silver resources, Guazapares Mining District, Chihuahua, Mexico, prepared for Paramount Gold and Silver Corp.: Reno, NV, Mine Development Associates, 176 p.

Henry, C., and Aranda-Gómez, J. J., 2000, Plate interactions control middle-late Miocene, proto-Gulf and Basin and Range extension in the southern Basin and Range: Tectonophysics, v. 218, p. 1-26.

Henry, C. D., McIntosh, W., McDowell, F. W., Lipman, P. W., Chapin, C. E., and Richardson, M. T., 2010, Distribution, timing, and controls of the mid-Cenozoic ignimbrite flareup in western North America: Geological Society of America Abstracts with Programs, v. 42, no. 5, p. 144.

Jerram, D., and Petford, N., 2011, The Field Description of Igneous Rocks, The Geological Field Guide Series: Chichester, UK, Wiley-Blackwell, 238 p.

Lipman, P. W., 2007, Incremental assembly and prolonged consolidation of Cordilleran magma chambers: Evidence from the Southern Rocky Mountain volcanic field: Geosphere, v. 3, no. 1, p. 42-70.

McDowell, F. W., 2007, Geologic transect across the northern Sierra Madre Occidental volcanic field, Chihuahua and Sonora, Mexico: Geological Society of America Digital Map and Chart Series 6, 70 p.

McDowell, F. W., and Clabaugh, S. E., 1979, Ignimbrites of the Sierra Madre Occidental and their relation to the tectonic history of western Mexico, *in* Chapin, C. E., and Elston, W. E., eds., Ash-Flow Tuffs: Geological Society of America Special Paper 180, p. 113-124.

McDowell, F. W., and Keizer, R. P., 1977, Timing of mid-Tertiary volcanism in the Sierra Madre Occidental between Durango City and Mazatlan, Mexico: Geological Society of America Bulletin, v. 88, p. 1479-1487.

McDowell, F. W., and Mauger, R. L., 1994, K-Ar and U-Pb zircon chronology of Late Cretaceous and Tertiary magmatism in central Chihuahua State, Mexico: Geological Society of America Bulletin, v. 106, p. 118-132.

McDowell, F. W., and McIntosh, W. C., 2012, Timing of intense magmatic episodes in the northern and central Sierra Madre Occidental, western Mexico: Geosphere, v. 8, no. 6, p. 1502-1526.

McDowell, F. W., Roldán-Quintana, J., and Amaya-Martínez, R., 1997, Interrelationship of sedimentary and volcanic deposits associated with Tertiary extension in Sonora, Mexico: Geological Society of America Bulletin, v. 109, no. 10, p. 1349-1360.

McDowell, F. W., Roldán-Quintana, J., and Connelly, J. N., 2001, Duration of Late Cretaceous-early Tertiary magmatism in east-central Sonora, Mexico: Geological Society of America Bulletin, v. 113, p. 521-531.

Minjárez Sosa, I., Montaño Jiménez, T. R., Ochoa Granillo, J. A., Grijalva Noriega, F. J., Ochoa Landín, L. H., Herrera Urbina, S., Guzmán Espinosa, J. B., and Mancilla Gutiérrez, A. A., 2002, Carta Geológico-Minera Ciudad Obregón G12-3 Sonora, Chihuahua y Sinaloa: Servicio Geológico Mexicano, scale 1:250,000.

Murray, B. P., Busby, C. J., Ferrari, L., and Solari, L. A., 2013, Synvolcanic crustal extension during the mid-Cenozoic ignimbrite flare-up in the northern Sierra Madre Occidental, Mexico: Evidence from the Guazapares Mining District region, western Chihuahua: Geosphere, v. 9, no. 5, p. 1201-1235.

Nieto-Samaniego, Á. F., Ferrari, L., Alaniz-Álvarez, S. A., Labarthe-Hernández, G., and Rosas-Elguera, J., 1999, Variation of Cenozoic extension and volcanism across the southern Sierra Madre Occidental volcanic province, Mexico: Geological Society of America Bulletin, v. 111, no. 3, p. 347-363.

Price, J. G., Conlon, S. T., and Henry, C. D., 1988, Tectonic controls on orientation and size of epithermal veins, Univ. Mo., Rolla, MO.

Ramírez Tello, E., and Garcia Peralta, Á. A., 2004, Carta Geológico-Minera Témoris G12-B39 Chihuahua: Servicio Geológico Mexicano, scale 1:50,000.

Randall R., J. A., Saldana A., E., and Clark, K. F., 1994, Exploration in a volcano-plutonic center at Guanajuato, Mexico: Economic Geology, v. 89, p. 1722-1751.

Roy, D., Trinder, I. D., and Lustig, G., 2008, Report on the San Miguel project, Guazapares Mining District, Chihuahua, Mexico for Paramount Gold and Silver Corp.: Toronto, Ontario, A.C.A. Howe International Limited, 205 p.

Scheubel, F. R., Clark, K. F., and Porter, E. W., 1988, Geology, tectonic environment, and structural controls in the San Martín de Bolaños district, Jalisco, Mexico: Economic Geology, v. 83, p. 1703-1720.

Sellepack, S. M., 1997, The geology and geochemistry of the El Sauzal gold prospect, southwest Chihuahua, Mexico [M.S. thesis]: University of Texas, El Paso, 118 p.

Sigurdsson, H., Houghton, B. F., McNutt, S. R., Rymer, H., and Stix, J., 2000, Encyclopedia of Volcanoes: San Diego, California, Academic Press, 1471 p.

Staude, J. G., and Barton, M. D., 2001, Jurassic to Holocene tectonics, magmatism, and metallogeny of northwestern Mexico: Geological Society of America Bulletin, v. 113, no. 10, p. 1357-1374.

Ward, P. L., 1991, On plate tectonics and the geologic evolution of southwestern North America: Journal of Geophysical Research, v. 96, no. B7, p. 12,479-12,496.

Wark, D. A., 1991, Oligocene ash flow volcanism, northem Sierra Madre Occidental: role of mafic and intermediate-composition magmas in rhyolite genesis: Journal of Geophysical Research, v. 96, no. B8, p. 13,389-13,411.

Wark, D. A., Kempter, K. A., and McDowell, F. W., 1990, Evolution of waning subduction-related magmatism, northern Sierra Madre Occidental, Mexico: Geological Society of America Bulletin, v. 102, p. 1555-1564.

Wilkerson, G., Deng, Q., Llavona, R., and Goodell, P., 1988, Batopilas Mining District, Chihuahua, Mexico: Economic Geology, v. 83, p. 1721-1736.

Wong, M. S., Gans, P. B., and Scheier, J., 2010, The $^{40}Ar/^{39}Ar$ thermochronology of core complexes and other basement rocks in Sonora, Mexico: Implications for Cenozoic tectonic evolution of northwestern Mexico: Journal of Geophysical Research, v. 115, no. B07414, doi: 10.1029/2009JB007032.

Wood, D. R., and Durgin, D. C., 2009, Technical report project update: San Miguel project, Chihuahua, Mexico, prepared for Paramount Gold and Silver Corp.: Sparks, Nevada, Delve Consultants, L.L.C., 86 p.

CHAPTER 3

EXTENSION AND MAGMATISM IN THE CEROCAHUI BASIN, NORTHERN SIERRA MADRE OCCIDENTAL, WESTERN CHIHUAHUA, MEXICO

ABSTRACT

The Sierra Madre Occidental of northwestern Mexico is the biggest silicic large igneous province of the Cenozoic, yet very little is known about its geology due to difficulties of access to much of this region. This study presents geologic maps and two new U-Pb zircon laser ablation–inductively coupled plasma–mass spectrometry ages from the Cerocahui basin, a previously unmapped and undated ~25 km-long by ~12 km-wide half-graben along the western edge of the relatively unextended core of the northern Sierra Madre Occidental silicic large igneous province. Five stratigraphic units are defined in the study area: (1) undated welded to nonwelded silicic ignimbrites that underlie the rocks of the Cerocahui basin, likely correlative to Oligocene-age ignimbrites to the east and west; (2) the ca. 27.5–26 Ma Bahuichivo Volcanics, comprising mafic-intermediate lavas and subvolcanic intrusions in the Cerocahui basin; (3) alluvial fan deposits and interbedded distal nonwelded silicic ignimbrites of the Cerocahui clastic unit, (4) basalt lavas erupted into the Cerocahui basin following alluvial deposition; and (5) silicic hypabyssal intrusions emplaced along the eastern margin of the basin and to a lesser degree within the basin deposits. Evidence of syndepositional extension in the half-graben (e.g., growth strata) indicates that normal faulting was active during deposition in the Cerocahui basin (Bahuichivo Volcanics, Cerocahui clastic unit, and basalt lavas), and may have been active earlier based on regional correlations.

The rocks in the Cerocahui basin and adjacent areas record: (1) the eruption of a silicic outflow ignimbrite sheets, likely from caldera sources to the east during the Early Oligocene pulse of the mid-Cenozoic ignimbrite flare-up, mostly prior to synextensional deposition in the Cerocahui basin (pre-27.5 Ma); (2) synextensional Late Oligocene mafic-intermediate composition magmatism and alluvial fan sedimentation (ca. 27.5–24.5 Ma), which occurred during the lull between the Early Oligocene and Early Miocene pulses of the ignimbrite flare-up; and (3) postextensional emplacement of silicic hypabyssal intrusions along preexisting normal faults, likely during the Early Miocene pulse of the ignimbrite flare-up (younger than ca. 24.5 Ma). The timing of extensional faulting and magmatism in the Cerocahui basin and surrounding area generally coincides with previous models of regional-scale Middle Eocene to Early Miocene southwestward migration of active volcanism and crustal extension in the northern Sierra Madre Occidental controlled by post-Late Eocene (ca. 40 Ma) rollback/fallback of the subducted Farallon slab.

INTRODUCTION

Silicic large igneous provinces are significant in the geologic record, due to their unusually extensive areal coverage (>100,000 km^2) and large volumes (>250,000 km^3) (Bryan, 2007; Bryan and Ernst, 2008; Bryan and Ferrari, 2013). Compositions within silicic large igneous provinces range from basalt to high-silica rhyolite, but are volumetrically dominated (>80%) by dacite-rhyolite compositions, with >75% of the total magmatic volume emplaced during short duration (~1-5 Myr) pulses over a maximum province lifespan of ~50 Myr (Bryan, 2007; Bryan and Ernst, 2008). The Sierra Madre Occidental of western Mexico is the third biggest (up to 400,000 km^3) and best preserved silicic large igneous province in Earth's history and is the largest of the Cenozoic (Fig. 1; Bryan, 2007; Ferrari et al., 2007;

Bryan and Ernst, 2008; Bryan and Ferrari, 2013). Despite its size and preservation, very little is known about the geology of the Sierra Madre Occidental due to difficulties of access to much of this region. A large part of the Sierra Madre Occidental remains unmapped and undated (>90%; Swanson et al., 2006), with previous work primarily restricted to the southern region of the igneous province and to the major highways that transverse the northern and central regions (e.g., McDowell and Keizer, 1977; Swanson and McDowell, 1984, 1985; Wark et al., 1990; Aguirre-Díaz and McDowell, 1991, 1993; McDowell and Mauger, 1994; Ferrari et al., 2002; McDowell, 2007; McDowell and McIntosh, 2012). Due to increased accessibility to the region, recent studies in the northern Sierra Madre Occidental have focused on the Creel-Divisadero area (Fig. 1; Swanson et al., 2006) and the Guazapares Mining District region (Fig. 2; Murray et al., 2013) in southwestern Chihuahua.

Previous studies of silicic large igneous provinces suggest that they typically initiate as magmatic events in continental regions undergoing broad lithospheric extension, prior to rupture of continental lithosphere (Bryan et al., 2002; Bryan, 2007; Best et al., 2013; Bryan and Ferrari, 2013). In addition, crustal extension has been suggested to favor the generation of large silicic magma volumes (e.g., Hildreth, 1981) and very large magnitude explosive silicic eruptions (Aguirre-Díaz and Labarthe-Hernández, 2003; Costa et al., 2011). Therefore, studying the relationships between the timing of extensional deformation and magmatism is an important consideration toward understanding the development of the Sierra Madre Occidental.

Here we present new geologic mapping, stratigraphy, and geochronology in an extensional basin located between the Creel-Divisadero area and the Guazpares Mining District that has not been previously recognized in the Sierra Madre Occidental (Fig. 1). We refer to this basin as the "Cerocahui basin" (Figs. 2, 3, and 4), and show that it is an extensive

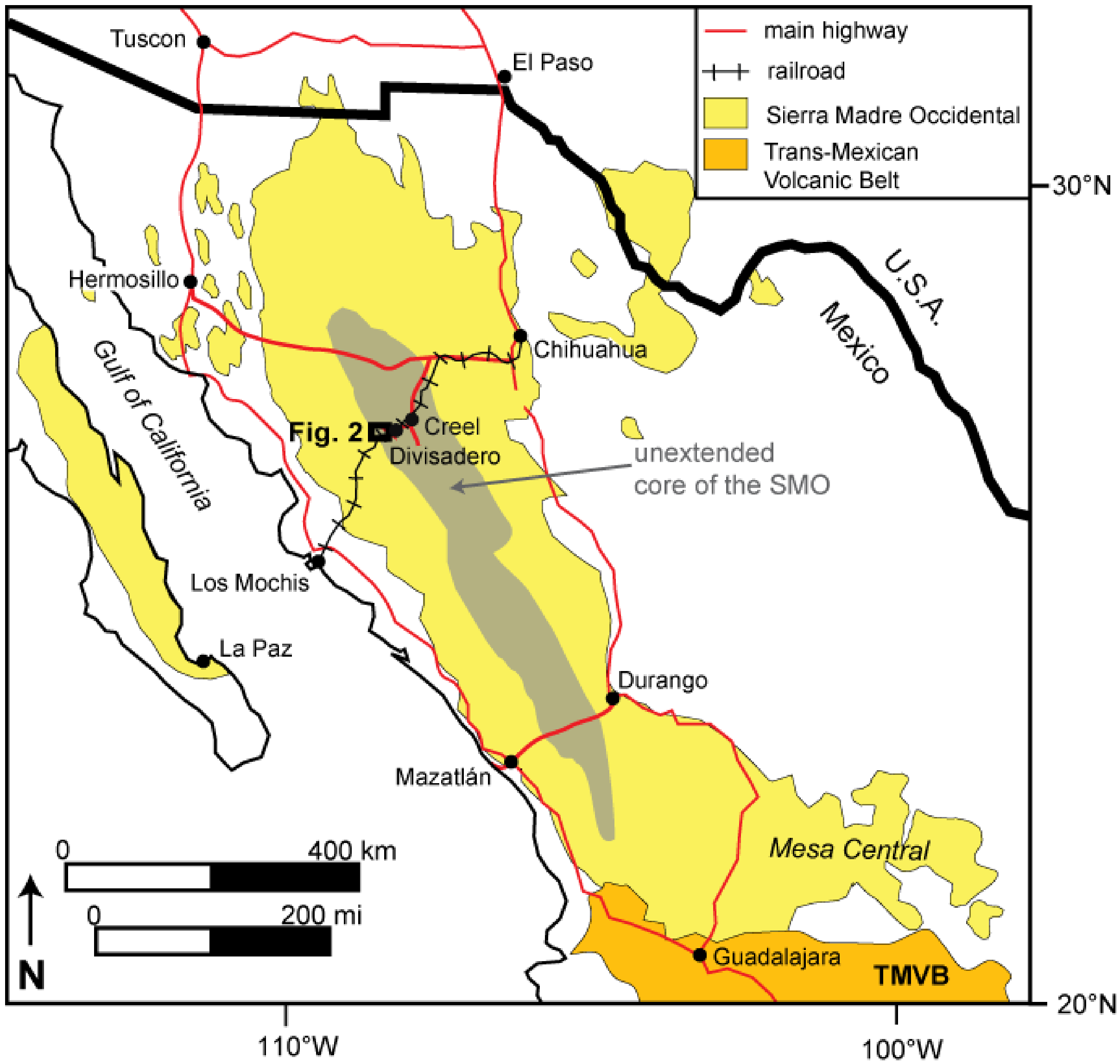

Figure 1. Map of western Mexico showing the extent of the Sierra Madre Occidental (SMO) silicic large igneous province and the unextended core (gray) of the SMO (after Henry and Aranda-Gómez, 2000; Ferrari et al., 2002; Bryan et al., 2013). The location of the study area and the adjacent Guazapares Mining District region, described by Murray et al. (2013), is indicated by black box (Fig. 2) on the western edge of the unextended core. TMVB—Trans-Mexican Volcanic Belt.

Figure 2 (*next page*). Simplified geologic map of the Cerocahui basin and the adjacent Guazapares Mining District region to the west (green box). The extent of the main lithologic units discussed herein (see Fig. 5) and the locations of major faults are shown. The red box indicates the area of the geologic map in Figure 3; detailed maps of the Guazapares Mining District region (green box) are presented in Murray et al. (2013). The location of the main roads and the "Chepe" Copper Canyon railroad that transect the study area are also shown. Map coordinates in black are Universal Transverse Mercator (UTM) zone 12, North American Datum 1927 (NAD27).

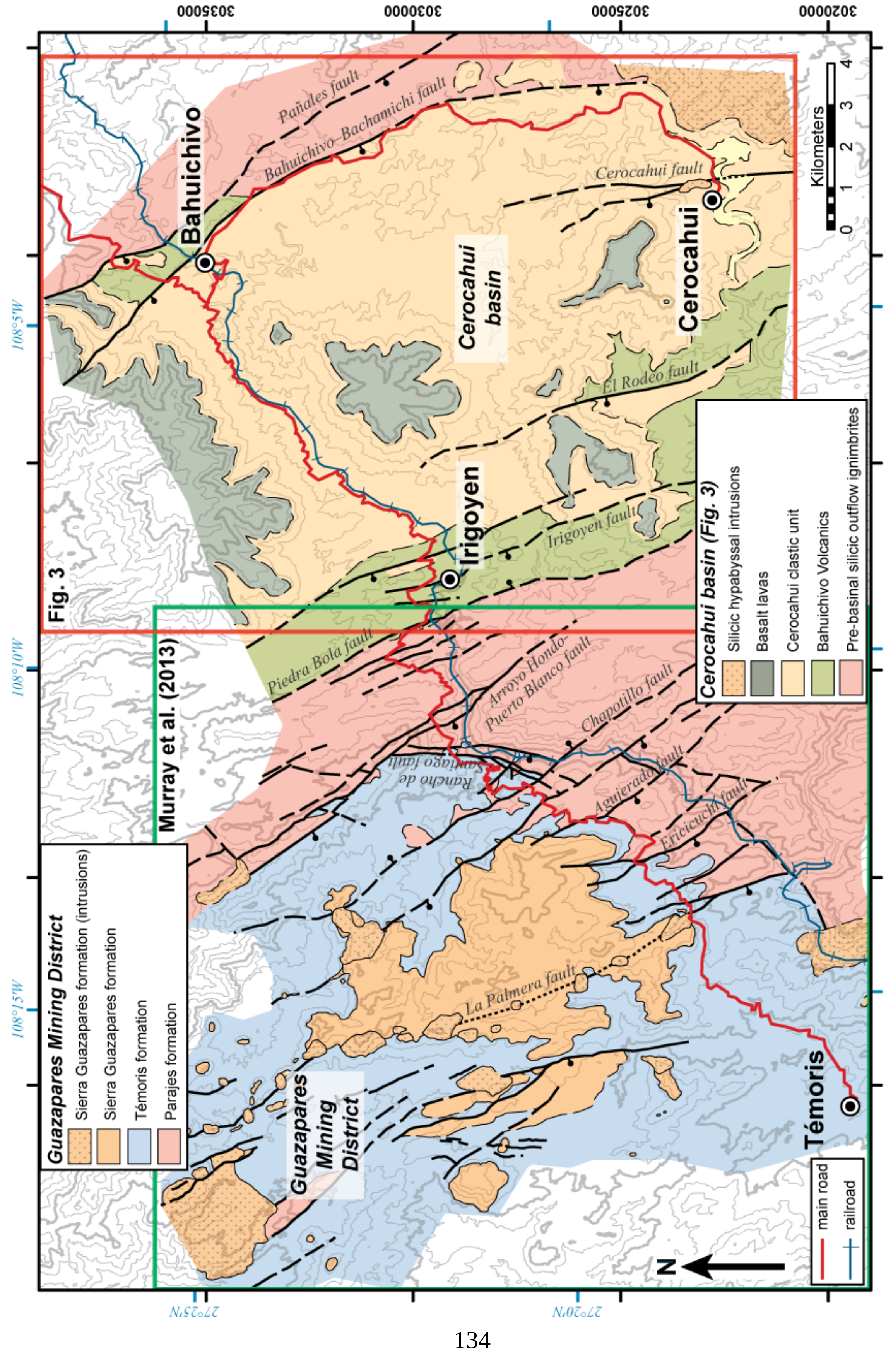

Guazapares Mining District
Sierra Guazapares formation (intrusions)
Sierra Guazapares formation
Témoris formation
Parajes formation
Cerocahui basin (Fig. 3)
Silicic hypabyssal intrusions
Basalt lavas
Cerocahui clastic unit
Bahuichivo Volcanics
Pre-basinal silicic outflow ignimbrites
main road
railroad
Kilometers
0 1 2 3 4
Fig. 3
Murray et al. (2013)
Bahuichivo
Irigoyen
Cerocahui
Cerocahui basin
Témoris
Guazapares Mining District
Pañales fault
Bahuichivo–Bachamichi fault
Cerocahui fault
El Rodeo fault
Irigoyen fault
Piedra Bola fault
Arroyo Hondo-Puerto Blanco fault
Chapotillo fault
Rancho de Santiago fault
Agujerado fault
Ericicuchi fault
La Palmera fault
N
3035000
3030000
3025000
3020000
795000
790000
785000
780000
775000
770000
108°5'W
108°10'W
108°15'W
27°25'N
27°20'N

and thick section of red beds and mafic-intermediate composition volcanic rocks that accumulated between two major pulses of silicic magmatism during the mid-Cenozoic ignimbrite flare-up in the northern Sierra Madre Occidental. The rock exposure and topographic relief in this region make it an excellent locality for examining the relationships between extensional basin development and silicic large igneous province magmatism in the Sierra Madre Occidental. With these data, we are able to correlate magmatic and extensional events over a broader region than initially described by Murray et al. (2013) in the adjacent Guazapares Mining District to the west (Fig. 2), and show that the timing of magmatism and synextensional deposition in this region of the northern Sierra Madre Occidental that includes both the Cerocahui basin and Guazapares Mining District supports the interpretation that crustal extension and silicic flare-up magmatism migrated southwestward with time across western Mexico.

GEOLOGIC SETTING

Regional Geology

The Sierra Madre Occidental silicic large igneous province forms a major component of the extensive mid-Cenozoic ignimbrite flare-up that affected much of the southwestern North American Cordillera from the Middle Eocene to Late Miocene (e.g., Coney, 1978; Armstrong and Ward, 1991; Ward, 1991; Ferrari et al., 2002; Lipman, 2007; Cather et al., 2009; Henry et al., 2010; Henry et al., 2012; Best et al., 2013). The mid-Cenozoic ignimbrite flare-up occurred above a subducting slab that progressively fell back and steepened towards the trench, following Early Cenozoic low-angle subduction, as shown by the southwestward sweep of volcanism with time (e.g., Best and Christiansen, 1991; Dickinson, 2006; Ferrari et al., 2007; Henry et al., 2010; McQuarrie and Oskin, 2010; Dickinson, 2013). In western

Mexico, Eocene to Miocene slab fallback and arc extension associated with it led ultimately to Miocene rifting in the Gulf of Mexico (Ferrari et al., 2007; Ferrari et al., 2013).

The Sierra Madre Occidental (Fig. 1) consists primarily of Late Eocene to Early Miocene ignimbrites that cover an area of ~400,000 km^2 with an average thickness of 1 km (McDowell and Keizer, 1977; McDowell and Clabaugh, 1979; Aguirre-Díaz and Labarthe-Hernández, 2003; Bryan and Ferrari, 2013). There were at least two main pulses of silicic ignimbrite volcanism during the mid-Cenozoic ignimbrite flare-up in the Sierra Madre Occidental, one during the Late Eocene–Early Oligocene (ca. 36–28 Ma) and another during the Early Miocene (ca. 24–20 Ma) (Ferrari et al., 2002; Ferrari et al., 2007; McDowell and McIntosh, 2012). During the final stages of and after each silicic ignimbrite pulse, basaltic andesite lavas, commonly referred to as the Southern Cordillera basaltic andesite province (SCORBA) were intermittently erupted across all of the northern Sierra Madre Occidental (Cameron et al., 1989; Ferrari et al., 2007).

Following the Laramide orogeny (Late Eocene, ca. 40 Ma) in western North America, the age distribution of volcanic rocks in the southwestern U.S. and the Sierra Madre Occidental suggests that ignimbrite flare-up magmatism generally migrated southwestward over time (e.g., Coney and Reynolds, 1977; Damon et al., 1981; Best and Christiansen, 1991; Christiansen and Yates, 1992; Dickinson, 2002, 2006; Ferrari et al., 2007; Henry et al., 2010; McQuarrie and Oskin, 2010; McDowell, 2012; Bryan et al., 2013; Busby, 2013; Dickinson, 2013). This post-Laramide age trend is likely related to removal of the flat to low-angle subducted Farallon plate from the base of the North American plate by either steepening (slab rollback) and/or possible detachment of the deeper part of the subducted slab (e.g., Dickinson and Snyder, 1978; Best and Christiansen, 1991; Ferrari et al., 2007; Henry et al., 2010;

McQuarrie and Oskin, 2010; Best et al., 2013; Busby, 2013; Dickinson, 2013); as a result, commencing by ca. 40 Ma, magmatism migrated southwestward towards the paleotrench.

The timing of extension in the Sierra Madre Occidental has variously been interpreted to have preceded (e.g., Dreier, 1984; Ferrari et al., 2007), postdated (e.g., McDowell and Clabaugh, 1979; Wark et al., 1990; McDowell and Mauger, 1994; Gans, 1997; McDowell et al., 1997; Grijalva-Noriega and Roldán-Quintana, 1998; Gans et al., 2003), or begun during (e.g., Aguirre-Díaz and McDowell, 1993; Luhr et al., 2001; Murray et al., 2013) the Late Eocene–Early Oligocene pulse of the mid-Cenozoic ignimbrite flare-up. The eruptions of the Southern Cordillera basaltic andesite (SCORBA) following the Early Oligocene ignimbrite pulse has been interpreted as magmatism recording the initiation of regional-scale crustal extension in the northern Sierra Madre Occidental (e.g., Cameron et al., 1989; Cochemé and Demant, 1991; Gans, 1997; McDowell et al., 1997; González León et al., 2000; Ferrari et al., 2007). The central core of the Sierra Madre Occidental is relatively unextended in comparison to the surrounding Late Oligocene- to Miocene-age extensional belts of the southern Basin and Range to the east and the Gulf Extensional Province to the west (Fig. 1; Nieto-Samaniego et al., 1999; Henry and Aranda-Gómez, 2000).

Guazapares Mining District

The recent study of the Guazapares Mining District region near Témoris (Fig. 2) to the west of the Cerocahui basin (Murray et al., 2013) provides a stratigraphic and structural context for the Cerocahui basin. Three informal formations are recognized in the Guazapares Mining District region (Fig. 2). The oldest, the Parajes formation, consists primarily of welded silicic outflow ignimbrite sheets erupted ca. 27.5 Ma (and possibly older). These ignimbrites were erupted near the end of the Early Oligocene pulse of the ignimbrite flare-up, presumably from calderas of similar age that lie largely to the east of both the Guazapares

Mining District (Murray et al., 2013) and the Cerocahui basin, described herein. The ca. 27–24.5 Ma Témoris formation (Fig. 2), which unconformably overlies the Parajes formation, records local, fault-controlled mafic to intermediate composition magmatism and subsequent distal silicic ignimbrite volcanism, synchronous with extension. Given the similar age and composition, the Témoris formation may be related to the Southern Cordillera basaltic andesite (SCORBA) province erupted in other parts of northern Sierra Madre Occidental following the Early Oligocene ignimbrite pulse (Murray et al., 2013). The ca. 24.5–23 Ma Sierra Guazapares formation (Fig. 2), which overlies the Témoris formation in angular unconformity, records local silicic magmatism, including vent-to-proximal-facies ignimbrite deposits, lavas, and hypabyssal rocks; these were erupted from and intruded into fault-controlled fissure vents within the Guazapares Mining District region. The Sierra Guazapares formation records the onset of the Early Miocene pulse of the mid-Cenozoic ignimbrite flare-up (Murray et al., 2013).

The main geologic structures in the Guazapares Mining District region are NNW-trending normal faults that bound a series of closely spaced half-graben basins (Fig. 2). Growth strata and angular unconformities between each formation indicate that these half-graben basins began to form by the time the upper part of the Parajes formation was erupted (ca. 27.5 Ma) and continued to develop during deposition of the Témoris and Sierra Guazapares formations. In addition, several of these extensional structures controlled the localization of andesitic and silicic volcanic vents and shallow level intrusions of the Témoris and Sierra Guazapares formations (Murray et al., 2013).

THE CEROCAHUI BASIN

We coin the term "Cerocahui basin" for the approximately 12 km-wide basin with a mapped length of approximately 25 km (Figs. 2 and 3; Supplemental File 2)[2], although it could extend further north and south. It is named for the village of Cerocahui in the southeastern part of the basin, located ~12 km south of the town of Bahuichivo, a stop on the famous “Chepe” Copper Canyon train (Figs. 2 and 3; Supplemental File 2 [see footnote 2]). The Cerocahui basin lies on in the western edge of the largely unextended core of the northern Sierra Madre Occidental (Fig. 1). Previous work in the Cerocahui basin region has been restricted to regional 1:50,000 and 1:250,000 geologic mapping (Minjárez Sosa et al., 2002; Ramírez Tello and Garcia Peralta, 2004) and unpublished mining company reports, none of which recognized that the region is dominated by a half-graben basin. The geologic mapping for this study was primarily centered on the village of Cerocahui and around Bahuichivo, and on the two main roads that transect the basin on the north and east (Figs. 2 and 3; Supplemental File 2 [see footnote 2]). Much of the central and southwestern sections of the basin are inaccessible due to lack of roads or hazards related to drug cultivation activities in the region; however, the geology located in these areas (noted on Fig. 3) is interpreted from aerial imagery (Supplemental File 3)[2] and may not be accurate in detail, but is based on known geologic relationships from the more accessible areas along the major roads and around population centers (Fig. 2).

North-northwest-trending normal faults are the primary geologic structures in the Cerocahui basin and adjacent region (Figs. 2, 3, and 4; Supplemental File 2 [see footnote 2]). The W-dipping Bahuichivo–Bachamichi fault forms the eastern boundary of the Cerocahui

[2] Supplemental File 2: Geologic map of the Cerocahui basin (1:24,000 scale) and Supplemental File 3: Aerial imagery of the Cerocahui basin; submitted as additional files with dissertation

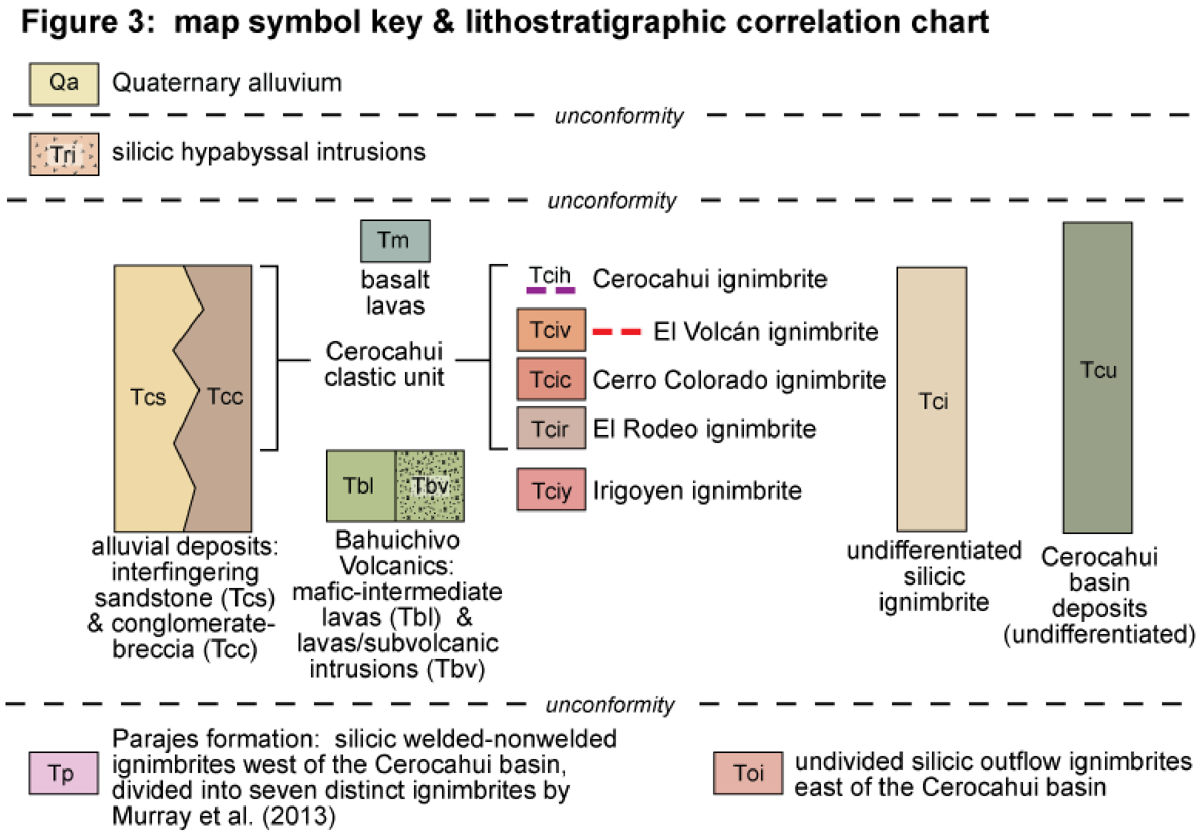

Figure 3 (*this and next 2 pages*). Geologic map of the Cerocahui basin, with lithostratigraphic correlation chart and key for the map units and symbols. The location of cross-sections A and B (Fig. 4) and the measured stratigraphic section (Fig. 7) are indicated. Much of the basin is inaccessible, with interpretations of the geology in these areas (noted by gray hatch pattern) based on aerial imagery and known geologic relationships from accessible areas. A more detailed (1:24,000) geologic map for the study area is presented in Supplemental File 2 (see footnote 2). Topographic base map from Instituto Nacional de Estadística, Geografía e Informática (INEGI), original 1:50,000 scale ITRF92 datum projected to NAD27 UTM zone 12 (black coordinates).

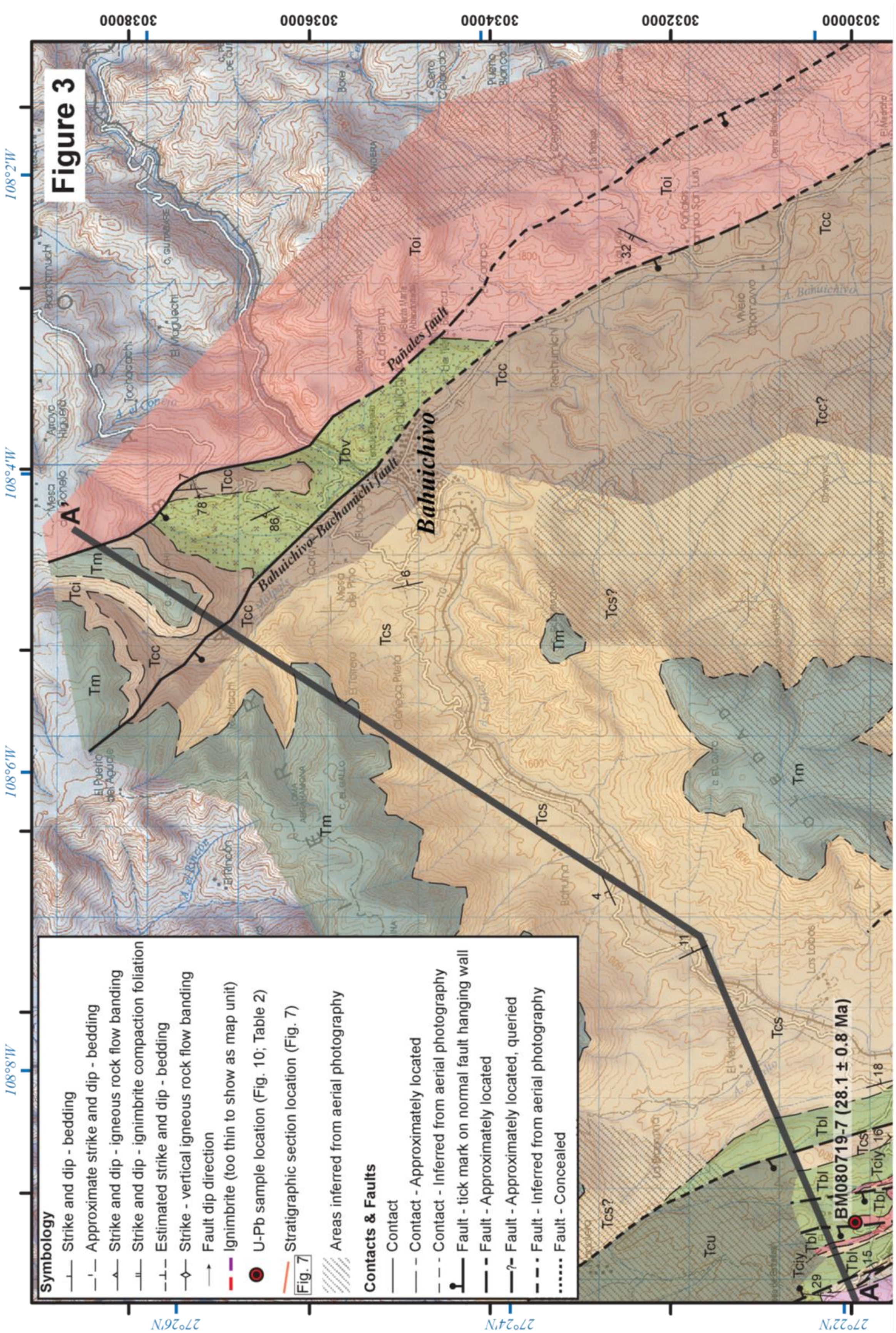

Figure 3
Symbology
Strike and dip - bedding
Approximate strike and dip - bedding
Strike and dip - igneous rock flow banding
Strike and dip - ignimbrite compaction foliation
Estimated strike and dip - bedding
Strike - vertical igneous rock flow banding
Fault dip direction
Ignimbrite (too thin to show as map unit)
U-Pb sample location (Fig. 10; Table 2)
Stratigraphic section location (Fig. 7)
Fig. 7
Areas inferred from aerial photography
Contacts & Faults
Contact
Contact - Approximately located
Contact - Inferred from aerial photography
Fault - tick mark on normal fault hanging wall
Fault - Approximately located
Fault - Approximately located, queried
Fault - Inferred from aerial photography
Fault - Concealed
BM080719-7 (28.1 ± 0.8 Ma)
Bahuichivo
Bahuichivo–Bachamichi fault
Pañales fault
A
A'
Toi
Tcc
Tcc?
Tbv
Tm
Tci
Tcs
Tcs?
Tcu
Tbl
Tciy
108°2'W
108°4'W
108°6'W
108°8'W
27°26'N
27°24'N
27°22'N
3038000
3036000
3034000
3032000
3030000

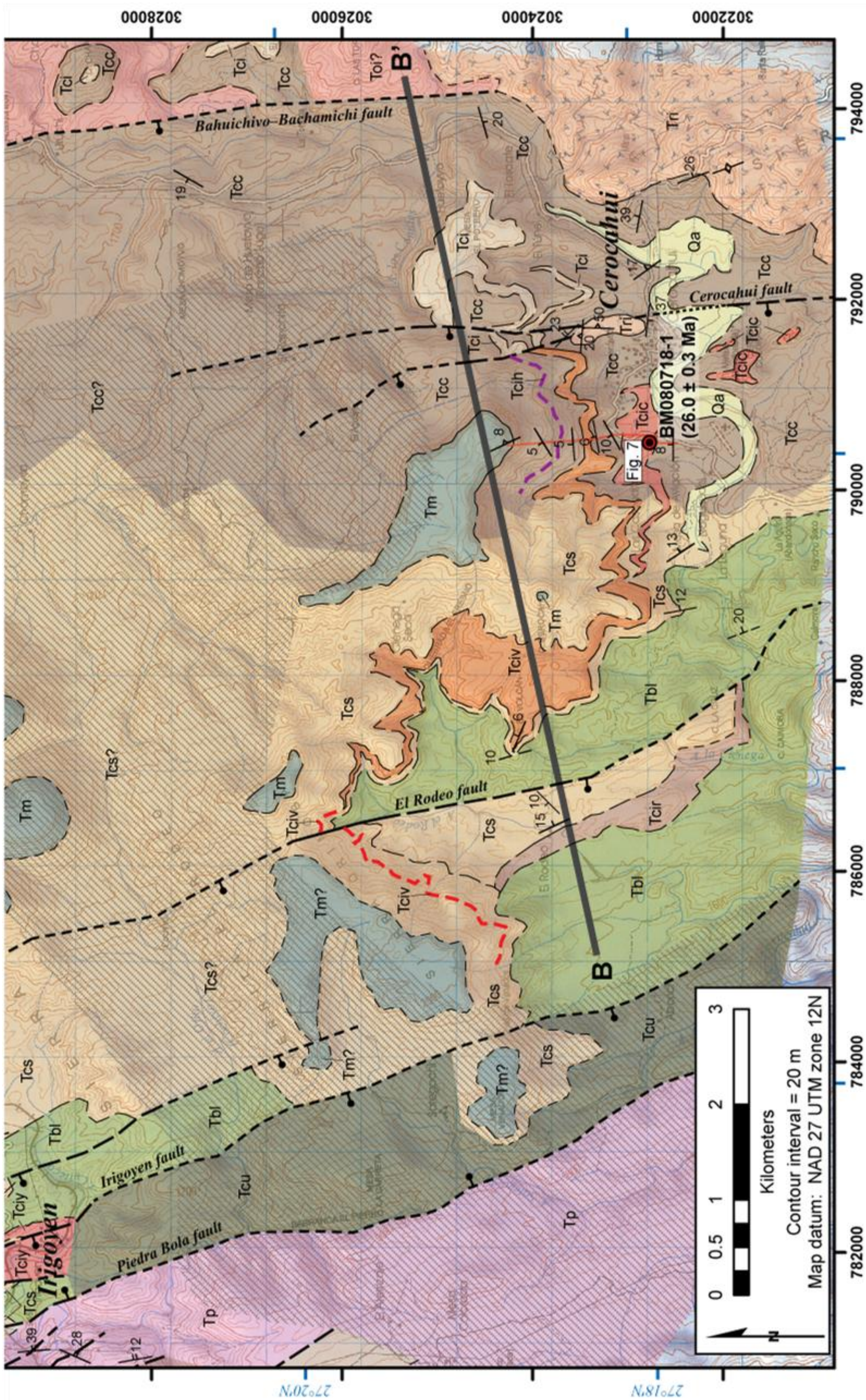

3028000
3026000
3024000
3022000
794000
792000
790000
788000
786000
784000
782000
27°20'N
27°18'N
B'
B
Bahuichivo–Bachamichi fault
Cerocahui fault
El Rodeo fault
Irigoyen fault
Piedra Bola fault
Cerocahui
Irigoyen
BM080718-1
(26.0 ± 0.3 Ma)
Fig. 7
Tcc
Tci
Toi?
Tcc?
Tri
Qa
Tcic
Tcih
Tm
Tcs
Tciv
Tbl
Tcir
Tcs?
Tm?
Tcu
Tciy
Tp
Kilometers
0 0.5 1 2 3
Contour interval = 20 m
Map datum: NAD 27 UTM zone 12N
N

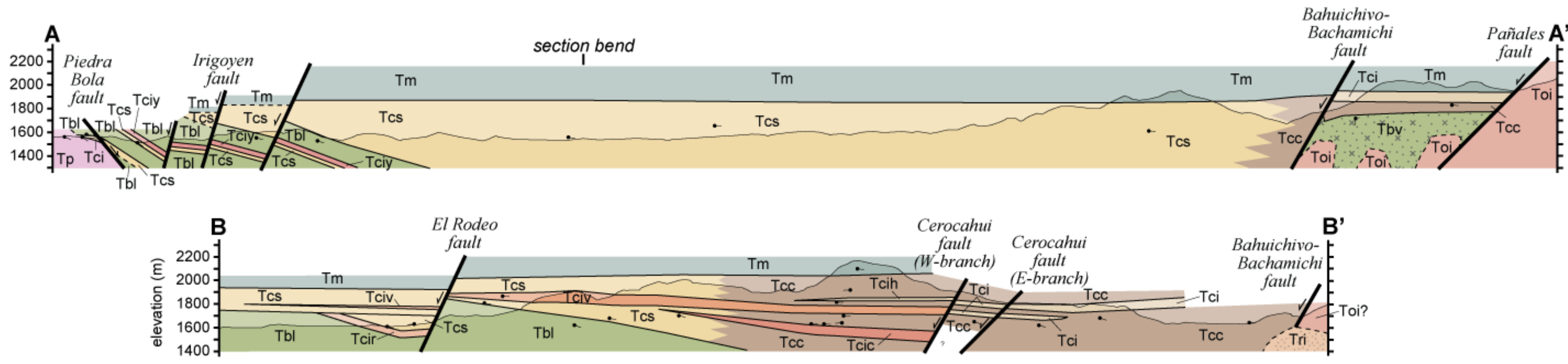

Figure 4. Geologic cross-sections across the northern and southern mapped sections of the Cerocahui basin, with no vertical exaggeration. Rock units inferred above topography are indicated by subdued color shades. Bedding orientations are indicated by tick marks. See Figure 3 for key to map unit symbols and colors and for cross-section locations. (A) Cross-section A–A' between Irigoyen and Bahuichivo in the northern section of the Cerocahui basin, showing decreased dip of map units upsection and offset of the Cerocahui basin deposits. Mafic-intermediate lavas (Tbl), sandstone, and an undifferentiated silicic ignimbrite (Tci) of the Bahuichivo Volcanics are deposited in angular unconformity above the pre-basinal silicic outflow ignimbrites (Tp) on the footwall of the Piedra Bola fault; downdropping of the hanging wall cut these deposits that onlapped the fault prior to slip, and also steepened bedding on the footwall adjacent to the Piedra Bola fault (drag anticline). (B) Cross-section B–B' between the El Rodeo fault and Cerocahui in the southern section of the Cerocahui basin, showing decreased dip of map units upsection and thickening eastward, suggesting syndepositional extension of the eastern basin-bounding normal fault. Evidence of syndepositional extension of the El Rodeo fault is suggested by the restriction of the El Rodeo ignimbrite (Tcir) to the hanging wall, and the increased thickness and angular unconformity within the Cerocahui clastic unit (Tcs) across the fault.

basin. Immediately east (<1 km) and trending parallel to the Bahuichivo–Bachamichi fault is the W-dipping Pañales fault, which has a much thinner section of volcanic and sedimentary rocks on its hanging wall and lacks these rocks on its footwall; this fault thus represents a minor strand of the main basin-bounding fault (Figs. 3 and 4A; Supplemental File 2 [see footnote 2]). Several W-dipping normal faults offset the deposits within the Cerocahui basin, including the Cerocahui, El Rodeo, and Irigoyen faults, but these have less offset than the eastern basin-bounding fault (Figs. 3 and 4; Supplemental File 2 [see footnote 2]). Extension on these faults has gently to moderately tilted the strata of the Cerocahui basin to the north-to-northeast (~5–30°). The western boundary of the Cerocahui basin is inferred to be roughly in the location of the NW-trending, E-dipping Piedra Bola fault (Figs. 2 and 3; Supplemental File 2 [see footnote 2]). This fault offsets the lowermost deposits of the Cerocahui basin, which extend westward onto the footwall block (Figs. 3 and 4A; Supplemental File 2 [see footnote 2]). Additionally, the basin fill on the hanging wall (east side) of the Piedra Bola fault dips away from the fault rather than towards it; therefore, the Piedra Bola fault is not considered a basin-bounding normal fault.

Basin Stratigraphy and Relation to Extensional Structures

The rocks exposed in the Cerocahui basin and surrounding area are subdivided into five lithologic units described in the following (from oldest to youngest): (1) pre-basinal silicic outflow ignimbrites, (2) the Bahuichivo Volcanics, consisting mainly of mafic-intermediate composition lavas and subvolcanic intrusions, (3) the Cerocahui clastic unit, composed of alluvial fan sandstones, conglomerates, and breccias and interbedded silicic ignimbrites, (4) basalt lavas, and (5) silicic hypabyssal intrusions (Figs. 3 and 5).

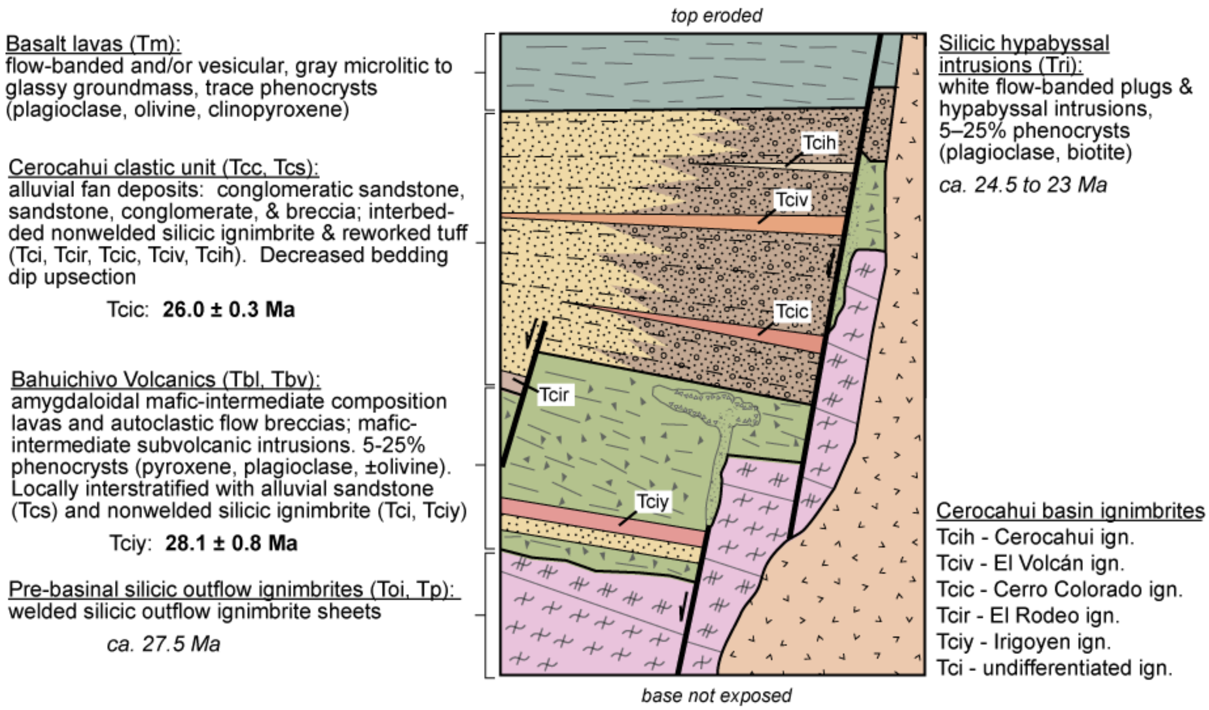

Figure 5. Rock units of the Cerocahui basin and substrate, depicting the characteristics and depositional relationships between the pre-basinal silicic outflow ignimbrites, Bahuichivo Volcanics, Cerocahui clastic unit, basalt lavas, and silicic hypabyssal intrusions. Unit symbols are the same as Figure 3. The ages in bold are from this study (Fig. 10; Table 2), and the approximate ages in italics are from Murray et al. (2013) and are based on inferred stratigraphic correlations in the Guazapares Mining District to the west (see text for discussion).

Silicic outflow ignimbrites of pre-basinal origin (Toi & Tp)

A section of tabular, largely welded silicic outflow ignimbrites is exposed in the footwall of the W-dipping Bahuichivo–Bachamichi and Pañales faults on the east side of the Cerocahui basin (map unit Toi) and in the footwall of the E-dipping Piedra Bola fault on the west side of the basin (Tp) (Figs. 2 and 3). These two map units are tentatively correlated, although the ignimbrites east of the basin have not been studied in the same detail as those located west of the basin (Parajes Formation [Tp]) by Murray et al. (2013). At least seven distinct ignimbrites have been identified in the Parajes formation (Tp) on the west side of the Cerocahui basin; each ignimbrite ranges from ~20 to ~210 m-thick, has a densely welded to partially welded lower section that passes upward into a less welded to nonwelded top, and has normal coarse-tail grading of lithic fragments and inverse coarse-tail grading of pumice (Murray et al., 2013).

Because the silicic outflow ignimbrite section bounds the Cerocahui basin on both sides, and forms a widespread sheet where it has been mapped to the west and east (Figs. 3 and 4), it is inferred to underlie the deposits of the Cerocahui basin. This interpretation is supported by an angular unconformity between gently dipping (~10° E) mafic-intermediate lavas (Tbl), fluvial sandstone, and an undifferentiated silicic ignimbrite (Tci) interpreted as part of the lowermost deposits of the Cerocahui basin (Bahuichivo Volcanics, described below) and the underlying moderately dipping (~25° E) Parajes formation (Tp) on the western side (footwall) of the Piedra Bola fault near Irigoyen (Figs. 3 and 4A; Supplemental File 2 [see footnote 2]). In the Guazapares Mining District region immediately west of the Cerocahui basin, normal faulting began during deposition of the youngest units in the Parajes formation (Tp) silicic outflow ignimbrite section after 27.6 ± 0.3 Ma (Murray et al., 2013).

Map data in the silicic outflow ignimbrite section east of the Cerocahui basin are insufficient to determine whether any of the units are synextensional.

The silicic outflow ignimbrites on the east side of the Cerocahui basin are interpreted as the medial facies of outflow ignimbrite sheets, based on their sheet-like geometry and the presence of cliff-forming welded sections, similar to the ca. 27.5 Ma Parajes formation (Tp) to the west of the basin (Murray et al., 2013). Their sheet-like geometry is also similar to that of ignimbrites in the unextended core of the Sierra Madre Occidental, although that region also contains caldera-filling ignimbrites (e.g., Swanson et al., 2006). The silicic outflow ignimbrites on the east side of the Cerocahui basin (Toi) have not been dated directly, but they are clearly older than the basal basin-filling sedimentary deposits, and an intrusion of the Bahuichivo Volcanics (Tbv) crosscuts one of the ignimbrites (Fig. 6A). The silicic outflow ignimbrite section includes seven distinct ignimbrites in the Guazapares Mining District region (Murray et al., 2013), but the ignimbrite section east of the Cerocahui basin has not been studied in detail. The ignimbrites generally have <15% phenocrysts, and like many of the ignimbrites of the Sierra Madre Occidental, they lack potassium feldspar (e.g., Swanson et al., 2006; Murray et al., 2013). Crystal-rich ignimbrites are rare and may prove correlatable by future workers; one such ignimbrite is located ~3.5 km southeast of Bahuichivo (Fig. 3), with 30–35% phenocrysts of plagioclase, biotite (to 3 mm), quartz, hornblende, and 10% andesitic volcanic lithic lapilli.

Bahuichivo Volcanics (Tbl & Tbv): lowermost Cerocahui basin fill

The stratigraphically lowest rocks considered part of the Cerocahui basin fill are the Bahuichivo Volcanics, an informally named unit consisting of dark-colored pyroxene-plagioclase-±olivine-bearing amygdaloidal lavas and autoclastic flow breccias (Tbl), and associated dikes and subvolcanic intrusions (Tbv) (Figs. 3, 4, 5, and 6). Based on the

Figure 6 (*next page*). Representative photographs of the Bahuichivo Volcanics; locations of the photos are given (NAD27). (A) East-dipping mafic-intermediate lava (Tbl) deposited on massive red bed sandstone (Tcs) along the Bahuichivo–Irigoyen road (27.36320 ° N, 108.15692 ° W). Wet sediment–lava intermixing (peperitic texture) is found between the orange-tan sandstone (Tcs) and a lower reddish-gray mafic-intermediate lava (arrows). (B) Mafic-intermediate hypabyssal intrusion (Tbv) emplaced into lithic-rich pre-basinal nonwelded silicic outflow ignimbrite (Toi) along the Bahuichivo–Cerocahui road (27.36228° N, 108.03371° W). (C) Mafic-intermediate hypabyssal intrusion (Tbv) emplaced into conglomerates and sandstones (Tcc) north of Bahuichivo (looking northwest from 27.42259° N, 108.07175° W). Intrusion and sedimentary rocks are offset by the Bahuichivo–Bachamichi fault (yellow dashed line, tick mark on the hanging wall). Cliff of silicic ignimbrite (Tci) deposited over Tcc is ~50 m-tall. (D) West-dipping mafic-intermediate composition dike exhibiting columnar jointing emplaced along a small-scale structure that trends subparallel to the Irigoyen fault, along the Bahuichivo–Irigoyen road (27.36493° N, 108.14926° W). Small-offset faults related to the Irigoyen fault (arrows) cut lavas of the Bahuichivo Volcanics to the right of the dike.

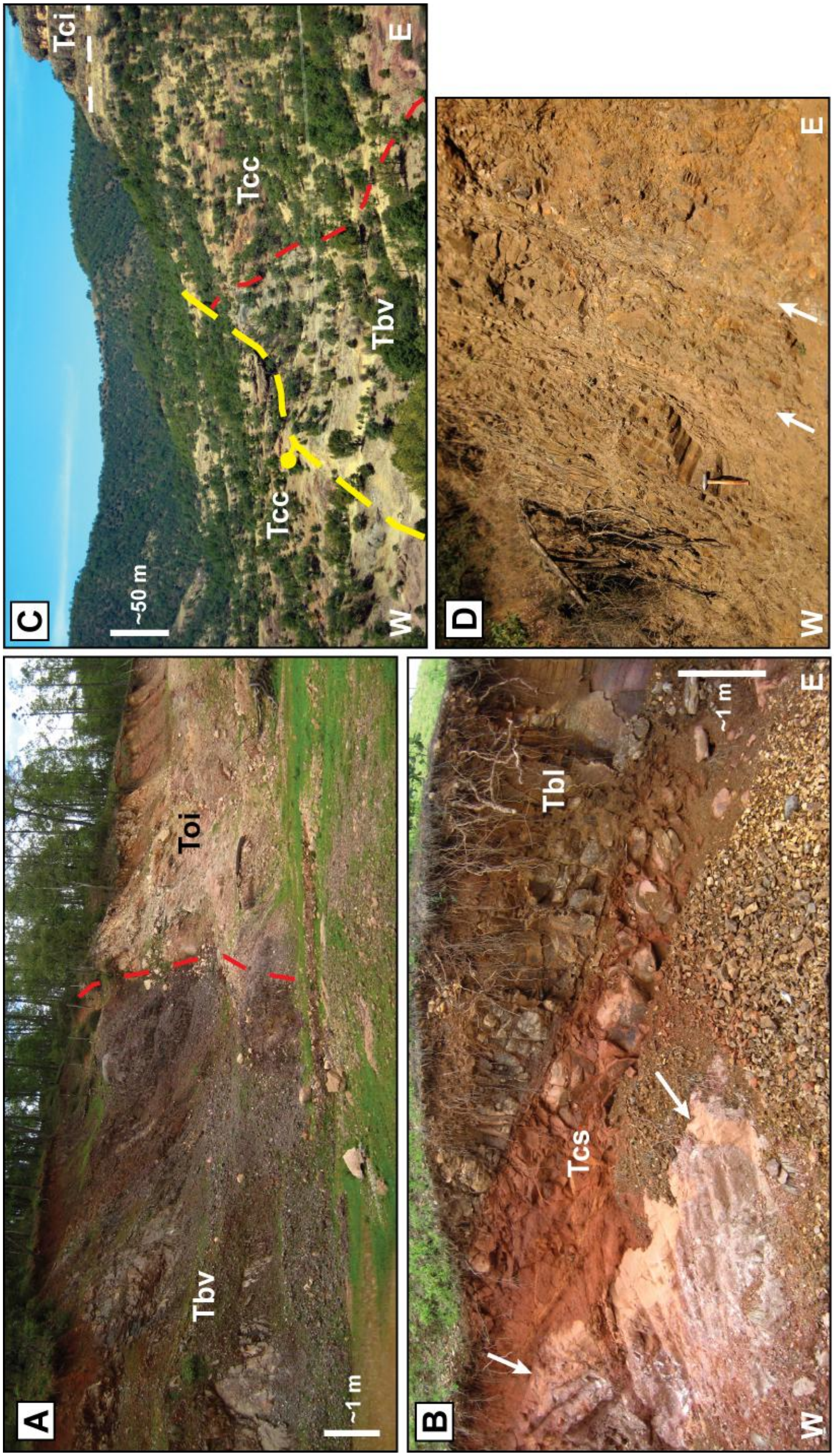
A
Tbv
Toi
~1 m
B
Tcs
Tbl
~1 m
W
E
C
~50 m
Tcc
Tbv
Tcc
Tci
W
E
D
W
E

phenocryst assemblage (olivine, pyroxene, and plagioclase), these rocks suggest a mafic to intermediate composition.

Within the Cerocahui basin, the Bahuichivo Volcanics are dominantly lavas, with individual flows up to ~20 m-thick that dip moderately eastward (to ~20° E) toward the eastern basin bounding faults (Figs. 3 and 4). The base of the Bahuichivo Volcanics is not exposed in the Cerocahui basin; the unit is thickest (>500 m-thick) in the southwestern mapped part of the basin and likely extends westward to the Piedra Bola fault based on aerial imagery. In the northwestern mapped part of the basin near Irigoyen (Fig, 3), lavas of the Bahuichivo Volcanics (Tbl) are interstratified with alluvial red bed sandstones (Tcs) identical to those throughout the basin described below (Figs. 3 and 4A), and locally wet sediment–lava intermixing (peperite) is present (Fig. 6B). Also interbedded with the Bahuichivo Volcanics in this area is the Irigoyen ignimbrite (Tciy), a light gray, crystal-poor, nonwelded silicic ignimbrite with faint compaction foliation of slightly flattened white to tan pumice fragments. Based on this evidence, the lavas of the Bahuichivo Volcanics are considered part of the Cerocahui basin fill.

The Bahuichivo Volcanics are inferred to have been erupted from fault-controlled volcanic centers along the eastern half-graben basin margin. Subvolcanic intrusions occur in the Bahuichivo area, where dikes and intrusions emplaced along small-offset NW-trending structures in the fault-block between the Pañales and Bahuichivo–Bachamichi faults complexly crosscut related lava flows (Tbv), as well as sandstones and conglomerates inferred to be related to the basin fill (Tcc and Tcs, described below) and pre-basinal silicic outflow ignimbrites (Toi) described above (Figs. 3, 6A, and 6C; Supplemental File 2 [see footnote 2]). A mafic-intermediate dike that parallels the Irigoyen fault on the western side of the basin (Figs. 3 and 6D) may have been an additional vent for the volcanic rocks (Tbl) located in this area. The localization of these shallow intrusions on NW-trending structures that trend parallel to the basin-bounding normal faults suggest that these structures provided a conduit for mafic to intermediate magmatism, and that extensional deformation occurred prior to and during emplacement of the Bahuichivo Volcanics.

Cerocahui clastic unit (Tcc & Tcs): Cerocahui basin fill

The majority of the rocks in the Cerocahui basin are part of the over 700 m-thick Cerocahui clastic unit (Tcc and Tcs; Figs. 3, 4, 5, 7, and 8). The rocks of the Cerocahui clastic unit are subdivided into eight sedimentary lithofacies (after Miall, 1985; Uba et al., 2005; Murray et al., 2010) that allow for interpretations of depositional processes (Table 1). This unit consists of volcaniclastic sandstones, conglomerates, and breccias, with interbedded nonwelded silicic ignimbrites and fluvially reworked tuffs (Figs. 5, 7, and 8), deposited in angular unconformity over the mafic-intermediate lavas of the Bahuichivo Volcanics (Figs. 3 and 4). All of the deposits of this stratigraphic unit thicken and coarsen eastward towards the basin-bounding normal faults, with conglomerates and breccias (lithofacies Gm and Gc; Table 1) restricted to the area adjacent to the Bahuichivo–Bachamichi fault (Figs. 3, 4, and 8A–8D). The bulk of the deposits in the Cerocahui clastic unit consist of medium to very thickly bedded (~10 cm- to greater than 1 m-thick), moderately to very poorly sorted, medium-to-very coarse-grained volcaniclastic sandstones and conglomeratic sandstones (lithofacies Sm; Table 1; Figs. 5, 7, and 8B). The conglomeratic sandstones are composed of <30% gravel-sized (>2 mm, to 0.5 m-diameter) subrounded to subangular clasts derived from amygdaloidal mafic-intermediate lavas, silicic flow-banded lavas, and silicic welded to nonwelded ignimbrites. Intercalated with the conglomeratic sandstones on the eastern margin of the basin are medium to very thickly bedded (~10 cm- to greater than 1 m-thick) matrix-supported granule to boulder (to 1 m-diameter) angular-to-subrounded conglomerates and

Figure 7 (*next 2 pages*). Measured stratigraphic section of the Cerocahui clastic unit (map unit Tcc) through basalt lavas (Tm) in the Cerocahui village area (see Fig. 3 for location), depicting facies types of sedimentary units (Table 1) and paleocurrent data from trough limbs (method I of DeCelles et al., 1983). The dominant clast type (>50%) observed in conglomerates and conglomeratic sandstones are listed where recorded in the section; polymictic rocks without a single dominant clast type (<50%) are listed in order of relative abundance. The three informally named nonwelded silicic ignimbrites interbedded within the Cerocahui clastic unit and the stratigraphic position of U-Pb sample BM080718-1 (Fig. 10; Table 2) are also indicated. Lithofacies associations suggest that this stratigraphic section represents medial-proximal alluvial fan deposits in the Cerocahui basin.

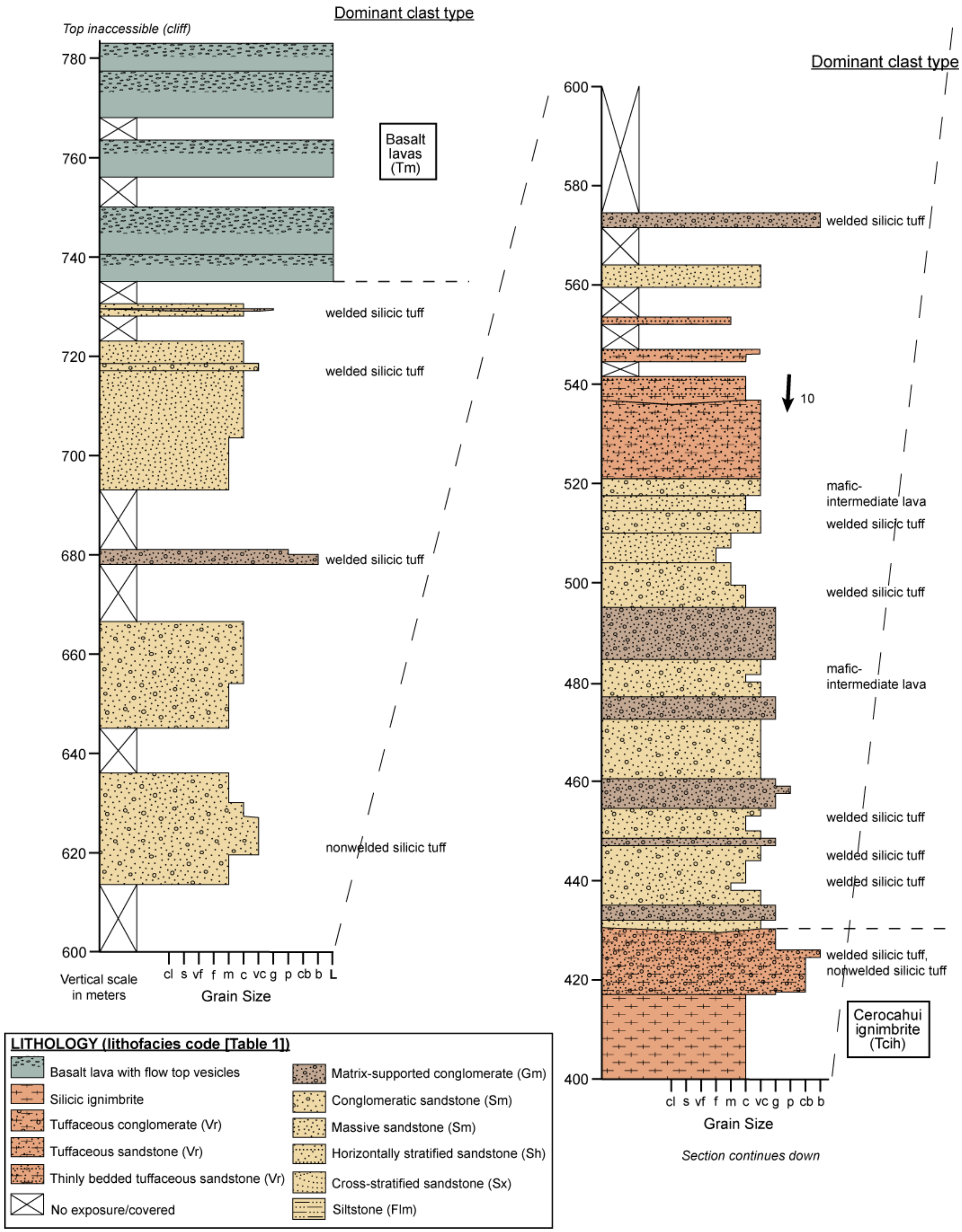
Dominant clast type
Top inaccessible (cliff)
780
760
740
720
700
680
660
640
620
600
Basalt lavas (Tm)
welded silicic tuff
welded silicic tuff
welded silicic tuff
nonwelded silicic tuff
cl s vf f m c vc g p cb b L
Vertical scale in meters
Grain Size
Dominant clast type
600
580
560
540
520
500
480
460
440
420
400
welded silicic tuff
10
mafic-intermediate lava
welded silicic tuff
welded silicic tuff
mafic-intermediate lava
welded silicic tuff
welded silicic tuff
welded silicic tuff
welded silicic tuff, nonwelded silicic tuff
Cerocahui ignimbrite (Tcih)
cl s vf f m c vc g p cb b
Grain Size
Section continues down
LITHOLOGY (lithofacies code [Table 1])
Basalt lava with flow top vesicles
Silicic ignimbrite
Tuffaceous conglomerate (Vr)
Tuffaceous sandstone (Vr)
Thinly bedded tuffaceous sandstone (Vr)
No exposure/covered
Matrix-supported conglomerate (Gm)
Conglomeratic sandstone (Sm)
Massive sandstone (Sm)
Horizontally stratified sandstone (Sh)
Cross-stratified sandstone (Sx)
Siltstone (Flm)

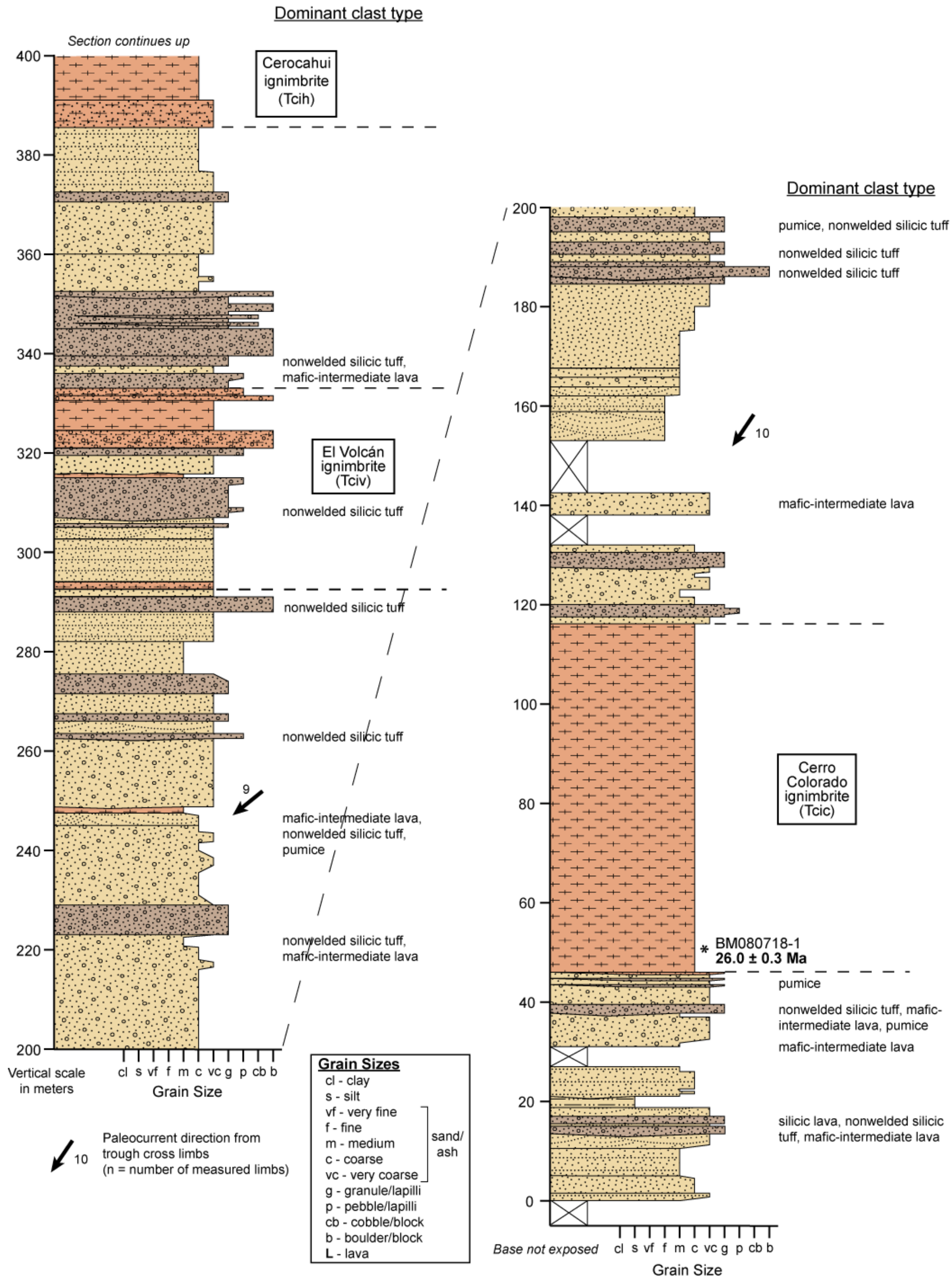
Dominant clast type
Section continues up
Cerocahui ignimbrite (Tcih)
nonwelded silicic tuff, mafic-intermediate lava
El Volcán ignimbrite (Tciv)
nonwelded silicic tuff
nonwelded silicic tuff
nonwelded silicic tuff
9
mafic-intermediate lava, nonwelded silicic tuff, pumice
nonwelded silicic tuff, mafic-intermediate lava
Vertical scale in meters
cl s vf f m c vc g p cb b
Grain Size
Paleocurrent direction from trough cross limbs (n = number of measured limbs)
10
Grain Sizes
cl - clay
s - silt
vf - very fine
f - fine
m - medium
c - coarse
vc - very coarse
sand/ash
g - granule/lapilli
p - pebble/lapilli
cb - cobble/block
b - boulder/block
L - lava
Dominant clast type
pumice, nonwelded silicic tuff
nonwelded silicic tuff
nonwelded silicic tuff
10
mafic-intermediate lava
Cerro Colorado ignimbrite (Tcic)
* BM080718-1
26.0 ± 0.3 Ma
pumice
nonwelded silicic tuff, mafic-intermediate lava, pumice
mafic-intermediate lava
silicic lava, nonwelded silicic tuff, mafic-intermediate lava
Base not exposed
cl s vf f m c vc g p cb b
Grain Size

Figure 8 (*next 2 pages*). Representative photographs of the Cerocahui clastic unit and interbedded silicic ignimbrites; locations of photos are given (NAD27). (A) Overview photograph and geologic interpretation of the Cerocahui basin (looking west from 27.29390° N, 108.03736° W), showing moderately east-dipping (to ~20° E) Cerocahui clastic unit (Tcc) and Cerro Colorado ignimbrite (Tcic) below gently east-dipping to subhorizontal Cerocahui clastic unit, El Volcán ignimbrite (Tciv), Cerocahui ignimbrite (Tcih), and undifferentiated silicic ignimbrite (Tci). The bedding dip decreases and dips slightly more northerly upsection (possibly reflecting the slightly tilted original orientation of the alluvial fan deposits), with basalt lavas (Tm) conformably deposited over the Cerocahui clastic unit. The N-trending Cerocahui fault (tick marks on hanging wall) downdrops the Cerocahui clastic unit to the west, with a silicic hypabyssal intrusion (Tri) emplaced along the fault and crosscutting it. (B) Massive (~4 m-thick) matrix-supported conglomerate (lithofacies Gm; Table 1) with weak inverse grading (left of person) interbedded within conglomeratic sandstone at 225 m on measured stratigraphic section (Fig. 7). Clasts consist of subangular reddish-gray mafic-intermediate volcanic and white nonwelded silicic ignimbrite fragments (27.30315° N, 108.06420° W). (C) Clast-supported conglomerate-breccia (lithofacies Gc; Table 1) with mafic-intermediate volcanic boulders to ~1 m in a medium-to-very coarse-grained sand matrix, interpreted as proximal alluvial fan debris flow deposits adjacent to the Bahuichivo–Bachamichi fault along the Bahuichivo–Cerocahui road (27.34576° N, 108.03776° W). (D) East-dipping matrix-supported conglomerate (lithofacies Gm; Table 1) cutting and filling a channel (arrow) in underlying conglomeratic sandstone (lithofacies Sm; Table 1) adjacent to the Bahuichivo–Bachamichi fault northeast of Cerocahui (27.30809° N, 108.04059° W). (E) Horizontally-stratified fine-to-medium-grained sandstone (lithofacies Sh, Ss; Table 1), with small-scale cut-and-fill structures (arrows) (27.30210° N, 108.06152° W). (F) Reworked pumice lapilli-tuff at the base of the Cerro Colorado ignimbrite (Tcic), infilling a ~4 m-deep channel cut into underlying conglomeratic sandstone (Tcc); close-up of this pumice lapilli-tuff shown in Figure 8G (27.29829° N, 108.06447° W). (G) Close-up of basal reworked pumice lapilli-tuff (lithofacies Vr; Table 1) of the Cerro Colorado ignimbrite (Fig. 8F), with well-sorted lenses of granule to pebble subangular pumice (tan) interbedded within gray tuff (27.29829° N, 108.06447° W). (H) View looking southeast from near base of measured stratigraphic section (Fig. 3; 27.29358° N, 108.06592° W) at Cerro Colorado, with N-dipping white Cerro Colorado ignimbrite (Tcic) capping hill, above red Cerocahui clastic unit (Tcc). (I) Overview photograph and geologic interpretation of growth strata east of the El Rodeo fault in the south-central section of the Cerocahui basin (Fig. 3), looking north from Cerro El Volcán (27.31205 ° N, 108.09606° W). The dip of the units change from ~20° E in the lowermost mafic-intermediate lavas (Tbl), through 10° to 5° within the Cerocahui clastic-unit (Tcs), to ~0° in the capping basalt lavas (Tm), and the unit thicknesses of the Cerocahui clastic unit (Tcs) and El Volcán ignimbrite (Tciv) also increase eastward, indicating syndepositional extension of the eastern fault-bounded margin of the Cerocahui basin. Similar depositional relationships are found on the hanging wall of the El Rodeo fault (Fig. 4B), suggesting syndepositional extension of this fault, with continued postdepositional extension that downdropped the basalt lavas (Tm) to the west.

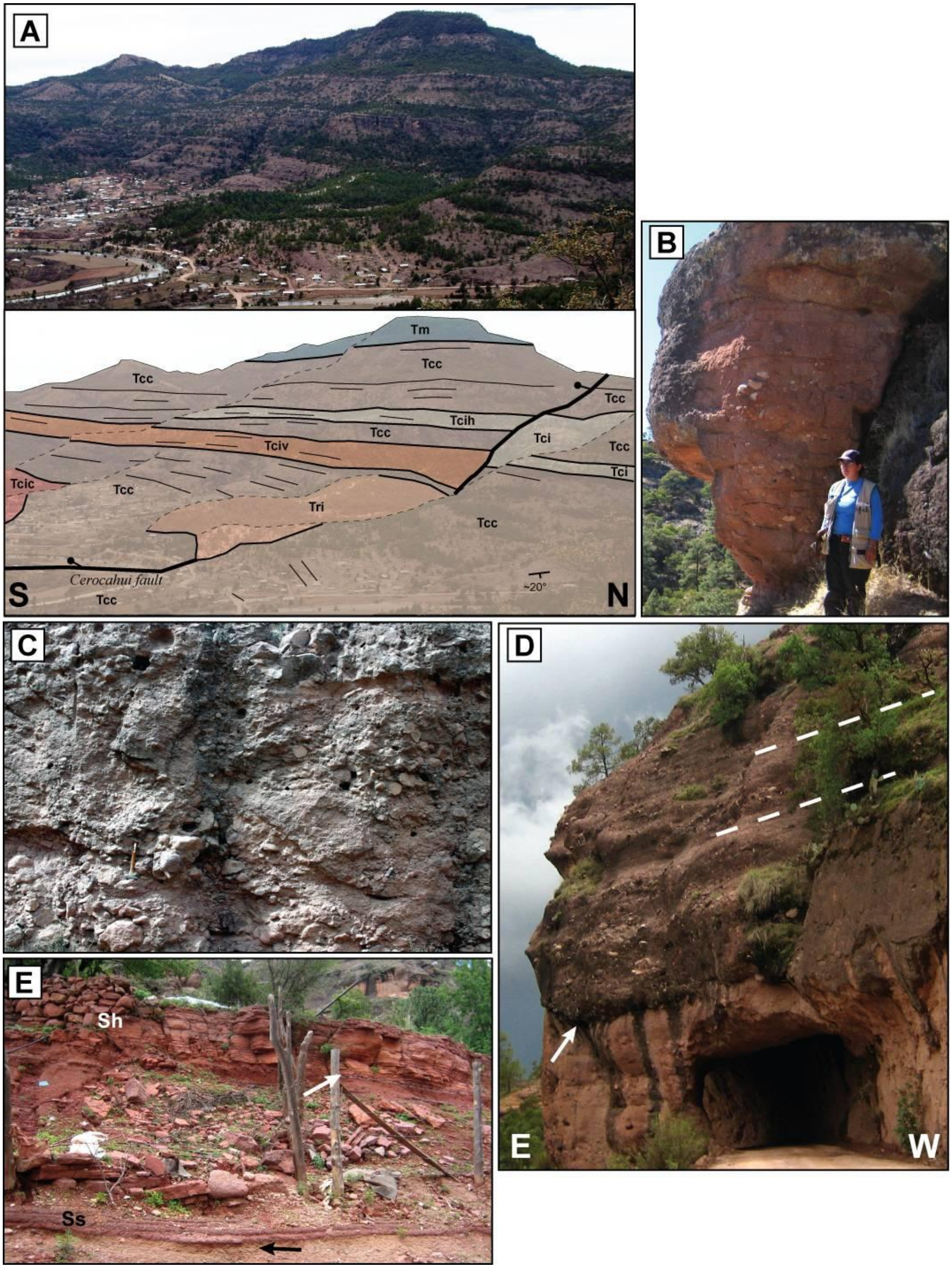

A
B
Tm
Tcc
Tcc
Tcc
Tcih
Tcc
Tci
Tcc
Tciv
Tci
Tcic
Tcc
Tri
Tcc
Cerocahui fault
~20°
S
N
Tcc
C
D
E
W
E
Sh
Ss

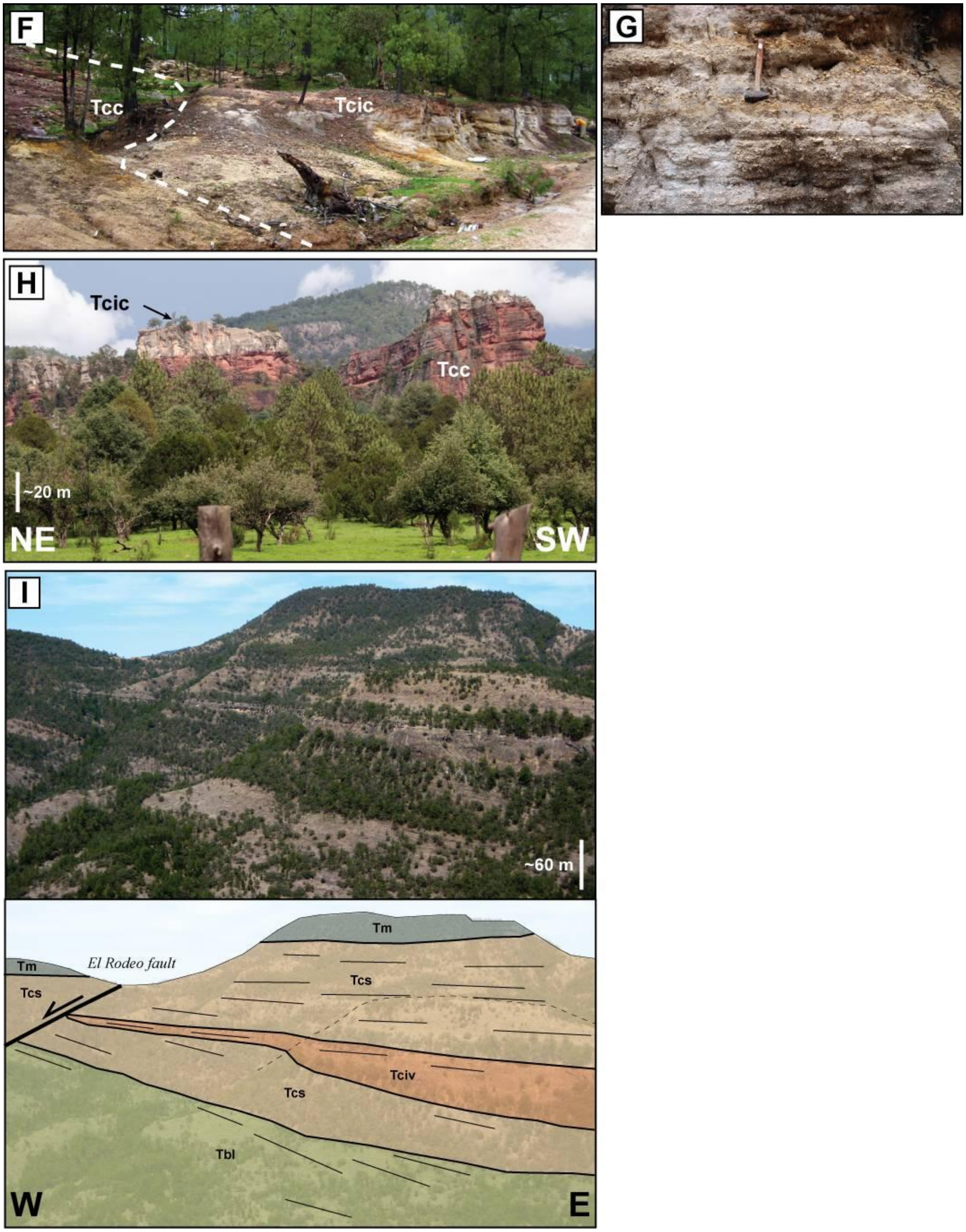
F
Tcc
Tcic
G
H
Tcic
Tcc
~20 m
NE
SW
I
~60 m
Tm
El Rodeo fault
Tm
Tcs
Tcs
Tciv
Tcs
Tbl
W
E

TABLE 1. SEDIMENTARY LITHOFACIES OF THE CEROCAHUI CLASTIC UNIT*

Facies code	Description	Interpretation
Gc	Clast-supported, massive conglomerate and breccia. Dark red to gray. Very poorly sorted, angular to subrounded. Pebbles to boulders with fine-to-very coarse-grained sand matrix. Thickly to very thickly bedded, lobate to tabular bedding extending laterally for several meters to a few hundred meters. No to very poorly developed normal to inverse grading.	Clast-rich debris flow deposits, rapid deposition by stream-floods with concentrated clasts
Gm	Matrix-supported, massive conglomerate. Dark red to gray. Very poorly sorted, subangular to subrounded. Granules to boulders in medium-to-very coarse-grained sand matrix. Medium to very thickly bedded, lenticular to tabular bedding extending laterally for several meters to several hundred meters. No to very poorly developed normal to inverse grading.	Plastic debris flow deposits, deposited from hyperconcentrated or turbulent flow
Sm	Massive sandstone. Tan to red. Medium-to-very coarse-grained, locally conglomeratic with <30% subrounded to subangular pebbles to boulders. Moderately to very poorly sorted. Medium to very thickly bedded, lenticular to tabular bedding extending laterally for tens of meters to a several hundred meters. No to very poorly developed normal to inverse grading.	Hyperconcentrated sediment-gravity flows, rapid deposition
Sx	Cross-stratified sandstone. Tan to red. Trough and low-angle (<10°) cross-stratification. Fine-to-very coarse-grained. Thinly to thickly bedded, lenticular bedding extending laterally for tens of meters, trace lenses of granule to pebbles. Moderately to well sorted.	Channel fills, crevasse splays, dune migration
Sh	Horizontally stratifed sandstone. Tan to red. Very fine-to-coarse-grained, trace lenses of cobbles and pebbles. Well to moderately sorted. Very thinly to thickly bedded, tabular bedding extending laterally for several tens of meters to a few hundred meters.	Planar bed flow, upper flow regime
Ss	Sandstone with basal scour surface. Red to tan. Very coarse-to-medium-grained, locally conglomeratic with <30% granules to pebbles. Normal grading. Lenticular, extending laterally for several meters.	Erosive channel fills
Flm	Massive or laminated siltstone. Red. Lenticular to tabular bedding, extending laterally for tens of meters.	Overbank, abandoned channel or suspension deposits
Vr	Tuffaceous sandstone or conglomerate. White to light tan. Medium-to-very coarse grained sand, granules to boulders. Subangular to subrounded pumice fragments. Laminated to thickly bedded, lenticular to tabular bedding extending laterally for less than one meter to tens of meters. Moderately to poorly sorted.	Reworked primary silicic tuff
* after Miall, 1985; Uba et al., 2005, Murray et al., 2010		

breccias (lithofacies Gc and Gm; Table 1), which have similar clast compositions as the conglomeratic sandstones (Figs. 7 and 8B–8D). The rocks of this unit contain sedimentary structures indicative of fluvial deposition, including channels that indicating southwestward-directed paleoflow, cut-and-fill structures, trough and low-angle cross-stratification (lithofacies Sx; Table 1), and normal to inverse graded bedding (Figs. 7, 8B, and 8D–8G).

Silicic nonwelded ignimbrites and fluvially reworked tuff (tuffaceous sandstones and conglomerates, lithofacies Vr; Table 1) are interbedded within the Cerocahui clastic unit, with four distinct and informally named ignimbrites recognized: the El Rodeo, Cerro Colorado, El Volcán, and Cerocahui ignimbrites (Figs. 3, 4, 7, 8A, 8F–8I; Supplemental File 2 [see footnote 2]). Of these four ignimbrites, the El Rodeo ignimbrite (Tcir) is the stratigraphically lowest. Exposures of this ignimbrite are restricted to the west side (hanging wall) of the El Rodeo fault (described below), where it is deposited directly on the underlying mafic-intermediate lavas of the Bahuichivo Volcanics (Figs. 3 and 4B). The El Rodeo ignimbrite is nonwelded with a tan to light pink groundmass, 20% phenocrysts of plagioclase, biotite, and hornblende, trace lithic fragments, and 25% yellow and salmon colored pumice fragments. The Cerro Colorado ignimbrite (Tcic) crops out in the low-lying areas near Cerocahui and caps Cerro Colorado to the south of the village (Figs. 3, 8A, and 8H). The Cerro Colorado ignimbrite is at least 70 m-thick (Fig. 7), has a light tan groundmass near the base that transitions to light gray at the top, ~5% phenocrysts of plagioclase (to 1.5 mm) and biotite (<1 mm), trace white long-tube pumice fragments (to 2 cm), and trace mafic-intermediate volcanic lithic fragments (to 5 mm). The base of the Cerro Colorado ignimbrite locally consists of a reworked pumice lapilli-tuff deposit (lithofacies Vr; Table 1) that infills a ~4 m-deep channel cut into underlying sandstone (Figs. 8F–8G). The El Volcán ignimbrite (Tciv) forms a prominent ~80 m cliff in the middle part of the ridge north of Cerocahui and extends westward for ~6.5 km, pinching out north of El Rodeo (Figs. 3, 7, 8A, and 8I; Supplemental File 2 [see footnote 2]). This ignimbrite consist of several thin (<5 m-thick) nonwelded primary outflow sheets with a tan to white groundmass, 10–20% phenocrysts (<1 mm) of plagioclase, biotite, and trace clinopyroxene, hornblende, and quartz, <5% lithic fragments (<1 mm), and 15–30% white to yellow long-tube pumice fragments (to 10 mm). The El Volcán ignimbrite is predominantly fluvially reworked and interbedded with conglomerates and sandstones at the location of the measured stratigraphic section northwest of Cerocahui (Fig. 7). The deposits of this ignimbrite located further west at Cerro El Volcán, however, have limited reworking and no interbedded sedimentary deposits. The Cerocahui ignimbrite (Tcih) is a ~27 m-thick unit that crops out on the ridge north of Cerocahui (Fig. 3, 7, and 8A). This ignimbrite is nonwelded with a white groundmass, 10–15% phenocrysts of plagioclase, biotite, quartz, and hornblende, 5–10% lithic fragments (~1 mm), and 15% yellow pumice fragments. The base and top of the Cerocahui ignimbrite consist of tuffaceous sandstone and conglomerate (reworked tuff) that is more stratified and better sorted than the rest of the ignimbrite deposit (Fig. 7).

Based on stratigraphic relations and sedimentary lithofacies (Table 1), the Cerocahui clastic unit likely represents deposition in alluvial fan systems (e.g., Miall, 1985; Kelly and Olsen, 1993; Blair and McPherson, 1994; Collinson, 1996; Murray et al., 2010). The interpretation of these sedimentary rocks as alluvial deposits is supported by the presence of clast-to-matrix-supported conglomerates, breccias (lithofacies Gc and Gm; Table 1), and conglomeratic sandstones (lithofacies Sm; Table 1) interpreted as sediment-gravity flow deposits, stratified to cross-stratified sandstones (lithofacies Sh and Sx; Table 1) interpreted as fluvial deposits, and deposits that infill channels cut into underlying strata (Figs. 7 and 8B–8G). The silicic ignimbrites interstratified with the volcaniclastic rocks were likely erupted from distal sources and deposited in the basin, based on their nonwelded nature and high proportion of interstratified fluvially reworked tuff (Fig. 7).

Deposition of the Cerocahui clastic unit likely occurred during extensional deformation of the eastern basin-bounding normal faults. Evidence of synextensional deposition includes the increased thickness and coarseness of the Cerocahui clastic unit towards the basin-bounding fault, with these deposits either ending at the Bahuichivo–Bachamichi fault or thinning onto the fault-block between the Bahuichivo–Bachamichi and Pañales faults (Figs. 3 and 4; Supplemental File 2 [see footnote 2]). Evidence of possible growth strata is indicated by an upsection decrease in bedding dip from ~18° E to 6° E is observed within the Cerocahui clastic unit along the Irigoyen–Bahuichivo road, as well as an upsection dip decrease from 13° E to 5° N in the vicinity of the measured stratigraphic section near Cerocahui (Figs. 3 and 4; Supplemental File 2 [see footnote 2]). In addition, angular unconformities between and within the Bahuichivo Volcanics, Cerocahui clastic unit, and basalt lavas (described below) are observed within the basin (Figs. 3, 4, 8A, and 8I; Supplemental File 2 [see footnote 2]). These unconformities and upsection changes in bedding dip angle can be explained by either crustal flexural subsidence related to sediment loading, or by syndepositional tilting related to normal fault motion on the eastern half-graben margin (i.e., growth strata). The latter explanation of synextensional deposition is preferred, given the limited, thinner exposures of Cerocahui basin deposits east of the Bahuichivo–Bachamichi fault and the subparallel NW-alignment of Bahuichivo Volcanic intrusions to the half-graben bound fault system. Syndepositional extension of the El Rodeo fault within the basin is suggested by the restriction of the El Rodeo ignimbrite to the hanging wall of this fault, as well as gently dipping (<5° E) Cerocahui clastic unit rocks deposited in angular unconformity above moderately tilted (15° E) Cerocahui clastic unit sandstone on the hanging wall of the fault (Figs. 4B and 8I). Additional syndepositional to postdepositional offset of the Bahuichivo–Bachamichi and El Rodeo faults resulted in the development of drag synclines on the hanging wall adjacent to these faults (Figs. 3 and 4B; Supplemental File 2 [see footnote 2]).

Basalt lavas: uppermost Cerocahui basin fill

Conformably overlying the Cerocahui clastic unit is a flat lying to gently dipping (<10°) basalt lava unit (Tm; Figs. 3, 4, 7, and 8A; Supplemental File 2 [see footnote 2]). The basalt lavas are widespread and appear to cap all of the ridges within the study area (Fig. 3; Supplemental File 2 [see footnote 2]). This unit is composed of several lavas that have flow-banded interiors and vesicular flow tops, with individual flows to ~10 m-thick (Fig. 7). These basalt lavas are gray with a microlitic to glassy groundmass, and contain trace phenocrysts of plagioclase, olivine, and clinopyroxene. The entire stratigraphic unit has an estimated thickness of over 300 m, with the greatest thickness in the northwestern part of the basin (Fig. 3; Supplemental File 2 [see footnote 2]). The vents for the basalt lava flows have not been identified within the study area. The basalts appear to have been erupted prior to the end of extensional deformation in the basin, because the stratigraphic unit appears to be vertically offset across the El Rodeo fault and the Bahuichivo–Bachamichi fault north of Bahuichivo, and is not present on the footwall of the Pañales fault (Fig. 4A).

Silicic hypabyssal intrusions: post-basinal magmatism

The youngest lithologic unit in the study area is composed of silicic hypabyssal intrusions/plugs (Tri) that were emplaced following volcaniclastic and volcanic deposition in the Cerocahui basin (Figs. 3, 5, 8A, and 9). These subvertically flow-banded intrusions are located along the southern mapped section of the basin-bounding Bahuichivo–Bachamichi fault (Fig. 9A) and within the Cerocahui clastic unit along the Cerocahui fault where this

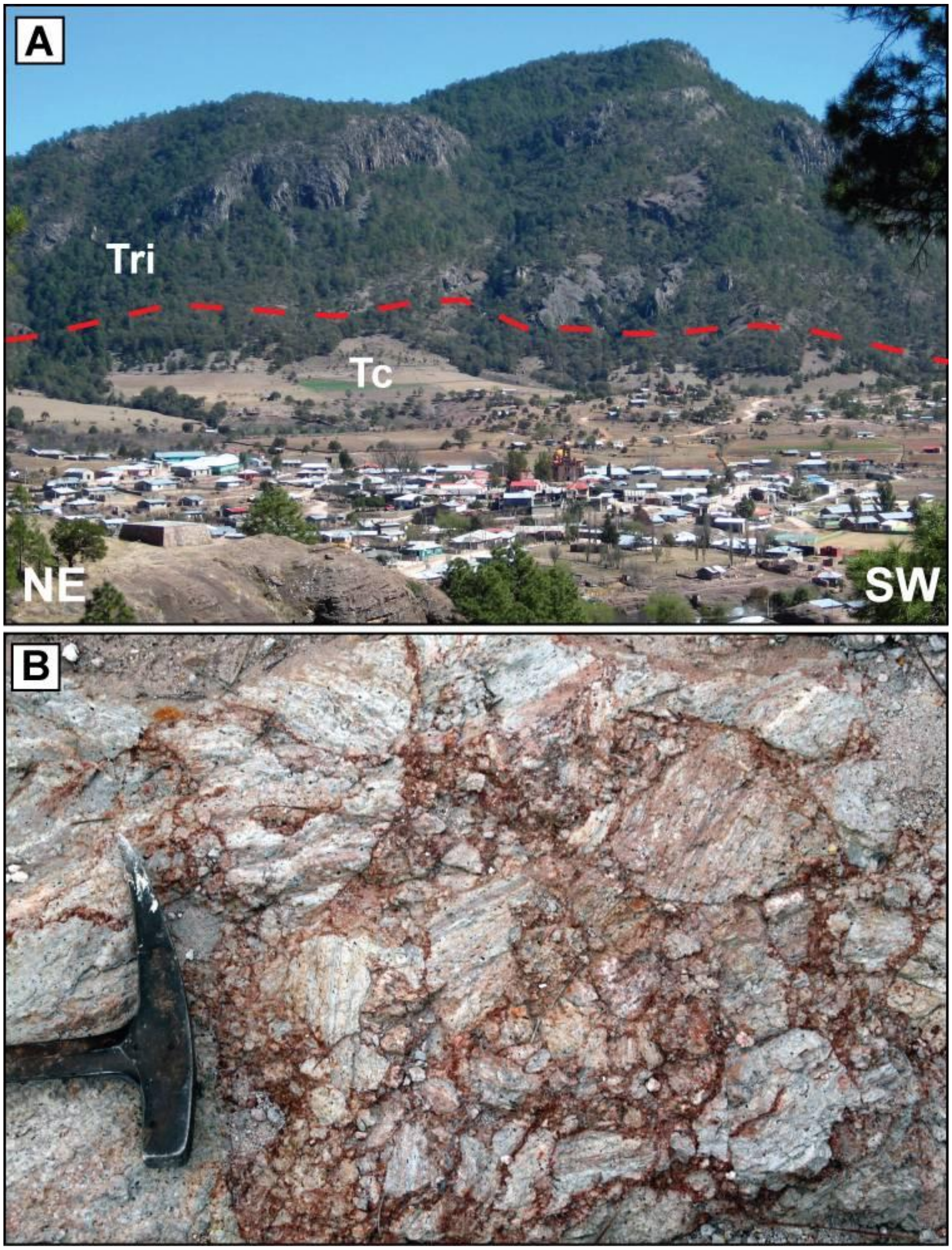

Figure 9. Representative photographs of the silicic hypabyssal intrusions (Tri); locations of photos are given (NAD27). (A) Subvertically flow-banded intrusions (Tri) emplaced into Cerocahui basin deposits (Tc) and forming a prominent ridge southeast of Cerocahui (foreground) along the southern projection Bahuichivo–Bachamichi fault (Fig. 3; looking southeast from 27.30569° N, 108.06423° W). Approximate location of intrusive contact indicated. (B) Flow-banded blocks in the brecciated perimeter of the silicic hypabyssal intrusion intruded along the Cerocahui fault (27.30202 ° N, 108.05304° W).

fault that cuts the Cerocahui clastic unit diverges into two branches in the village of Cerocahui (Figs. 3 and 8A). Increased tilting of the Cerocahui clastic unit occurred adjacent to the margins of the intrusions during emplacement (Supplemental File 2 [see footnote 2]). The silicic hypabyssal intrusion near Cerocahui has a perimeter of flow-banded blocks (Fig. 9B), suggesting brecciation during emplacement. The rocks of this intrusion are white, flow-banded, with 5–25% euhedral phenocrysts of plagioclase and biotite.

DEPOSITIONAL AGE CONSTRAINTS

Methodology & Age Interpretations

U-Pb zircon ages were obtained from two silicic ignimbrites within the Cerocahui basin, providing constraints on the age of these previously undated deposits. Laser ablation–inductively coupled plasma–mass spectrometry (LA–ICP-MS) U-Pb analyses were performed at the Laboratorio de Estudios Isotópicos, Centro de Geociencias, Universidad Nacional Autónoma de México (UNAM) on zircons separated from the two silicic ignimbrite samples (Fig. 10; Table 2; Appendix 4), using the analytical methods and age calculations detailed in Murray et al. (2013).

It is common to observe mixed age populations due to zircon inheritance in Tertiary samples previously dated in the Sierra Madre Occidental (e.g., Bryan et al., 2008; Ferrari et al., 2013; Murray et al., 2013). The inherited zircons in our analyzed samples are inferred to include both xenocrysts and antecrysts, with the latter formed during earlier phases of related magmatism within the igneous province (e.g., Charlier et al., 2004; Bryan et al., 2008). In the Sierra Madre Occidental, which has a long-lived 15–20 Myr history of continuous magmatism, inheritance signatures are a common problem for zircons dated from the younger (Early Miocene) rocks (e.g., Bryan et al., 2008; Ferrari et al., 2013; Murray et al., 2013) and

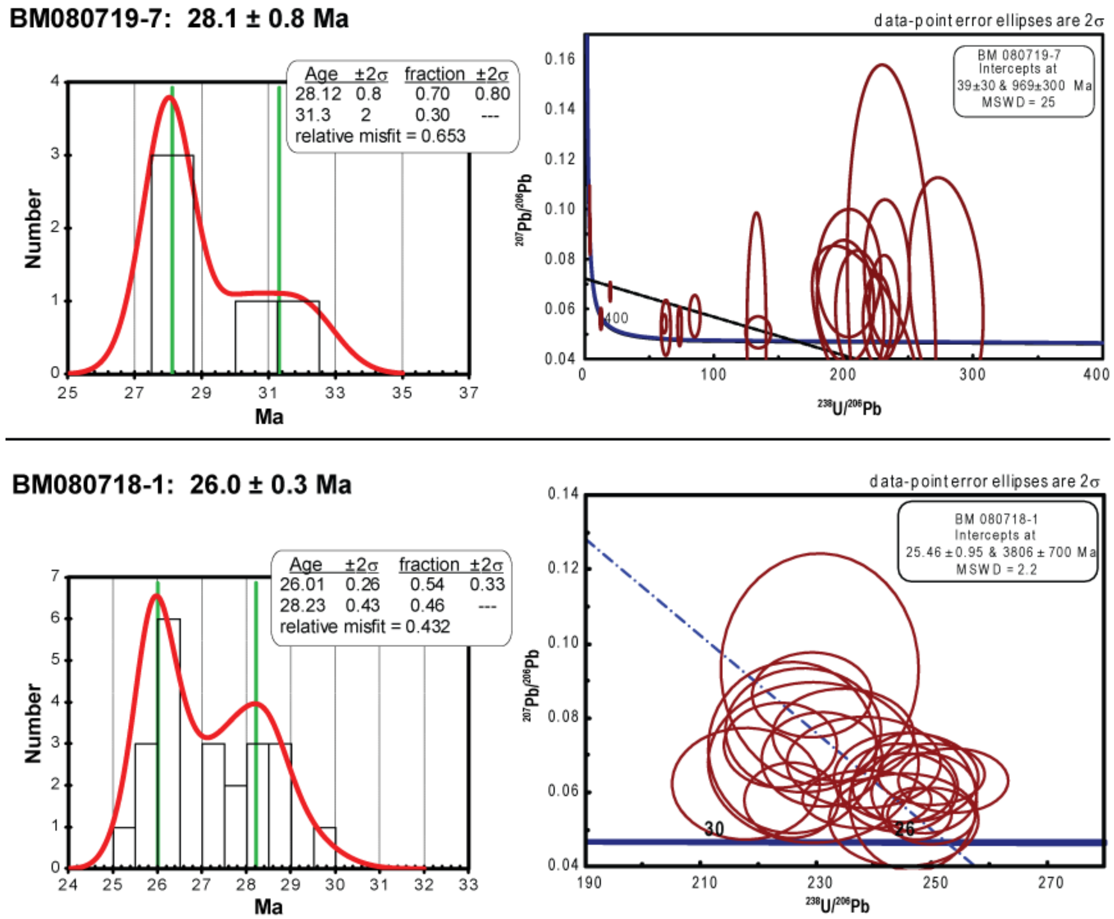

Figure 10. Summary of zircon U-Pb LA–ICP–MS analyses for samples listed in Table 2, with mean $^{206}Pb/^{238}U$ ages of the youngest zircon population (interpreted phenocryst crystallization age) for each sample is listed. For each sample, probability density distribution plots with age calculations (left) using the deconvolution method in Isoplot 3.70 (Ludwig, 2008) and Tera-Wasserburg concordia plots (right) are shown. MSWD—mean square of weighted deviates. Details on the experiments are given in Appendix 4.

TABLE 2. SUMMARY OF ZIRCON U-Pb LA-ICP-MS RESULTS

Sample	Map unit	Lithology	Age (Ma)*	±2σ (Ma)	n	Latitude (°N)	Longitude (°W)
BM080718-1	Tcic	Cerro Colorado ignimbrite	26.0	0.3	12	27.29832	108.06507
			28.2	*0.4*	10		
BM080719-7	Tciy	Irigoyen ignimbrite	28.1	0.8	3	27.36548	108.15269
			31.3	*2*	2		

Notes : LA-ICP-MS—laser ablation–inductively coupled plasma–mass spectrometry. Ages in italics represent the zircon antecryst (proposed by Charlier et al., 2004; crystals that predate crystallization and eruption of a host magma, but formed during an earlier phase of related magmatism) age population in a given sample. The youngest age population of each sample is interpreted as the preferred eruption or emplacement age. Details of each analysis are given in Appendix 4. North American Datum 1927 (NAD27) datum is used for latitude and longitude. Map unit labels correspond to Figure 3. The relative stratigraphic position of ages are shown in Figure 5. Locations of the samples are shown in Figures 3 and 7 and on Supplemental File 2 (see footnote 2).
n—number of zircons used for age calculation

* Mean $^{206}Pb/^{238}U$ age calculated using the deconvolution method in Isoplot 3.70 (Ludwig, 2008)

distinguishing antecrysts from xenocrysts that are unrelated to earlier phases of magmatism is difficult, as antecryst ages may be older than the host magma phenocryst ages by more than 10 Myr (Bryan et al., 2008). In addition, given the higher uncertainty of LA–ICP-MS dating compared to other U-Pb geochronology methods (e.g., SIMS, TIMS, SHRIMP), it is difficult to differentiate zircons into antecrysts and xenocrysts at time scales <1 Myr; generally within the Sierra Madre Occidental, any zircon younger than 38 Ma was likely produced by magmatism associated with the silicic large igneous province, i.e. antecrysts, while older zircons (older than 38 Ma) were likely incorporated into the host magma from mid-lower crustal rocks unrelated to the Sierra Madre Occidental magmatism, i.e. xenocrysts (Ferrari et al., 2013).

In our analyses, we interpret the oldest zircon age population that is less than ca. 38 Ma in a sample to represent the crystallization age of antecrysts incorporated into the host magma and that the youngest zircon age population indicates the age of phenocryst crystallization, which we interpret as an approximation of the eruption age of the rock. Age results are presented in the following and summarized in Figure 10 and Table 2, with the locations of the samples shown in Figure 3 and Supplemental File 2 (see footnote 2); detailed analytical data are given in Appendix 4.

Results

Sample BM080719-7 is from the Irigoyen ignimbrite (Tciy) at the northwestern basin margin near Irigoyen (Figs. 3, 4A, and 5). This ignimbrite (described above) is interstratified with lavas of the Bahuichivo Volcanics (Tbl) and the lowermost sandstones (Tcc) of the Cerocahui basin (Figs. 3 & 4A; Supplemental File 2 [see footnote 2]). U-Pb data for this sample reveal the presence of several xenocrysts with Proterozoic (ca. 1.7 Ga; n=1), Paleozoic (ca. 481 and 318 Ma; n=2), Late Cretaceous (ca. 104–75 Ma; n=4), and Early

Eocene (ca. 48 Ma; n=2) ages (Appendix 4). From the analysis of five non-xenocrystic zircons (Table 2; Appendix 4), two age populations are recognized in sample BM080719-7 consisting of an older grouping having a mean age of 31.3 ± 2 Ma and a younger grouping with a mean age of 28.1 ± 0.8 Ma (Fig. 10; Table 2). The zircons of the older age population are likely antecrysts, while the zircons from the younger age population are interpreted as phenocrysts. The phenocryst age overlaps within uncertainty with ages of the pre-basinal silicic outflow ignimbrites to the west (e.g., 27.6 ± 0.3 Ma Puerto Blanco ignimbrite of the Parajes formation; Murray et al., 2013). Given the stratigraphic constraints and the large age uncertainties with sample BM080719-7 due to limited number of analyzed non-xenocrystic zircons, the Irigoyen ignimbrite (Tciy) is likely equivalent-age or slightly younger than the underlying Puerto Blanco ignimbrite, with an eruption age (based on uncertainties) between ca. 27.9–27.3 Ma. This age suggests that initial eruption of the Bahuichivo Volcanics within the Cerocahui basin occurred ca. 27.5 Ma.

Sample BM080718-1 is from the base of the Cerro Colorado ignimbrite (Tcic; described above) near Cerocahui, which is interbedded in the lower section of the Cerocahui clastic unit stratigraphically above the Bahuichivo Volcanics (Figs. 3, 4B, 5, and 7). Unlike the previous sample, xenocrysts were not found in this sample. From the analysis of 22 zircons (Table 2; Appendix 4), two age populations are recognized in sample BM080718-1, consisting of an older group with a mean age of 28.2 ± 0.4 Ma and a younger group that has a mean age of 26.0 ± 0.3 Ma (Fig. 10; Table 2). Similar to the sample above, the older zircon age population is likely antecrystic, and the population of younger zircons is interpreted as phenocrysts. This phenocryst age overlaps within uncertainty with the age of the Témoris Formation in the Guazapares Mining District region, which is bracketed at ca. 27–24.5 Ma by U-Pb zircon ages of the underlying and overlying formations (Parajes and Sierra Guazapares formations, respectively) and interbedded silicic ignimbrites (Murray et al., 2013). In addition, this data provides a minimum age for the eruption of the underlying Bahuichivo Volcanics at ca. 26 Ma.

DISCUSSION

Cerocahui Basin Evolution

The new geologic mapping, stratigraphy, and geochronology presented in this study show that the rocks of the Cerocahui basin region record Late Oligocene (ca. 27.5 Ma to likely older than 24.5 Ma) synextensional volcanism and volcaniclastic alluvial deposition during the mid-Cenozoic ignimbrite flare-up in the northern Sierra Madre Occidental. The developmental history of the Cerocahui basin includes (Fig. 11): (1) deposition of welded silicic outflow ignimbrite sheets; (2) synextensional magmatism and deposition of the Bahuichivo Volcanics, Cerocahui clastic unit, and basalt lavas in the Cerocahui basin during a lull in silicic ignimbrite flare-up volcanism; and (3) emplacement of silicic hypabyssal intrusions along preexisting extensional faults in the Cerocahui basin.

The silicic outflow ignimbrite sheets that underlie the Cerocahui basin are similar to Late Oligocene outflow ignimbrite sheets in adjacent regions of the northern Sierra Madre Occidental, erupted during the end of the Early Oligocene pulse of the ignimbrite flare-up (Swanson et al., 2006; Murray et al., 2013). Similar to the ignimbrites of the Parajes formation in the Guazapares Mining District region (Murray et al., 2013), the degree of welding and flow thicknesses of the pre-basinal ignimbrites suggest that these rocks were also possibly erupted from calderas within 50–100 km of the Cerocahui basin region that temporally overlap with the end of Late Oligocene ignimbrite flare-up volcanism to the east, although more geochronologic data are needed to confirm this interpretation. There is no

Figure 11 (*next page*). Schematic block diagrams illustrating the developmental history of the Cerocahui basin. The colors correspond to the map units in Figure 3. (A) Pre-basinal eruption of plateau-forming welded silicic outflow ignimbrites from distant (>50 km) sources, with sheets extending eastward from the Cerocahui basin and westward to the Guazapares Mining District region. (B) Initiation of crustal extension resulted in eruption of the Bahuichivo Volcanics from fault-controlled vents, primarily along the eastern basin margin, into the Cerocahui basin and onto the basin-bounding footwall. The lavas of the Bahuichivo Volcanics are interstratified with alluvial sandstone and the Irigoyen ignimbrite in the basin. (C) Extensional uplift related to continued motion of the basin-bounding normal faults triggers erosion of the Bahuichivo Volcanics, with resulting mafic-intermediate volcanic-rich material (green clasts) deposited in the lower part of the Cerocahui clastic unit. (D) Further extensional deformation of the basin-bounding normal faults unroofs the older silicic outflow ignimbrites, resulting in mixed nonwelded to welded silicic ignimbrite (pink clasts) and mafic-intermediate volcanic detritus (green clasts) deposited in the upper section of the Cerocahui clastic unit. (E) Eruption of the basalt lavas into the Cerocahui basin, followed by offset of the basalt lava unit across the Bahuichivo–Bachamichi fault. Silicic hypabyssal intrusions were emplaced along the basin-bounding Bahuichivo–Bachamichi fault and normal faults within the basin that offset older deposits.

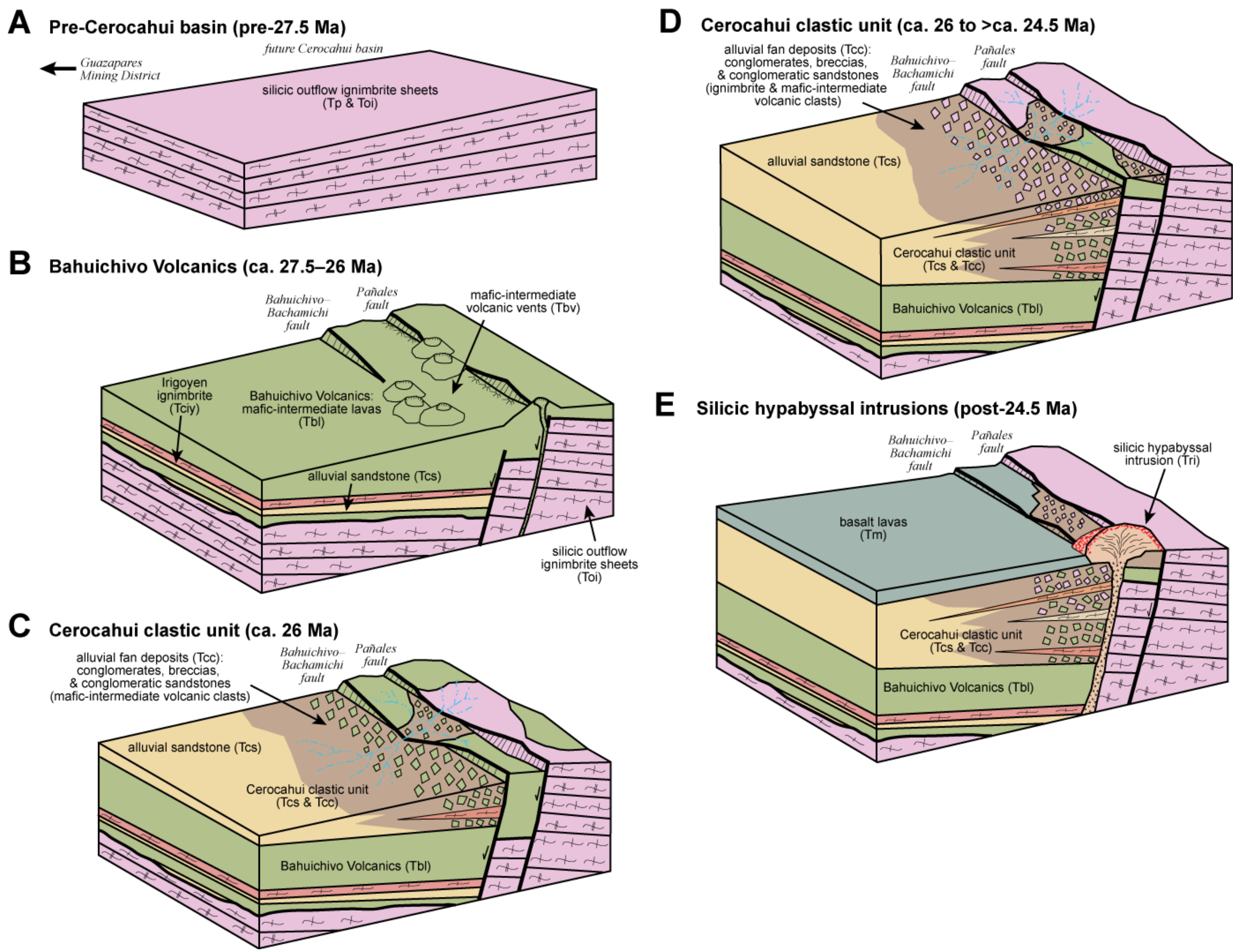
A
Pre-Cerocahui basin (pre-27.5 Ma)
future Cerocahui basin
Guazapares
Mining District
silicic outflow ignimbrite sheets
(Tp & Toi)
B
Bahuichivo Volcanics (ca. 27.5–26 Ma)
Bahuichivo–
Bachamichi
fault
Pañales
fault
mafic-intermediate
volcanic vents (Tbv)
Irigoyen
ignimbrite
(Tciy)
Bahuichivo Volcanics:
mafic-intermediate lavas
(Tbl)
alluvial sandstone (Tcs)
silicic outflow
ignimbrite sheets
(Toi)
C
Cerocahui clastic unit (ca. 26 Ma)
alluvial fan deposits (Tcc):
conglomerates, breccias,
& conglomeratic sandstones
(mafic-intermediate volcanic clasts)
Bahuichivo–
Bachamichi
fault
Pañales
fault
alluvial sandstone (Tcs)
Cerocahui clastic unit
(Tcs & Tcc)
Bahuichivo Volcanics (Tbl)
D
Cerocahui clastic unit (ca. 26 to >ca. 24.5 Ma)
alluvial fan deposits (Tcc):
conglomerates, breccias,
& conglomeratic sandstones
(ignimbrite & mafic-intermediate
volcanic clasts)
Bahuichivo–
Bachamichi
fault
Pañales
fault
alluvial sandstone (Tcs)
Cerocahui clastic unit
(Tcs & Tcc)
Bahuichivo Volcanics (Tbl)
E
Silicic hypabyssal intrusions (post-24.5 Ma)
Bahuichivo–
Bachamichi
fault
Pañales
fault
silicic hypabyssal
intrusion (Tri)
basalt lavas
(Tm)
Cerocahui clastic unit
(Tcs & Tcc)
Bahuichivo Volcanics (Tbl)

direct evidence of extensional deformation in the region of the Cerocahui basin during deposition of the silicic outflow ignimbrite sheets (Fig. 11A), such as occurred during deposition of the upper (post-ca. 27.5 Ma) part of the ignimbrite section in the Guazapares Mining District region (Murray et al., 2013). However, given that the oldest age within the Cerocahui basin is from a thin nonwelded ignimbrite interbedded with the Bahuichivo Volcanics that overlie the Parajes formation near the Piedra Bola fault (28.1 ± 0.8 Ma), and this is the same age (within uncertainty) of the timing of the onset of extension to the west, extension in the Cerocahui basin region may have also begun during deposition of the youngest silicic outflow ignimbrites.

Depositional relationships, growth strata, and subvolcanic intrusions that are likely fault-localized suggest that the Bahuichivo Volcanics, Cerocahui clastic unit, and basalt lavas represent the synextensional growth of mafic-intermediate volcanic centers and volcaniclastic alluvial deposition in the Cerocahui basin during the Late Oligocene (Figs. 11B–11E). The alluvial fan deposits of the Cerocahui clastic unit likely formed a bajada along the eastern margin of the Cerocahui basin adjacent to the basin-bounding fault and prograded into the subsiding half-graben from the east and accumulated over the Bahuichivo Volcanics (Figs. 11C–11D).

The stratigraphic trend in conglomerate-breccia clast compositions in the Cerocahui clastic unit shows an upsection decrease in mafic-intermediate volcanic fragments and an upsection increase in welded and nonwelded ignimbrite clasts, with fragments of silicic lava restricted to the lowest rocks of the section (Fig. 7). The flow-banded silicic lava clasts suggest erosion of silicic volcanoes or plugs in the vicinity of the Cerocahui basin, as mafic-intermediate volcanic fragments are intermingled with the silicic lava clasts in the alluvial deposits; further study is needed to determine the source of these silicic lava clasts and its relative timing to the eruption of the Bahuichivo Volcanics. The upsection trends in clast composition appear to record inverse stratigraphy related to unroofing of the active half-graben footwall block (Figs. 7 and 11C–11D), with erosion of the Bahuichivo Volcanics (Fig. 11C) followed by erosion of the silicic outflow ignimbrite sheets (Fig. 11D). The rocks on the footwall of the Bahuichivo–Bachamichi fault consist of silicic outflow ignimbrites, the Bahuichivo Volcanics, and limited conglomerate and ignimbrite deposits of the Cerocahui clastic unit, whereas rocks on the footwall of the Pañales fault to the east are restricted to pre-basinal silicic outflow ignimbrites; sedimentary and volcanic deposits related to the Cerocahui basin strata described above are not identified immediately east of this fault (Fig. 3; Supplemental File 2 [see footnote 2]). This absence of Cerocahui basin fill supports the interpretation that extensional footwall uplift led to erosion of the Bahuichivo Volcanics first, and then the underlying silicic outflow ignimbrites, with their erosional products deposited in the adjacent half-graben basin to the west (Figs. 11C–11D).

Following deposition of the Cerocahui clastic unit, basalt lavas were erupted and ponded within the Cerocahui basin (Fig. 11E). As noted above, these lavas are offset by the basin-bounding fault system and normal faults within the basin (Figs. 3 and 4; Supplemental File 2 [see footnote 2]), suggesting synvolcanic extension. Although there are no direct crosscutting relationships, the silicic hypabyssal intrusions are inferred to be younger than the basalt lavas. This relative age relationship is based on the undeformed nature of the silicic intrusions, and that they are emplaced along the southern projection of the basin-bounding fault near Cerocahui, a fault that offsets the basalt lavas to the north near Bahuichivo (Fig. 3; Supplemental File 2 [see footnote 2]), as well as along faults within the basin that offset older deposits of the Cerocahui clastic unit. The somewhat close association of the silicic hypabyssal intrusions with normal faults suggests that these preexisting structures were utilized as pathways for magma accent and emplacement (Fig. 11E).

Regional Correlations

Based on similar lithology, timing of synextensional deposition, and proximity, the three stratigraphic subdivisions within the Cerocahui basin (Bahuichivo Volcanics, Cerocahui clastic unit, and basalt lavas) are broadly correlative with the ca. 27–24.5 Ma Témoris formation in the Guazapares Mining District region (e.g., Murray et al., 2013). Like the stratigraphy of the Cerocahui basin, the Témoris formation is dominated by synextensional mafic-intermediate volcanic rocks and fault-localized intrusive equivalents, volcaniclastic alluvial fan deposits, and an upper section of interbedded alluvial deposits and distal silicic ignimbrites deposited above the mafic-intermediate lavas. However, there are much greater proportions of sandstones, conglomerates, and breccias in the Cerocahui basin than there are in the Témoris Formation. In addition, the basalt lavas that cap the Cerocahui basin deposits are not present in the Témoris formation to the west.

The sizes of half-graben basins in the Cerocahui and Guazapares Mining District regions also differ. In the Guazapares Mining District region, several closely spaced half-graben basins are generally smaller (~1 to 4 km-wide, 100 to >600 m-deep) than the ~12 km-wide, >1,200 m-deep Cerocahui basin (Fig. 2). Perhaps this size difference is related to the position of the Cerocahui basin immediately adjacent to the unextended core of the Sierra Madre Occidental to the east, and the more diffusely faulted Guazapares Mining District region to the west represents a transition into the Gulf Extensional Province.

The silicic hypabyssal intrusions in the Cerocahui basin are not dated directly, but they are tentatively correlated with the ca. 24.5–23 Ma Sierra Guazapares formation of the Guazapares Mining District region (e.g., Murray et al., 2013), which records the onset of local silicic flare-up-related magmatism ~20 km to the west during the onset of the Early Miocene pulse of the ignimbrite flare-up. The Sierra Guazapares formation includes fault-localized fissure magmatism with silicic hypabyssal intrusions emplaced along preexisting faults (Murray et al., 2013), similar to the fault-controlled silicic intrusions in the Cerocahui basin (Fig. 11E). However, as noted above, in the Cerocahui basin, these intrusions do not pass upward into ignimbrites or lavas as they do in the Sierra Guazapares formation; it is not known whether this is an artifact of preservation (i.e., the top of the section is eroded), or if silicic volcanism was minimal in the Cerocahui region.

The Late Oligocene timing of volcanism and synextensional deposition in the Cerocahui basin is generally consistent with regional data patterns suggesting a post- ca. 40 Ma southwestward migration of extension and arc-front magmatism across Sierra Madre Occidental (e.g., Damon et al., 1981; Gans, 1997; Gans et al., 2003; Ferrari et al., 2007; Henry et al., 2010). The ca. 27.5–26 Ma Bahuichivo Volcanics postdate Late Eocene to Early Oligocene volcanism to the northeast of the study area, and are older than to coeval with Late Oligocene to Early Miocene volcanism to the west in Sonora (Ferrari et al., 2007; Murray et al., 2013 and references therein). Likewise, the Late Oligocene age of extension of the Cerocahui basin is roughly coeval with the onset of extension in the Guazapares Mining District immediately to the west and is slightly older (~1–6 Myr) than the onset of extension in the end Oligocene–Early Miocene fault-bound grabens and core complexes farther west in Sonora (Gans, 1997; McDowell et al., 1997; Wong et al., 2010).

CONCLUSIONS

The rocks in the Cerocahui basin and adjacent Guazapares Mining District region record Late Oligocene to Early Miocene magmatism and synextensional deposition in the northern Sierra Madre Occidental during the mid-Cenozoic ignimbrite flare-up. The oldest rocks in this region are silicic outflow ignimbrite sheets erupted during the end of the Early Oligocene pulse of the ignimbrite flare-up from sources likely to the east, representing medial outflow facies that were mostly deposited prior to development of the Cerocahui half-graben basin. These ignimbrites are likely correlative with the ca. 27.5 Ma Parajes formation immediately to the west in the Guazapares Mining District region, which suggests synextensional deposition of the youngest ignimbrites of the formation, and to ignimbrite sections described to the east by Swanson et al. (2006). The overlying synextensional deposits of the Cerocahui basin include: (1) the basal basin fill, consisting of the ca. 27.5–26 Ma Bahuichivo Volcanics, mafic-intermediate lavas erupted from fault-localized synextensional volcanic centers primarily on the eastern half-graben margin; (2) the Cerocahui clastic unit, consisting largely of a bajada of alluvial fan-fluvial systems with minor interbedded distal ignimbrites that prograded into the half-graben basin from the active eastern fault margin; and (3) a >300 m-thick section of basalt lavas ponded within, and restricted to, the Cerocahui basin. The mafic-intermediate volcanic and alluvial deposits of the Cerocahui basin are likely equivalent to the ca. 27.5–24.5 Ma Témoris formation in the Guazapares Mining District and represent a period of the Southern Cordillera basaltic andesite (SCORBA) magmatism erupted after the Early Oligocene ignimbrite pulse. Following deposition in the Cerocahui basin, silicic hypabyssal intrusions were emplaced along normal faults in the Cerocahui basin. These silicic intrusions are likely related to the 24.5–23 Ma Sierra Guazapares formation in the Guazapares Mining District, which were emplaced during the Early Miocene pulse of the ignimbrite flare-up. The Late Oligocene to Early Miocene timing of magmatism and synextensional deposition in the Cerocahui basin and Guazapares Mining District regions generally supports the regional interpretation that ignimbrite flare-up magmatism and crustal extension migrated southwestward with time.

REFERENCES CITED

Aguirre-Díaz, G. J., and Labarthe-Hernández, G., 2003, Fissure ignimbrites: Fissure-source origin for voluminous ignimbrites of the Sierra Madre Occidental and its relationship with Basin and Range faulting: Geology, v. 31, no. 9, p. 773–776.

Aguirre-Díaz, G. J., and McDowell, F. W., 1991, The volcanic section at Nazas, Durango, Mexico, and the possibility of widespread Eocene volcanism within the Sierra Madre Occidental: Journal of Geophysical Research, v. 96, no. B8, p. 13373-13388.

Aguirre-Díaz, G. J., and McDowell, F. W., 1993, Nature and timing of faulting and synextensional magmatism in the southern Basin and Range, central-eastern Durango, Mexico: Geological Society of America Bulletin, v. 105, p. 1435-1444.

Armstrong, R. L., and Ward, P. L., 1991, Evolving geographic patterns of Cenozoic magmatism in the North American Cordillera: the temporal and spatial association of magmatism and metamorphic core complexes: Journal of Geophysical Research, v. 96, no. B8, p. 13,201-13,224.

Best, M. G., and Christiansen, E. H., 1991, Limited extension during peak Tertiary volcanism, Great Basin of Nevada and Utah: Journal of Geophysical Research, v. 96, p. 13509-13528.

Best, M. G., Christiansen, E. H., and Gromme, S., 2013, Introduction: The 36-18 Ma southern Great Basin, USA, ignimbrite province and flareup: Swarms of subduction-related supervolcanoes: Geosphere, v. 9, p. 260-274.

Blair, T. C., and McPherson, J. G., 1994, Alluvial fans and their natural distinction from rivers based on morphology, hydraulic processes, sedimentary processes, and facies assemblages: Journal of Sedimentary Research, v. A64, no. 3, p. 450-489.

Bryan, S., 2007, Silicic large igneous provinces: Episodes, v. 30, no. 1, p. 1-12.

Bryan, S. E., and Ernst, R. E., 2008, Revised definition of Large Igneous Provinces (LIPs): Earth-Science Reviews, v. 86, p. 175-202.

Bryan, S. E., and Ferrari, L., 2013, Large igneous provinces and silicic large igneous provinces: Progress in our understanding over the last 25 yr: Geological Society of America Bulletin, v. 125, no. 7/8, p. 1053-1078.

Bryan, S. E., Ferrari, L., Reiners, P. W., Allen, C. M., Petrone, C. M., Ramos-Rosique, A., and Campbell, I. H., 2008, New insights into crustal contributions to large-volume rhyolite generation in the mid-Tertiary Sierra Madre Occidental Province, Mexico, revealed by U-Pb geochronology: Journal of Petrology, v. 49, no. 1, p. 47-77.

Bryan, S. E., Orozco-Esquivel, T., Ferrari, L., and López-Martínez, M., 2013, Pulling apart the mid to late Cenozoic magmatic record of the Gulf of California: Is there a Comondú arc?, *in* Gomez-Tuena, A., Straub, S. M., and Zellmer, G. F., eds., Orogenic Andesites and Crustal Growth, Geological Society of London Special Publication 385 (*in press*).

Bryan, S. E., Riley, T. R., Jerram, D. A., Leat, P. T., and Stephens, C. J., 2002, Silicic volcanism: An undervalued component of large igneous provinces and volcanic rifted

margins, *in* Menzies, M. A., Klemperer, S. L., Ebinger, C. J., and J., B., eds., Volcanic Rifted Margins: Geological Society of America Special Paper 362, p. 97-118.
Busby, C. J., 2013, Birth of a plate boundary ca. 12 ma in the Ancestral Cascades arc, Walker Lane belt of California and Nevada: Geosphere, v. 9, no. 5, p. 1147-1160.
Cameron, K. L., Nimz, G. J., Niemeyer, S., and Gunn, S., 1989, Southern Cordilleran basaltic andesite suite, southern Chihuahua, Mexico: a link between Tertiary continental arc and flood basalt magmatism in North America: Journal of Geophysical Research, v. 94, no. B6, p. 7817-7840.
Cather, S. M., Dunbar, N. W., McDowell, F. W., McIntosh, W. C., and Scholle, P. A., 2009, Climate forcing by iron fertilization from repeated ignimbrite eruptions: The icehouse -silicic large igneous province (SLIP) hypothesis: Geosphere, v. 5, no. 3, p. 315-324.
Charlier, B. L. A., Wilson, C. J. N., Lowenstern, J. B., Blake, S., Van Calsteren, P. W., and Davidson, J. P., 2004, Magma generation at a large, hyperactive silicic volcano (Taupo, New Zealand) revealed by U-Th and U-Pb systematics in zircons: Journal of Petrology, v. 46, p. 3-32.
Christiansen, R. L., and Yates, R. S., 1992, Post-Laramide geology of the western U.S. Cordillera, *in* Burchfiel, B. C., Lipman, P. W., and Zoback, M. L., eds., The Cordilleran Orogen: conterminous U. S.: The Geology of North America, Decade of North American Geology, Volume G-3: Boulder, CO, Geological Society of America, p. 261-406.
Cochemé, J. J., and Demant, A., 1991, Geology of the Yécora area, northern Sierra Madre Occidental, Mexico, *in* Pérez-Segura, E., and Jacques-Ayala, C., eds., Studies in Sonoran Geology: Geological Society of America Special Paper 254, p. 81-94.
Collinson, J. D., 1996, Alluvial sediments, *in* Reading, H. G., ed., Sedimentary Environments: Processes, Facies and Stratigraphy, 3rd Edition: Oxford, Blackwell Science, p. 37-82.
Coney, P. J., 1978, Mesozoic-Cenozoic Cordilleran plate tectonics, *in* Smith, R. B., and Eaton, G. P., eds., Cenozoic tectonics and regional geophysics of the Western Cordillera: Geological Society of America Memoir 152: Boulder, CO, Geological Society of America, p. 33-50.
Coney, P. J., and Reynolds, S. J., 1977, Cordilleran Benioff zones: Nature, v. 270, p. 403-406.
Costa, A., Gottsmann, J., Melnik, O., and Sparks, R. S. J., 2011, A stress-controlled mechanism for the intensity of very large magnitude explosive eruptions: Earth and Planetary Science Letters, v. 310, no. 1-2, p. 161-166.
Damon, P. E., Shafiqullah, M., and Clark, K. F., 1981, Age trends of igneous activity in relation to metallogenesis in the southern Cordillera: Arizona Geological Society Digest, v. 14, p. 137-154.
DeCelles, P. G., Langford, R. P., and Schwartz, R. K., 1983, Two new methods of paleocurrent determination from trough cross-stratification: Journal of Sedimentary Petrology, v. 53, p. 629-642.
Dickinson, W. R., 2002, The Basin and Range Province as a composite extensional domain: International Geology Review, v. 44, p. 1-38.
Dickinson, W. R., 2006, Geotectonic evolution of the Great Basin: Geosphere, v. 2, no. 7, p. 353-368.

Dickinson, W. R., 2013, Phanerozoic palinspastic reconstructions of Great Basin geotectonics (Nevada-Utah, USA): Geosphere, v. 9, no. 5, p. 1384-1396.

Dickinson, W. R., and Snyder, W. S., 1978, Plate tectonics of the Laramide orogeny, *in* Matthews, V., ed., Laramide Folding Associated with Basement Block Faulting in the Western United States Geological Society of America Memoir 151, p. 355-366.

Dreier, J., 1984, Regional tectonic control of epithermal veins in the Western United States and Mexico, *in* Wilkins, J., ed., Gold and silver deposits of the Basin and Range Province, Western U.S.A., Arizona Geological Society Digest, v. 15, p. 28-50.

Ferrari, L., López-Martínez, M., Orozco-Esquivel, T., Bryan, S. E., Duque-Trujillo, J., Lonsdale, P., and Solari, L., 2013, Late Oligocene to Middle Miocene rifting and synextensional magmatism in the southwestern Sierra Madre Occidental, Mexico: The beginning of the Gulf of California rift: Geosphere, v. 9, no. 5, p. 1161-1200.

Ferrari, L., López-Martínez, M., and Rosas-Elguera, J., 2002, Ignimbrite flare-up and deformation in the southern Sierra Madre Occidental, western Mexico: Implications for the late subduction history of the Farallon plate: Tectonics, v. 21, no. 4, p. 1-24.

Ferrari, L., Valencia-Moreno, M., and Bryan, S., 2007, Magmatism and tectonics of the Sierra Madre Occidental and its relation with the evolution of the western margin of North America, *in* Alaniz-Álvarez, S. A., and Nieto-Samaniego, Á. F., eds., Geology of México: Celebrating the Centenary of the Geological Society of México: Geological Society of America Special Paper 422, p. 1-39.

Gans, P. B., 1997, Large-magnitude Oligo-Miocene extension in southern Sonora: Implications for the tectonic evolution of northwest Mexico: Tectonics, v. 16, p. 388-408.

Gans, P. B., Blair, K. D., MacMillan, I., Wong, M. S., and Roldán-Quintana, J., 2003, Structural and magmatic evolution of the Sonoran rifted margin: A preliminary report: Geological Society of America Abstracts with Programs, v. 35, no. 4, p. 21.

González León, C. M., McIntosh, W. C., Lozano-Santacruz, R., Valencia-Moreno, M., Amaya-Martínez, R., and Rodríguez-Castañeda, J. L., 2000, Cretaceous and Tertiary sedimentary, magmatic, and tectonic evolution of north-central Sonora (Arizpe and Bacanuchi Quadrangles), northwest Mexico: Geological Society of America Bulletin, v. 112, no. 4, p. 600-610.

Grijalva-Noriega, F. J., and Roldán-Quintana, J., 1998, An overview of the Cenozoic tectonic and magmatic evolution of Sonora, northwestern Mexico: Revista Mexicana de Ciencias, v. 15, no. 2, p. 145-156.

Henry, C., and Aranda-Gómez, J. J., 2000, Plate interactions control middle-late Miocene, proto-Gulf and Basin and Range extension in the southern Basin and Range: Tectonophysics, v. 218, p. 1-26.

Henry, C. D., McIntosh, W., McDowell, F. W., Lipman, P. W., Chapin, C. E., and Richardson, M. T., 2010, Distribution, timing, and controls of the mid-Cenozoic ignimbrite flareup in western North America: Geological Society of America Abstracts with Programs, v. 42, no. 5, p. 144.

Henry, C. D., McIntosh, W. C., McDowell, F. W., Lipman, P. W., and Chapin, C. E., 2012, The Cenozoic ignimbrite flareup in western North America: distribution, timing, volume, and tectonic relations: Geological Society of America Abstracts with Programs, v. 44, no. 3, p. 21.

Hildreth, W., 1981, Gradients in silicic magma chambers: Implications for lithospheric magmatism: Journal of Geophysical Research, v. 86, no. B11, p. 10153-10192.

Kelly, S. B., and Olsen, H., 1993, Terminal fans - a review with reference to Devonian examples: Sedimentary Geology, v. 85, p. 339-374.
Lipman, P. W., 2007, Incremental assembly and prolonged consolidation of Cordilleran magma chambers: Evidence from the Southern Rocky Mountain volcanic field: Geosphere, v. 3, no. 1, p. 42-70.
Luhr, J. F., Henry, C. D., Housh, T. B., Aranda-Gómez, J. J., and McIntosh, W. C., 2001, Early extension and associated mafic alkalic volcanism from the southern Basin and Range Province: Geology and petrology of the Rodeo and Nazas volcanic fields, Durango (Mexico): Geological Society of America Bulletin, v. 113, p. 760–773.
McDowell, F. W., 2007, Geologic transect across the northern Sierra Madre Occidental volcanic field, Chihuahua and Sonora, Mexico: Geological Society of America Digital Map and Chart Series 6, 70 p.
McDowell, F. W., 2012, Timing of intense magmatic episodes in the northern and central Sierra Madre Occidental, western Mexico: Geological Society of America Abstracts with Programs, v. 44, no. 3, p. 21.
McDowell, F. W., and Clabaugh, S. E., 1979, Ignimbrites of the Sierra Madre Occidental and their relation to the tectonic history of western Mexico, *in* Chapin, C. E., and Elston, W. E., eds., Ash-Flow Tuffs: Geological Society of America Special Paper 180, p. 113-124.
McDowell, F. W., and Keizer, R. P., 1977, Timing of mid-Tertiary volcanism in the Sierra Madre Occidental between Durango City and Mazatlan, Mexico: Geological Society of America Bulletin, v. 88, p. 1479-1487.
McDowell, F. W., and Mauger, R. L., 1994, K-Ar and U-Pb zircon chronology of Late Cretaceous and Tertiary magmatism in central Chihuahua State, Mexico: Geological Society of America Bulletin, v. 106, p. 118-132.
McDowell, F. W., and McIntosh, W. C., 2012, Timing of intense magmatic episodes in the northern and central Sierra Madre Occidental, western Mexico: Geosphere, v. 8, no. 6, p. 1502-1526.
McDowell, F. W., Roldán-Quintana, J., and Amaya-Martínez, R., 1997, Interrelationship of sedimentary and volcanic deposits associated with Tertiary extension in Sonora, Mexico: Geological Society of America Bulletin, v. 109, no. 10, p. 1349-1360.
McQuarrie, N., and Oskin, M., 2010, Palinspastic restoration of NAVDat and implications for the origin of magmatism in southwestern North America: Journal of Geophysical Research, v. 115, no. B10401
Miall, A. D., 1985, Architectural-element analysis: A new method of facies analysis applied to fluvial deposits: Earth Science Review, v. 22, p. 261-308.
Minjárez Sosa, I., Montaño Jiménez, T. R., Ochoa Granillo, J. A., Grijalva Noriega, F. J., Ochoa Landín, L. H., Herrera Urbina, S., Guzmán Espinosa, J. B., and Mancilla Gutiérrez, A. A., 2002, Carta Geológico-Minera Ciudad Obregón G12-3 Sonora, Chihuahua y Sinaloa: Servicio Geológico Mexicano, scale 1:250,000.
Murray, B. P., Busby, C. J., Ferrari, L., and Solari, L. A., 2013, Synvolcanic crustal extension during the mid-Cenozoic ignimbrite flare-up in the northern Sierra Madre Occidental, Mexico: Evidence from the Guazapares Mining District region, western Chihuahua: Geosphere, v. 9, no. 5, p. 1201-1235.
Murray, B. P., Horton, B. K., Matos, R., and Heizler, M. T., 2010, Oligocene–Miocene basin evolution in the northern Altiplano, Bolivia: Implications for evolution of the central

Andean backthrust belt and high plateau: Geological Society of America Bulletin, v. 122, no. 9/10, p. 1443-1462.
Nieto-Samaniego, Á. F., Ferrari, L., Alaniz-Álvarez, S. A., Labarthe-Hernández, G., and Rosas-Elguera, J., 1999, Variation of Cenozoic extension and volcanism across the southern Sierra Madre Occidental volcanic province, Mexico: Geological Society of America Bulletin, v. 111, no. 3, p. 347-363.
Ramírez Tello, E., and Garcia Peralta, Á. A., 2004, Carta Geológico-Minera Témoris G12-B39 Chihuahua: Servicio Geológico Mexicano, scale 1:50,000.
Swanson, E. R., Kempter, K. A., McDowell, F. W., and McIntosh, W. C., 2006, Major ignimbrites and volcanic centers of the Copper Canyon area: A view into the core of Mexico's Sierra Madre Occidental: Geosphere, v. 2, no. 3, p. 125-141.
Swanson, E. R., and McDowell, F. W., 1984, Calderas of the Sierra Madre Occidental volcanic field, western Mexico: Journal of Geophysical Research, v. 89, p. 8787-8799.
Swanson, E. R., and McDowell, F. W., 1985, Geology and geochronology of the Tomochic caldera, Chihuahua, Mexico: Geological Society of America Bulletin, v. 96, p. 1477-1482.
Uba, C. E., Heubeck, C., and Hulka, C., 2005, Facies analysis and basin architecture of the Neogene Subandean synorogenic wedge, southern Bolivia: Sedimentary Geology, v. 180, p. 91-123.
Ward, P. L., 1991, On plate tectonics and the geologic evolution of southwestern North America: Journal of Geophysical Research, v. 96, no. B7, p. 12,479-12,496.
Wark, D. A., Kempter, K. A., and McDowell, F. W., 1990, Evolution of waning subduction-related magmatism, northern Sierra Madre Occidental, Mexico: Geological Society of America Bulletin, v. 102, p. 1555-1564.
Wong, M. S., Gans, P. B., and Scheier, J., 2010, The $^{40}Ar/^{39}Ar$ thermochronology of core complexes and other basement rocks in Sonora, Mexico: Implications for Cenozoic tectonic evolution of northwestern Mexico: Journal of Geophysical Research, v. 115, no. B07414, doi: 10.1029/2009JB007032.

APPENDIX 1:

MODAL POINT-COUNT ANALYSES

Sample #	Map Unit (rock type)	UTM (E)	UTM (N)	Plagioclase	K-feldspar	Quartz	Olivine (iddingsite)	Clinopyroxene	Orthopyroxene	Pyroxene (altered)	Hornblende	Biotite	Lithic (intermediate volcanic)	Lithic (silicic volcanic)	Lithic (sedimentary)	Oxide	Pumice/ Fiamme	Glass shards	Groundmass (<30 µm)
Volcanic and intrusive rocks																			
BM080716-3	Tsv (lapilli-tuff)	767488	3035631	122	0	5	0	0	0	0	0	12	41	346	0	17	12	0	445
BM080913-2	Tsv (dome collapse breccia)	767553	3035717	113	1	2	0	0	0	0	0	12	0	0	0	2	0	0	870
BM081108-2	Tsiw (high-silica rhyolite plug)	769509	3033142	110	0	0	0	0	0	0	0	14	0	0	0	0	0	0	876
BM081030-2	Tsi (rhyolite plug)	774067	3023722	105	0	0	0	0	0	0	0	16	0	0	0	8	0	0	871
BM080717-2	Tsi (rhyolite plug)	770930	3030946	44	0	0	0	0	0	0	0	3	0	0	0	0	0	0	953
BM081106-2	Tsl (rhyolite lava)	769569	3027995	220	0	11	0	0	0	0	0	39	0	0	0	13	0	0	717
BM081109-3	Tsl (rhyolite lava)	771278	3030001	125	0	0	0	0	0	0	0	12	0	0	0	5	0	0	858
BM080915-1	Tsl (rhyolite lava)	773483	3023362	123	0	2	0	0	0	0	0	26	0	0	0	2	0	38	809
BM080714-5	Tst (rhyolite ignimbrite)	773776	3023237	102	0	0	0	0	0	0	0	16	0	10	0	10	0	88	774
BM081106-3	Tst (rhyolite ignimbrite)	769695	3028093	59	0	0	0	0	0	0	0	10	20	86	2	5	396	22	400
BM081109-2	Tsxi (cross-bedded ignimbrite)	771513	3030486	99	0	0	0	0	0	0	0	11	43	98	0	11	446	11	281
BM080917-3	Tsxi (cross-bedded ignimbrite)	772576	3023996	132	0	1	0	0	0	0	0	15	63	67	0	10	111	13	588
BM080720-5B	Tsxi (cross-bedded ignimbrite)	767886	3027810	28	3	9	0	0	0	0	0	3	51	39	0	1	407	33	426
BM080914-5	Tti (rhyolite ignimbrite)	773353	3023292	45	0	0	0	0	0	0	0	9	3	50	0	4	192	70	627
BM080720-1A	Tti (rhyolite ignimbrite)	768486	3027279	29	11	0	0	0	0	0	0	8	13	76	0	3	551	33	276
BM081111-4	Tta (andesite lava)	775962	3025045	225	0	0	0	9	8	0	0	0	0	0	0	4	0	0	754
BM080914-4	Tta (andesite lava)	773280	3023250	290	0	0	0	12	9	32	0	0	0	0	0	19	0	0	638
BM080624-3	Ttat (andesite lapilli-tuff)	770411	3028741	105	0	0	0	0	0	12	0	0	165	27	0	45	36	23	587
BM080623-2	Ttb (basaltic trachy-andesite lava)	769956	3035620	308	0	0	27	5	0	0	0	0	0	0	0	27	0	0	633
BM080914-1	Ttba (andesite lava)	773050	3022995	319	0	0	3	10	5	0	0	0	0	0	0	12	0	0	651
BM080714-1	Ttv (basalt lava)	771758	3021613	367	0	0	2	1	0	0	0	0	0	0	0	16	0	0	614
BM081215-2	Ttv (andesite intrusion)	772102	3020878	269	0	0	0	3	0	19	0	0	0	0	0	7	0	0	702
BM080714-2	Ttv (basaltic andesite lava)	771836	3021633	275	0	0	0	16	0	37	0	0	0	0	0	6	0	0	666
BM100308-2	Ttai (andesitic intrusion)	777809	3027569	226	0	0	0	0	0	2	0	0	0	0	0	0	0	0	772
BM100311-2	Ttt (silicic tuff)	781009	3029940	70	0	0	0	0	0	0	0	5	8	23	0	9	0	1	884
BM100317-1	Tpt (Traza ignimbrite)	780593	3027899	147	0	0	0	4	0	8	0	0	71	66	0	12	56	111	525
BM100311-1	Tpk (KM ignimbrite)	779351	3029336	67	0	1	0	0	0	1	1	0	22	64	0	4	286	21	533
BM081206-3	Tpr (Rancho de Santiago ign.)	776466	3032270	77	0	0	0	0	0	8	2	0	22	29	0	10	22	31	799
BM081102-1	Tpr (Rancho de Santiago ign.)	776630	3028619	127	0	0	0	0	0	19	5	0	32	134	0	13	51	8	611
BM081213-1	Tpr (Rancho de Santiago ign.)	780963	3029226	129	0	0	0	0	0	14	0	0	21	27	0	14	68	59	668
BM100310-1	Tpr (Rancho de Santiago ign.)	778344	3029085	210	0	0	0	14	1	15	0	0	37	21	0	16	73	21	592
BM100308-1	Tpb (Puerto Blanco ignimbrite)	777703	3027352	61	0	0	0	1	0	1	1	0	78	41	0	5	171	120	521
BM100310-2	Tpb (Puerto Blanco ignimbrite)	779492	3028758	87	0	0	0	0	0	0	0	15	95	28	2	8	99	132	534
BM100306-6	Tpb (Puerto Blanco ignimbrite)	778205	3029126	67	0	0	0	0	0	0	0	6	21	27	5	7	127	57	683
BM081031-4B	Tpp (Portero ignimbrite)	775575	3024549	104	0	5	0	9	0	4	5	0	20	18	0	10	74	161	590
BM100317-2	Tpe (Ericicuchi ignimbrite)	779559	3023057	81	0	0	0	8	0	6	2	9	105	29	0	3	75	40	642
BM081031-3	Tpe (Ericicuchi ignimbrite)	775440	3024642	105	0	0	1	4	1	8	1	3	168	30	0	12	11	55	601
BM100309-1	Tpc (Chepe ignimbrite)	777984	3025713	193	0	79	0	0	0	0	0	30	8	5	0	4	206	0	475
BM-DIV-2	Divisadero Tuff	220954	3048433	174	0	64	0	0	0	0	4	35	4	11	0	10	170	16	512
Sandstones																			
BM080702-2	Ttss (feldspathic litharenite)	769026	3026813	64	0	0	0	9	0	0	0	1	60	53	2	6	10	0	95
BM080712-2	Ttas (feldspathic litharenite)	769302	3032491	83	9	2	0	0	0	3	0	0	52	38	4	17	0	0	92

Notes: Universal Transverse Mercator (UTM) coordinates are based on the North American Datum 1927 (NAD27) zone 12 (BM-DIV-2 located in zone 13). Map unit labels correspond to Table 1. For volcanic and intrusive rocks, 1000 point counts per thin section; for sandstones 300 point counts per thin section

APPENDIX 2:

GUAZAPARES MINING DISTRICT REGION ZIRCON U-Pb LASER ABLATION ICP-MS ANALYTICAL RESULTS

BM100306-1	Ericicuchi ignimbrite (Tpe)			Mean $^{206}Pb/^{238}U$ age (±2σ): 27.6 ± 0.3 Ma															
				CORRECTED RATIOS[2]									CORRECTED AGES (Ma)						
	U[1] (ppm)	Th[1] (ppm)	Th/U	$^{207}Pb/^{206}Pb$	±1σ[3]	$^{207}Pb/^{235}U$	±1σ[3]	$^{206}Pb/^{238}U$	±1σ[3]	$^{208}Pb/^{232}Th$	±1σ[3]	Rho	$^{206}Pb/^{238}U$	±1σ	$^{207}Pb/^{235}U$	±1σ	Best age (Ma)	±1σ	notes
Zircon_1_008	92	50	0.51	0.06129	0.00634	0.03906	0.00435	0.00462	0.0001	0.00142	0.00003	0.23	29.7	0.7	39	4	29.7	0.7	
Zircon_10_018	197	199	0.94	0.07384	0.00952	0.04525	0.00608	0.00444	9E-05	0.00134	0.00003	0.19	28.6	0.6	45	6	28.6	0.6	
Zircon_12_021	108	97	0.84	0.07523	0.00835	0.04898	0.00579	0.00472	0.0001	0.00142	0.00003	0.2	30.4	0.7	49	6	30.4	0.7	
Zircon_13_022	542	495	0.85	0.05383	0.00314	0.03012	0.00194	0.00406	5E-05	0.00127	0.00002	0.28	26.1	0.3	30	2	26.1	0.3	
Zircon_14_023	92	93	0.93	0.07951	0.01244	0.05123	0.0087	0.00467	0.0001	0.0014	0.00003	0.34	30.1	0.8	51	8	30.1	0.8	
Zircon_15_024	122	100	0.76	0.06654	0.01027	0.04116	0.00674	0.00449	0.0001	0.00137	0.00004	0.3	28.9	0.7	41	7	28.9	0.7	
Zircon_16_026	121	85	0.66	0.06151	0.0075	0.03867	0.00491	0.00456	8E-05	0.0014	0.00003	0.2	29.3	0.5	39	5	29.3	0.5	
Zircon_17_027	479	650	1.26	0.06771	0.00393	0.03921	0.00234	0.00424	6E-05	0.00137	0.00004	0.23	27.3	0.4	39	2	27.3	0.4	
Zircon_18_028	85	43	0.46	0.07266	0.00934	0.04787	0.00647	0.00478	0.0001	0.00144	0.00004	0.24	30.7	0.7	47	6	30.7	0.7	
Zircon_19_029	174	106	0.57	0.07111	0.00492	0.04202	0.00315	0.00429	7E-05	0.0013	0.00002	0.27	27.6	0.5	42	3	27.6	0.5	
Zircon_2_009	359	385	1.00	0.06142	0.008	0.03618	0.00499	0.00427	7E-05	0.00132	0.00002	0.29	27.5	0.4	36	5	27.5	0.4	
Zircon_20_030	170	186	1.02	0.07081	0.00829	0.04444	0.00567	0.00455	0.0001	0.00138	0.00003	0.27	29.3	0.7	44	6	29.3	0.7	
Zircon_21_032	86	55	0.60	0.06278	0.00615	0.03958	0.00397	0.0046	0.0001	0.00157	0.00009	0.21	29.6	0.6	39	4	29.6	0.6	
Zircon_22_033	119	68	0.54	0.06667	0.00584	0.04169	0.00392	0.00453	8E-05	0.00138	0.00003	0.29	29.2	0.5	41	4	29.2	0.5	
Zircon_23_034	120	96	0.75	0.06199	0.00771	0.0379	0.00491	0.00443	8E-05	0.00136	0.00003	0.17	28.5	0.5	38	5	28.5	0.5	
Zircon_24_035	155	197	1.18	0.06063	0.00708	0.03922	0.00503	0.00469	0.0001	0.00145	0.00003	0.36	30.2	0.6	39	5	30.2	0.6	
Zircon_25_036	106	92	0.81	0.07751	0.00742	0.04867	0.00507	0.00455	0.0001	0.00137	0.00003	0.29	29.3	0.6	48	5	29.3	0.6	
Zircon_28_040	203	158	0.73	0.06269	0.00414	0.03734	0.00251	0.0044	6E-05	0.00142	0.00004	0.19	28.3	0.4	37	2	28.3	0.4	
Zircon_3_010	170	96	0.52	0.05997	0.00588	0.03941	0.00412	0.00477	9E-05	0.00147	0.00003	0.25	30.7	0.6	39	4	30.7	0.6	
Zircon_30_042	93	49	0.49	0.04795	0.00453	0.03037	0.00296	0.00459	8E-05	0.00146	0.00011	0.18	29.5	0.5	30	3	29.5	0.5	
Zircon_31_044	193	84	0.40	0.05631	0.00327	0.05812	0.00343	0.00756	8E-05	0.00231	0.00007	0.18	48.6	0.5	57	3	48.6	0.5	
Zircon_32_045	257	135	0.49	0.05477	0.00345	0.03289	0.00212	0.00445	6E-05	0.00138	0.00006	0.21	28.6	0.4	33	2	28.6	0.4	
Zircon_33_046	201	102	0.47	0.04611	0.00382	0.02717	0.00233	0.00427	6E-05	0.00139	0.0001	0.18	27.5	0.4	27	2	27.5	0.4	
Zircon_34_047	93	83	0.83	0.06892	0.01033	0.04407	0.00727	0.00464	0.0001	0.00141	0.00003	0.26	29.8	0.7	44	7	29.8	0.7	
~~Zircon_35_048~~	~~148~~	~~131~~	~~0.82~~	~~0.07073~~	~~0.0098~~	~~0.04238~~	~~0.00656~~	~~0.00435~~	~~0.0001~~	~~0.00132~~	~~0.00004~~	~~0.4~~	28	~~0.8~~	~~42~~	~~6~~	~~28.0~~	~~0.8~~	High P
Zircon_36_050	88	53	0.56	0.091	0.00683	0.05588	0.00438	0.00455	0.0001	0.00151	0.00008	0.29	29.3	0.6	55	4	29.3	0.6	
Zircon_37_051	88	49	0.52	0.07683	0.00522	0.04989	0.00352	0.00476	9E-05	0.00114	0.00008	0.27	30.6	0.6	49	3	30.6	0.6	
Zircon_38_052	212	152	0.67	0.07042	0.0058	0.0409	0.0036	0.00421	6E-05	0.00128	0.00002	0.2	27.1	0.4	41	4	27.1	0.4	
Zircon_4_011	82	42	0.48	0.06222	0.01208	0.04046	0.00835	0.00472	0.0001	0.00145	0.00008	0.27	30.3	0.9	40	8	30.3	0.9	
Zircon_5_012	295	294	0.93	0.06928	0.01081	0.0445	0.00758	0.00466	0.0001	0.00142	0.00004	0.29	30	0.8	44	7	30.0	0.8	
Zircon_6_014	99	51	0.48	0.07757	0.0052	0.05002	0.00343	0.00474	7E-05	0.00162	0.00014	0.21	30.5	0.4	50	3	30.5	0.4	
Zircon_8_016	153	125	0.76	0.05765	0.0063	0.03506	0.00412	0.00441	8E-05	0.00137	0.00003	0.24	28.4	0.5	35	4	28.4	0.5	
Zircon_9_017	399	232	0.54	0.05627	0.00146	0.06853	0.0019	0.0089	9E-05	0.0029	0.00006	0.35	57.1	0.6	67	2	57.1	0.6	

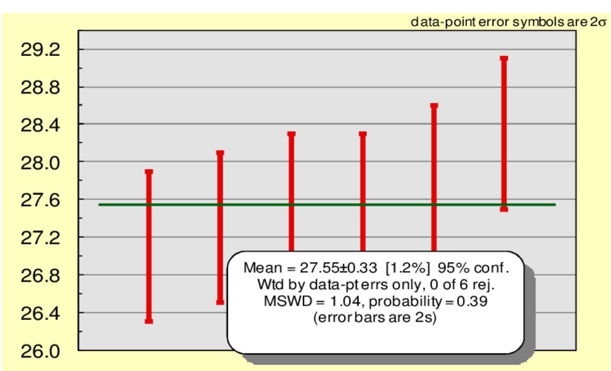

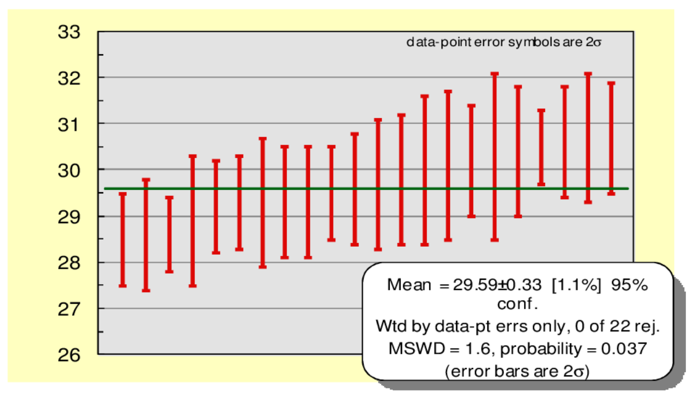

BM100306-1	Ericicuchi ignimbrite (Tpe)																			
Trace elements (ppm)	P	Ti	Y	Nb	La	Ce	Pr	Nd	Sm	Eu	Gd	Tb	Dy	Ho	Er	Yb	Lu	Hf	Th	U	notes
Zircon_1_BM06-1_008	333	14	843	1	0	7	0	1	2	1	13	5	63	27	135	335	77	8093	50.22	92.49	
Zircon_10_018	672	5	1959	3	3	59	1	10	10	2	43	14	172	66	298	575	118	10387	199.30	197.15	
Zircon_12_021	310	15	2113	1	0	24	0	6	10	4	54	17	200	74	320	567	113	9276	96.98	107.82	
Zircon_13_022	733	21	3745	4	2	73	1	12	16	6	83	27	323	122	557	1121	231	10694	494.60	541.74	
Zircon_14_023	533	31	1114	2	0	23	0	3	4	1	23	8	96	37	166	319	66	10414	92.68	92.43	
Zircon_15_024	582	657	1646	2	3	38	1	8	8	2	37	12	144	55	249	468	96	10581	99.89	122.07	
Zircon_16_026	245	14	1311	2	1	30	0	3	4	1	26	9	109	42	196	393	81	12420	85.16	120.67	
Zircon_17_027	1086	16	4989	6	3	127	2	17	25	6	128	41	469	168	723	1242	241	10773	649.57	479.46	
Zircon_18_028	1191	12	904	2	8	34	3	15	5	1	17	6	71	28	135	301	66	11002	42.63	85.42	
Zircon_19_029	338	20	1401	2	0	31	0	3	5	2	27	9	118	45	209	406	84	11670	105.59	173.97	
Zircon_2_009	566	100	1928	8	7	84	3	17	10	2	42	14	173	65	299	569	113	9502	384.52	358.60	
Zircon_20_030	1052	5	3153	2	6	61	3	22	22	9	100	29	312	107	440	728	141	9047	186.19	170.07	
Zircon_21_032	393	9	1229	1	0	17	0	3	6	2	29	9	109	41	182	338	70	9823	55.38	85.81	
Zircon_22_033	496	158	1655	3	0	24	0	4	6	2	35	12	141	54	251	492	102	9669	68.11	118.60	
Zircon_23_034	467	20	2154	2	1	27	1	7	9	3	50	16	194	72	326	598	122	8875	96.11	119.94	
Zircon_24_035	497	27	2970	3	0	66	1	8	14	7	76	23	270	100	441	799	165	8981	196.90	155.28	
Zircon_25_036	712	17	2315	1	0	22	0	7	13	5	61	19	215	77	336	601	120	9249	92.24	106.46	
Zircon_28_040	793	24	2728	3	0	37	0	6	10	4	53	18	222	87	404	785	164	10318	158.11	202.73	
Zircon_3_010	344	9	1268	3	0	33	0	2	4	1	23	8	106	42	201	417	88	10660	96.02	170.42	
Zircon_30_042	231	bdl	1062	2	0	21	0	2	3	1	18	6	82	33	163	353	76	11159	48.78	93.09	
Zircon_31_044	283	2	593	1	0	13	0	2	2	1	10	3	45	18	88	210	50	11307	83.61	192.57	
Zircon_32_045	269	bdl	835	2	0	24	0	2	3	1	13	5	61	26	133	329	75	11980	134.73	257.37	
Zircon_33_046	602	4	1878	4	1	37	0	4	6	2	35	12	153	60	285	584	123	10966	102.11	200.88	
Zircon_34_047	486	19	1867	1	3	38	2	10	9	3	46	15	170	62	270	482	97	10287	83.19	92.93	
~~Zircon_35_048~~	~~8228~~	~~19~~	~~2972~~	~~2~~	~~38~~	~~132~~	~~13~~	~~71~~	~~27~~	~~9~~	~~88~~	~~24~~	~~274~~	~~99~~	~~421~~	~~735~~	~~148~~	~~9317~~	~~130.93~~	~~148.40~~	high P
Zircon_36_050	196	12	1000	1	0	16	0	2	3	1	17	6	80	31	148	312	66	12003	53.25	88.05	
Zircon_37_051	146	19	897	2	0	19	0	2	2	1	15	6	70	28	134	283	60	11575	48.99	87.76	
Zircon_38_052	519	bdl	1880	2	1	26	1	5	7	2	39	13	156	59	275	555	117	10490	151.84	212.25	
Zircon_4_011	179	5	711	1	0	15	0	2	3	1	13	5	58	23	113	249	54	9623	42.18	81.63	
Zircon_5_012	481	12	2857	3	0	40	1	8	14	5	66	21	246	93	430	922	196	9277	294.08	294.60	
Zircon_6_014	112	4	867	2	0	30	0	2	3	1	15	5	70	28	137	290	62	12157	51.16	98.74	
Zircon_8_016	450	18	1918	1	2	25	1	9	10	4	50	15	177	64	282	536	110	9348	124.87	152.63	
Zircon_9_017	35	8	847	2	0	17	0	2	3	1	14	5	65	26	130	320	76	11433	232.40	398.97	

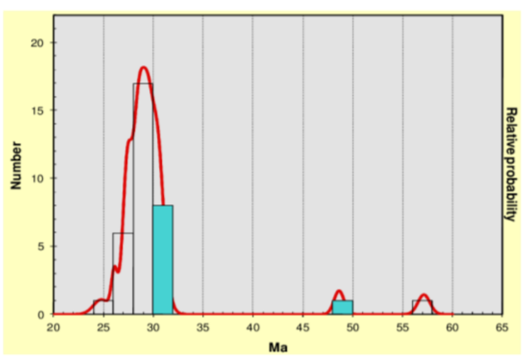

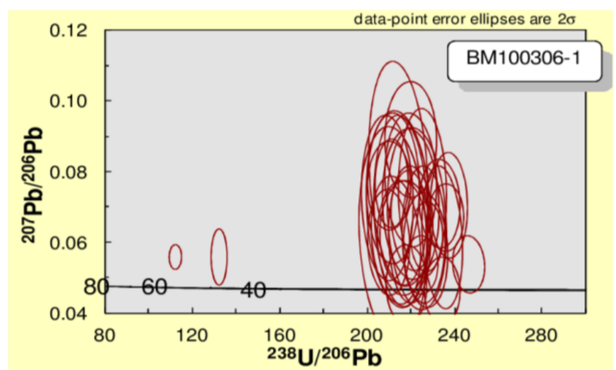

BM100306-3	Ericicuchi ignimbrite (Tpe)			Mean $^{206}Pb/^{238}U$ age ($\pm 2\sigma$): 27.0 ± 0.7 Ma															
				CORRECTED RATIOS[2]									CORRECTED AGES (Ma)						
	U[1] (ppm)	Th[1] (ppm)	Th/U	$^{207}Pb/^{206}Pb$	$\pm 1\sigma$[3]	$^{207}Pb/^{235}U$	$\pm 1\sigma$[3]	$^{206}Pb/^{238}U$	$\pm 1\sigma$[3]	$^{208}Pb/^{232}Th$	$\pm 1\sigma$[3]	Rho	$^{206}Pb/^{238}U$	$\pm 1\sigma$	$^{207}Pb/^{235}U$	$\pm 1\sigma$	Best age (Ma)	$\pm 1\sigma$	notes
Zircon_1_008	488	125	0.24	0.04982	0.00135	0.08166	0.0023	0.01192	0.0001	0.00391	0.00009	0.27	76.4	0.6	80	2	76.4	0.6	
Zircon_10_018	196	95	0.45	0.04609	0.00213	0.0495	0.00249	0.00779	0.0001	0.00258	0.00015	0.27	50	0.7	49	2	50.0	0.7	
Zircon_12_021	173	154	0.82	0.05817	0.00629	0.03472	0.00388	0.00433	6E-05	0.00134	0.00002	0.17	27.8	0.4	35	4	27.8	0.4	
Zircon_13_022	203	213	0.97	0.08677	0.02661	0.04876	0.0148	0.00408	8E-05	0.00121	0.00007	0.07	26.2	0.5	48	14	26.2	0.5	
Zircon_14_023	193	144	0.69	0.05411	0.00516	0.03362	0.00334	0.00451	6E-05	0.00141	0.00003	0.2	29	0.4	34	3	29.0	0.4	
Zircon_15_024	457	299	0.60	0.05189	0.00281	0.03207	0.00187	0.00448	5E-05	0.00141	0.00002	0.28	28.8	0.3	32	2	28.8	0.3	
Zircon_16_026	230	201	0.81	0.05966	0.00322	0.03755	0.00207	0.00461	5E-05	0.00147	0.00003	0.2	29.6	0.3	37	2	29.6	0.3	
Zircon_18_028	232	223	0.89	0.06063	0.00674	0.0395	0.00577	0.00473	0.0002	0.00146	0.00006	0.63	30	1.0	39	6	30.0	1.0	
Zircon_19_029	113	70	0.57	0.07244	0.00577	0.04507	0.00388	0.00451	9E-05	0.00136	0.00003	0.28	29	0.6	45	4	29.0	0.6	
Zircon_2_009	120	105	0.80	0.08057	0.0112	0.05076	0.00776	0.00457	0.0001	0.00137	0.00003	0.41	29.4	0.7	50	7	29.4	0.7	
Zircon_20_030	96	79	0.77	0.06373	0.00966	0.03922	0.00616	0.00446	8E-05	0.00137	0.00003	0.22	28.7	0.5	39	6	28.7	0.5	
Zircon_21_032	868	704	0.75	0.04715	0.00176	0.03839	0.00157	0.00591	5E-05	0.00188	0.00003	0.31	38	0.3	38	2	38.0	0.3	
Zircon_23_034	117	74	0.59	0.06153	0.00685	0.03768	0.00449	0.00444	8E-05	0.00137	0.00003	0.27	28.6	0.5	38	4	28.6	0.5	
Zircon_24_035	397	426	0.99	0.05096	0.0036	0.02994	0.00227	0.00426	5E-05	0.00134	0.00002	0.2	27.4	0.3	30	2	27.4	0.3	
Zircon_25_036	275	152	0.51	0.05493	0.00258	0.03334	0.00163	0.00444	6E-05	0.00133	0.00005	0.28	28.6	0.4	33	2	28.6	0.4	
~~Zircon_26_038~~	~~1064~~	~~2036~~	~~1.77~~	~~0.05617~~	~~0.00157~~	~~0.0314~~	~~0.00091~~	~~0.00404~~	~~3E-05~~	~~0.00122~~	~~0.00002~~	~~0.26~~	~~26~~	~~0.2~~	~~31~~	~~1~~	~~26.0~~	~~0.2~~	High U Th
Zircon_27_039	436	417	0.89	0.05712	0.00413	0.03943	0.00315	0.00501	8E-05	0.00156	0.00002	0.22	32.2	0.5	39	3	32.2	0.5	
Zircon_28_040	315	175	0.51	0.05501	0.00253	0.03548	0.00183	0.00468	7E-05	0.00146	0.00002	0.27	30.1	0.4	35	2	30.1	0.4	
Zircon_29_041	546	368	0.62	0.05234	0.00227	0.03349	0.00156	0.00464	5E-05	0.00146	0.00001	0.16	29.8	0.3	33	2	29.8	0.3	
Zircon_3_010	126	80	0.59	0.06845	0.01119	0.04151	0.0073	0.0044	0.0001	0.00134	0.00004	0.3	28.3	0.8	41	7	28.3	0.8	
Zircon_30_042	313	233	0.69	0.05541	0.00421	0.03683	0.00301	0.00482	6E-05	0.0015	0.00002	0.25	31	0.4	37	3	31.0	0.4	
~~Zircon_31_043~~	~~1119~~	~~2012~~	~~1.66~~	~~0.06284~~	~~0.00441~~	~~0.03475~~	~~0.00269~~	~~0.00401~~	~~4E-05~~	~~0.00123~~	~~0.00001~~	~~0.28~~	~~25.8~~	~~0.3~~	~~35~~	~~3~~	~~25.8~~	~~0.3~~	High U Th
Zircon_32_044	96	68	0.65	0.065	0.00644	0.03973	0.004	0.00453	9E-05	0.0014	0.00008	0.18	29.1	0.6	40	4	29.1	0.6	
Zircon_4_011	775	314	0.37	0.08043	0.01442	0.04438	0.00863	0.004	0.0001	0.0012	0.00005	0.37	25.7	0.7	44	8	25.7	0.7	
Zircon_5_012	139	102	0.68	0.05508	0.00771	0.03144	0.00443	0.00413	7E-05	0.00123	0.00011	0.11	26.6	0.4	31	4	26.6	0.4	
Zircon_6_014	114	81	0.66	0.05877	0.00757	0.0353	0.00469	0.00436	8E-05	0.00135	0.00003	0.13	28	0.5	35	5	28.0	0.5	
Zircon_7_015	97	76	0.73	0.07476	0.01201	0.04519	0.00857	0.00438	0.0002	0.00132	0.00006	0.48	28	1.0	45	8	28.0	1.0	
Zircon_8_016	216	260	1.11	0.06376	0.00344	0.03614	0.00276	0.00427	0.0002	0.00125	0.00003	0.71	27	1.0	36	3	27.0	1.0	
Zircon_11_020	217	170	0.72	0.07438	0.01748	0.04959	0.01266	0.00484	0.0002	0.00146	0.00006	0.36	31	1.0	49	12	31.0	1.0	
Zircon_17_027	130	104	0.74	0.05544	0.00826	0.03313	0.00535	0.00433	0.0001	0.00135	0.00005	0.25	27.9	0.7	33	5	27.9	0.7	
Zircon_22_033	145	120	0.77	0.08285	0.01959	0.04954	0.01261	0.00434	0.0001	0.00129	0.00005	0.37	27.9	0.9	49	12	27.9	0.9	

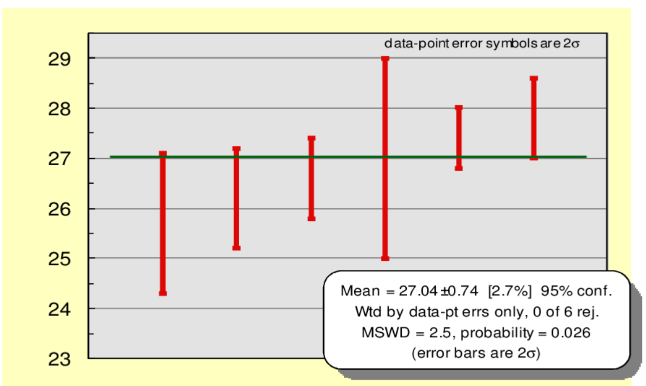

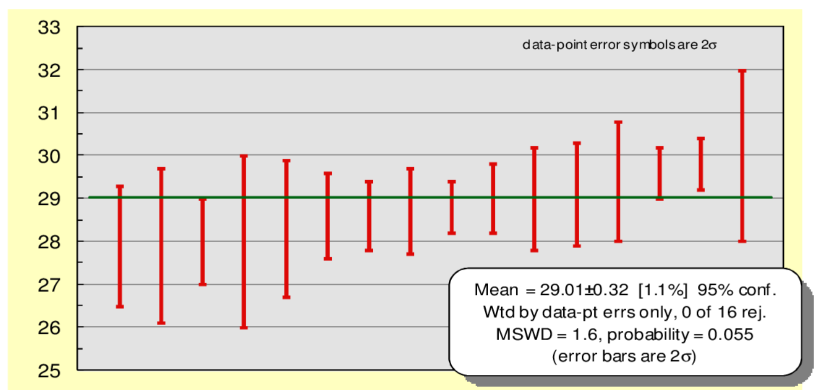

BM100306-3 Ericicuchi ignimbrite (Tpe)

Trace elements (ppm)	P	Ti	Y	Nb	La	Ce	Pr	Nd	Sm	Eu	Gd	Tb	Dy	Ho	Er	Yb	Lu	Hf	Th	U	notes
Zircon_1_BM06-3_008	25	15	1449	3	0	25	0	2	3	1	20	7	97	41	206	521	122	25687	125.41	488.40	
Zircon_10_018	32	bdl	1021	1	0	18	0	2	3	1	17	6	70	28	145	368	87	24697	94.66	195.58	
Zircon_12_021	247	34	2911	4	22	102	7	43	17	5	64	20	237	89	406	792	165	20679	154.06	172.91	
Zircon_13_022	74	18	4041	5	4	100	2	17	19	6	90	29	336	124	550	1007	201	19367	213.38	202.66	
Zircon_14_023	136	34	3757	4	5	68	2	15	16	5	72	25	297	114	532	1108	237	21658	143.63	193.07	
Zircon_15_024	187	45	3667	8	11	116	4	23	14	3	62	21	271	108	527	1156	246	25450	298.64	456.90	
Zircon_16_026	28	bdl	1228	3	0	36	0	3	3	1	18	6	84	35	175	422	97	22862	201.35	229.69	
Zircon_18_028	419	31	3862	5	38	171	12	66	27	6	92	28	327	121	532	964	195	20321	222.55	231.86	
Zircon_19_029	153	37	2620	3	10	60	4	21	12	3	50	16	200	79	370	762	163	20552	70.07	113.00	
Zircon_2_009	59	94	3123	2	1	37	1	8	12	4	61	21	253	96	440	878	184	19687	104.79	120.47	
Zircon_20_030	181	38	2812	3	13	75	5	28	16	5	62	19	229	86	388	730	150	19617	79.39	95.96	
Zircon_21_032	58	37	2489	7	3	93	1	8	10	2	47	16	194	74	338	688	146	22522	703.61	867.51	
Zircon_23_034	88	5	2115	3	1	39	1	5	6	2	35	12	158	63	305	642	137	20911	74.40	116.79	
Zircon_24_035	99	47	6356	4	0	51	1	15	21	4	124	42	513	191	838	1439	285	20821	425.62	397.40	
Zircon_25_036	48	1	3913	1	0	14	0	7	12	3	64	22	292	120	570	1109	235	20879	152.24	275.12	
~~Zircon_26_038~~	~~635~~	~~39~~	~~9123~~	~~32~~	~~43~~	~~511~~	~~16~~	~~92~~	~~52~~	~~10~~	~~214~~	~~66~~	~~769~~	~~282~~	~~1231~~	~~2194~~	~~425~~	~~21842~~	~~2035.96~~	~~1063.60~~	High Th U
Zircon_27_039	121	53	3955	10	0	92	1	10	16	1	84	28	335	121	526	950	182	18950	417.45	435.58	
Zircon_28_040	100	29	3200	7	0	56	0	3	6	2	42	16	213	93	476	1122	250	21566	174.72	315.15	
Zircon_29_041	241	13	4345	7	16	123	5	27	14	3	69	24	314	129	632	1380	298	24318	367.76	545.96	
Zircon_3_010	66	70	2260	3	2	85	1	8	9	3	46	15	179	68	313	634	134	20744	79.61	125.54	
Zircon_30_042	78	4	3911	5	1	65	1	8	12	4	67	23	295	117	564	1212	257	20443	233.30	312.95	
~~Zircon_31_043~~	~~385~~	~~49~~	~~17952~~	~~51~~	~~8~~	~~695~~	~~5~~	~~51~~	~~89~~	~~22~~	~~472~~	~~142~~	~~1604~~	~~567~~	~~2346~~	~~3834~~	~~715~~	~~18386~~	~~2011.52~~	~~1118.87~~	High Th U
Zircon_32_044	69	36	2361	2	0	35	0	5	8	3	48	16	190	73	332	633	133	20539	68.05	96.17	
Zircon_4_011	53	113	2230	5	4	57	2	10	9	3	43	14	171	68	316	700	156	22156	313.65	774.58	
Zircon_5_012	78	38	2569	3	4	61	2	12	9	2	51	17	203	77	355	706	147	21776	101.76	139.22	
Zircon_6_014	63	78	2550	3	1	39	0	5	9	4	48	17	200	79	364	709	149	17555	81.45	113.82	
Zircon_7_015	132	28	2891	3	5	60	2	15	12	4	60	20	240	91	415	792	164	18280	76.42	96.73	
Zircon_8_016	248	41	4780	5	18	138	7	41	26	8	116	36	420	153	659	1173	234	19134	260.20	216.47	
Zircon_11_020	109	0	3821	4	5	76	47	12	13	4	71	24	290	114	543	1170	250	23089	169.76	217.20	
Zircon_17_027	69	2	1696	3	0	25	0	4	5	2	27	10	119	49	240	553	126	22945	103.74	130.07	
Zircon_22_033	61	bdl	2957	3	1	65	1	9	12	4	59	20	233	91	417	803	169	18722	119.87	144.85	

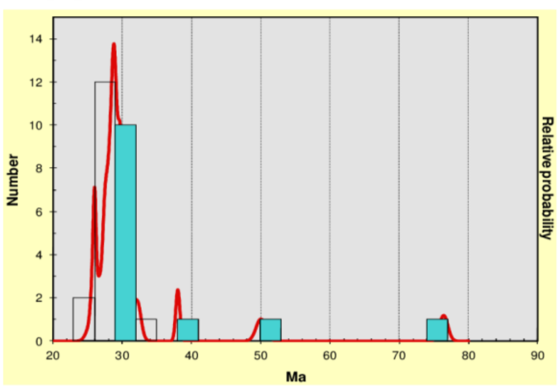

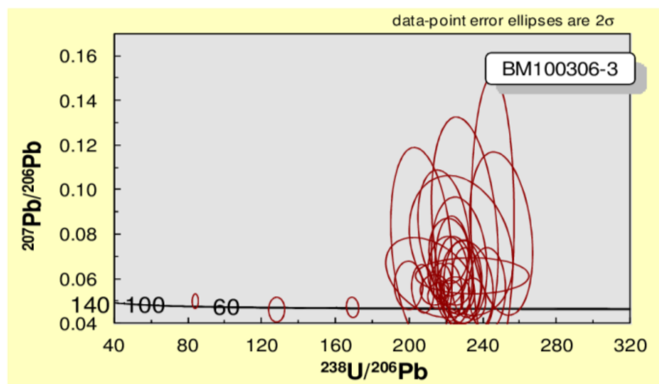

BM100306-6 Puerto Blanco ignimbrite (Tpb) Mean $^{206}Pb/^{238}U$ age (±2σ): 27.6 ± 0.3 Ma

				CORRECTED RATIOS[2]									CORRECTED AGES (Ma)						
	U[1] (ppm)	Th[1] (ppm)	Th/U	$^{207}Pb/^{206}Pb$	±1σ[3]	$^{207}Pb/^{235}U$	±1σ[3]	$^{206}Pb/^{238}U$	±1σ[3]	$^{208}Pb/^{232}Th$	±1σ[3]	Rho	$^{206}Pb/^{238}U$	±1σ	$^{207}Pb/^{235}U$	±1σ	Best age (Ma)	±1σ	notes
Zircon_1_BM100306-6_008	133	92	0.64	0.06982	0.007	0.0425	0.0046	0.00441	8E-05	0.00134	0.00002	0.28	28.4	0.5	42	4	28.4	0.5	
Zircon_10_017	177	141	0.74	0.05854	0.00718	0.0361	0.00467	0.00447	7E-05	0.00139	0.00003	0.24	28.8	0.4	36	5	28.8	0.4	
Zircon_12_020	358	186	0.48	0.04912	0.00265	0.02829	0.00157	0.00416	5E-05	0.00128	0.00004	0.24	26.8	0.3	28	2	26.8	0.3	
Zircon_13_021	229	193	0.79	0.06776	0.00429	0.0403	0.00288	0.00431	7E-05	0.00131	0.00002	0.28	27.7	0.5	40	3	27.7	0.5	
Zircon_14_022	259	220	0.79	0.06066	0.00918	0.03591	0.0057	0.00429	7E-05	0.00132	0.00004	0.29	27.6	0.4	36	6	27.6	0.4	
Zircon_15_023	263	273	0.97	0.05567	0.00262	0.03184	0.00156	0.00418	6E-05	0.0013	0.00003	0.28	26.9	0.4	32	2	26.9	0.4	
Zircon_16_025	311	313	0.94	0.0684	0.01094	0.04007	0.00696	0.00425	9E-05	0.00129	0.00003	0.4	27.3	0.6	40	7	27.3	0.6	
Zircon_18_027	87	46	0.49	0.07115	0.00662	0.04817	0.00457	0.00505	0.0001	0.0016	0.00008	0.2	32.5	0.6	48	4	32.5	0.6	
Zircon_19_028	177	84	0.44	0.06422	0.00475	0.0383	0.0029	0.00441	7E-05	0.00141	0.00006	0.21	28.4	0.4	38	3	28.4	0.4	
Zircon_2_009	282	238	0.79	0.06279	0.00359	0.03737	0.00239	0.00432	6E-05	0.00133	0.00002	0.26	27.8	0.4	37	2	27.8	0.4	
Zircon_20_029	139	97	0.65	0.07443	0.00724	0.0464	0.00494	0.00452	0.0001	0.00136	0.00003	0.24	29.1	0.7	46	5	29.1	0.7	
Zircon_21_031	167	124	0.69	0.08417	0.01581	0.05132	0.01063	0.00442	0.0001	0.00132	0.00004	0.4	28.4	0.9	51	10	28.4	0.9	
Zircon_22_032	156	120	0.72	0.0757	0.00774	0.04573	0.00519	0.00438	0.0001	0.00132	0.00003	0.28	28.2	0.7	45	5	28.2	0.7	
Zircon_24_033	252	172	0.64	0.05848	0.00333	0.03379	0.00198	0.00428	6E-05	0.0013	0.00005	0.24	27.5	0.4	34	2	27.5	0.4	
Zircon_25_034	318	268	0.79	0.0624	0.00384	0.03667	0.00245	0.00426	6E-05	0.00131	0.00002	0.22	27.4	0.4	37	2	27.4	0.4	
Zircon_26_036	185	118	0.60	0.05789	0.00699	0.03396	0.00439	0.00425	8E-05	0.00132	0.00003	0.2	27.4	0.5	34	4	27.4	0.5	
Zircon_27_037	225	162	0.67	0.04899	0.00353	0.02894	0.00211	0.00431	5E-05	0.00129	0.00006	0.15	27.7	0.3	29	2	27.7	0.3	
Zircon_28_038	363	418	1.07	0.04813	0.00412	0.02761	0.00265	0.00416	7E-05	0.00132	0.00004	0.32	26.8	0.4	28	3	26.8	0.4	
Zircon_29_039	185	146	0.73	0.05602	0.00571	0.0339	0.00376	0.00439	9E-05	0.00137	0.00003	0.26	28.2	0.6	34	4	28.2	0.6	
Zircon_3_010	307	321	0.97	0.0599	0.01097	0.03645	0.00719	0.00441	0.0001	0.00136	0.00005	0.22	28.4	0.7	36	7	28.4	0.7	
Zircon_30_040	167	125	0.70	0.06995	0.00551	0.0405	0.00349	0.0042	7E-05	0.00127	0.00002	0.26	27	0.4	40	3	27.0	0.4	
Zircon_31_042	342	363	0.99	0.05437	0.0032	0.03125	0.0021	0.00417	6E-05	0.0013	0.00002	0.27	26.8	0.4	31	2	26.8	0.4	
Zircon_32_043	299	301	0.94	0.06181	0.0026	0.0353	0.00154	0.00415	5E-05	0.00124	0.00003	0.27	26.7	0.3	35	2	26.7	0.3	
Zircon_33_044	137	146	0.99	0.10203	0.01126	0.06141	0.00727	0.00436	0.0001	0.00127	0.00003	0.21	28.1	0.7	61	7	28.1	0.7	
Zircon_34_045	69	29	0.39	0.07715	0.00756	0.05038	0.00515	0.00484	0.0001	0.00173	0.00016	0.28	31.1	0.9	50	5	31.1	0.9	
Zircon_35_046	142	137	0.90	0.07965	0.00865	0.04777	0.00576	0.00435	0.0001	0.0013	0.00003	0.23	28	0.6	47	6	28.0	0.6	
Zircon_37_049	183	117	0.60	0.06451	0.00527	0.03778	0.00335	0.00425	7E-05	0.0013	0.00002	0.26	27.3	0.4	38	3	27.3	0.4	
Zircon_39_050	258	239	0.86	0.05102	0.00405	0.02954	0.00254	0.0042	7E-05	0.00132	0.00003	0.17	27	0.4	30	3	27.0	0.4	
Zircon_4_011	543	335	0.57	0.05122	0.00209	0.03277	0.00153	0.00464	5E-05	0.00146	0.00002	0.29	29.8	0.3	33	1	29.8	0.3	
Zircon_40_051	73	59	0.76	0.11963	0.01065	0.07289	0.00668	0.00454	0.0001	0.00134	0.00008	0.24	29.2	0.6	71	6	29.2	0.6	
Zircon_5_012	164	119	0.67	0.05705	0.00814	0.0341	0.00511	0.00434	0.0001	0.00135	0.00006	0.18	27.9	0.7	34	5	27.9	0.7	
Zircon_6_014	285	277	0.90	0.05842	0.00714	0.03618	0.00467	0.00449	7E-05	0.00139	0.00003	0.25	28.9	0.5	36	5	28.9	0.5	
Zircon_8_015	168	134	0.74	0.08393	0.00663	0.05189	0.00452	0.00448	8E-05	0.00133	0.00003	0.29	28.8	0.5	51	4	28.8	0.5	
Zircon_9_016	242	249	0.96	0.04621	0.00277	0.02706	0.00185	0.00425	7E-05	0.00136	0.00005	0.23	27.3	0.4	27	2	27.3	0.4	

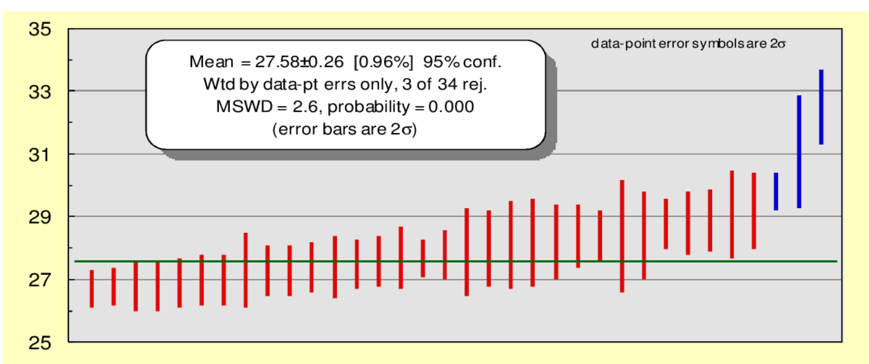

BM100306-6 Puerto Blanco ignimbrite (Tpb)

Trace elements (ppm)	P	Ti	Y	Nb	La	Ce	Pr	Nd	Sm	Eu	Gd	Tb	Dy	Ho	Er	Yb	Lu	Hf	Th	U	notes
Zircon_1_BM06-6_008	509	13	1779	2	0	38	1	5	7	3	39	13	156	60	278	584	123	9708	92	133	
Zircon_10_017	422	31	2269	2	1	28	0	7	10	5	54	17	201	76	342	702	147	8947	141	177	
Zircon_12_020	1210	18	2987	3	0	28	0	3	8	2	47	18	237	98	472	1048	225	10998	186	358	
Zircon_13_021	756	14	3417	3	2	86	2	16	17	7	84	27	315	118	527	1019	209	9073	193	229	
Zircon_14_022	2083	63	3811	3	10	67	3	23	20	7	98	31	360	133	586	1085	220	7915	220	259	
Zircon_15_023	946	19	4208	3	0	45	1	16	26	11	120	37	403	147	637	1235	257	8796	273	263	
Zircon_16_025	955	20	4505	3	2	96	3	24	28	12	122	37	419	154	687	1365	288	8103	313	311	
Zircon_18_027	417	12	1001	2	0	18	0	3	4	1	17	6	79	32	157	363	80	11014	46	87	
Zircon_19_028	282	5	1272	3	0	19	0	2	3	1	18	7	94	40	203	500	113	10377	84	177	
Zircon_2_009	2644	13	3192	3	16	81	6	33	20	7	81	26	292	109	487	1000	211	8515	238	282	
Zircon_20_029	519	21	1927	2	1	33	1	8	9	4	43	14	165	63	300	641	140	9090	97	139	
Zircon_21_031	539	36	2111	2	2	41	1	9	9	4	45	15	181	70	326	689	147	9174	124	167	
Zircon_22_032	557	24	2100	3	1	68	1	9	9	3	44	15	180	71	322	636	132	9554	120	156	
Zircon_24_033	732	11	2560	2	0	28	0	4	8	3	48	17	213	86	404	851	181	9921	172	252	
Zircon_25_034	1178	7	3384	3	16	96	5	31	22	7	85	27	304	113	508	1026	212	9934	268	318	
Zircon_26_036	803	23	2129	2	1	35	1	6	8	3	40	14	174	69	323	693	148	9860	118	185	
Zircon_27_037	759	13	2988	3	0	30	0	5	10	5	61	21	252	99	461	950	202	8985	162	225	
Zircon_28_038	1268	20	4499	5	2	125	2	16	21	6	105	35	404	152	661	1217	243	10165	418	363	
Zircon_29_039	956	8	2305	2	4	71	2	18	13	5	54	17	200	77	351	734	155	9432	146	185	
Zircon_3_010	1142	22	5317	4	1	61	1	17	31	13	154	48	530	189	806	1438	287	7801	321	307	
Zircon_30_040	616	6	2593	2	0	37	0	5	9	4	53	18	226	88	399	786	160	9483	125	167	
Zircon_31_042	1245	17	5068	4	1	69	1	19	31	13	139	42	471	169	739	1453	299	8701	363	342	
Zircon_32_043	943	2	4131	3	1	51	1	17	27	11	117	35	389	139	606	1191	245	9541	301	299	
Zircon_33_044	520	5	2075	3	4	150	3	22	15	4	52	16	186	69	312	618	127	10411	146	137	
Zircon_34_045	311	3	867	1	0	11	0	2	2	1	14	5	68	28	137	312	68	11036	29	69	
Zircon_35_046	421	19	1938	2	2	65	2	18	13	5	49	15	172	65	294	607	128	9328	137	142	
Zircon_37_049	667	6	2073	2	0	28	0	5	7	3	40	14	173	68	320	674	143	9823	117	183	
Zircon_39_050	1500	4	3331	2	7	64	3	22	20	8	89	27	305	111	491	976	205	9674	239	258	
Zircon_4_011	652	14	1577	6	4	64	1	8	5	1	25	10	127	53	265	593	126	11125	335	543	
Zircon_40_051	151	19	928	2	3	86	2	16	8	2	22	7	77	30	141	318	70	11501	59	73	
Zircon_5_012	601	17	2177	3	1	56	1	10	9	3	47	16	194	74	338	683	143	9271	119	164	
Zircon_6_014	971	48	4261	4	1	49	1	10	20	8	107	35	401	149	655	1229	250	7788	277	285	
Zircon_8_015	487	14	2018	2	1	62	1	10	10	3	41	14	166	65	301	629	133	10146	134	168	
Zircon_9_016	982	23	3894	2	2	43	1	17	25	11	115	34	375	133	580	1127	232	8487	249	242	

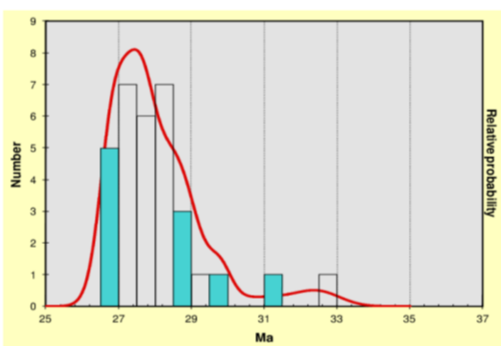

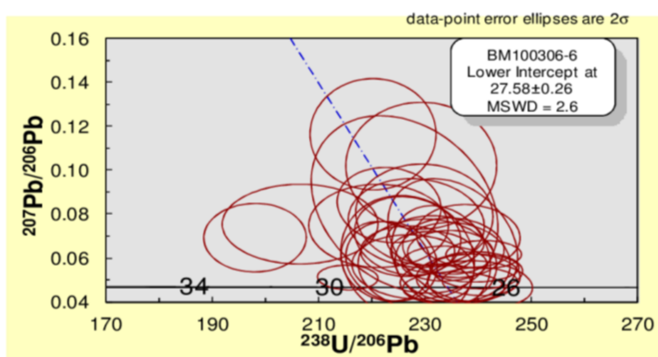

BM100305-4 Témoris Formation (Ttss) Mean $^{206}Pb/^{238}U$ age (±2σ): 27.3 ± 0.3 Ma

				CORRECTED RATIOS[2]									CORRECTED AGES (Ma)						
	U[1] (ppm)	Th[1] (ppm)	Th/U	$^{207}Pb/^{206}Pb$	±1σ[3]	$^{207}Pb/^{235}U$	±1σ[3]	$^{206}Pb/^{238}U$	±1σ[3]	$^{208}Pb/^{232}Th$	±1σ[3]	Rho	$^{206}Pb/^{238}U$	±1σ	$^{207}Pb/^{235}U$	±1σ	Best age (Ma)	±1σ	notes
Zircon_11_020	355	301	0.78	0.05898	0.00313	0.03352	0.00182	0.00416	5E-05	0.00146	0.00017	0.21	26.8	0.3	33	2	26.8	0.3	
Zircon_12_021	94	46	0.45	0.04608	0.00142	0.02871	0.00112	0.00452	0.0001	0.00166	0.00019	0.23	29.1	0.7	29	1	29.1	0.7	
Zircon_13_022	151	135	0.82	0.06107	0.00736	0.03561	0.00469	0.00423	9E-05	0.0013	0.00003	0.28	27.2	0.6	36	5	27.2	0.6	
Zircon_14_023	77	54	0.64	0.06494	0.01039	0.04227	0.00716	0.00472	0.0001	0.00144	0.00005	0.23	30.4	0.8	42	7	30.4	0.8	
Zircon_15_024	149	159	0.98	0.0709	0.01267	0.04009	0.00751	0.0041	0.0001	0.00124	0.00004	0.18	26.4	0.7	40	7	26.4	0.7	
Zircon_17_027	141	114	0.74	0.06544	0.01126	0.0383	0.0069	0.00424	9E-05	0.0013	0.00004	0.21	27.3	0.6	38	7	27.3	0.6	
Zircon_18_028	106	57	0.50	0.06094	0.00792	0.03857	0.00507	0.00451	9E-05	0.0016	0.0001	0.15	29	0.6	38	5	29.0	0.6	
Zircon_19_029	73	37	0.46	0.04607	0.00267	0.03143	0.00201	0.00495	0.0001	0.00188	0.00029	0.23	31.8	0.8	31	2	31.8	0.8	
Zircon_20_030	118	79	0.62	0.04607	0.00211	0.02651	0.00141	0.00417	0.0001	0.00159	0.00021	0.2	26.8	0.7	27	1	26.8	0.7	
~~Zircon_22_033~~	~~95~~	~~63~~	~~0.61~~	~~0.06066~~	~~0.00781~~	~~0.03892~~	~~0.00532~~	~~0.00465~~	~~0.0001~~	~~0.00144~~	~~0.00004~~	~~0.24~~	~~29.9~~	~~0.7~~	~~39~~	~~5~~	~~29.9~~	~~0.7~~	High P
Zircon_23_034	119	89	0.68	0.06728	0.01244	0.04087	0.00777	0.00441	9E-05	0.00134	0.00005	0.13	28.3	0.6	41	8	28.3	0.6	
Zircon_24_035	101	78	0.70	0.04608	0.00847	0.02784	0.00559	0.00438	0.0001	0.00151	0.00024	0.29	28.2	0.7	28	6	28.2	0.7	
Zircon_25_036	81	55	0.63	0.06686	0.01632	0.04288	0.01161	0.00465	0.0002	0.00142	0.00012	0.39	30	1.0	43	11	30.0	1.0	
Zircon_26_038	154	129	0.77	0.05051	0.00943	0.0295	0.00589	0.00424	0.0001	0.00134	0.00013	0.16	27.3	0.7	30	6	27.3	0.7	
Zircon_27_039	139	77	0.51	0.05783	0.01303	0.03304	0.00795	0.00414	0.0001	0.00129	0.00016	0.18	26.7	0.8	33	8	26.7	0.8	
Zircon_28_040	109	66	0.55	0.06355	0.00589	0.03985	0.00402	0.00455	9E-05	0.0014	0.00003	0.27	29.3	0.6	40	4	29.3	0.6	
Zircon_29_041	84	54	0.59	0.06278	0.01686	0.03932	0.01139	0.00454	0.0001	0.0014	0.00019	0.32	29.2	0.9	39	11	29.2	0.9	
~~Zircon_30_042~~	~~138~~	~~111~~	~~0.74~~	~~0.05882~~	~~0.00838~~	~~0.0338~~	~~0.00508~~	~~0.00417~~	~~7E-05~~	~~0.00129~~	~~0.00004~~	~~0.29~~	~~26.8~~	~~0.5~~	~~34~~	~~5~~	~~26.8~~	~~0.5~~	High P
Zircon_31_044	97	64	0.60	0.07195	0.01123	0.04158	0.00688	0.00419	0.0001	0.00127	0.00004	0.25	27	0.7	41	7	27.0	0.7	
Zircon_32_045	62	36	0.54	0.05897	0.00721	0.03682	0.00477	0.00453	9E-05	0.0014	0.00004	0.24	29.1	0.6	37	5	29.1	0.6	
Zircon_33_046	87	76	0.80	0.05734	0.00904	0.03346	0.00554	0.00423	9E-05	0.00131	0.00006	0.17	27.2	0.6	33	5	27.2	0.6	
Zircon_35_048	116	78	0.62	0.05237	0.00484	0.03146	0.00309	0.00436	7E-05	0.00137	0.00004	0.18	28	0.5	31	3	28.0	0.5	
Zircon_37_051	249	234	0.86	0.05357	0.00387	0.03003	0.00234	0.00407	5E-05	0.00127	0.00002	0.19	26.2	0.3	30	2	26.2	0.3	
Zircon_38_052	99	62	0.58	0.06154	0.00617	0.03793	0.0042	0.00447	0.0001	0.00138	0.00003	0.34	28.8	0.7	38	4	28.8	0.7	
Zircon_39_053	125	119	0.87	0.04748	0.00694	0.02752	0.00425	0.0042	9E-05	0.00134	0.00011	0.18	27	0.6	28	4	27.0	0.6	
Zircon_4_011	170	155	0.84	0.04672	0.00515	0.02653	0.00311	0.00412	6E-05	0.00131	0.00008	0.21	26.5	0.4	27	3	26.5	0.4	
Zircon_6_014	169	144	0.78	0.05087	0.00456	0.02957	0.00283	0.00422	7E-05	0.00133	0.00004	0.21	27.1	0.5	30	3	27.1	0.5	
Zircon_7_015	224	240	0.98	0.05963	0.00413	0.03474	0.00264	0.00423	5E-05	0.00131	0.00002	0.26	27.2	0.3	35	3	27.2	0.3	
Zircon_8_016	96	65	0.62	0.07806	0.00585	0.04679	0.00361	0.00444	8E-05	0.00126	0.00008	0.24	28.6	0.5	46	4	28.6	0.5	
Zircon_9_017	119	69	0.53	0.05441	0.00431	0.03346	0.00294	0.00446	9E-05	0.00139	0.00003	0.3	28.7	0.6	33	3	28.7	0.6	
Zircon_21_032	66	41	0.56	0.08172	0.00809	0.05282	0.00536	0.00479	0.0001	0.00148	0.00011	0.22	30.8	0.7	52	5	30.8	0.7	
Zircon_5_012	67	42	0.58	0.09313	0.01466	0.06366	0.01101	0.00496	0.0002	0.00146	0.00005	0.4	31.9	1.0	63	11	~~31.9~~	~~1.0~~	

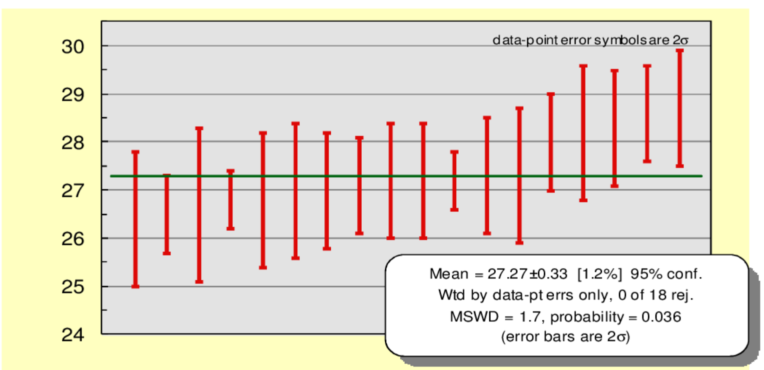

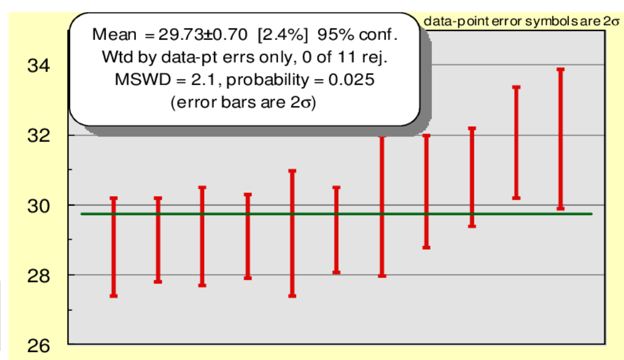

BM100305-4	Témoris Formation (Ttss)																				
Trace elements (ppm)	P	Ti	Y	Nb	La	Ce	Pr	Nd	Sm	Eu	Gd	Tb	Dy	Ho	Er	Yb	Lu	Hf	Th	U	notes
Zircon_11_020	310	bdl	2246	7	0	89	0	5	10	2	51	17	203	76	336	653	132	11920	301	355	
Zircon_12_021	271	7	981	2	2	24	1	5	3	1	17	6	75	31	154	365	81	10149	46	94	
Zircon_13_022	291	4	1641	3	0	36	0	5	8	2	38	12	145	55	246	504	105	9944	135	151	
Zircon_14_023	237	18	924	2	2	29	1	5	4	1	20	7	77	30	142	309	67	10000	54	77	
Zircon_15_024	202	15	1356	2	0	39	0	5	7	2	32	10	118	44	200	420	90	9530	159	149	
Zircon_17_027	346	13	1889	3	0	39	0	4	9	3	42	14	163	62	278	574	121	10027	114	141	
Zircon_18_028	205	8	1149	2	0	21	0	3	4	1	21	7	91	36	178	412	92	10552	57	106	
Zircon_19_029	175	9	784	1	0	19	0	2	3	1	14	5	61	25	121	283	64	10876	37	73	
Zircon_20_030	246	2	1289	2	0	28	0	3	5	1	27	9	107	42	194	423	92	10626	79	118	
~~Zircon_22_033~~	~~1426~~	~~2~~	~~1179~~	~~1~~	~~16~~	~~55~~	~~5~~	~~22~~	~~8~~	~~2~~	~~29~~	~~9~~	~~100~~	~~38~~	~~175~~	~~378~~	~~81~~	~~10715~~	~~63~~	~~95~~	High P
Zircon_23_034	207	15	1306	2	0	25	0	4	6	2	29	10	112	43	196	420	90	10549	89	119	
Zircon_24_035	226	2	1224	2	0	22	0	4	6	2	28	9	105	40	184	394	86	9747	78	101	
Zircon_25_036	216	27	1015	1	1	45	1	5	5	2	22	7	85	33	152	335	72	9230	55	81	
Zircon_26_038	262	22	1752	2	0	32	0	5	9	3	43	13	153	57	256	535	114	9570	129	154	
Zircon_27_039	211	6	1317	3	1	29	0	3	4	1	22	8	101	41	202	470	104	10471	77	139	
Zircon_28_040	306	bdl	1116	1	1	21	0	3	4	1	21	7	90	36	172	388	85	10952	66	109	
Zircon_29_041	212	bdl	967	1	3	39	1	6	4	1	19	7	80	31	147	317	68	10888	54	84	
~~Zircon_30_042~~	~~3284~~	~~23~~	~~1756~~	~~2~~	~~48~~	~~144~~	~~14~~	~~61~~	~~17~~	~~3~~	~~49~~	~~14~~	~~158~~	~~58~~	~~259~~	~~539~~	~~115~~	~~10273~~	~~111~~	~~138~~	High P
Zircon_31_044	230	bdl	1029	1	0	33	0	3	4	1	21	7	85	33	155	345	75	10875	64	97	
Zircon_32_045	118	9	805	1	0	14	0	2	3	1	17	6	66	26	122	274	60	10226	36	62	
Zircon_33_046	203	10	1766	1	0	26	0	7	10	4	49	14	163	58	254	514	108	9506	76	87	
Zircon_35_048	299	18	1351	2	0	22	0	3	5	2	27	9	111	43	203	452	100	9519	78	116	
Zircon_37_051	465	5	2075	3	0	59	1	7	10	4	48	15	178	66	303	653	144	8367	234	249	
Zircon_38_052	245	bdl	1084	1	0	21	0	3	4	1	22	7	90	35	164	361	78	11076	62	99	
Zircon_39_053	291	2	1869	2	0	54	1	8	11	4	52	16	175	63	272	529	109	10181	119	125	
Zircon_4_011	573	8	2157	2	4	47	1	11	12	4	55	17	194	71	319	664	140	9549	155	170	
Zircon_6_014	329	18	1654	3	1	62	1	6	7	2	36	12	143	54	246	520	110	10917	144	169	
Zircon_7_015	740	bdl	4011	4	2	79	1	17	24	8	114	35	388	137	579	1067	213	9601	240	224	
Zircon_8_016	209	7	1294	1	0	18	0	4	6	2	28	9	110	42	193	419	91	9940	65	96	
Zircon_9_017	213	bdl	1065	3	0	24	0	2	3	1	18	7	83	34	162	373	82	10204	69	119	
Zircon_21_032	190	11	879	1	0	16	0	2	3	1	19	6	73	28	133	292	63	10162	41	66	
Zircon_5_012	194	31	888	1	0	28	0	3	4	2	20	6	77	29	136	294	63	10710	42	67	

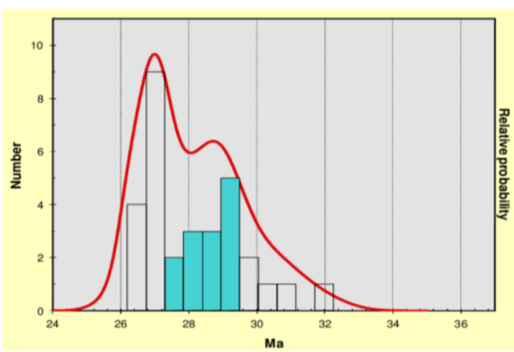

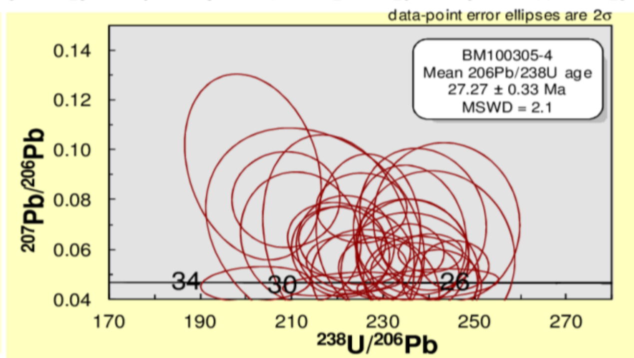

BM100304-5	Témoris Formation (Tti)		Mean $^{206}Pb/^{238}U$ age ($\pm2\sigma$): 24.6 ± 0.2 Ma																
				CORRECTED RATIOS[2]									CORRECTED AGES (Ma)						
	U[1] (ppm)	Th[1] (ppm)	Th/U	$^{207}Pb/^{206}Pb$	$\pm1\sigma^3$	$^{207}Pb/^{235}U$	$\pm1\sigma^3$	$^{206}Pb/^{238}U$	$\pm1\sigma^3$	$^{208}Pb/^{232}Th$	$\pm1\sigma^3$	Rho	$^{206}Pb/^{238}U$	$\pm1\sigma$	$^{207}Pb/^{235}U$	$\pm1\sigma$	Best age (Ma)	$\pm1\sigma$	notes
Zircon_1_BM04-5_008	127	114	0.78	0.07901	0.01617	0.04675	0.01035	0.00429	0.0001	0.00128	0.00004	0.26	27.6	0.8	46	10	27.6	0.8	
Zircon_10_018	101	75	0.64	0.07419	0.01192	0.04013	0.00697	0.00392	0.0001	0.00118	0.00003	0.28	25.2	0.6	40	7	25.2	0.6	
Zircon_11_020	209	278	1.15	0.05926	0.0029	0.03366	0.00171	0.00417	5E-05	0.00132	0.00003	0.27	26.8	0.3	34	2	26.8	0.3	
Zircon_12_021	121	74	0.53	0.08783	0.0094	0.04833	0.00551	0.00399	9E-05	0.00118	0.00003	0.24	25.7	0.6	48	5	25.7	0.6	
Zircon_13_022	118	92	0.67	0.05697	0.00369	0.03176	0.0022	0.00404	5E-05	0.00126	0.00001	0.19	26	0.3	32	2	26.0	0.3	
Zircon_14_023	88	83	0.81	0.05659	0.00506	0.03118	0.00312	0.004	8E-05	0.00124	0.00002	0.29	25.7	0.5	31	3	25.7	0.5	
Zircon_15_024	173	162	0.81	0.05792	0.00261	0.03061	0.00143	0.00388	5E-05	0.00121	0.00003	0.26	25	0.3	31	1	25.0	0.3	
Zircon_16_026	166	158	0.82	0.05814	0.00291	0.03205	0.00166	0.00403	6E-05	0.00118	0.00003	0.26	25.9	0.4	32	2	25.9	0.4	
~~Zircon_17_027~~	~~127~~	~~122~~	~~0.83~~	~~0.08553~~	~~0.0124~~	~~0.04572~~	~~0.00731~~	~~0.00388~~	~~0.0001~~	~~0.00115~~	~~0.00003~~	~~0.36~~	~~24.9~~	~~0.7~~	~~45~~	~~7~~	~~24.9~~	~~0.7~~	High P
Zircon_18_028	73	33	0.39	0.06889	0.00516	0.03816	0.00311	0.00402	8E-05	0.00122	0.00002	0.26	25.9	0.5	38	3	25.9	0.5	
Zircon_19_029	179	224	1.08	0.0857	0.01353	0.04733	0.0082	0.00401	0.0001	0.00119	0.00003	0.39	25.8	0.6	47	8	25.8	0.6	
Zircon_2_009	107	85	0.69	0.06172	0.00389	0.03353	0.00219	0.004	7E-05	0.00125	0.00004	0.26	25.7	0.4	33	2	25.7	0.4	
Zircon_21_032	246	316	1.11	0.07071	0.00718	0.03672	0.00411	0.00377	7E-05	0.00114	0.00002	0.28	24.2	0.4	37	4	24.2	0.4	
Zircon_22_033	123	122	0.86	0.07497	0.00405	0.04107	0.00234	0.00398	7E-05	0.00127	0.00004	0.32	25.6	0.4	41	2	25.6	0.4	
Zircon_23_034	91	73	0.70	0.08697	0.01504	0.05194	0.00958	0.00433	0.0001	0.00128	0.00004	0.32	27.9	0.8	51	9	27.9	0.8	
Zircon_25_036	99	92	0.80	0.0642	0.00468	0.03403	0.00279	0.00384	7E-05	0.00118	0.00002	0.26	24.7	0.5	34	3	24.7	0.5	
Zircon_26_038	155	170	0.95	0.05794	0.00446	0.03054	0.00238	0.00384	5E-05	0.00116	0.00003	0.16	24.7	0.3	31	2	24.7	0.3	
Zircon_27_039	152	129	0.73	0.06928	0.00388	0.037	0.00213	0.00389	5E-05	0.00122	0.00004	0.23	25	0.3	37	2	25.0	0.3	
Zircon_28_040	93	98	0.91	0.0709	0.00447	0.04017	0.00262	0.00414	7E-05	0.00129	0.00004	0.26	26.6	0.4	40	3	26.6	0.4	
Zircon_29_041	169	102	0.52	0.06139	0.00479	0.03942	0.00331	0.00466	7E-05	0.00143	0.00002	0.27	30	0.4	39	3	30.0	0.4	
Zircon_3_010	113	80	0.62	0.07475	0.00965	0.04334	0.0061	0.00421	0.0001	0.00127	0.00003	0.28	27.1	0.7	43	6	27.1	0.7	
Zircon_30_042	178	202	0.98	0.06488	0.00443	0.03392	0.00261	0.00379	6E-05	0.00116	0.00002	0.29	24.4	0.4	34	3	24.4	0.4	
Zircon_31_044	164	149	0.79	0.05463	0.00328	0.02814	0.00173	0.00376	5E-05	0.00113	0.00003	0.22	24.2	0.3	28	2	24.2	0.3	
Zircon_32_045	89	62	0.61	0.05809	0.00775	0.03224	0.00461	0.00403	8E-05	0.00125	0.00004	0.34	25.9	0.5	32	5	25.9	0.5	
Zircon_33_046	252	115	0.40	0.05117	0.00271	0.02651	0.00144	0.00376	4E-05	0.00123	0.00004	0.22	24.2	0.3	27	1	24.2	0.3	
Zircon_34_047	125	80	0.56	0.0579	0.00486	0.03177	0.00284	0.00398	6E-05	0.00123	0.00002	0.23	25.6	0.4	32	3	25.6	0.4	
Zircon_35_048	101	79	0.67	0.07061	0.00729	0.03872	0.00426	0.00398	7E-05	0.00121	0.00002	0.26	25.6	0.4	39	4	25.6	0.4	
Zircon_36_050	151	164	0.94	0.06025	0.0047	0.0334	0.0029	0.00402	7E-05	0.00124	0.00002	0.31	25.9	0.4	33	3	25.9	0.4	
Zircon_38_052	116	101	0.75	0.06661	0.00366	0.03495	0.00201	0.00389	7E-05	0.00123	0.00005	0.3	25	0.4	35	2	25.0	0.4	
Zircon_40_054	246	126	0.44	0.05756	0.00284	0.03002	0.00164	0.00378	5E-05	0.00117	0.00002	0.31	24.3	0.3	30	2	24.3	0.3	
Zircon_5_012	239	330	1.19	0.055	0.00258	0.02886	0.0014	0.00384	5E-05	0.00118	0.00004	0.26	24.7	0.3	29	1	24.7	0.3	
Zircon_6_014	126	91	0.63	0.05785	0.00388	0.0324	0.00221	0.00407	5E-05	0.00131	0.00005	0.18	26.2	0.3	32	2	26.2	0.3	
Zircon_8_016	108	120	0.96	0.06745	0.00492	0.03727	0.00281	0.00409	8E-05	0.00124	0.00004	0.25	26.3	0.5	37	3	26.3	0.5	
Zircon_9_017	162	130	0.69	0.06359	0.00621	0.03353	0.0035	0.00382	7E-05	0.00117	0.00002	0.23	24.6	0.4	33	3	24.6	0.4	

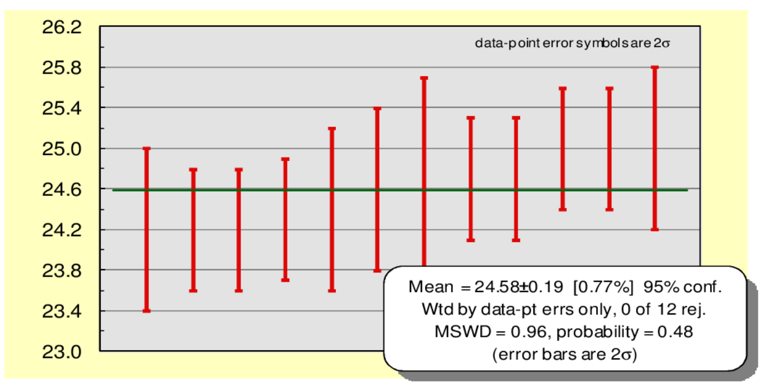

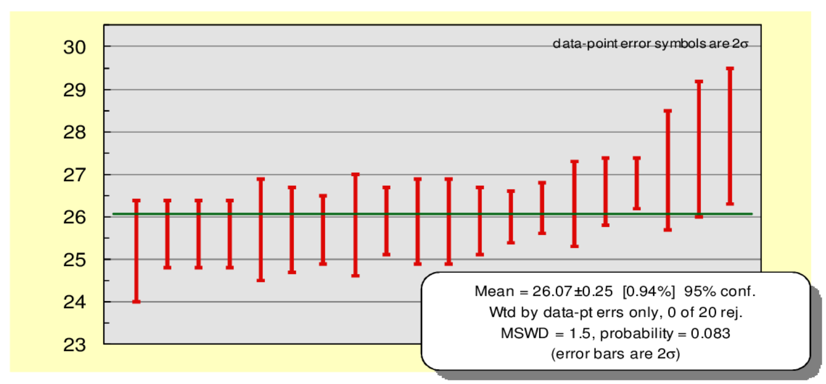

BM100304-5 Témoris Formation (Tti)

Trace elements (ppm)	P	Ti	Y	Nb	La	Ce	Pr	Nd	Sm	Eu	Gd	Tb	Dy	Ho	Er	Yb	Lu	Hf	Th	U	notes
Zircon_1_BM04-5_008	2203	27	1855	2	30	106	11	56	20	5	56	16	174	63	275	526	103	8615	114	127	
Zircon_10_018	335	3	1505	2	0	30	0	4	6	2	33	11	135	51	229	464	90	11816	75	101	
Zircon_11_020	620	13	4383	4	0	90	1	17	29	12	140	41	446	153	636	1127	212	8380	278	209	
Zircon_12_021	786	2	1745	2	8	114	3	17	10	2	39	13	159	59	263	518	99	11862	74	121	
Zircon_13_022	447	7	2250	2	0	33	0	5	11	4	56	18	207	77	342	653	128	10015	92	118	
Zircon_14_023	324	17	1750	2	1	72	1	9	12	5	53	16	172	61	258	487	94	9964	83	88	
Zircon_15_024	457	bdl	2378	3	0	44	0	8	12	4	60	19	219	80	356	704	137	10804	162	173	
Zircon_16_026	703	8	2645	4	5	72	2	14	14	5	67	21	247	90	390	741	141	9762	158	166	
~~Zircon_17_027~~	~~4006~~	~~24~~	~~2098~~	~~2~~	~~50~~	~~182~~	~~16~~	~~82~~	~~27~~	~~7~~	~~69~~	~~19~~	~~204~~	~~72~~	~~308~~	~~586~~	~~117~~	~~9388~~	~~122~~	~~127~~	High P La
Zircon_18_028	293	11	1003	2	0	21	0	2	3	1	17	6	83	33	157	335	67	11681	33	73	
Zircon_19_029	551	31	3883	3	0	86	1	17	28	10	127	37	400	137	567	994	186	8793	224	179	
Zircon_2_009	327	10	1900	2	0	28	0	4	8	3	43	14	168	64	286	562	111	9084	85	107	
Zircon_21_032	306	29	2500	2	1	57	1	11	17	5	73	22	241	86	369	694	139	9247	316	246	
Zircon_22_033	403	15	1918	2	0	44	1	7	11	3	51	16	182	65	282	538	104	9812	122	123	
Zircon_23_034	244	16	1603	1	0	28	0	5	9	3	43	13	152	55	238	449	86	9808	73	91	
Zircon_25_036	220	11	1909	1	0	32	0	7	11	4	55	16	183	66	281	527	103	9289	92	99	
Zircon_26_038	424	13	3031	2	0	49	1	11	19	7	92	27	301	106	446	810	155	8804	170	155	
Zircon_27_039	416	14	2415	2	0	38	0	6	11	4	59	19	223	82	358	682	131	10255	129	152	
Zircon_28_040	412	2	2071	1	2	36	1	13	16	6	68	19	206	71	300	559	109	8390	98	93	
Zircon_29_041	699	0	1050	3	4	44	1	6	3	1	16	6	79	33	169	412	88	12235	102	169	
Zircon_3_010	1548	5	1951	2	19	67	6	31	14	3	51	16	185	67	291	556	106	10887	80	113	
Zircon_30_042	437	18	2175	2	2	56	1	11	14	5	64	19	209	75	320	610	120	8621	202	178	
Zircon_31_044	554	7	2471	2	0	44	0	5	10	4	58	19	225	84	371	710	138	9773	149	164	
Zircon_32_045	289	8	1332	2	0	25	0	2	5	1	28	10	119	45	201	394	76	11711	62	89	
Zircon_33_046	547	6	2776	8	0	42	0	2	6	2	42	17	227	92	435	896	176	12031	115	252	
Zircon_34_047	443	6	1846	2	0	28	0	3	7	2	39	13	165	62	281	561	110	11041	80	125	
Zircon_35_048	341	5	1323	2	0	26	0	3	5	2	28	9	116	44	203	414	82	10642	79	101	
Zircon_36_050	1712	14	3464	3	21	98	7	42	27	9	107	31	343	121	513	930	178	8526	164	151	
Zircon_38_052	358	10	1882	2	0	34	0	5	10	4	49	15	175	64	277	537	104	8932	101	116	
Zircon_40_054	498	11	2100	3	2	44	1	4	7	2	42	15	183	71	321	640	125	11707	126	246	
Zircon_5_012	786	9	6150	6	0	112	1	23	41	16	191	57	619	216	886	1514	278	8254	330	239	
Zircon_6_014	383	12	1951	2	1	34	0	4	7	2	44	15	179	67	294	552	105	11756	91	126	
Zircon_8_016	387	11	3219	2	0	56	1	14	24	10	106	31	332	114	469	820	154	8803	120	108	
Zircon_9_017	471	10	2351	4	1	63	1	6	9	3	50	17	210	80	360	701	136	9719	130	162	

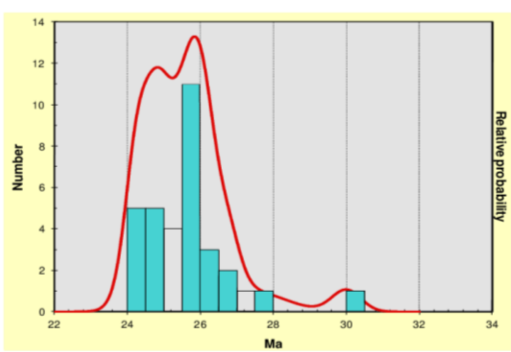

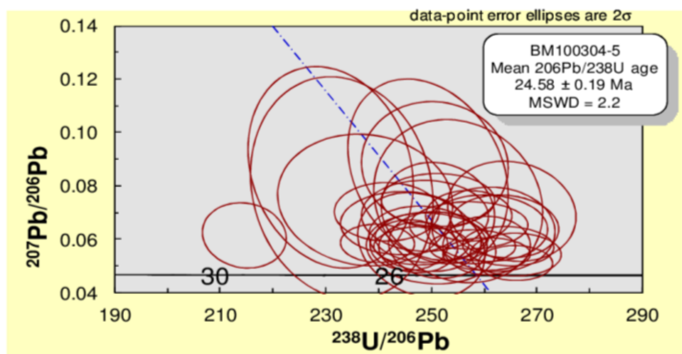

BM100305-1 Témoris Formation (Tti) Mean $^{206}Pb/^{238}U$ age (±2σ): 24.1 ± 0.3 Ma

				CORRECTED RATIOS[2]									CORRECTED AGES (Ma)						
	U[1] (ppm)	Th[1] (ppm)	Th/U	$^{207}Pb/^{206}Pb$	±1σ[3]	$^{207}Pb/^{235}U$	±1σ[3]	$^{206}Pb/^{238}U$	±1σ[3]	$^{208}Pb/^{232}Th$	±1σ[3]	Rho	$^{206}Pb/^{238}U$	±1σ	$^{207}Pb/^{235}U$	±1σ	Best age (Ma)	±1σ	notes
Zircon_1_BM05-1_008	242	171	0.63	0.05811	0.00314	0.02973	0.00165	0.00376	5E-05	0.0011	0.00004	0.23	24.2	0.3	30	2	24	0.3	
~~**Zircon_10_018**~~	~~351~~	~~556~~	~~1.40~~	~~0.04809~~	~~0.00557~~	~~0.02188~~	~~0.00274~~	~~0.0033~~	~~5E-05~~	~~0.00105~~	~~0.00004~~	~~0.24~~	~~21.2~~	~~0.3~~	~~22~~	~~3~~	~~21~~	~~0.3~~	High P La
Zircon_11_020	299	265	0.78	0.0639	0.00281	0.03262	0.00148	0.00372	4E-05	0.00116	0.00003	0.25	23.9	0.3	33	1	24	0.3	
~~**Zircon_12_021**~~	~~204~~	~~205~~	~~0.89~~	~~0.0461~~	~~0.00309~~	~~0.02445~~	~~0.0017~~	~~0.00385~~	~~6E-05~~	~~0.00127~~	~~0.00007~~	~~0.13~~	~~24.8~~	~~0.4~~	~~25~~	~~2~~	~~25~~	~~0.4~~	High P La
Zircon_13_022	124	72	0.52	0.07781	0.00574	0.04425	0.0036	0.00412	7E-05	0.00124	0.00002	0.33	26.5	0.5	44	3	27	0.5	
~~Zircon_14_023~~	~~265~~	~~313~~	~~1.05~~	~~0.0659~~	~~0.00519~~	~~0.03462~~	~~0.00297~~	~~0.00381~~	~~5E-05~~	~~0.00116~~	~~0.00001~~	~~0.27~~	~~24.5~~	~~0.3~~	~~35~~	~~3~~	~~25~~	~~0.3~~	High P La
Zircon_15_024	98	76	0.69	0.08589	0.01591	0.04765	0.00956	0.00402	0.0001	0.00119	0.00004	0.27	25.9	0.8	47	9	26	0.8	
Zircon_16_026	155	154	0.88	0.07372	0.01066	0.04065	0.0063	0.004	8E-05	0.00121	0.00002	0.2	25.7	0.5	40	6	26	0.5	
Zircon_17_027	199	239	1.07	0.07481	0.00714	0.04056	0.00418	0.00393	6E-05	0.00118	0.00002	0.21	25.3	0.4	40	4	25	0.4	
Zircon_18_028	135	182	1.19	0.06122	0.00386	0.03339	0.00216	0.00394	6E-05	0.00116	0.00003	0.22	25.3	0.4	33	2	25	0.4	
~~Zircon_19_029~~	~~148~~	~~140~~	~~0.84~~	~~0.06241~~	~~0.00676~~	~~0.03337~~	~~0.00389~~	~~0.00388~~	~~7E-05~~	~~0.00119~~	~~0.00002~~	~~0.22~~	~~25~~	~~0.4~~	~~33~~	~~4~~	~~25~~	~~0.4~~	High P
Zircon_2_009	186	258	1.23	0.04607	0.00181	0.02538	0.00122	0.004	9E-05	0.00157	0.00018	0.14	25.7	0.6	25	1	26	0.6	
Zircon_20_030	207	243	1.04	0.09593	0.02913	0.05502	0.01869	0.00416	0.0002	0.00122	0.00008	0.35	27	1.0	54	18	27	1.0	
Zircon_21_032	149	159	0.95	0.07234	0.00712	0.03905	0.00419	0.00392	7E-05	0.00118	0.00002	0.28	25.2	0.4	39	4	25	0.4	
Zircon_22_033	116	112	0.85	0.07385	0.00812	0.04113	0.00458	0.00403	7E-05	0.0013	0.00005	0.16	25.9	0.4	41	4	26	0.4	
~~**Zircon_23_034**~~	~~236~~	~~198~~	~~0.74~~	~~0.04886~~	~~0.00352~~	~~0.02503~~	~~0.00183~~	~~0.00379~~	~~5E-05~~	~~0.00131~~	~~0.00009~~	~~0.17~~	~~24.4~~	~~0.3~~	~~25~~	~~2~~	~~24~~	~~0.3~~	High P La
Zircon_25_036	277	301	0.96	0.06299	0.00328	0.03233	0.00171	0.00375	4E-05	0.00117	0.00004	0.18	24.1	0.3	32	2	24	0.3	
Zircon_26_038	99	97	0.86	0.07283	0.00548	0.04034	0.00335	0.00402	7E-05	0.00121	0.00002	0.25	25.8	0.4	40	3	26	0.4	
Zircon_27_039	186	153	0.73	0.06113	0.00512	0.03329	0.00302	0.00395	7E-05	0.00122	0.00002	0.24	25.4	0.4	33	3	25	0.4	
Zircon_28_040	216	271	1.11	0.07058	0.0351	0.03835	0.02194	0.00394	0.0003	0.00119	0.00022	0.52	25	2.0	38	21	~~25~~	~~2.0~~	High error
Zircon_29_041	132	159	1.07	0.07007	0.00455	0.0357	0.00241	0.00379	7E-05	0.00124	0.00005	0.27	24.4	0.4	36	2	24	0.4	
Zircon_30_042	229	157	0.61	0.06223	0.00511	0.0331	0.00288	0.00386	5E-05	0.00119	0.00002	0.2	24.8	0.4	33	3	25	0.4	
Zircon_31_044	144	170	1.04	0.07729	0.00433	0.04057	0.00234	0.00387	5E-05	0.00124	0.00009	0.24	24.9	0.3	40	2	25	0.3	
~~Zircon_32_045~~	~~228~~	~~202~~	~~0.79~~	~~0.06882~~	~~0.00372~~	~~0.03533~~	~~0.00433~~	~~0.00419~~	~~0.0005~~	~~0.00116~~	~~0.00004~~	~~0.9~~	~~27~~	~~3.0~~	~~35~~	4	~~27~~	~~3.0~~	High error
Zircon_33_046	98	94	0.85	0.08011	0.02399	0.04542	0.01475	0.00411	0.0002	0.00123	0.00008	0.33	26	1.0	45	14	~~26~~	~~1.0~~	
Zircon_34_047	124	106	0.76	0.09089	0.0069	0.05076	0.00429	0.00405	8E-05	0.00119	0.00002	0.32	26.1	0.5	50	4	26	0.5	
Zircon_35_048	311	315	0.90	0.09327	0.01422	0.04755	0.00773	0.0037	8E-05	0.00109	0.00002	0.22	23.8	0.5	47	7	24	0.5	
Zircon_36_050	193	224	1.03	0.11816	0.01318	0.06765	0.00832	0.00415	8E-05	0.00119	0.00003	0.34	26.7	0.5	66	8	27	0.5	
Zircon_37_051	163	176	0.96	0.06079	0.01273	0.03063	0.00672	0.00365	9E-05	0.00113	0.00006	0.13	23.5	0.6	31	7	24	0.6	
Zircon_38_052	127	111	0.78	0.05886	0.01257	0.03095	0.00714	0.00381	0.0001	0.00118	0.00008	0.26	24.5	0.7	31	7	25	0.7	
Zircon_39_053	198	145	0.65	0.0615	0.00326	0.0339	0.00187	0.00404	6E-05	0.00125	0.00004	0.28	26	0.4	34	2	26	0.4	
Zircon_40_054	155	210	1.20	0.07087	0.00593	0.03689	0.00338	0.00378	6E-05	0.00114	0.00002	0.22	24.3	0.4	37	3	24	0.4	
Zircon_5_012	191	201	0.93	0.06225	0.00495	0.03268	0.00281	0.00381	6E-05	0.00117	0.00002	0.21	24.5	0.4	33	3	25	0.4	
Zircon_8_016	151	143	0.84	0.09674	0.01326	0.05353	0.00805	0.00401	0.0001	0.00118	0.00003	0.38	25.8	0.6	53	8	26	0.6	
Zircon_9_017	641	1324	1.83	0.06293	0.0022	0.03079	0.0011	0.00355	3E-05	0.00105	0.00003	0.21	22.8	0.2	31	1	23	0.2	

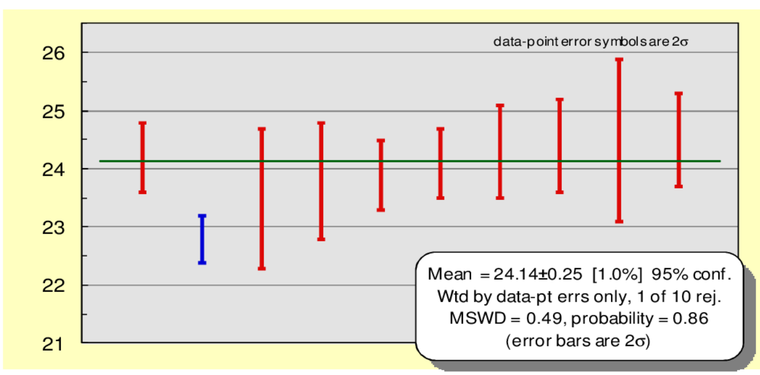

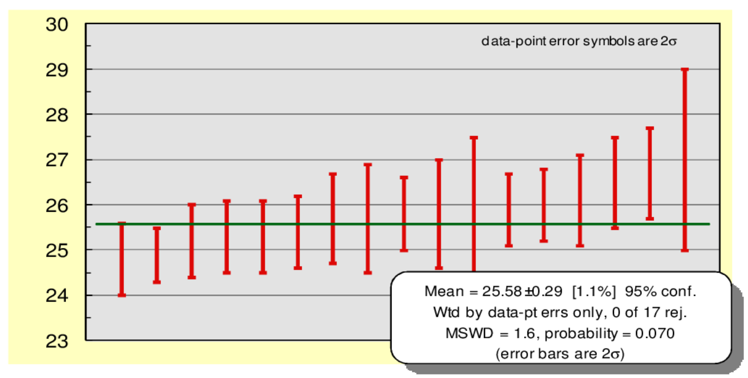

BM100305-1 Témoris Formation (Tti)

Trace elements (ppm)	P	Ti	Y	Nb	La	Ce	Pr	Nd	Sm	Eu	Gd	Tb	Dy	Ho	Er	Yb	Lu	Hf	Th	U	notes
Zircon_1_BM05-1_008	133	2	1374	2	0	34	0	4	6	2	32	10	123	47	212	447	89	10035	171	242	
Zircon_10_018	1229	47	7002	26	48	2513	54	360	211	54	424	95	841	246	929	1513	274	8469	556	351	High P La
Zircon_11_020	445	9	3213	6	0	81	0	4	10	4	67	23	283	108	485	975	179	11213	265	299	
Zircon_12_021	1237	6	2605	3	978	1706	160	571	72	8	92	22	246	89	385	726	135	14460	205	204	High P La
Zircon_13_022	375	15	1559	2	1	26	0	3	5	2	31	11	135	52	236	477	93	13250	72	124	
Zircon_14_023	2919	20	3584	4	34	176	13	73	35	10	115	32	352	124	531	1001	191	9552	313	265	High P La
Zircon_15_024	124	19	1090	1	0	23	0	4	6	2	28	9	100	37	164	343	68	9045	76	98	
Zircon_16_026	425	21	2199	3	1	53	1	6	9	3	51	17	198	75	330	642	123	9806	154	155	
Zircon_17_027	606	23	3212	3	2	82	1	13	19	7	96	28	317	112	472	871	161	11287	239	199	
Zircon_18_028	203	10	2279	2	0	67	1	14	20	7	80	22	231	80	336	622	117	11871	182	135	
Zircon_19_029	3014	0	2610	2	19	86	7	39	22	7	82	24	259	91	383	728	138	10573	140	148	High P
Zircon_2_009	496	22	2323	2	3	70	2	19	21	7	80	22	233	80	341	648	127	8615	258	186	
Zircon_20_030	425	42	3421	3	2	75	1	16	24	9	107	31	340	119	497	909	171	10522	243	207	
Zircon_21_032	568	30	3036	2	1	52	1	18	26	11	108	30	312	105	432	762	145	11700	159	149	
Zircon_22_033	292	11	2624	2	0	47	1	10	17	7	82	24	265	94	391	709	132	10488	112	116	
Zircon_23_034	1567	10	2839	3	755	1327	136	478	62	7	86	22	260	98	440	864	164	13614	198	236	High P La
Zircon_25_036	629	15	3658	5	1	85	1	9	16	6	90	29	338	124	535	1003	190	10630	301	277	
Zircon_26_038	337	8	2468	2	0	42	1	11	17	7	80	23	251	87	367	654	122	10606	97	99	
Zircon_27_039	341	7	1667	3	0	35	0	3	7	2	37	13	151	57	255	520	100	11294	153	186	
Zircon_28_040	526	35	2901	4	6	159	4	24	22	7	86	25	276	99	419	771	156	10151	271	216	
Zircon_29_041	375	13	2224	2	0	50	1	12	17	7	75	21	220	76	320	602	118	10931	159	132	
Zircon_30_042	561	0	2719	4	0	46	0	7	12	4	63	21	247	92	409	808	155	13574	157	229	
Zircon_31_044	514	10	2842	2	0	58	1	12	19	8	90	26	284	99	413	755	144	11163	170	144	
Zircon_32_045	486	12	2725	4	2	54	1	9	14	5	69	22	249	91	402	782	153	13027	202	228	
Zircon_33_046	407	56	1919	2	2	42	1	10	13	5	55	16	181	65	281	554	108	10887	94	98	
Zircon_34_047	172	21	1730	2	0	37	0	6	10	3	45	14	161	59	257	496	98	12084	106	124	
Zircon_35_048	749	44	3866	6	1	95	1	8	15	6	87	29	342	128	568	1070	217	11090	315	311	
Zircon_36_050	521	45	3048	3	1	65	1	14	21	7	94	28	300	106	447	813	156	10492	224	193	
Zircon_37_051	539	bdl	2540	3	0	54	1	9	14	6	69	21	243	88	379	729	141	10631	176	163	
Zircon_38_052	441	7	1572	2	0	34	0	4	7	3	37	12	140	53	234	466	92	11565	111	127	
Zircon_39_053	448	11	2264	2	0	38	0	5	10	3	54	18	210	77	336	654	123	14996	145	198	
Zircon_40_054	537	12	3364	2	0	54	1	19	30	14	122	33	342	116	482	892	173	12016	210	155	
Zircon_5_012	357	25	3566	5	0	89	1	11	19	7	98	30	344	126	539	962	187	9343	201	191	
Zircon_8_016	537	43	2565	2	1	43	1	11	16	7	76	23	253	89	380	712	135	9909	143	151	
Zircon_9_017	954	11	4971	10	1	178	1	17	30	11	141	43	485	174	734	1351	251	11931	1324	641	

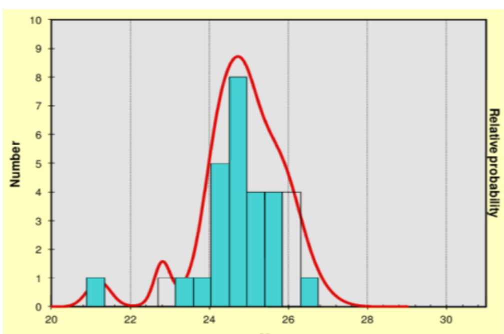

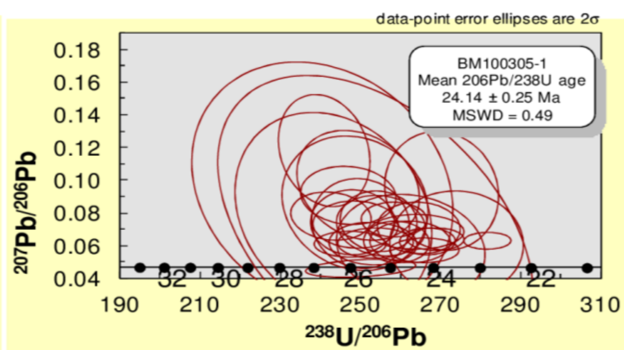

BM100304-4 Sierra Guazapares fm. (Tsxi) Mean $^{206}Pb/^{238}U$ age (±2σ): 24.7 ± 0.2 Ma

				CORRECTED RATIOS[2]									CORRECTED AGES (Ma)						
	U[1] (ppm)	Th[1] (ppm)	Th/U	$^{207}Pb/^{206}Pb$	±1σ[3]	$^{207}Pb/^{235}U$	±1σ[3]	$^{206}Pb/^{238}U$	±1σ[3]	$^{208}Pb/^{232}Th$	±1σ[3]	Rho	$^{206}Pb/^{238}U$	±1σ	$^{207}Pb/^{235}U$	±1σ	Best age (Ma)	±1σ	notes
Zircon_1_BM100304-4_008	163	108	0.61	0.06075	0.00383	0.03235	0.00209	0.00389	6E-05	0.00113	0.00004	0.22	25	0.4	32	2	25.0	0.4	
Zircon_11_020	133	100	0.69	0.06319	0.00348	0.03345	0.00192	0.00391	6E-05	0.00133	0.00007	0.28	25.2	0.4	33	2	25.2	0.4	
Zircon_12_021	461	513	1.02	0.04966	0.00209	0.02481	0.00107	0.00364	4E-05	0.00105	0.00002	0.22	23.4	0.3	25	1	23.4	0.3	
Zircon_13_022	163	165	0.93	0.07302	0.00758	0.03836	0.00434	0.00381	7E-05	0.00115	0.00002	0.22	24.5	0.5	38	4	24.5	0.5	
Zircon_15_024	84	51	0.55	0.08299	0.00697	0.04588	0.00393	0.00408	7E-05	0.00126	0.00008	0.2	26.2	0.4	46	4	26.2	0.4	
Zircon_16_026	204	164	0.73	0.05284	0.00285	0.02712	0.00152	0.00373	6E-05	0.00109	0.00003	0.27	24	0.4	27	2	24.0	0.4	
Zircon_17_027	153	148	0.88	0.06269	0.00426	0.03289	0.0023	0.00389	6E-05	0.00123	0.00004	0.24	25	0.4	33	2	25.0	0.4	
Zircon_19_029	124	116	0.86	0.06426	0.00605	0.03662	0.00384	0.00413	9E-05	0.00127	0.00003	0.24	26.6	0.6	37	4	26.6	0.6	
Zircon_2_009	368	497	1.24	0.05248	0.00247	0.02615	0.00126	0.00364	4E-05	0.00112	0.00002	0.21	23.4	0.3	26	1	23.4	0.3	
Zircon_20_030	295	428	1.33	0.06283	0.01225	0.03285	0.00689	0.00379	0.0001	0.00116	0.00005	0.23	24.4	0.7	33	7	24.4	0.7	
Zircon_22_033	190	218	1.05	0.0652	0.0141	0.03657	0.00862	0.00407	0.0001	0.00124	0.00007	0.31	26.2	0.9	36	8	26.2	0.9	
Zircon_23_034	121	162	1.23	0.06341	0.00463	0.03427	0.00259	0.00391	7E-05	0.00122	0.00005	0.26	25.2	0.4	34	3	25.2	0.4	
Zircon_24_035	171	148	0.79	0.05931	0.0035	0.03075	0.00187	0.00382	6E-05	0.00116	0.00004	0.24	24.6	0.4	31	2	24.6	0.4	
Zircon_26_038	120	96	0.73	0.06768	0.00992	0.03579	0.00578	0.00384	0.0001	0.00117	0.00003	0.32	24.7	0.7	36	6	24.7	0.7	
Zircon_29_041	108	101	0.86	0.06981	0.00593	0.03703	0.00323	0.00393	7E-05	0.00128	0.00005	0.23	25.3	0.4	37	3	25.3	0.4	
Zircon_31_044	226	208	0.84	0.05524	0.00456	0.02902	0.00267	0.00381	7E-05	0.00119	0.00002	0.29	24.5	0.4	29	3	24.5	0.4	
Zircon_33_046	52	41	0.72	0.07033	0.00985	0.04065	0.00576	0.00425	9E-05	0.00126	0.00014	0.15	27.3	0.6	40	6	27.3	0.6	
Zircon_34_047	146	139	0.87	0.04608	0.00373	0.02461	0.00218	0.00387	7E-05	0.00132	0.00011	0.26	24.9	0.5	25	2	24.9	0.5	
Zircon_35_048	177	206	1.06	0.05611	0.00337	0.02857	0.00177	0.00375	6E-05	0.00115	0.00003	0.25	24.1	0.4	29	2	24.1	0.4	
Zircon_36_050	158	200	1.16	0.04609	0.0083	0.02463	0.00491	0.00388	0.0001	0.00134	0.00015	0.31	24.9	0.8	25	5	24.9	0.8	
Zircon_37_051	126	95	0.69	0.05958	0.00457	0.03142	0.00264	0.00382	6E-05	0.00118	0.00002	0.26	24.6	0.4	31	3	24.6	0.4	
Zircon_38_052	144	121	0.77	0.05633	0.0036	0.03013	0.00199	0.00394	6E-05	0.00122	0.00004	0.25	25.3	0.4	30	2	25.3	0.4	
Zircon_39_053	215	250	1.06	0.05535	0.00567	0.02808	0.00305	0.00368	6E-05	0.00115	0.00002	0.21	23.7	0.4	28	3	23.7	0.4	
Zircon_40_054	193	170	0.81	0.05904	0.00401	0.03064	0.00212	0.00378	5E-05	0.00114	0.00004	0.19	24.3	0.3	31	2	24.3	0.3	

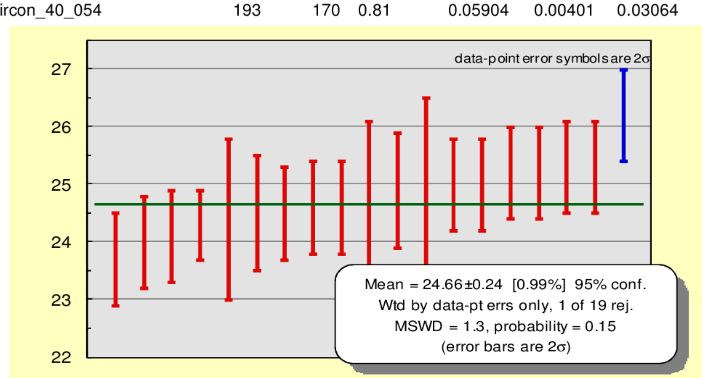

BM100304-4 Sierra Guazapares fm. (Tsxi)

Trace elements (ppm)	P	Ti	Y	Nb	La	Ce	Pr	Nd	Sm	Eu	Gd	Tb	Dy	Ho	Er	Yb	Lu	Hf	Th	U	notes
Zircon_1_BM04-4_008	842	4	2836	15	0	46	0	1	4	1	33	15	212	92	460	1040	205	12115	108	163	
Zircon_11_020	758	2	3669	13	0	115	0	3	9	3	70	26	332	127	557	1026	189	12023	100	133	
Zircon_12_021	1002	3	3372	13	0	52	0	2	5	1	44	19	269	111	532	1132	220	12465	513	461	
Zircon_13_022	1856	11	4599	12	1	32	0	2	7	1	61	27	367	149	703	1449	291	11957	165	163	
Zircon_15_024	910	9	3876	8	0	101	0	5	11	4	71	27	333	128	581	1149	214	11925	51	84	
Zircon_16_026	571	11	2610	3	0	44	0	4	7	4	46	16	211	85	406	924	191	8871	164	204	
Zircon_17_027	404	9	2820	3	0	45	1	9	15	7	71	22	255	94	425	935	192	8041	148	153	
Zircon_19_029	935	1	2715	5	0	44	0	3	8	2	47	18	229	90	416	866	169	10837	116	124	
Zircon_2_009	951	5	3035	7	0	54	0	4	9	3	52	20	255	101	472	981	194	10160	497	368	
Zircon_20_030	344	3	1198	2	1	28	0	2	4	1	24	8	104	40	184	377	76	10894	428	295	
Zircon_22_033	559	1	1819	3	0	24	0	2	4	2	29	11	148	60	284	626	127	11257	162	121	
Zircon_23_034	1081	8	3097	9	0	47	0	2	5	2	43	18	247	101	487	1030	203	11639	148	171	
Zircon_24_035	1300	bdl	3202	10	0	31	0	2	5	1	40	18	251	101	479	1041	207	11696	96	120	
Zircon_26_038	736	6	2981	14	0	54	0	2	5	1	38	16	232	98	473	1023	200	11198	279	260	
Zircon_29_041	1371	9	4185	5	0	63	0	4	10	3	65	26	340	137	648	1344	266	11770	41	52	
Zircon_31_044	1294	8	2999	4	0	21	0	2	4	1	35	17	237	98	474	1016	198	11809	206	177	
Zircon_33_046	835	27	2769	9	0	42	0	2	5	1	36	16	220	91	434	907	180	11802	210	103	
Zircon_34_047	2912	20	8186	26	0	59	0	3	11	2	92	44	628	258	1229	2501	479	14195	95	126	
Zircon_35_048	280	9	1701	2	0	36	0	4	7	3	37	12	150	57	263	574	117	8978	121	144	
Zircon_36_050	2926	7	7409	20	1	37	0	3	8	1	74	38	560	234	1136	2363	460	14307	250	215	
Zircon_37_051	2255	bdl	6110	8	0	49	0	4	11	3	86	36	486	197	934	1911	382	12250	251	265	
Zircon_38_052	1054	5	2345	4	2	53	1	7	8	3	45	16	193	76	361	775	165	9464	170	193	
Zircon_39_053	359	bdl	1527	2	0	28	0	3	7	2	36	12	142	51	230	440	85	10731	331	183	
Zircon_40_054	444	31	2018	2	8	32	2	9	11	4	52	17	190	69	304	591	117	8266	358	297	

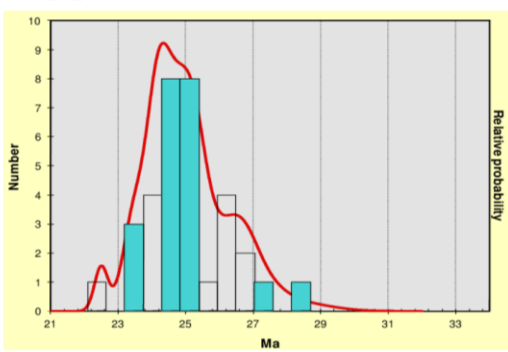

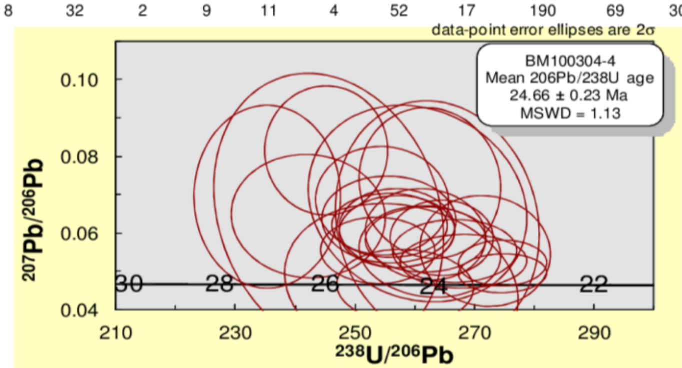

BM100307-1 Sierra Guazapares fm. (Tsl) Mean $^{206}Pb/^{238}U$ age ($\pm 2\sigma$): 23.7 ± 0.2 Ma

				CORRECTED RATIOS[2]									CORRECTED AGES (Ma)						
	U[1] (ppm)	Th[1] (ppm)	Th/U	$^{207}Pb/^{206}Pb$	$\pm 1\sigma^3$	$^{207}Pb/^{235}U$	$\pm 1\sigma^3$	$^{206}Pb/^{238}U$	$\pm 1\sigma^3$	$^{208}Pb/^{232}Th$	$\pm 1\sigma^3$	Rho	$^{206}Pb/^{238}U$	$\pm 1\sigma$	$^{207}Pb/^{235}U$	$\pm 1\sigma$	Best age (Ma)	$\pm 1\sigma$	notes
Zircon_1_BM100307-1_008	303	271	0.83	0.06633	0.02477	0.03575	0.01477	0.00391	0.0002	0.00119	0.00017	0.35	25	1.0	36	14	25.0	1.0	
Zircon_10_018	212	177	0.78	0.06258	0.00444	0.03433	0.00248	0.00407	5E-05	0.00134	0.00004	0.19	26.2	0.3	34	2	26.2	0.3	
Zircon_11_020	832	656	0.73	0.04844	0.00126	0.02464	0.00067	0.0037	3E-05	0.00117	0.00002	0.29	23.8	0.2	24.7	0.7	23.8	0.2	
Zircon_12_021	143	84	0.55	0.05633	0.0045	0.03087	0.00262	0.00397	6E-05	0.00124	0.00002	0.21	25.6	0.4	31	3	25.6	0.4	
Zircon_13_022	396	399	0.93	0.05059	0.00253	0.02562	0.00131	0.00371	4E-05	0.00116	0.00002	0.21	23.9	0.3	26	1	23.9	0.3	
Zircon_14_023	65	32	0.46	0.06404	0.00615	0.03805	0.00372	0.00433	8E-05	0.00118	0.00012	0.19	27.9	0.5	38	4	27.9	0.5	
Zircon_15_024	105	69	0.61	0.06836	0.01231	0.03726	0.00674	0.00407	7E-05	0.00134	0.00015	0.09	26.2	0.4	37	7	26.2	0.4	
Zircon_16_026	319	324	0.94	0.06275	0.00377	0.03381	0.00207	0.0039	5E-05	0.00125	0.00004	0.19	25.1	0.3	34	2	25.1	0.3	
Zircon_17_027	90	63	0.66	0.08897	0.01868	0.04955	0.01046	0.00423	9E-05	0.00139	0.00005	0.1	27.2	0.6	49	10	27.2	0.6	
Zircon_19_029	83	38	0.43	0.05483	0.00543	0.03294	0.0033	0.00437	7E-05	0.00119	0.00008	0.15	28.1	0.4	33	3	28.1	0.4	
Zircon_20_030	81	52	0.59	0.0917	0.02017	0.05336	0.01178	0.00417	8E-05	0.00118	0.00008	0.09	26.8	0.5	53	11	26.8	0.5	
Zircon_21_032	43	15	0.32	0.06141	0.00862	0.03957	0.0058	0.00467	0.0001	0.00144	0.00005	0.2	30.1	0.8	39	6	30.1	0.8	
Zircon_22_033	77	59	0.71	0.07961	0.00796	0.04451	0.00456	0.00423	9E-05	0.00142	0.00009	0.22	27.2	0.6	44	4	27.2	0.6	
Zircon_24_035	271	154	0.53	0.06021	0.00355	0.03292	0.00199	0.00397	5E-05	0.00135	0.00009	0.22	25.5	0.3	33	2	25.5	0.3	
Zircon_25_036	126	76	0.56	0.05367	0.0044	0.02829	0.00238	0.00391	7E-05	0.0013	0.00006	0.22	25.2	0.4	28	2	25.2	0.4	
Zircon_26_038	210	177	0.78	0.06299	0.00359	0.03142	0.00184	0.00363	5E-05	0.00116	0.00003	0.23	23.4	0.3	31	2	23.4	0.3	
Zircon_27_039	58	25	0.41	0.08542	0.00959	0.05243	0.00616	0.00445	0.0001	0.00132	0.00004	0.21	28.6	0.7	52	6	28.6	0.7	
Zircon_28_040	144	80	0.51	0.06313	0.00519	0.0338	0.00299	0.00388	7E-05	0.00119	0.00002	0.24	25	0.5	34	3	25.0	0.5	
Zircon_29_041	232	211	0.85	0.0539	0.00286	0.02841	0.00155	0.00384	5E-05	0.00115	0.00003	0.23	24.7	0.3	28	2	24.7	0.3	
Zircon_3_010	249	182	0.68	0.0606	0.0037	0.03181	0.00197	0.00384	4E-05	0.0012	0.00003	0.17	24.7	0.3	32	2	24.7	0.3	
~~Zircon_30_042~~	~~586~~	~~614~~	~~0.97~~	~~0.05044~~	~~0.00207~~	~~0.02569~~	~~0.0011~~	~~0.0037~~	~~4E-05~~	~~0.00113~~	~~0.00002~~	~~0.29~~	~~23.8~~	~~0.3~~	~~26~~	~~1~~	~~23.8~~	~~0.3~~	High P
Zircon_31_044	575	564	0.91	0.05147	0.0016	0.02594	0.00084	0.00367	3E-05	0.00115	0.00002	0.28	23.6	0.2	26	0.8	23.6	0.2	
Zircon_32_045	470	598	1.18	0.05795	0.00686	0.03144	0.00397	0.00394	6E-05	0.00122	0.00002	0.27	25.3	0.4	31	4	25.3	0.4	
Zircon_33_046	136	85	0.58	0.06983	0.00738	0.03867	0.00428	0.00402	7E-05	0.00122	0.00002	0.17	25.8	0.5	39	4	25.8	0.5	
Zircon_34_047	108	70	0.60	0.08067	0.00946	0.04584	0.00569	0.00412	7E-05	0.00123	0.00002	0.22	26.5	0.4	46	6	26.5	0.4	
~~Zircon_35_048~~	~~278~~	~~149~~	~~0.50~~	~~0.05641~~	~~0.00428~~	~~0.02848~~	~~0.00231~~	~~0.00366~~	~~5E-05~~	~~0.00114~~	~~0.00002~~	~~0.22~~	~~23.6~~	~~0.3~~	~~29~~	~~2~~	~~23.6~~	~~0.3~~	High P
Zircon_36_050	296	139	0.43	0.07809	0.01445	0.0439	0.00871	0.00408	0.0001	0.00122	0.00005	0.26	26.2	0.7	44	8	26.2	0.7	
Zircon_37_051	133	81	0.56	0.07543	0.01219	0.04276	0.00697	0.00411	6E-05	0.00124	0.00003	0.09	26.4	0.4	43	7	26.4	0.4	
~~Zircon_38_052~~	~~171~~	~~126~~	~~0.68~~	~~0.05556~~	~~0.01055~~	~~0.03047~~	~~0.00625~~	~~0.00398~~	~~8E-05~~	~~0.00124~~	~~0.00009~~	~~0.24~~	~~25.6~~	~~0.5~~	~~30~~	~~6~~	~~25.6~~	~~0.5~~	High P La
Zircon_39_053	136	97	0.67	0.06799	0.00884	0.03779	0.00495	0.00402	6E-05	0.0013	0.00006	0.12	25.9	0.4	38	5	25.9	0.4	
Zircon_4_011	91	43	0.44	0.07359	0.00957	0.04387	0.00577	0.00435	9E-05	0.0013	0.00007	0.15	28	0.6	44	6	28.0	0.6	
~~Zircon_40_054~~	~~881~~	~~1734~~	~~1.82~~	~~0.05076~~	~~0.00147~~	~~0.02508~~	~~0.00076~~	~~0.00361~~	~~3E-05~~	~~0.00105~~	~~0.00001~~	~~0.3~~	~~23.2~~	~~0.2~~	~~25.2~~	~~0.8~~	~~23.2~~	~~0.2~~	High P Th
Zircon_5_012	181	118	0.60	0.05509	0.00502	0.03029	0.00303	0.00399	7E-05	0.00124	0.00002	0.3	25.7	0.5	30	3	25.7	0.5	
Zircon_6_014	341	314	0.85	0.05085	0.00249	0.02688	0.00134	0.00386	4E-05	0.0012	0.00003	0.19	24.8	0.3	27	1	24.8	0.3	
Zircon_8_016	159	116	0.68	0.04672	0.00794	0.02445	0.00444	0.0038	8E-05	0.00121	0.00013	0.19	24.4	0.5	25	4	24.4	0.5	
Zircon_9_017	136	95	0.65	0.06507	0.00462	0.03554	0.00259	0.00404	6E-05	0.00124	0.00005	0.23	26	0.4	35	3	26.0	0.4	

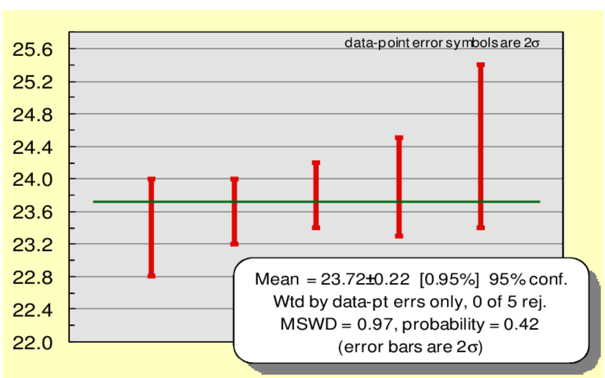

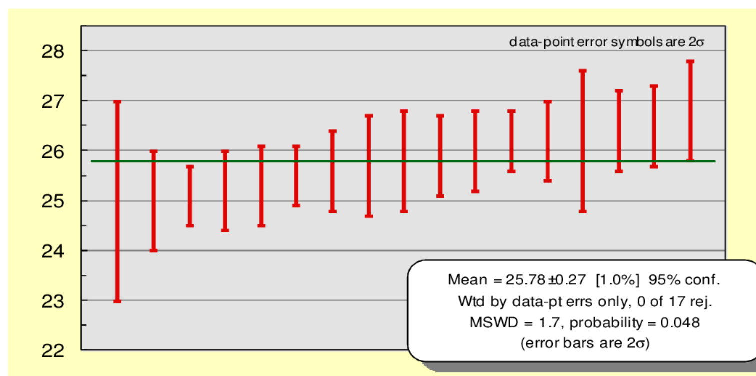

BM100307-1	Sierra Guazapares fm. (Tsl)																			
Trace elements (ppm)	P	Ti	Y	Nb	La	Ce	Pr	Nd	Sm	Eu	Gd	Tb	Dy	Ho	Er	Yb	Lu	Hf	Th	U	notes
Zircon_1_BM07-1_008	911	5	2742	6	0	59	0	4	10	3	58	20	240	92	421	823	167	9251	271	303	
Zircon_10_018	746	8	1987	3	0	41	0	3	6	2	39	14	172	66	292	557	112	11436	177	212	
Zircon_11_020	1974	10	6901	8	0	148	1	16	34	13	175	55	631	231	999	1773	346	9271	656	832	
Zircon_12_021	469	10	1735	3	0	25	0	3	5	2	32	11	141	55	264	546	117	9910	84	143	
Zircon_13_022	1473	7	4736	8	0	118	0	8	17	6	107	37	429	157	674	1195	227	10877	399	396	
Zircon_14_023	177	0	826	1	0	13	0	2	3	1	18	6	70	27	123	254	54	10796	32	65	
Zircon_15_024	526	10	1564	2	0	22	0	3	5	2	31	11	130	51	233	466	98	9669	69	105	
Zircon_16_026	1209	16	3334	6	1	82	1	6	11	5	68	23	272	104	473	897	179	10793	324	319	
Zircon_17_027	641	6	1508	1	0	18	0	5	8	3	40	12	137	50	220	426	89	9763	63	90	
Zircon_19_029	315	9	836	1	0	14	0	1	2	1	14	5	65	27	129	280	61	11544	38	83	
Zircon_20_030	178	15	1256	1	0	18	0	4	7	3	33	10	113	42	183	351	73	10462	52	81	
Zircon_21_032	86	4	425	1	0	9	0	1	1	0	7	3	33	13	65	151	33	11765	15	43	
Zircon_22_033	605	12	1392	1	0	17	0	6	9	4	41	12	130	46	200	376	78	9254	59	77	
Zircon_24_035	1139	9	2096	5	1	34	0	4	6	2	37	14	174	69	312	614	123	13313	154	271	
Zircon_25_036	683	3	1517	2	0	27	0	2	5	2	31	11	129	49	223	439	89	10876	76	126	
Zircon_26_038	884	3	2797	3	0	47	1	11	17	7	77	24	256	92	397	740	149	9361	177	210	
Zircon_27_039	345	5	626	1	0	14	0	1	2	1	11	4	51	20	96	204	43	11846	25	58	
Zircon_28_040	565	4	1474	3	0	26	0	2	4	2	25	9	117	48	222	452	95	10927	80	144	
Zircon_29_041	995	7	3208	3	0	51	1	11	21	8	93	28	297	106	457	856	175	9513	211	232	
Zircon_3_010	560	10	1780	3	0	40	0	4	7	2	38	13	158	60	268	520	106	11449	182	249	
Zircon_30_042	3248	bdl	7306	9	0	140	1	11	26	9	150	51	608	235	1062	2021	406	9127	614	586	High P
Zircon_31_044	1409	1	4254	7	0	106	0	6	15	6	91	30	368	141	623	1136	227	10440	564	575	
Zircon_32_045	853	16	1713	7	1	57	0	3	6	1	36	12	149	56	246	465	91	11334	598	470	
Zircon_33_046	616	bdl	1288	2	0	29	0	2	3	1	22	8	103	41	193	394	81	11405	85	136	
Zircon_34_047	460	12	1132	2	0	21	0	2	4	1	22	7	92	36	172	356	75	10789	70	108	
Zircon_35_048	2474	5	1953	6	8	59	3	16	8	2	34	12	153	62	291	597	123	12134	149	278	High P
Zircon_36_050	1709	17	3221	3	1	29	0	5	11	4	65	23	277	104	464	872	172	12662	139	296	
Zircon_37_051	421	6	1419	2	0	26	0	3	7	2	32	11	125	46	205	391	78	12137	81	133	
Zircon_38_052	6688	14	1929	3	24	95	8	40	16	4	53	16	175	64	277	514	102	11126	126	171	High P La
Zircon_39_053	521	8	1474	2	0	28	0	2	5	2	30	10	122	47	214	428	89	11423	97	136	
Zircon_4_011	295	5	957	2	0	18	0	2	3	1	19	7	82	32	147	304	63	10733	43	91	
Zircon_40_054	2638	7	9217	17	0	283	1	18	37	13	220	73	835	296	1195	1865	338	10290	1734	881	High P Th
Zircon_5_012	977	7	1849	3	0	30	0	2	5	2	33	12	155	60	267	518	101	10919	118	181	
Zircon_6_014	925	13	3220	5	0	68	0	6	13	5	77	25	294	109	476	869	174	9779	314	341	
Zircon_8_016	417	8	1449	2	0	31	0	3	5	2	30	10	122	48	219	436	92	11019	116	159	
Zircon_9_017	349	6	1785	2	0	26	0	5	9	3	44	14	157	59	264	517	109	10144	95	136	

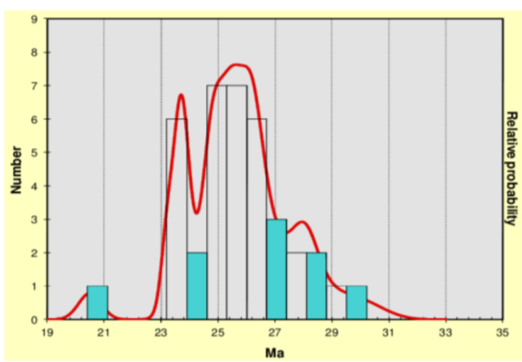

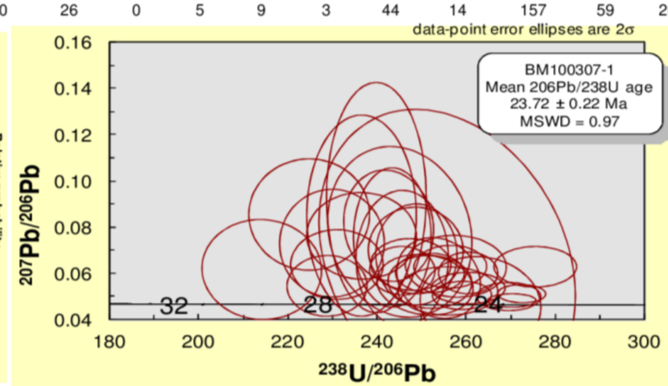

BM100305-2	Sierra Guazapares fm. (Tsl)		Mean $^{206}Pb/^{238}U$ age ($\pm2\sigma$): 23.9 ± 0.3 Ma																
				CORRECTED RATIOS[2]									CORRECTED AGES (Ma)						
	U[1] (ppm)	Th[1] (ppm)	Th/U	$^{207}Pb/^{206}Pb$	$\pm1\sigma^3$	$^{207}Pb/^{235}U$	$\pm1\sigma^3$	$^{206}Pb/^{238}U$	$\pm1\sigma^3$	$^{208}Pb/^{232}Th$	$\pm1\sigma^3$	Rho	$^{206}Pb/^{238}U$	$\pm1\sigma$	$^{207}Pb/^{235}U$	$\pm1\sigma$	Best age (Ma)	$\pm1\sigma$	notes
~~Zircon_1_BM05-2_008~~	~~128~~	~~102~~	~~0.74~~	~~0.05435~~	~~0.00897~~	~~0.02498~~	~~0.00455~~	~~0.00333~~	~~7E-05~~	~~0.00104~~	~~0.00004~~	~~0.33~~	~~21.4~~	~~0.4~~	~~25~~	~~5~~	~~21~~	~~0.4~~	
~~Zircon_10_018~~	~~246~~	~~205~~	~~0.77~~	~~0.0608~~	~~0.00575~~	~~0.03102~~	~~0.00343~~	~~0.0037~~	~~7E-05~~	~~0.00114~~	~~0.00001~~	~~0.28~~	~~23.8~~	~~0.5~~	~~31~~	~~3~~	~~24~~	~~0.5~~	
Zircon_11_020	110	138	1.17	0.07102	0.02252	0.0382	0.01337	0.0039	0.0001	0.00118	0.00007	0.27	25.1	0.9	38	13	25	0.9	
Zircon_12_021	167	204	1.13	0.06707	0.00464	0.03582	0.00319	0.00393	9E-05	0.00124	0.00006	0.24	25.3	0.6	36	3	25	0.6	
Zircon_13_022	101	82	0.75	0.06667	0.02065	0.03591	0.01223	0.00391	0.0001	0.00119	0.00013	0.32	25.1	0.9	36	12	25	0.9	
Zircon_15_024	195	265	1.26	0.05802	0.00771	0.03012	0.00451	0.00376	7E-05	0.00117	0.00002	0.32	24.2	0.5	30	4	24	0.5	
Zircon_16_026	136	106	0.72	0.0572	0.00658	0.03068	0.00407	0.00389	8E-05	0.00121	0.00002	0.26	25	0.5	31	4	25	0.5	
Zircon_17_027	156	138	0.82	0.05818	0.009	0.03171	0.00547	0.00395	8E-05	0.00123	0.00003	0.16	25.4	0.5	32	5	25	0.5	
Zircon_18_028	110	113	0.95	0.08391	0.00454	0.04566	0.00534	0.00436	0.0004	0.00123	0.00005	0.23	28	2.0	45	5	28	2.0	
Zircon_19_029	122	100	0.75	0.07139	0.0195	0.04138	0.01259	0.0042	0.0001	0.00127	0.00008	0.26	27	0.9	41	12	27	0.9	
Zircon_2_009	266	356	1.23	0.05416	0.0062	0.02888	0.0037	0.00387	6E-05	0.00121	0.00002	0.27	24.9	0.4	29	4	25	0.4	
~~Zircon_20_030~~	~~109~~	~~86~~	~~0.73~~	~~0.05031~~	~~0.01433~~	~~0.0287~~	~~0.00873~~	~~0.00414~~	~~9E-05~~	~~0.00131~~	~~0.00021~~	~~0.28~~	~~26.6~~	~~0.6~~	~~29~~	~~9~~	~~27~~	~~0.6~~	
~~Zircon_21_032~~	~~201~~	~~311~~	~~1.43~~	~~0.04673~~	~~0.01503~~	~~0.02283~~	~~0.00776~~	~~0.00354~~	~~7E-05~~	~~0.00113~~	~~0.00012~~	~~0.29~~	~~22.8~~	~~0.5~~	~~23~~	~~8~~	~~23~~	~~0.5~~	
Zircon_22_033	113	110	0.90	0.07695	0.00731	0.04235	0.00488	0.00399	9E-05	0.0012	0.00002	0.22	25.7	0.6	42	5	26	0.6	
~~Zircon_24_035~~	~~122~~	~~100~~	~~0.76~~	~~0.05856~~	~~0.02279~~	~~0.03043~~	~~0.01278~~	~~0.00377~~	~~0.0001~~	~~0.00117~~	~~0.00023~~	~~0.34~~	~~24.3~~	~~0.8~~	~~30~~	~~13~~	~~24~~	~~0.8~~	
Zircon_26_038	222	238	0.99	0.06074	0.0083	0.03074	0.00468	0.00367	6E-05	0.00113	0.00001	0.22	23.6	0.4	31	5	24	0.4	
Zircon_27_039	208	216	0.96	0.06055	0.00584	0.03115	0.00345	0.00373	6E-05	0.00115	0.00001	0.23	24	0.4	31	3	24	0.4	
Zircon_28_040	103	78	0.70	0.07484	0.01715	0.04243	0.01099	0.00411	0.0001	0.00124	0.00004	0.21	26.5	0.9	42	11	27	0.9	
Zircon_30_042	130	144	1.02	0.06905	0.01014	0.03572	0.00589	0.00375	7E-05	0.00114	0.00001	0.22	24.1	0.5	36	6	24	0.5	
Zircon_31_044	209	282	1.25	0.06279	0.00524	0.03233	0.0031	0.00373	5E-05	0.00115	0.00001	0.31	24	0.3	32	3	24	0.3	
Zircon_32_045	61	49	0.74	0.06311	0.00639	0.03532	0.00432	0.00418	0.0001	0.00113	0.00009	0.28	26.9	0.6	35	4	27	0.6	
Zircon_33_046	192	201	0.97	0.05557	0.00898	0.02759	0.00492	0.0036	7E-05	0.00112	0.00004	0.29	23.2	0.4	28	5	23	0.4	
Zircon_34_047	145	157	1.00	0.06573	0.00679	0.0353	0.00437	0.00389	9E-05	0.00119	0.00002	0.26	25.1	0.6	35	4	25	0.6	
Zircon_35_048	88	75	0.79	0.07812	0.00971	0.04306	0.00613	0.004	8E-05	0.0012	0.00001	0.25	25.7	0.5	43	6	26	0.5	
Zircon_37_051	126	115	0.84	0.07626	0.01843	0.03866	0.01047	0.00368	0.0001	0.00111	0.00004	0.21	23.7	0.8	39	10	24	0.8	
Zircon_39_053	149	150	0.93	0.06569	0.00606	0.03564	0.00369	0.00393	5E-05	0.0012	0.00001	0.22	25.3	0.3	36	4	25	0.3	
Zircon_4_011	84	79	0.87	0.06871	0.00453	0.03787	0.00328	0.00417	0.0001	0.00123	0.00007	0.34	26.8	0.6	38	3	27	0.6	
Zircon_40_055	84	49	0.54	0.05595	0.00587	0.03169	0.00386	0.00417	8E-05	0.00135	0.00007	0.31	26.8	0.5	32	4	27	0.5	
Zircon_5_012	134	129	0.89	0.08205	0.01921	0.04527	0.01176	0.004	0.0001	0.00119	0.00004	0.29	25.7	0.7	45	11	26	0.7	
Zircon_6_014	137	113	0.77	0.05853	0.00737	0.03067	0.00434	0.0038	7E-05	0.00118	0.00002	0.18	24.5	0.4	31	4	25	0.4	
Zircon_7_015	88	109	1.14	0.10444	0.02368	0.06526	0.01679	0.00453	0.0002	0.00132	0.00004	0.37	29.2	1.0	64	16	29	1.0	
Zircon_8_016	96	73	0.71	0.09137	0.01799	0.05015	0.01124	0.00398	0.0001	0.00117	0.00002	0.2	25.6	0.8	50	11	26	0.8	
Zircon_23_034	107	91	0.79	0.08316	0.00659	0.04671	0.0046	0.00409	9E-05	0.00134	0.00009	0.24	26.3	0.6	46	4	26	0.6	
Zircon_25_036	90	73	0.74	0.08359	0.00429	0.04682	0.00338	0.0041	0.0001	0.00133	0.0001	0.4	26.4	0.6	46	3	26	0.6	
Zircon_36_050	76	70	0.85	0.09145	0.01946	0.05272	0.0127	0.00418	0.0001	0.00123	0.00004	0.31	26.9	0.8	52	12	27	0.8	
Zircon_38_052	128	126	0.91	0.05947	0.01191	0.03214	0.00702	0.00392	8E-05	0.00121	0.00005	0.33	25.2	0.5	32	7	25	0.5	

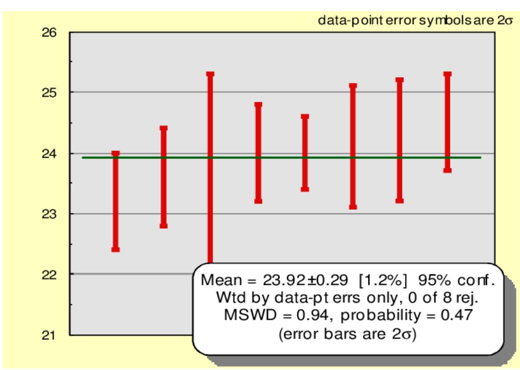

BM100305-2 Sierra Guazapares fm. (Tsl)

Trace elements (ppm)	P	Ti	Y	Nb	La	Ce	Pr	Nd	Sm	Eu	Gd	Tb	Dy	Ho	Er	Yb	Lu	Hf	Th	U	notes
Zircon_1_BM05-2_008	712	583	5074	12	66	56	52	350	178	18	320	66	546	155	578	909	173	7592	102	128	
Zircon_10_018	618	10	2771	3	91	263	22	104	35	6	90	25	262	92	404	767	155	9347	205	246	
Zircon_11_020	355	22	2423	2	1	41	1	16	21	8	84	24	245	83	348	636	129	7555	138	110	
Zircon_12_021	622	7	2941	3	1	55	1	11	18	6	88	27	291	100	419	731	144	8438	204	167	
Zircon_13_022	2577	11	2581	3	20	84	6	33	17	5	64	20	228	86	385	744	152	9633	82	101	
Zircon_15_024	485	20	3572	3	1	84	2	21	30	10	122	35	369	123	503	861	167	9161	265	195	
Zircon_16_026	531	5	1897	2	0	38	0	6	8	2	41	14	170	63	276	528	104	11198	106	136	
Zircon_17_027	380	8	2666	5	1	70	0	8	12	5	63	21	245	91	405	746	150	8750	138	156	
Zircon_18_028	261	23	1934	1	0	30	1	9	15	6	62	18	192	67	287	531	107	8665	113	110	
Zircon_19_029	412	26	1846	2	1	33	0	6	9	3	46	15	169	62	275	538	111	9012	100	122	
Zircon_2_009	929	9	4380	3	3	99	3	32	45	19	179	48	476	156	639	1110	219	7303	356	266	
Zircon_20_030	436	21	1531	2	180	335	30	111	18	3	41	12	139	51	228	441	90	9860	86	109	
Zircon_21_032	1435	14	4039	3	54	157	32	182	82	17	189	44	412	129	514	867	170	9467	311	201	
Zircon_22_033	486	11	2299	2	0	38	1	13	17	6	72	21	221	76	321	593	120	8744	110	113	
Zircon_24_035	674	17	3305	2	34	47	28	163	66	12	146	33	316	100	409	721	144	8826	100	122	
Zircon_26_038	914	4	3304	4	3	70	2	15	16	5	79	26	307	111	481	890	176	10483	238	222	
Zircon_27_039	804	15	3646	3	0	62	1	12	21	8	100	31	348	125	546	1003	203	9036	216	208	
Zircon_28_040	388	bdl	1739	2	1	31	1	6	8	3	43	14	157	58	258	497	100	9088	78	103	
Zircon_30_042	347	18	2274	2	1	43	1	11	16	6	71	21	222	77	329	591	119	9038	144	130	
Zircon_31_044	598	77	3225	4	1	84	1	19	26	9	111	31	324	110	459	805	159	8969	282	209	
Zircon_32_045	294	8	1205	1	0	16	0	5	7	3	33	10	111	40	178	354	75	8588	49	61	
Zircon_33_046	748	19	3641	3	9	66	9	58	42	10	130	37	373	123	507	870	170	8920	201	192	
Zircon_34_047	467	14	2536	2	0	51	1	12	17	6	75	22	243	86	376	707	144	8016	157	145	
Zircon_35_048	1589	bdl	1612	1	13	55	4	23	13	4	47	14	153	55	238	453	93	8691	75	88	
Zircon_37_051	987	13	2533	2	7	59	3	21	19	6	74	22	243	85	368	667	134	8728	115	126	
Zircon_39_053	402	13	2993	2	0	40	1	11	19	8	88	26	288	101	440	799	163	8722	150	149	
Zircon_4_011	351	1	1675	2	0	28	0	5	9	3	42	14	156	57	252	476	98	8364	79	84	
Zircon_40_055	362	12	1138	1	0	23	0	2	5	1	24	8	100	38	175	357	74	10555	49	84	
Zircon_5_012	387	68	2195	3	1	40	1	9	12	5	59	19	209	75	326	608	124	8122	129	134	
Zircon_6_014	745	17	2766	2	1	46	1	12	17	5	71	22	248	92	417	805	166	8427	113	137	
Zircon_7_015	317	70	1525	2	2	40	1	10	12	5	52	14	150	52	226	422	88	8040	109	88	
Zircon_8_016	201	15	1546	1	0	25	0	5	8	3	39	13	144	52	233	450	93	9433	73	96	
Zircon_23_034	441	8	2009	1	0	27	0	7	12	4	54	17	188	68	295	558	115	9221	91	107	
Zircon_25_036	305	15	1276	1	0	22	0	6	8	3	36	11	124	44	198	377	78	8476	73	90	
Zircon_36_050	536	34	2175	1	3	38	3	25	26	7	81	22	224	74	310	551	110	8225	70	76	
Zircon_38_052	582	6	2341	2	1	41	1	13	17	6	70	21	226	78	342	642	131	9430	126	128	

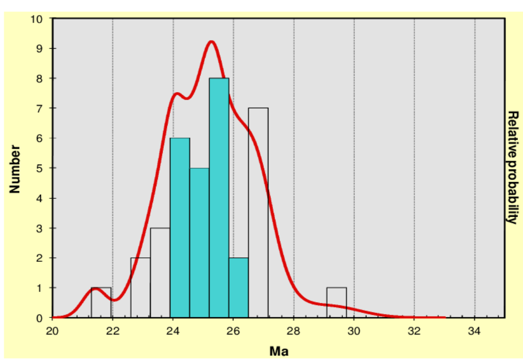

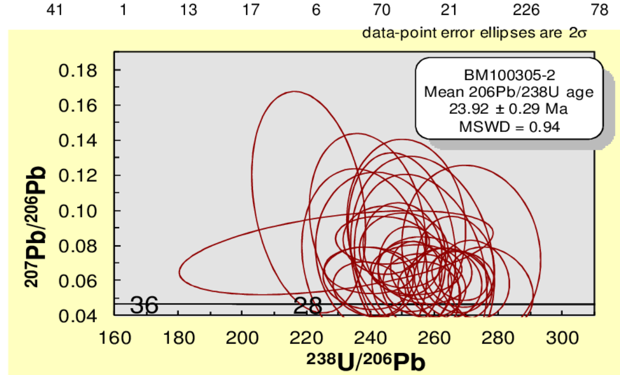

BM1000304-1 Sierra Guazapares fm. (Tsl) Mean $^{206}Pb/^{238}U$ age (±2σ): 22.9 ± 0.3 Ma

				CORRECTED RATIOS[2]													CORRECTED AGES (Ma)		
	U[1] (ppm)	Th[1] (ppm)	Th/U	$^{207}Pb/^{206}Pb$	±1σ[3]	$^{207}Pb/^{235}U$	±1σ[3]	$^{206}Pb/^{238}U$	±1σ[3]	$^{208}Pb/^{232}Th$	±1σ[3]	Rho	$^{206}Pb/^{238}U$	±1σ	$^{207}Pb/^{235}U$	±1σ	Best age (Ma)	±1σ	notes
Zircon_10_018	63	41	0.56	0.09236	0.01551	0.0563	0.01034	0.00442	0.0001	0.0013	0.00006	0.36	28.4	0.8	56	10	28	0.8	
Zircon_11_020	140	108	0.68	0.05889	0.0069	0.03124	0.00393	0.00385	7E-05	0.00119	0.00003	0.23	24.8	0.5	31	4	25	0.5	
Zircon_13_022	200	200	0.88	0.06805	0.0057	0.03582	0.00328	0.00382	6E-05	0.00116	0.00002	0.28	24.6	0.4	36	3	25	0.4	
Zircon_14_023	175	138	0.69	0.08305	0.01189	0.04509	0.00703	0.00394	9E-05	0.00117	0.00003	0.27	25.3	0.6	45	7	25	0.6	
Zircon_15_024	617	373	0.53	0.07118	0.00643	0.03518	0.00349	0.00358	5E-05	0.00109	0.00002	0.39	23.1	0.3	35	3	23	0.3	
~~Zircon_16_026~~	~~441~~	~~390~~	~~0.78~~	~~0.05296~~	~~0.00186~~	~~0.02815~~	~~0.00112~~	~~0.00386~~	~~4E-05~~	~~0.00121~~	~~0.00001~~	~~0.25~~	~~24.8~~	~~0.2~~	~~28~~	~~1~~	~~25~~	~~0.2~~	High P La
Zircon_17_027	151	104	0.61	0.09714	0.02386	0.05597	0.01367	0.00418	0.0001	0.00122	0.00007	0.09	26.9	0.6	55	13	27	0.6	
Zircon_18_028	125	110	0.78	0.07317	0.02678	0.03987	0.01667	0.00395	0.0003	0.00119	0.00017	0.41	25	2.0	40	16	~~25~~	~~2.0~~	
Zircon_19_029	583	682	1.03	0.05421	0.00179	0.02661	0.00091	0.00356	3E-05	0.00111	0.00002	0.26	22.9	0.2	26.7	0.9	23	0.2	
Zircon_2_009	296	237	0.70	0.05911	0.00254	0.03061	0.00136	0.00379	4E-05	0.00121	0.00003	0.25	24.4	0.3	31	1	24	0.3	
~~Zircon_20_030~~	~~76~~	~~53~~	~~0.61~~	~~0.15078~~	~~0.04033~~	~~0.10863~~	~~0.03392~~	~~0.00523~~	~~0.0003~~	~~0.00146~~	~~0.00016~~	~~0.65~~	~~34~~	~~2.0~~	~~105~~	~~31~~	~~34~~	~~2.0~~	
Zircon_21_032	174	182	0.92	0.08635	0.01	0.048	0.00587	0.00403	6E-05	0.0012	0.00002	0.23	25.9	0.4	48	6	26	0.4	
Zircon_22_033	160	142	0.78	0.06978	0.00617	0.03836	0.00365	0.00399	7E-05	0.00121	0.00002	0.24	25.7	0.4	38	4	26	0.4	
Zircon_23_034	247	263	0.93	0.07917	0.00776	0.04206	0.00436	0.00385	6E-05	0.00115	0.00002	0.21	24.8	0.4	42	4	25	0.4	
Zircon_24_035	330	292	0.78	0.08097	0.01728	0.04536	0.01048	0.00406	0.0001	0.00121	0.00004	0.37	26.1	0.7	45	10	26	0.7	
~~Zircon_25_036~~	~~440~~	~~423~~	~~0.84~~	~~0.0545~~	~~0.00486~~	~~0.02797~~	~~0.00265~~	~~0.00372~~	~~5E-05~~	~~0.00116~~	~~0.00002~~	~~0.19~~	~~24~~	~~0.3~~	~~28~~	~~3~~	~~24~~	~~0.3~~	High P La
Zircon_26_038	145	114	0.69	0.06255	0.00522	0.03401	0.00307	0.00394	6E-05	0.00121	0.00002	0.25	25.4	0.4	34	3	25	0.4	
Zircon_27_039	236	217	0.81	0.05958	0.00286	0.03144	0.00156	0.00383	5E-05	0.00126	0.00004	0.25	24.6	0.3	31	2	25	0.3	
Zircon_28_040	430	473	0.97	0.05699	0.00307	0.02961	0.00181	0.00377	4E-05	0.00117	0.00001	0.32	24.2	0.3	30	2	24	0.3	
Zircon_29_041	146	181	1.09	0.05358	0.0064	0.02853	0.00366	0.00386	7E-05	0.00121	0.00003	0.22	24.8	0.4	29	4	25	0.4	
Zircon_3_010	193	195	0.89	0.06963	0.00403	0.03782	0.00243	0.00394	5E-05	0.0012	0.00002	0.24	25.3	0.4	38	2	25	0.4	
Zircon_30_042	140	98	0.61	0.05383	0.0052	0.02987	0.00307	0.00402	6E-05	0.00126	0.00003	0.23	25.9	0.4	30	3	26	0.4	
Zircon_31_044	141	105	0.65	0.08071	0.01613	0.04252	0.00921	0.00382	0.0001	0.00114	0.00004	0.31	24.6	0.7	42	9	25	0.7	
~~Zircon_32_045~~	~~215~~	~~168~~	~~0.69~~	~~0.12352~~	~~0.05132~~	~~0.08395~~	~~0.04463~~	~~0.00493~~	~~0.0006~~	~~0.00141~~	~~0.00028~~	~~0.88~~	~~32~~	~~4.0~~	~~82~~	~~42~~	~~32~~	~~4.0~~	
Zircon_33_046	473	366	0.68	0.05503	0.0041	0.02702	0.00213	0.00356	3E-05	0.00111	0.00001	0.18	22.9	0.2	27	2	23	0.2	
Zircon_35_048	182	178	0.86	0.07441	0.01036	0.04148	0.00622	0.00404	8E-05	0.00122	0.00002	0.26	26	0.5	41	6	26	0.5	
Zircon_36_050	131	120	0.80	0.08303	0.01101	0.04387	0.00635	0.00383	8E-05	0.00114	0.00002	0.32	24.7	0.5	44	6	25	0.5	
Zircon_37_051	292	358	1.08	0.08128	0.00531	0.0381	0.00273	0.0034	5E-05	0.00101	0.00001	0.21	21.9	0.3	38	3	22	0.3	
Zircon_38_052	183	154	0.74	0.06289	0.00814	0.03341	0.00463	0.00385	8E-05	0.00118	0.00003	0.24	24.8	0.5	33	5	25	0.5	
~~Zircon_39_053~~	~~302~~	~~298~~	~~0.87~~	~~0.07926~~	~~0.02939~~	~~0.041~~	~~0.01734~~	~~0.00375~~	~~0.0002~~	~~0.00112~~	~~0.00013~~	~~0.32~~	~~24~~	~~1.0~~	~~41~~	~~17~~	~~24~~	~~1.0~~	
Zircon_5_012	144	160	0.97	0.07149	0.00472	0.03878	0.00264	0.00397	7E-05	0.0013	0.00005	0.24	25.5	0.4	39	3	26	0.4	
Zircon_6_014	255	216	0.74	0.06127	0.00419	0.0326	0.00244	0.00386	5E-05	0.00119	0.00001	0.2	24.8	0.3	33	2	25	0.3	
Zircon_7_015	168	172	0.90	0.06141	0.0047	0.03197	0.00277	0.00378	7E-05	0.00116	0.00002	0.26	24.3	0.4	32	3	24	0.4	
~~Zircon_8_016~~	~~256~~	~~241~~	~~0.83~~	~~0.09373~~	~~0.12061~~	~~0.0472~~	~~0.10421~~	~~0.00365~~	~~0.0013~~	~~0.00107~~	~~0.00222~~	~~0.89~~	~~24~~	~~8.0~~	~~47~~	~~101~~	~~24~~	~~8.0~~	
Zircon_34_047	181	195	0.95	0.08694	0.01442	0.04605	0.00809	0.00384	9E-05	0.00114	0.00003	0.21	24.7	0.6	46	8	25	0.6	
Zircon_9_017	121	103	0.75	0.0787	0.02186	0.04418	0.01345	0.00407	0.0002	0.00122	0.00009	0.26	26	1.0	44	13	26	1.0	

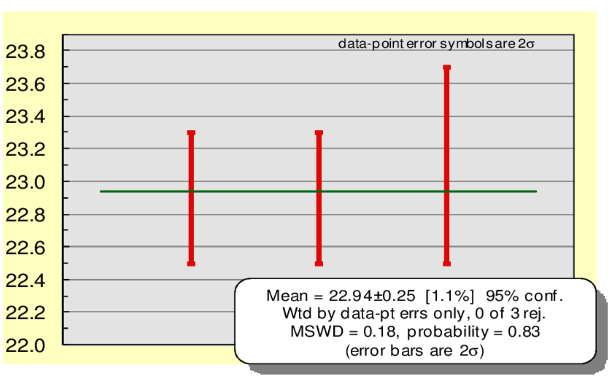

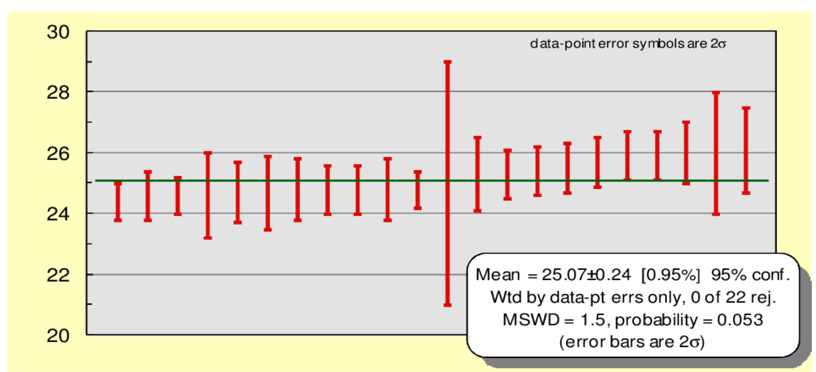

BM1000304-1 Sierra Guazapares fm. (Tsl)

Trace elements (ppm)	P	Ti	Y	Nb	La	Ce	Pr	Nd	Sm	Eu	Gd	Tb	Dy	Ho	Er	Yb	Lu	Hf	Th	U	notes
Zircon_11_020	732	4	2740	2	2	42	3	32	42	18	141	36	306	87	332	569	106	9990	108	140	
Zircon_13_022	783	87	3330	3	1	57	1	11	20	8	97	30	321	112	467	834	160	10229	200	200	
Zircon_14_023	606	18	2701	3	1	41	1	10	17	7	78	24	260	91	384	710	135	10581	138	175	
Zircon_15_024	1067	bdl	4133	10	6	68	1	8	11	4	76	29	358	137	601	1156	213	14385	373	617	
Zircon_16_026	1609	15	4585	7	139	319	23	87	27	8	113	36	423	153	650	1176	219	11983	390	441	High P La
Zircon_17_027	276	40	1890	2	0	32	0	7	10	4	50	16	176	64	276	535	101	11492	104	151	
Zircon_18_028	357	25	2419	2	0	34	1	10	17	7	73	22	233	81	344	639	126	10258	110	125	
Zircon_19_029	1064	16	4056	11	0	83	0	7	15	5	88	30	362	135	587	1095	202	13933	682	583	
Zircon_2_009	693	8	3346	4	0	64	0	8	16	6	84	27	313	113	480	873	163	10844	237	296	
Zircon_20_030	251	72	1153	2	3	27	1	6	6	2	29	9	108	39	170	330	62	9671	53	76	
Zircon_21_032	717	18	3339	3	32	120	9	53	35	12	118	32	329	110	452	803	151	9991	182	174	
Zircon_22_033	411	25	2190	3	0	43	0	4	9	4	51	17	196	72	315	600	118	10878	142	160	
Zircon_23_034	846	37	4775	3	1	66	1	19	30	12	133	40	451	161	691	1302	250	10060	263	247	
Zircon_24_035	818	bdl	4386	5	1	88	1	7	14	6	95	31	376	138	606	1088	217	9214	292	330	
Zircon_25_036	5183	11	4139	5	42	193	17	93	39	9	117	34	379	136	593	1120	218	12581	423	440	High P La
Zircon_26_038	336	16	2385	2	0	29	1	9	15	6	69	21	225	79	343	652	130	10158	114	145	
Zircon_27_039	663	11	2981	3	0	49	0	7	14	6	74	24	271	99	428	820	156	10077	217	236	
Zircon_28_040	732	7	3631	5	0	87	1	10	18	7	93	30	336	121	522	964	186	10581	473	430	
Zircon_29_041	385	14	2906	2	3	53	2	17	24	10	99	28	293	98	407	726	142	10762	181	146	
Zircon_3_010	496	9	3294	3	0	52	1	11	20	8	98	29	317	110	458	823	159	10396	195	193	
Zircon_30_042	482	1	2025	2	2	44	3	22	19	6	55	16	185	66	295	583	117	11094	98	140	
Zircon_31_044	366	6	1816	2	0	28	1	8	13	5	55	17	177	61	257	477	92	11629	105	141	
Zircon_32_045	664	10	2781	3	23	111	11	77	46	14	113	28	275	91	370	662	125	11274	168	215	
Zircon_33_046	967	12	4182	7	0	81	0	7	15	6	86	31	364	134	591	1082	213	12570	366	473	
Zircon_35_048	539	27	2811	3	0	45	1	12	20	8	89	26	279	96	396	712	134	10270	178	182	
Zircon_36_050	416	37	2502	2	1	37	0	7	13	6	65	21	231	83	360	673	133	10709	120	131	
Zircon_37_051	1423	6	5443	4	3	93	3	38	48	18	187	54	558	181	728	1231	233	10927	358	292	
Zircon_38_052	581	32	2476	3	1	47	0	5	9	4	55	18	215	80	348	644	130	10709	154	183	
Zircon_39_053	1144	22	3788	3	2	76	1	13	20	8	100	31	344	123	536	1002	206	9626	298	302	
Zircon_5_012	297	14	2042	1	0	29	1	9	15	6	65	18	200	68	290	570	111	9175	160	144	
Zircon_6_014	654	7	2939	5	2	76	1	10	13	5	72	23	272	99	423	791	145	10868	216	255	
Zircon_7_015	760	5	3462	2	34	211	42	304	118	39	188	40	368	117	477	844	158	10746	172	168	
Zircon_8_016	788	33	3138	4	2	71	1	13	16	7	84	26	289	102	435	798	159	9892	241	256	
Zircon_34_047	666	47	2846	4	1	54	1	7	11	4	63	21	246	92	404	744	151	9652	195	181	
Zircon_9_017	433	20	2088	2	1	33	1	7	11	4	56	17	194	69	297	571	109	10780	103	121	

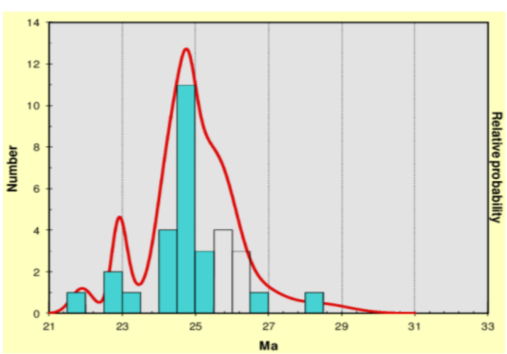

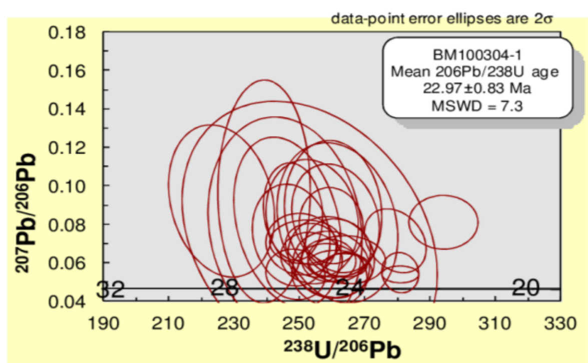

BM080717-3	Sierra Guazapares fm. (Tsi)		Mean $^{206}Pb/^{238}U$ age (±2σ): 25.0 ± 0.3 Ma																
				CORRECTED RATIOS[2]									CORRECTED AGES (Ma)						
	U[1] (ppm)	Th[1] (ppm)	Th/U	$^{207}Pb/^{206}Pb$	±1σ[3]	$^{207}Pb/^{235}U$	±1σ[3]	$^{206}Pb/^{238}U$	±1σ[3]	$^{208}Pb/^{232}Th$	±1σ[3]	Rho	$^{206}Pb/^{238}U$	±1σ	$^{207}Pb/^{235}U$	±1σ	Best age (Ma)	±1σ	notes
Zircon_12_021	103	94	0.83	0.0673	0.00464	0.0352	0.00256	0.00385	9E-05	0.00126	0.00004	0.32	24.8	0.6	35	3	24.8	0.6	
Zircon_13_022	122	65	0.48	0.05846	0.00607	0.03241	0.00358	0.00402	7E-05	0.00125	0.00002	0.21	25.9	0.4	32	4	25.9	0.4	
Zircon_14_023	84	79	0.86	0.09115	0.00656	0.05293	0.00402	0.00428	0.0001	0.00131	0.00006	0.32	27.5	0.6	52	4	27.5	0.6	
Zircon_16_026	203	101	0.45	0.06238	0.00648	0.03329	0.00364	0.00387	6E-05	0.00119	0.00003	0.26	24.9	0.4	33	4	24.9	0.4	
Zircon_18_028	60	79	1.20	0.11409	0.01848	0.0708	0.0125	0.0045	0.0002	0.0013	0.00004	0.23	29	1.0	69	12	29	1.0	
~~Zircon_19_029~~	~~192~~	~~115~~	~~0.54~~	~~0.06589~~	~~0.00728~~	~~0.03549~~	~~0.00421~~	~~0.00391~~	~~7E-05~~	~~0.00119~~	~~0.00003~~	~~0.34~~	~~25.1~~	~~0.5~~	~~35~~	4	~~25.1~~	~~0.5~~	
Zircon_2_009	227	122	0.49	0.06245	0.00325	0.03236	0.00176	0.00374	6E-05	0.00123	0.00005	0.29	24.1	0.4	32	2	24.1	0.4	
Zircon_20_030	113	102	0.82	0.06064	0.00761	0.03192	0.00439	0.00382	0.0001	0.00118	0.00003	0.28	24.6	0.6	32	4	24.6	0.6	
Zircon_21_032	52	25	0.43	0.09499	0.01621	0.06053	0.01107	0.00462	0.0001	0.00136	0.00005	0.3	29.7	0.9	60	11	29.7	0.9	
Zircon_22_033	140	81	0.53	0.07645	0.00931	0.04078	0.00541	0.00387	0.0001	0.00116	0.00003	0.35	24.9	0.7	41	5	24.9	0.7	
Zircon_23_034	138	110	0.73	0.07329	0.005	0.03923	0.00304	0.00388	8E-05	0.00117	0.00002	0.32	25	0.5	39	3	25	0.5	
Zircon_24_035	178	87	0.44	0.06035	0.00507	0.03127	0.00271	0.00375	8E-05	0.00123	0.00005	0.25	24.1	0.5	31	3	24.1	0.5	
Zircon_26_038	85	42	0.45	0.08235	0.01547	0.04774	0.00958	0.0042	0.0001	0.00125	0.00006	0.32	27	0.9	47	9	27	0.9	
Zircon_27_039	216	132	0.56	0.06416	0.00353	0.03389	0.00192	0.00385	5E-05	0.00117	0.00005	0.24	24.8	0.3	34	2	24.8	0.3	
Zircon_28_040	118	91	0.70	0.04937	0.00753	0.0273	0.00443	0.00401	9E-05	0.00127	0.00011	0.21	25.8	0.6	27	4	25.8	0.6	
Zircon_29_041	193	125	0.59	0.05137	0.00657	0.02767	0.00376	0.00391	8E-05	0.00123	0.00008	0.21	25.1	0.5	28	4	25.1	0.5	
Zircon_3_010	102	85	0.75	0.05323	0.00664	0.02818	0.00404	0.00384	0.0001	0.0012	0.00004	0.33	24.7	0.8	28	4	24.7	0.8	
Zircon_30_042	180	212	1.07	0.06482	0.00538	0.03537	0.00298	0.00402	6E-05	0.00122	0.00005	0.17	25.9	0.4	35	3	25.9	0.4	
Zircon_4_011	97	77	0.72	0.08017	0.00689	0.04494	0.00405	0.00403	0.0001	0.00238	0.00097	0.3	25.9	0.7	45	4	25.9	0.7	
Zircon_5_012	145	122	0.76	0.06481	0.00518	0.03519	0.0029	0.00401	8E-05	0.00129	0.00006	0.24	25.8	0.5	35	3	25.8	0.5	
Zircon_6_014	185	133	0.65	0.04608	0.00396	0.02508	0.0023	0.00395	7E-05	0.00136	0.00012	0.2	25.4	0.5	25	2	25.4	0.5	
Zircon_8_016	174	79	0.41	0.06179	0.00813	0.03242	0.00452	0.00381	8E-05	0.00117	0.00003	0.22	24.5	0.5	32	4	24.5	0.5	
Zircon_BM080717-3_008	153	81	0.48	0.06355	0.0054	0.0325	0.00286	0.0038	9E-05	0.00125	0.00007	0.26	24.4	0.6	32	3	24.4	0.6	
Zircon_9_017	53	26	0.46	0.08869	0.02028	0.05334	0.0134	0.00436	0.0002	0.00129	0.00007	0.32	28	1.0	53	13	28	1.0	

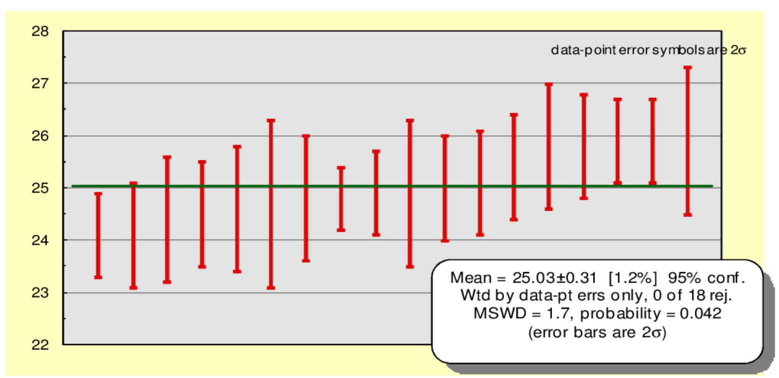

BM080717-3 Sierra Guazapares fm. (Tsi)

Trace elements (ppm)	P	Ti	Y	Nb	La	Ce	Pr	Nd	Sm	Eu	Gd	Tb	Dy	Ho	Er	Yb	Lu	Hf	Th	U
Zircon_1_BM017-3_008	189	5	2536	25	0	174	0	2	3	0	25	11	156	72	390	954	196	14035	81	153
Zircon_12_021	415	22	2731	4	0	42	0	6	10	3	56	19	238	91	410	782	150	10140	94	103
Zircon_13_022	166	9	2495	2	0	36	1	10	16	5	72	22	240	86	362	684	129	9673	65	122
Zircon_14_023	380	16	2695	4	6	52	1	10	12	4	62	21	246	91	400	748	141	9934	79	84
Zircon_16_026	484	11	3139	7	0	80	0	5	10	4	65	23	276	105	467	877	167	10439	101	203
Zircon_18_028	407	15	2330	2	2	37	1	9	11	3	56	18	215	79	339	610	115	10636	79	60
Zircon_19_029	2500	9	3157	16	111	403	39	192	50	5	97	26	283	105	467	905	171	13667	115	192
Zircon_2_009	445	16	2488	4	0	36	0	5	9	3	52	18	217	83	375	720	140	9281	122	227
Zircon_20_030	646	11	3908	4	5	81	6	40	32	11	131	39	405	131	539	956	181	10271	102	113
Zircon_21_032	150	3	1395	3	0	28	0	2	4	1	26	9	116	45	210	432	85	11988	25	52
Zircon_22_033	268	7	1369	3	0	28	0	2	4	1	25	9	109	44	209	455	93	11596	81	140
Zircon_23_034	406	bdl	2701	8	1	76	1	6	10	3	53	19	229	89	408	806	155	12345	110	138
Zircon_24_035	732	32	3633	5	3	81	1	14	19	7	95	30	341	123	534	992	188	10169	87	178
Zircon_26_038	536	7	2178	5	4	71	2	10	8	1	42	15	184	71	325	632	120	12751	42	85
Zircon_27_039	273	14	1126	2	0	27	0	3	4	1	24	8	97	37	169	330	65	11257	132	216
Zircon_28_040	188	10	1481	4	0	31	0	2	4	1	23	8	110	46	226	541	115	11889	91	118
Zircon_29_041	672	14	2250	2	5	46	2	14	13	3	56	18	204	75	328	617	118	11320	125	193
Zircon_3_010	362	5	1036	2	0	19	0	2	3	1	19	7	88	34	159	333	66	10437	85	102
Zircon_30_042	634	bdl	2666	3	4	50	1	8	12	4	61	20	236	89	396	770	150	10218	212	180
Zircon_4_011	258	6	1343	4	0	44	0	2	4	1	27	9	116	45	206	414	79	11681	77	97
Zircon_5_012	679	6	5453	6	1	108	1	17	31	10	150	47	527	187	797	1443	267	10248	122	145
Zircon_6_014	640	14	6481	8	8	155	3	29	41	13	186	57	636	223	941	1657	314	10756	133	185
Zircon_8_016	547	11	2664	3	1	43	1	8	13	5	69	22	246	90	395	747	145	9916	79	174
Zircon_9_017	255	17	1522	4	0	53	0	2	5	1	30	11	131	51	232	462	89	12160	26	53

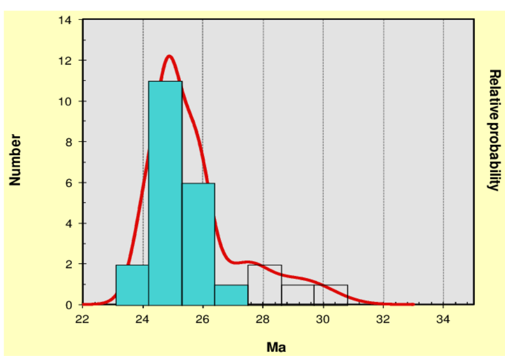

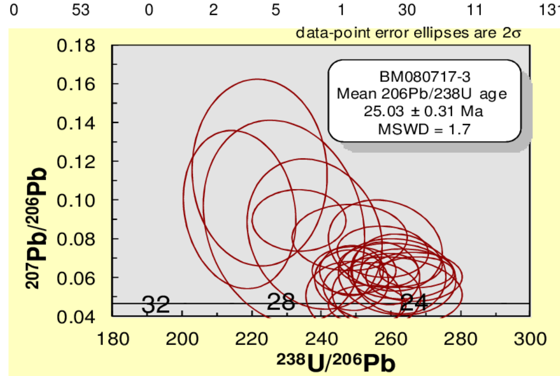

BM1000305-3	Sierra Guazapares fm. (Tsi)			Mean $^{206}Pb/^{238}U$ age (±2σ): 24.6 ± 0.2 Ma															
				CORRECTED RATIOS[2]									CORRECTED AGES (Ma)						
	U[1] (ppm)	Th[1] (ppm)	Th/U	$^{207}Pb/^{206}Pb$	±1σ[3]	$^{207}Pb/^{235}U$	±1σ[3]	$^{206}Pb/^{238}U$	±1σ[3]	$^{208}Pb/^{232}Th$	±1σ[3]	Rho	$^{206}Pb/^{238}U$	±1σ	$^{207}Pb/^{235}U$	±1σ	Best age (Ma)	±1σ	notes
Zircon_1_BM05-3_008	163	108	0.61	0.06075	0.00383	0.03235	0.00209	0.00389	6E-05	0.00113	0.00004	0.22	25	0.4	32	2	25	0.4	
Zircon_11_020	133	100	0.69	0.06319	0.00348	0.03345	0.00192	0.00391	6E-05	0.00133	0.00007	0.28	25.2	0.4	33	2	25	0.4	
Zircon_12_021	461	513	1.02	0.04966	0.00209	0.02481	0.00107	0.00364	4E-05	0.00105	0.00002	0.22	23.4	0.3	25	1	23	0.3	
Zircon_13_022	163	165	0.93	0.07302	0.00758	0.03836	0.00434	0.00381	7E-05	0.00115	0.00002	0.22	24.5	0.5	38	4	25	0.5	
Zircon_15_024	84	51	0.55	0.08299	0.00697	0.04588	0.00393	0.00408	7E-05	0.00126	0.00008	0.2	26.2	0.4	46	4	26	0.4	
Zircon_16_026	204	164	0.73	0.05284	0.00285	0.02712	0.00152	0.00373	6E-05	0.00109	0.00003	0.27	24	0.4	27	2	24	0.4	
Zircon_17_027	153	148	0.88	0.06269	0.00426	0.03289	0.0023	0.00389	6E-05	0.00123	0.00004	0.24	25	0.4	33	2	25	0.4	
~~Zircon_18_028~~	~~1061~~	~~1683~~	~~1.45~~	~~0.0599~~	~~0.0021~~	~~0.02944~~	~~0.00107~~	~~0.00349~~	~~3E-05~~	~~0.00106~~	~~0.00002~~	~~0.27~~	~~22.5~~	~~0.2~~	~~29~~	~~1~~	~~23~~	~~0.2~~	High Th U
Zircon_19_029	124	116	0.86	0.06426	0.00605	0.03662	0.00384	0.00413	9E-05	0.00127	0.00003	0.24	26.6	0.6	37	4	27	0.6	
Zircon_2_009	368	497	1.24	0.05248	0.00247	0.02615	0.00126	0.00364	4E-05	0.00112	0.00002	0.21	23.4	0.3	26	1	23	0.3	
Zircon_20_030	295	428	1.33	0.06283	0.01225	0.03285	0.00689	0.00379	0.0001	0.00116	0.00005	0.23	24.4	0.7	33	7	24	0.7	
~~Zircon_21_032~~	~~256~~	~~315~~	~~1.13~~	~~0.06609~~	~~0.00469~~	~~0.03463~~	~~0.00353~~	~~0.00401~~	~~0.0003~~	~~0.00119~~	~~0.00004~~	~~0.72~~	~~26~~	~~2.0~~	~~35~~	~~3~~	~~26~~	~~2.0~~	
~~Zircon_22_033~~	~~190~~	~~218~~	~~1.05~~	~~0.0652~~	~~0.0141~~	~~0.03657~~	~~0.00862~~	~~0.00407~~	~~0.0001~~	~~0.00124~~	~~0.00007~~	~~0.31~~	~~26.2~~	~~0.9~~	~~36~~	~~8~~	~~26~~	~~0.9~~	
Zircon_23_034	121	162	1.23	0.06341	0.00463	0.03427	0.00259	0.00391	7E-05	0.00122	0.00005	0.26	25.2	0.4	34	3	25	0.4	
Zircon_24_035	171	148	0.79	0.05931	0.0035	0.03075	0.00187	0.00382	6E-05	0.00116	0.00004	0.24	24.6	0.4	31	2	25	0.4	
Zircon_26_038	120	96	0.73	0.06768	0.00992	0.03579	0.00578	0.00384	0.0001	0.00117	0.00003	0.32	24.7	0.7	36	6	25	0.7	
Zircon_29_041	108	101	0.86	0.06981	0.00593	0.03703	0.00323	0.00393	7E-05	0.00128	0.00005	0.23	25.3	0.4	37	3	25	0.4	
Zircon_3_010	260	279	0.98	0.0611	0.00571	0.03324	0.00339	0.00395	6E-05	0.00122	0.00002	0.26	25.4	0.4	33	3	25	0.4	
Zircon_31_044	226	208	0.84	0.05524	0.00456	0.02902	0.00267	0.00381	7E-05	0.00119	0.00002	0.29	24.5	0.4	29	3	25	0.4	
Zircon_32_045	78	58	0.69	0.07919	0.02155	0.04426	0.01282	0.00405	0.0001	0.00121	0.00011	0.28	26.1	0.9	44	12	26	0.9	
Zircon_33_046	52	41	0.72	0.07033	0.00985	0.04065	0.00576	0.00425	9E-05	0.00126	0.00014	0.15	27.3	0.6	40	6	27	0.6	
Zircon_34_047	146	139	0.87	0.04608	0.00373	0.02461	0.00218	0.00387	7E-05	0.00132	0.00011	0.26	24.9	0.5	25	2	25	0.5	
Zircon_35_048	177	206	1.06	0.05611	0.00337	0.02857	0.00177	0.00375	6E-05	0.00115	0.00003	0.25	24.1	0.4	29	2	24	0.4	
Zircon_36_050	158	200	1.16	0.04609	0.0083	0.02463	0.00491	0.00388	0.0001	0.00134	0.00015	0.31	24.9	0.8	25	5	25	0.8	
Zircon_37_051	126	95	0.69	0.05958	0.00457	0.03142	0.00264	0.00382	6E-05	0.00118	0.00002	0.26	24.6	0.4	31	3	25	0.4	
Zircon_38_052	144	121	0.77	0.05633	0.0036	0.03013	0.00199	0.00394	6E-05	0.00122	0.00004	0.25	25.3	0.4	30	2	25	0.4	
Zircon_39_053	215	250	1.06	0.05535	0.00567	0.02808	0.00305	0.00368	6E-05	0.00115	0.00002	0.21	23.7	0.4	28	3	24	0.4	
Zircon_4_011	265	251	0.87	0.06957	0.0049	0.03564	0.00275	0.00372	6E-05	0.00113	0.00002	0.25	23.9	0.4	36	3	24	0.4	
Zircon_40_054	193	170	0.81	0.05904	0.00401	0.03064	0.00212	0.00378	5E-05	0.00114	0.00004	0.19	24.3	0.3	31	2	24	0.3	
~~Zircon_5_012~~	~~183~~	~~331~~	~~1.66~~	~~0.06866~~	~~0.00819~~	~~0.03887~~	~~0.00513~~	~~0.00411~~	~~8E-05~~	~~0.00125~~	~~0.00002~~	~~0.25~~	~~26.4~~	~~0.5~~	~~39~~	~~5~~	~~26~~	~~0.5~~	
Zircon_6_014	297	358	1.10	0.06319	0.00329	0.03277	0.00176	0.00374	5E-05	0.00115	0.00003	0.25	24.1	0.3	33	2	24	0.3	
Zircon_7_015	474	667	1.29	0.06115	0.00251	0.03181	0.00134	0.00375	4E-05	0.00118	0.00002	0.23	24.1	0.3	32	1	24	0.3	
Zircon_9_017	177	228	1.18	0.05569	0.00373	0.02876	0.002	0.00377	7E-05	0.00121	0.00004	0.27	24.3	0.4	29	2	24	0.4	
Zircon_old_14_023	76	52	0.62	0.05954	0.00976	0.03358	0.00602	0.00409	0.0001	0.00126	0.00006	0.41	26.3	0.8	34	6	26	0.8	
~~Zircon_old_8_016~~	~~103~~	~~210~~	~~1.86~~	~~0.07654~~	~~0.00681~~	~~0.04325~~	~~0.00392~~	~~0.00416~~	~~7E-05~~	~~0.00099~~	~~0.00004~~	~~0.19~~	~~26.8~~	~~0.4~~	~~43~~	~~4~~	~~27~~	~~0.4~~	
Zircon_27_039	78	47	0.55	0.05674	0.01386	0.03428	0.00912	0.00438	0.0002	0.00136	0.00018	0.48	28.2	1.0	34	9	28	1.0	

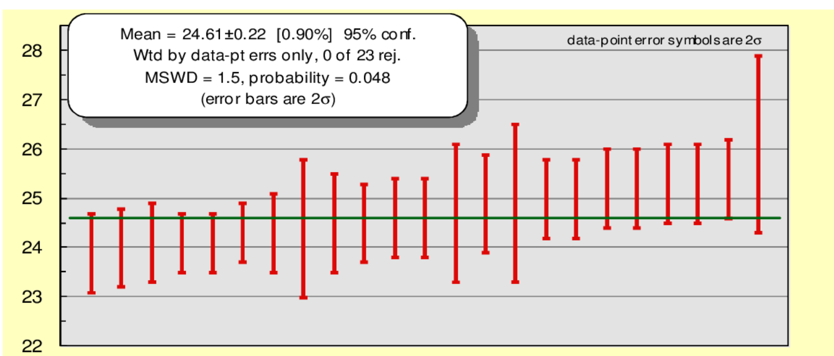

BM1000305-3	Sierra Guazapares fm. (Tsi)																			
Trace elements (ppm)	P	Ti	Y	Nb	La	Ce	Pr	Nd	Sm	Eu	Gd	Tb	Dy	Ho	Er	Yb	Lu	Hf	Th	U	
Zircon_1_BM05-3_008	374	bdl	1891	2	1	27	0	4	7	2	41	14	168	63	282	538	109	11554	108	163	
Zircon_10_018	183	38	1180	1	1	21	0	5	7	3	32	10	110	40	176	333	69	8598	46	60	
Zircon_11_020	431	6	2399	3	0	38	0	3	7	3	46	16	201	78	361	691	143	9215	100	133	
Zircon_12_021	588	16	4181	4	0	90	1	15	23	11	108	33	375	137	605	1176	243	8000	513	461	
Zircon_13_022	585	12	3149	2	0	51	1	11	18	6	87	27	298	108	463	828	165	9328	165	163	
Zircon_15_024	448	10	1338	1	0	19	0	3	5	2	28	10	114	44	201	403	85	10081	51	84	
Zircon_16_026	467	17	2461	5	0	62	0	3	7	3	46	17	203	80	368	711	147	9798	164	204	
Zircon_17_027	772	15	2982	2	1	48	1	10	17	6	80	25	281	101	436	791	161	9066	148	153	
~~Zircon_18_028~~	~~621~~	~~16~~	~~4419~~	~~7~~	~~1~~	~~144~~	~~1~~	~~15~~	~~28~~	~~8~~	~~127~~	~~38~~	~~416~~	~~147~~	~~621~~	~~1110~~	~~217~~	~~9279~~	~~1683~~	~~1061~~	High Th U
Zircon_19_029	378	5	2110	2	1	32	1	7	12	5	55	17	192	69	304	567	119	8629	116	124	
Zircon_2_009	1633	16	6945	8	2	164	4	40	53	14	203	60	654	230	977	1692	334	9086	497	368	High P La
Zircon_20_030	1497	545	5417	9	12	122	10	67	47	11	160	46	506	179	750	1267	244	9943	428	295	High P La Ti
Zircon_21_032	856	7	3487	3	1	84	1	13	20	8	98	30	327	115	482	853	167	8887	315	256	
Zircon_23_034	499	6	2609	2	0	45	1	14	21	9	80	23	246	87	374	725	150	8691	162	121	
Zircon_24_035	527	6	2637	2	0	50	0	8	13	5	71	22	245	89	381	689	137	11018	148	171	
Zircon_26_038	1080	22	1528	1	5	33	2	13	10	3	40	12	138	50	221	428	89	9277	96	120	
Zircon_29_041	343	10	2190	1	1	36	1	9	14	6	65	19	210	74	312	559	114	9727	101	108	
Zircon_3_010	843	5	3829	5	0	84	0	7	15	6	87	29	338	125	553	1016	204	9016	279	260	
Zircon_30_042	467	18	1559	1	0	26	0	4	7	3	38	12	138	51	226	434	91	9757	77	100	
Zircon_31_044	433	3	1969	2	0	34	0	7	11	4	49	15	172	64	288	578	123	9335	208	226	
Zircon_32_045	250	29	1330	1	1	23	0	5	7	3	33	10	118	44	194	370	77	9540	58	78	
Zircon_33_046	219	11	1174	1	0	18	0	4	7	3	33	10	109	39	168	320	67	9478	41	52	
Zircon_34_047	525	bdl	2667	3	0	59	1	10	17	6	76	24	252	90	381	684	137	11256	139	146	
Zircon_35_048	684	3	3189	2	0	71	1	15	22	8	96	28	304	106	448	797	158	11306	206	177	
Zircon_36_050	392	22	2207	2	0	49	1	9	14	5	61	19	207	74	317	568	116	9521	200	158	
Zircon_37_051	1229	8	2156	2	8	48	3	18	13	4	54	17	195	71	314	589	120	10483	95	126	
Zircon_38_052	506	17	2646	3	38	103	8	35	15	5	61	20	233	87	386	726	149	9320	121	144	
Zircon_39_053	678	12	3352	3	0	69	1	16	22	7	96	28	312	112	478	874	177	10767	250	215	
Zircon_4_011	599	21	2373	3	0	53	0	7	11	4	57	18	208	78	351	699	150	8442	251	265	
Zircon_40_054	524	2	2935	3	0	48	0	7	15	5	76	24	270	97	419	762	152	10947	170	193	
Zircon_6_014	498	18	3262	3	0	72	1	17	27	9	110	31	322	111	463	820	165	8552	358	297	
Zircon_7_015	932	8	3834	6	1	139	1	11	20	7	101	31	350	127	550	1015	203	10184	667	474	
Zircon_9_017	465	12	2595	2	0	69	1	11	18	7	80	23	248	87	370	666	137	9036	228	177	
Zircon_old_14_023	471	bdl	1600	2	0	25	0	4	7	3	36	12	142	54	244	481	101	9354	52	76	
Zircon_27_039	367	4	1333	1	0	21	0	3	6	2	29	10	116	44	199	387	80	9734	47	78	

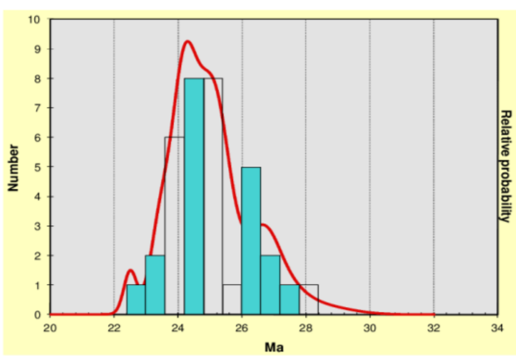

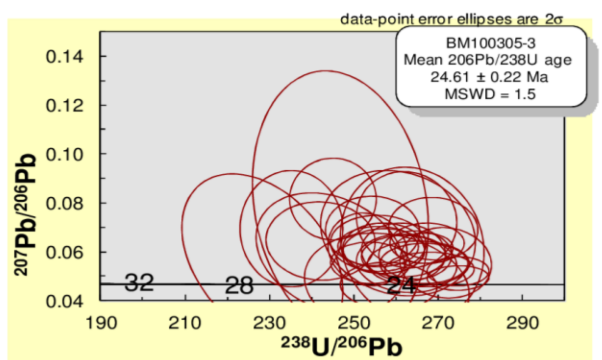

BM1000304-2 Sierra Guazapares fm. (Tsv) Mean $^{206}Pb/^{238}U$ age (±2σ): 24.2 ± 0.2 Ma

				CORRECTED RATIOS[2]									CORRECTED AGES (Ma)						
	U[1] (ppm)	Th[1] (ppm)	Th/U	$^{207}Pb/^{206}Pb$	±1σ[3]	$^{207}Pb/^{235}U$	±1σ[3]	$^{206}Pb/^{238}U$	±1σ[3]	$^{208}Pb/^{232}Th$	±1σ[3]	Rho	$^{206}Pb/^{238}U$	±1σ	$^{207}Pb/^{235}U$	±1σ	Best age (Ma)	±1σ	notes
Zircon_1_BM04-2_008	233	254	0.96	0.05532	0.0031	0.02892	0.00166	0.00377	5E-05	0.00109	0.00003	0.22	24.3	0.3	29	2	24	0.3	
Zircon_10_018	224	235	0.92	0.07421	0.00699	0.03826	0.00385	0.00374	6E-05	0.00113	0.00002	0.22	24.1	0.4	38	4	24	0.4	
Zircon_12_021	143	102	0.63	0.06803	0.00446	0.03525	0.00253	0.00376	6E-05	0.00114	0.00002	0.27	24.2	0.4	35	2	24	0.4	
Zircon_14_023	308	298	0.85	0.08507	0.0051	0.04579	0.00279	0.0039	4E-05	0.0012	0.00003	0.18	25.1	0.3	45	3	~~25~~	~~0.3~~	
Zircon_15_024	280	266	0.84	0.05824	0.00297	0.02987	0.00155	0.00371	4E-05	0.00112	0.00002	0.19	23.9	0.3	30	2	24	0.3	
Zircon_16_026	112	88	0.69	0.06241	0.00412	0.03464	0.00235	0.00407	7E-05	0.00111	0.00005	0.23	26.2	0.4	35	2	26	0.4	
Zircon_17_027	171	95	0.49	0.06123	0.00406	0.03192	0.00231	0.00378	5E-05	0.00116	0.00002	0.26	24.3	0.3	32	2	24	0.3	
~~Zircon_18_028~~	~~115~~	~~83~~	~~0.64~~	~~0.10789~~	~~0.01551~~	~~0.05094~~	~~0.00814~~	~~0.00342~~	~~9E-05~~	~~0.00099~~	~~0.00003~~	~~0.4~~	~~22~~	~~0.6~~	~~50~~	~~8~~	~~22~~	~~0.6~~	
Zircon_19_029	180	123	0.60	0.07048	0.00352	0.03689	0.00193	0.00383	6E-05	0.00121	0.00003	0.3	24.6	0.4	37	2	25	0.4	
Zircon_2_009	164	116	0.62	0.07362	0.00353	0.03799	0.0019	0.00377	5E-05	0.00123	0.00005	0.29	24.3	0.3	38	2	24	0.3	
Zircon_20_030	233	188	0.71	0.05426	0.00407	0.02866	0.00218	0.00383	5E-05	0.00101	0.00003	0.17	24.6	0.3	29	2	25	0.3	
Zircon_21_032	191	156	0.72	0.05948	0.00327	0.03137	0.00179	0.00382	6E-05	0.00118	0.00003	0.27	24.6	0.4	31	2	25	0.4	
Zircon_22_033	248	253	0.90	0.07462	0.01242	0.04144	0.00739	0.00403	9E-05	0.00121	0.00003	0.21	25.9	0.6	41	7	26	0.6	
Zircon_23_034	290	198	0.60	0.06297	0.00693	0.03822	0.00427	0.004	8E-05	0.00142	0.00016	0.17	25.7	0.5	38	4	26	0.5	
Zircon_24_035	325	234	0.63	0.06077	0.00201	0.03176	0.00112	0.00378	5E-05	0.00115	0.00003	0.35	24.3	0.3	32	1	24	0.3	
~~Zircon_25_036~~	~~332~~	~~337~~	~~0.89~~	~~0.06494~~	~~0.00703~~	~~0.0339~~	~~0.00396~~	~~0.00379~~	~~5E-05~~	~~0.00116~~	~~0.00001~~	~~0.28~~	~~24.4~~	~~0.3~~	34	4	~~24~~	~~0.3~~	High P La
Zircon_26_038	302	330	0.96	0.07577	0.00427	0.03999	0.00251	0.00383	5E-05	0.00115	0.00001	0.28	24.6	0.3	40	2	25	0.3	
Zircon_27_039	261	195	0.66	0.05998	0.00234	0.03155	0.00127	0.00384	4E-05	0.00113	0.00003	0.25	24.7	0.3	32	1	25	0.3	
Zircon_28_040	268	237	0.78	0.07371	0.00375	0.0381	0.00224	0.00375	6E-05	0.00113	0.00002	0.32	24.1	0.4	38	2	24	0.4	
Zircon_29_041	94	55	0.51	0.08347	0.00856	0.04899	0.00554	0.00426	0.0001	0.00127	0.00003	0.32	27.4	0.6	49	5	~~27~~	~~0.6~~	
Zircon_3_010	160	102	0.56	0.06612	0.00583	0.03535	0.00337	0.00388	7E-05	0.00118	0.00002	0.22	24.9	0.4	35	3	25	0.4	
Zircon_30_042	293	301	0.90	0.06828	0.0033	0.03547	0.00195	0.00377	4E-05	0.00115	0.00001	0.3	24.2	0.3	35	2	24	0.3	
Zircon_31_044	136	102	0.66	0.06526	0.00392	0.036	0.00224	0.00401	6E-05	0.00113	0.00004	0.26	25.8	0.4	36	2	26	0.4	
Zircon_32_045	175	138	0.69	0.07787	0.00894	0.03954	0.00495	0.00368	7E-05	0.0011	0.00002	0.3	23.7	0.4	39	5	24	0.4	
Zircon_34_047	138	107	0.68	0.0735	0.00691	0.04085	0.00431	0.00403	8E-05	0.00122	0.00002	0.3	25.9	0.5	41	4	26	0.5	
Zircon_35_048	296	244	0.73	0.05652	0.0022	0.02937	0.00118	0.00378	4E-05	0.00107	0.00002	0.25	24.3	0.3	29	1	24	0.3	
~~Zircon_36_050~~	~~247~~	~~148~~	~~0.53~~	~~0.07083~~	~~0.0068~~	~~0.03799~~	~~0.00396~~	~~0.00389~~	~~7E-05~~	~~0.00118~~	~~0.00002~~	~~0.22~~	~~25~~	~~0.4~~	~~38~~	4	~~25~~	~~0.4~~	High P La
Zircon_38_052	202	164	0.71	0.06593	0.00496	0.03672	0.00309	0.00404	7E-05	0.00123	0.00002	0.24	26	0.4	37	3	26	0.4	
~~Zircon_39_053~~	~~330~~	~~384~~	~~1.02~~	~~0.06862~~	~~0.00261~~	~~0.03614~~	~~0.00142~~	~~0.00384~~	~~4E-05~~	~~0.0011~~	~~0.00002~~	~~0.25~~	~~24.7~~	~~0.3~~	36	~~1~~	~~25~~	~~0.3~~	High P La
Zircon_4_011	255	202	0.70	0.05974	0.00472	0.0297	0.00237	0.00365	4E-05	0.00112	0.00003	0.14	23.5	0.3	30	2	24	0.3	
Zircon_40_054	168	126	0.66	0.05454	0.003	0.02928	0.00167	0.00395	6E-05	0.00111	0.00003	0.26	25.4	0.4	29	2	25	0.4	
Zircon_5_012	183	155	0.74	0.06822	0.00307	0.03381	0.00159	0.00364	5E-05	0.00116	0.00003	0.29	23.4	0.3	34	2	23	0.3	
Zircon_6_014	237	205	0.76	0.05467	0.00372	0.02878	0.00214	0.00382	5E-05	0.00119	0.00001	0.18	24.6	0.3	29	2	25	0.3	
Zircon_8_016	312	252	0.71	0.05529	0.00288	0.02799	0.00148	0.00371	4E-05	0.00107	0.00003	0.17	23.9	0.3	28	1	24	0.3	
Zircon_9_017	302	217	0.63	0.06771	0.00301	0.03411	0.00174	0.00365	4E-05	0.00111	0.00001	0.32	23.5	0.3	34	2	24	0.3	
Zircon_11_020	209	154	0.65	0.073	0.00438	0.03741	0.00231	0.00371	6E-05	0.0012	0.00005	0.24	23.9	0.4	37	2	24	0.4	
Zircon_37_051	288	227	0.69	0.07138	0.0046	0.03671	0.00256	0.00373	5E-05	0.00113	0.00001	0.17	24	0.3	37	3	24	0.3	

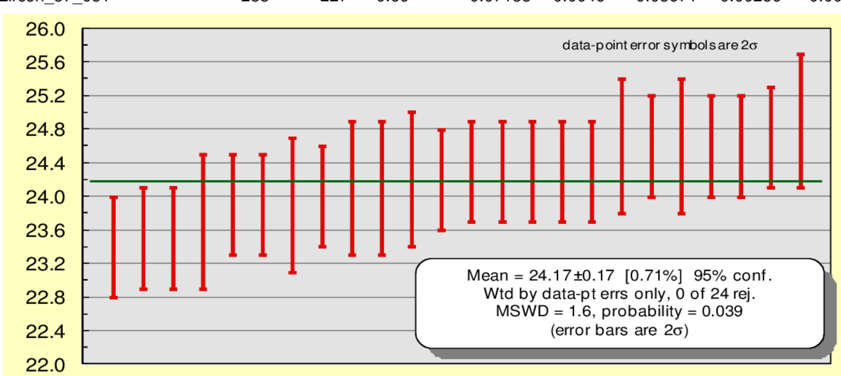

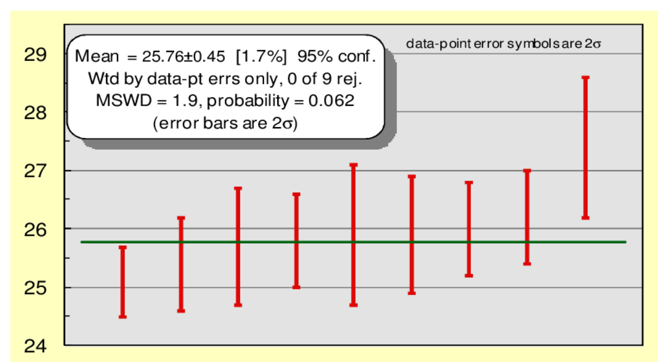

BM1000304-2 Sierra Guazapares fm. (Tsv)

Trace elements (ppm)	P	Ti	Y	Nb	La	Ce	Pr	Nd	Sm	Eu	Gd	Tb	Dy	Ho	Er	Yb	Lu	Hf	Th	U	
Zircon_1_BM04-2_008	822	14	5569	3	0	64	2	27	45	18	187	53	562	190	798	1467	279	8207	254	233	
Zircon_10_018	807	20	4522	3	1	59	1	20	34	14	150	45	464	155	626	1102	204	9372	235	224	
Zircon_12_021	483	14	2137	2	0	31	0	7	12	5	56	18	200	72	311	602	117	10402	102	143	
Zircon_14_023	687	9	3887	4	0	63	1	18	29	10	123	36	386	132	544	974	187	10127	298	308	
Zircon_15_024	1112	14	4381	3	2	61	1	12	19	8	107	35	400	145	627	1166	220	10279	266	280	
Zircon_16_026	385	9	2220	1	0	26	0	8	15	7	69	20	218	75	316	600	116	10308	88	112	
Zircon_17_027	452	5	2120	4	0	35	0	4	9	3	48	16	191	70	306	598	116	11331	95	171	
Zircon_18_028	474	16	1923	3	1	31	1	10	14	6	58	18	195	64	266	501	97	8372	83	115	
Zircon_19_029	727	10	2845	2	1	34	0	7	12	5	68	22	252	93	413	819	165	9856	123	180	
Zircon_2_009	512	6	2573	2	0	33	0	5	11	5	64	21	236	85	364	684	133	9911	116	164	
Zircon_20_030	665	8	3103	3	0	47	0	6	14	5	79	26	295	104	441	792	149	10681	188	233	
Zircon_21_032	571	10	3155	2	0	40	1	9	18	7	87	27	297	105	449	849	167	9991	156	191	
Zircon_22_033	839	36	4559	3	1	62	1	20	33	13	147	43	455	154	638	1156	218	8720	253	248	
Zircon_23_034	750	0	3466	5	0	58	0	6	14	5	84	27	320	115	494	919	172	11295	198	290	
Zircon_24_035	867	10	2794	4	0	37	0	4	8	3	54	19	241	92	411	819	157	11549	234	325	
~~Zircon_25_036~~	1417	36	6593	5	103	502	19	87	50	17	208	61	651	221	903	1541	294	10041	337	332	High P La
Zircon_26_038	820	22	4382	4	1	61	1	17	28	10	125	38	418	147	616	1100	214	9491	330	302	
Zircon_27_039	894	13	3276	3	0	47	0	7	14	6	79	26	293	108	467	877	174	10489	195	261	
Zircon_28_040	536	15	3492	3	0	54	1	9	17	8	93	29	329	116	490	906	177	8948	237	268	
Zircon_29_041	369	14	1417	1	0	20	0	3	6	2	33	11	127	47	204	398	78	11029	55	94	
Zircon_3_010	496	15	2060	2	0	30	0	5	9	4	48	16	183	67	294	564	113	9661	102	160	
Zircon_30_042	923	16	5754	5	1	90	2	27	44	17	194	57	594	194	771	1334	244	10272	301	293	
Zircon_31_044	308	24	1783	2	0	35	0	3	8	3	43	14	167	61	263	492	93	10512	102	136	
Zircon_32_045	743	7	3376	3	1	51	2	20	25	9	101	31	337	115	481	911	177	8294	138	175	
Zircon_34_047	390	15	2040	2	0	28	0	7	12	5	56	17	192	68	293	561	109	9782	107	138	
Zircon_35_048	1091	11	4456	3	0	51	0	8	18	8	100	33	388	146	648	1271	247	8680	244	296	
~~Zircon_36_050~~	2818	14	2724	3	21	89	8	43	18	5	67	21	245	89	394	771	152	11547	148	247	High P La
Zircon_38_052	760	10	3557	3	0	43	1	10	20	8	99	31	342	120	508	947	180	9348	164	202	
~~Zircon_39_053~~	2064	6	6941	5	11	127	6	52	58	21	241	69	717	237	947	1571	293	10255	384	330	High P La
Zircon_4_011	929	1	3488	3	0	46	0	6	15	6	84	28	322	117	496	914	170	10462	202	255	
Zircon_40_054	651	7	2571	2	0	36	0	5	12	5	67	21	243	87	362	658	122	10787	126	168	
Zircon_5_012	666	13	3026	2	0	35	0	8	15	7	78	24	278	101	437	841	165	8919	155	183	
Zircon_6_014	879	17	3683	3	0	46	1	9	19	8	96	30	343	124	529	996	189	8700	205	237	
Zircon_8_016	865	12	2989	4	1	39	1	6	10	3	64	23	272	99	428	798	154	11441	252	312	
Zircon_9_017	776	5	3595	6	0	65	1	8	14	6	84	28	329	118	501	913	177	10976	217	302	
Zircon_11_020	687	6	2875	3	1	41	1	12	18	8	77	25	276	97	410	765	142	10689	154	209	
Zircon_37_051	866	6	4103	4	0	60	1	12	22	8	109	34	383	134	569	1026	202	10188	227	288	

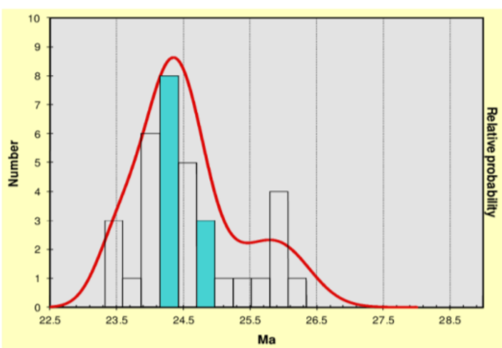

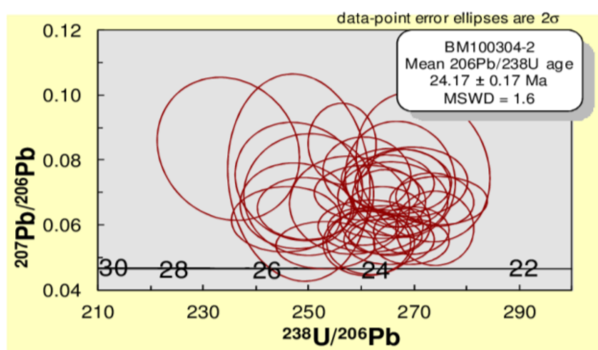

[1]: U and Th concetrations are calibrated relative to the analysis of NIST 612 trace element standard glass.
[2]: Isotopic ratios are corrected relative to analysis of the Plesovice standard zircon (Sláma et al., 2008) for mass bias and down-hole fractionation (see text for further explanations on error propagation). The Andersen (2002) common Pb correction method is further applied.
[3]: Isotopic ratio errors are absolute and expressed at 1-sigma level. See Solari et al. (2010) for further explanations
Apparent age errors are expressed at ± 1 sigma.

Andersen T., 2002, Correction of common lead in U–Pb analyses that do not report ^{204}Pb: Chemical Geology, 192, 59-79.

Sláma, J., Košler, J., Condon, D.J., Crowley, J.L., Gerdes, A., Hanchar, J.M., Horstwood, M.S.A., Morris, G.A., Nasdala, L., Norberg, N., Schaltegger, U., Schoene, B., Tubrett, M.N., Whitehouse, M.J., 2008. Plešovice zircon - A new natural reference material for U-Pb and Hf isotopic microanalysis. Chemical Geology, 249, 1-35.

Solari, L.A., Gómez-Tuena, A., Bernal, J.P., Pérez-Arvizu, O., Tanner, M., 2010. U-Pb zircon geochronology by an integrated LA-ICPMS microanalytical workstation: achievements in precision and accuracy. Geostandards and Geoanalytical Research, 34(1), 5-18.

APPENDIX 3:

CATHODOLUMINESCENCE IMAGES OF ZIRCONS FROM U-Pb LASER ABLATION ICP-MS ANALYSES

Cathodoluminescence images of zircons from U-Pb laser ablation–inductively coupled plasma–mass spectrometry analyses

Numbered red points: zircon number and laser spot location; spot size = 40 microns

See Appendix 2 for details

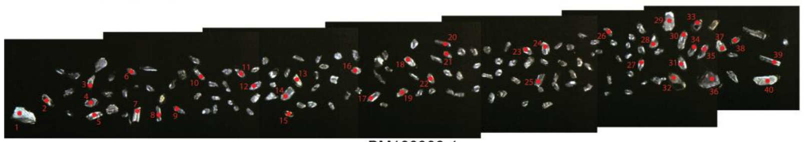

BM100306-1

BM100306-3

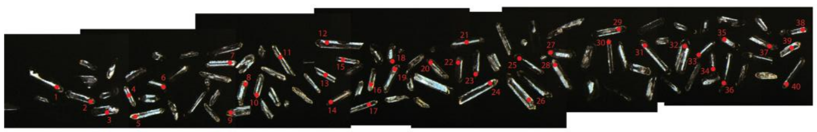

BM100305-4

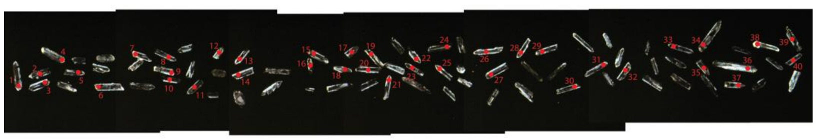

BM100306-6

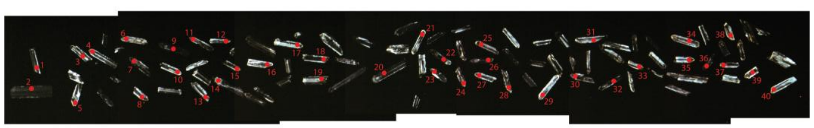

BM100305-2

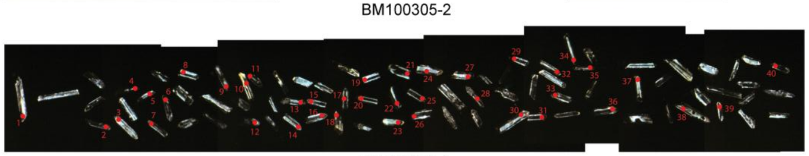

BM100305-1

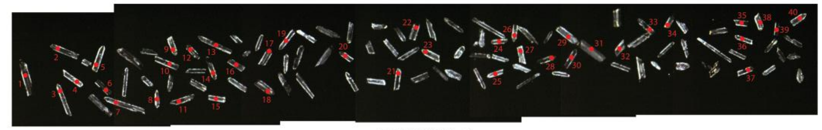

BM100304-2

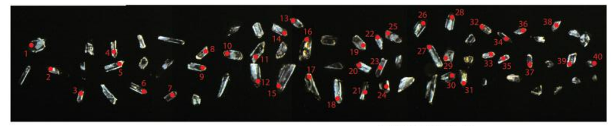

BM100304-4

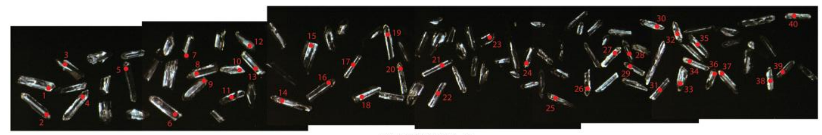

BM100304-5

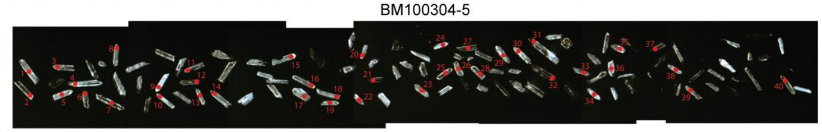

BM100304-1

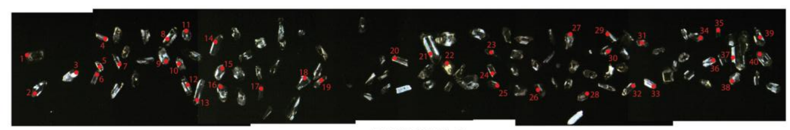

BM100304-3

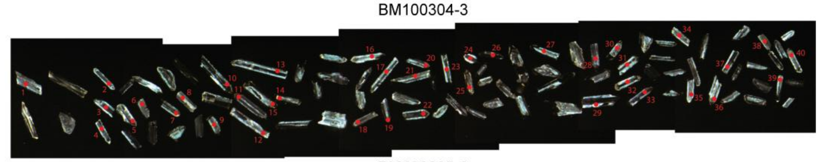

BM100305-3

BM100307-1

APPENDIX 4:

CEROCAHUI BASIN REGION ZIRCON U-Pb LASER ABLATION ICP-MS

ANALYTICAL RESULTS

BM080719-7 **Irigoyen ignimbrite (Tciy)** **Mean $^{206}Pb/^{238}U$ age (±2σ): 28.1 ± 0.8 Ma**

				CORRECTED RATIOS[2]									CORRECTED AGES (Ma)						
	U[1] (ppm)	Th[1] (ppm)	Th/U	$^{207}Pb/^{206}Pb$	±1σ[3]	$^{207}Pb/^{235}U$	±1σ[3]	$^{206}Pb/^{238}U$	±1σ[3]	$^{208}Pb/^{232}Th$	±1σ[3]	Rho	$^{206}Pb/^{238}U$	±1σ	$^{207}Pb/^{235}U$	±1σ	Best age (Ma)	±1σ	
Zircon_4_011	103	67	0.50	0.07446	0.01167	0.04398	0.00733	0.00428	0.00013	0.00129	0.00004	0.27	27.6	0.8	44	7	27.6	0.8	
Zircon_39_052	339	194	0.98	0.06252	0.00875	0.03624	0.00513	0.00432	0.00009	0.0012	0.00008	0.15	27.8	0.6	36	5	27.8	0.6	
Zircon_27_039	100	67	0.77	0.056	0.00728	0.0341	0.00449	0.00442	0.00009	0.00078	0.00008	0.16	28.4	0.6	34	4	28.4	0.6	
Zircon_19_029	281	194	0.61	0.05726	0.00997	0.03715	0.00717	0.0047	0.00017	0.00146	0.00009	0.29	30	1	37	7	30	1	
Zircon_26_038	93	53	0.70	0.06322	0.00921	0.0432	0.00723	0.00496	0.00022	0.00152	0.00006	0.32	32	1	43	7	32	1	
Zircon_28_040	92	60	0.62	0.03331	0.01332	0.05174	0.02073	0.00752	0.00017	0.00536	0.0005	0.06	48	1	51	20	48	1	*
Zircon_34_047	690	549	1.17	0.05136	0.00262	0.05205	0.00308	0.00745	0.00022	0.00221	0.00007	0.51	48	1	52	3	48	1	*
Zircon_2_009	197	138	0.59	0.0558	0.00329	0.09293	0.00579	0.01177	0.00024	0.00296	0.00033	0.32	75	2	90	5	75	2	*
Zircon_24_035	173	107	0.54	0.05347	0.00321	0.10014	0.00608	0.01366	0.00012	0.00456	0.00019	0.15	87.5	0.8	97	6	87.5	0.8	*
Zircon_14_023	74	43	0.55	0.0546	0.0047	0.11531	0.01033	0.01592	0.0004	0.00621	0.00048	0.28	102	3	111	9	102	3	*
Zircon_6_014	580	977	0.41	0.05425	0.00152	0.12162	0.00366	0.01628	0.00018	0.00524	0.00018	0.36	104	1	117	3	104	1	*
Zircon_31_044	186	150	0.20	0.06682	0.0016	0.46762	0.01235	0.05057	0.00056	0.0292	0.00102	0.42	318	3	390	9	318	3	*
Zircon_16_026	142	124	0.83	0.05698	0.00177	0.6	0.02428	0.07755	0.00202	0.02579	0.00083	0.64	481	12	477	15	481	12	*
Zircon_5_012	767	165	0.58	0.10442	0.00209	3.6066	0.08065	0.25101	0.00251	0.09532	0.00305	0.45	1444	13	1551	18	1704	36	*

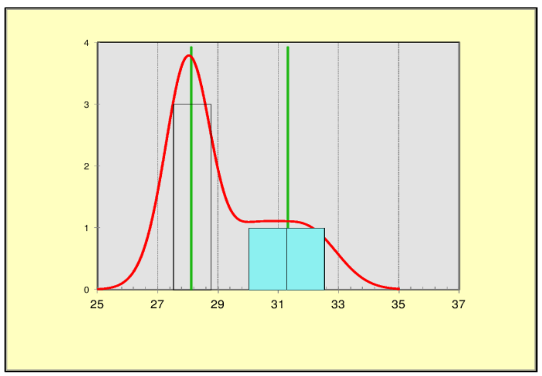

Age	±2σ	fraction	±2σ
28.12	0.8	0.70	0.80
31.3	2	0.30	---

relative misfit = 0.653

Sigma-Rho Matrix

	f1	t1	t2
f1	0.398	0.148	0.205
t1	0.148	.401	0.252

*** = xenocrystic zircons (> 38 Ma) excluded from age calculation**

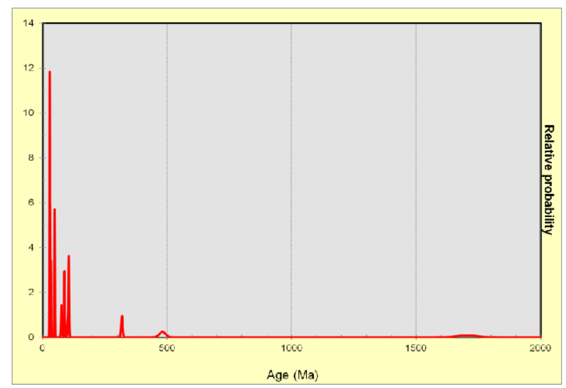

BM080718-1 **Cerro Colorado ignimbrite (Tcic)** **Mean $^{206}Pb/^{238}U$ age (±2σ): 26.0 ± 0.3 Ma**

	U^1 (ppm)	Th^1 (ppm)	Th/U	CORRECTED RATIOS[2] $^{207}Pb/^{206}Pb$	±1σ[3]	$^{207}Pb/^{235}U$	±1σ[3]	$^{206}Pb/^{238}U$	±1σ[3]	$^{208}Pb/^{232}Th$	±1σ[3]	Rho	CORRECTED AGES (Ma) $^{206}Pb/^{238}U$	±1σ	$^{207}Pb/^{235}U$	±1σ	Best age (Ma)	±1σ
Zircon_14_023	218	198	0.82	0.06301	0.00353	0.03391	0.00197	0.00394	0.00006	0.00121	0.00003	0.26	25.3	0.4	34	2	25.3	0.4
Zircon_29_041	226	207	0.83	0.06472	0.00337	0.0356	0.00192	0.004	0.00006	0.00128	0.00003	0.26	25.7	0.4	36	2	25.7	0.4
Zircon_30_042	215	195	0.82	0.05358	0.00316	0.0294	0.00178	0.004	0.00005	0.00124	0.00003	0.23	25.7	0.3	29	2	25.7	0.3
Zircon_28_040	145	122	0.76	0.05988	0.00437	0.03281	0.00245	0.00402	0.00006	0.00121	0.00004	0.21	25.9	0.4	33	2	25.9	0.4
Zircon_5_012	602	780	1.17	0.05432	0.00282	0.03022	0.00161	0.00404	0.00004	0.0013	0.00002	0.23	26	0.3	30	2	26	0.3
Zircon_13_022	155	166	0.96	0.05743	0.00766	0.03209	0.0046	0.00405	0.00007	0.00126	0.00003	0.22	26.1	0.5	32	5	26.1	0.5
Zircon_22_033	121	107	0.80	0.06385	0.00494	0.03583	0.00307	0.00407	0.00008	0.00125	0.00002	0.28	26.2	0.5	36	3	26.2	0.5
Zircon_3_010	313	254	0.73	0.06123	0.00374	0.03394	0.00213	0.00408	0.00006	0.00126	0.00004	0.23	26.2	0.4	34	2	26.2	0.4
Zircon_6_014	235	255	0.98	0.05267	0.00507	0.02962	0.00323	0.00408	0.00009	0.00128	0.00003	0.29	26.2	0.6	30	3	26.2	0.6
Zircon_12_021	215	227	0.95	0.06134	0.00487	0.03462	0.00311	0.00409	0.00007	0.00126	0.00002	0.34	26.3	0.4	35	3	26.3	0.4
Zircon_16_026	94	78	0.75	0.06793	0.00505	0.03932	0.00332	0.0042	0.0001	0.00128	0.00003	0.32	27	0.6	39	3	27	0.6
Zircon_4_011	271	189	0.63	0.05816	0.0032	0.0332	0.00192	0.00419	0.00008	0.00118	0.00004	0.31	27	0.5	33	2	27	0.5
Zircon_8_016	108	77	0.64	0.07537	0.00513	0.04319	0.00307	0.00426	0.00009	0.00139	0.00006	0.29	27.4	0.6	43	3	27.4	0.6
Zircon_2_009	112	73	0.59	0.09334	0.01274	0.0558	0.0084	0.00434	0.00013	0.00128	0.00004	0.47	27.9	0.8	55	8	27.9	0.8
Zircon_20_030	83	64	0.69	0.06894	0.00517	0.04067	0.00314	0.00433	0.00008	0.00137	0.00007	0.24	27.9	0.5	40	3	27.9	0.5
Zircon_10_018	83	69	0.75	0.08638	0.00466	0.05207	0.00298	0.00436	0.00008	0.00162	0.00021	0.33	28	0.5	52	3	28	0.5
Zircon_25_036	116	90	0.70	0.06802	0.00885	0.04086	0.00596	0.00436	0.00014	0.00133	0.00004	0.46	28	0.9	41	6	28	0.9
Zircon_27_039	95	60	0.57	0.07666	0.00679	0.04639	0.00449	0.00439	0.00011	0.00132	0.00003	0.33	28.2	0.7	46	4	28.2	0.7
Zircon_24_035	110	64	0.53	0.07213	0.00943	0.04403	0.00611	0.00443	0.00012	0.00134	0.00004	0.32	28.5	0.8	44	6	28.5	0.8
Zircon_9_017	186	168	0.82	0.05783	0.00421	0.03534	0.00285	0.00443	0.00007	0.00137	0.00002	0.28	28.5	0.4	35	3	28.5	0.4
Zircon_7_015	115	72	0.57	0.07259	0.00465	0.04436	0.00295	0.00447	0.00008	0.00142	0.00006	0.27	28.8	0.5	44	3	28.8	0.5
Zircon_19_029	78	42	0.49	0.06235	0.00617	0.03845	0.00393	0.00459	0.00011	0.00141	0.00008	0.25	29.5	0.7	38	4	29.5	0.7

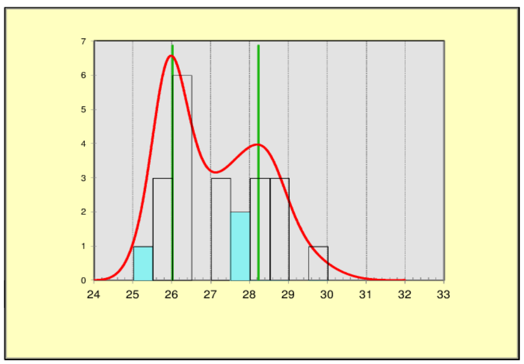

Age	±2σ	fraction	±2σ
26.01	0.26	0.54	0.33
28.23	0.43	0.46	---

relative misfit = 0.432

Sigma-Rho Matrix

	f1	t1	t2
f1	0.164	0.113	0.142
t1	0.113	.13	0.193

[1]: U and Th concetrations are calibrated relative to the analysis of NIST 612 trace element standard glass.

[2]: Isotopic ratios are corrected relative to analysis of the Plesovice standard zircon (Sláma et al., 2008) for mass bias and down-hole fractionation (see text for further explanations on error propagation). The Andersen (2002) common Pb correction method is further applied.

[3]: Isotopic ratio errors are absolute and expressed at 1-sigma level. See Solari et al. (2010) for further explanations

Apparent age errors are expressed at ± 1 sigma.

Andersen T., 2002, Correction of common lead in U–Pb analyses that do not report ^{204}Pb: Chemical Geology, 192, 59-79.

Sláma, J., Košler, J., Condon, D.J., Crowley, J.L., Gerdes, A., Hanchar, J.M., Horstwood, M.S.A., Morris, G.A., Nasdala, L., Norberg, N., Schaltegger, U., Schoene, B., Tubrett, M.N., Whitehouse, M.J., 2008. Plešovice zircon - A new natural reference material for U-Pb and Hf isotopic microanalysis. Chemical Geology, 249, 1-35.

Solari, L.A., Gómez-Tuena, A., Bernal, J.P., Pérez-Arvizu, O., Tanner, M., 2010. U-Pb zircon geochronology by an integrated LA-ICPMS microanalytical workstation: achievements in precision and accuracy. Geostandards and Geoanalytical Research, 34(1), 5-18.